

Effect of Deformation upon the Intensity of the Raman Radial Breathing Modes of Single-wall Carbon Nanotubes in Epoxy/SWNT Composites

A thesis submitted to
The University of Manchester
for the degree of
Doctor of Philosophy
in the
Faculty of Engineering and Physical Sciences

2005

Marcel Lucas

School of Materials

Contents

Acknowledgments	8
List of Symbols	9
List of Abbreviations	12
Abstract	14
Declaration	15
Copyright Statement	15
1 General Introduction	16
2 Carbon Nanotubes	18
2.1 Structure	18
2.2 Synthesis Methods	20
2.2.1 Arc-Discharge Method	20
2.2.2 Laser Vaporization	20
2.2.3 Chemical Vapor Deposition (CVD)	21
2.2.4 Gas Phase Catalytic Growth	21
2.3 Properties	22
2.3.1 Electronic Properties	22
2.3.2 Mechanical Properties	24
2.3.3 Chemical Properties	25
2.4 Applications	25
2.4.1 Nanoelectronics	25
2.4.2 Composite Reinforcement	26
2.4.3 Field Emission	26
2.4.4 Hydrogen Storage	27
2.4.5 Nanosensors	27

3 Raman Spectroscopy	29
3.1 Theory	29
3.1.1 Classical Description	29
3.1.2 Quantum Mechanical Description	31
3.1.3 Anti-Stokes/Stokes Intensity Ratio	32
3.2 Raman Spectroscopy on Carbon Nanotubes	33
3.2.1 G Band	33
3.2.2 D Band	33
3.2.3 G' Band	34
3.2.4 Radial Breathing Modes (RBMs)	35
3.2.5 Intermediate Range Peaks	35
3.3 Resonant Raman Spectroscopy	36
3.3.1 G Band	36
3.3.2 Radial Breathing Modes (RBMs)	37
3.3.3 G' Band	38
3.3.4 Stokes, Anti-Stokes Spectra	38
3.4 Polarized Raman Spectroscopy	40
3.5 Effect of Deformation on the Raman Spectra	41
3.6 Effect of Chemical Treatments on the Raman Spectra	44
3.7 Effect of Temperature on the Raman Spectra	46

4 Structure Determination and Chirality

Assignment	49
4.1 Control over the Structure of Synthesis Products ...	49
4.2 Scanning Tunneling Microscopy (STM)	50
4.3 Electron Diffraction	51
4.4 Raman Spectroscopy	52
4.5 Other Spectroscopic Techniques	53

4.6 Accuracy of the Chirality Assignment	54
4.6.1 Reliability of the Different Spectroscopic Techniques	54
4.6.2 Theoretical Values of the E_{ii} Values	55
4.6.3 Effect of Environment	56
5 Electronic Structure and Density of States	59
5.1 Tight-Binding Model Including Only Nearest-Neighbor Interactions (TB1)	59
5.1.1 Theoretical Approach	59
5.1.2 Results	64
5.1.3 Effect of Deformation	69
5.2 Tight-Binding Model Including Interactions with Third Nearest-Neighbor (TB3)	71
5.2.1 Theoretical Approach	71
5.2.2 Results	77
5.2.3 Effect of Deformation	83
5.3 Comparison with Experimental Results for Semiconducting Nanotubes	84
5.4 Comparison with Experimental Results for Metallic Nanotubes	88
5.5 Conclusions	92
6 Deformations of SWNTs Composites	94
6.1 Experimental Procedures	94
6.1.1 Nanotube Samples	94
6.1.2 Epoxy Composite Preparation	95
6.1.3 PVA Film Preparation	95
6.1.4 Raman Spectroscopy	95
6.1.5 Strain Gauge	97

6.1.6	Four-Point Bending Tests	98
6.2	Raman Spectroscopy on Carbon Nanotube Powder Before Deformation	99
6.2.1	HiPco Nanotubes	99
6.2.2	Elicarb Nanotubes	103
6.3	Raman Spectroscopy on SWNTs Composites	107
6.3.1	HiPco Nanotube Composites	107
6.3.2	Elicarb Nanotube Composites	109
6.3.3	Upshift of the RBM Positions in Composite	111
6.4	Deformation Test Results	112
6.4.1	HiPco Nanotube Composites	112
6.4.1.1	830 nm Laser ($E_{laser} = 1.49$ eV)	112
6.4.1.2	780 nm Laser ($E_{laser} = 1.59$ eV)	117
6.4.1.3	632 nm Laser ($E_{laser} = 1.96$ eV)	123
6.4.2	PVA/Elicarb Nanotube Films	128
6.4.2.1	830 nm Laser ($E_{laser} = 1.49$ eV) and 780 nm Laser ($E_{laser} = 1.59$ eV)	128
6.4.2.2	632 nm Laser ($E_{laser} = 1.96$ eV)	139
6.4.3	Discussion	143
6.5	Effect of Deformation on the RBM Intensity and Structure Determination	147
6.5.1	Resonance Theory	147
6.5.2	Efficiency of the Load Transfer	149
6.5.3	Structure Assignments Based on the TB1 Model	150
6.5.3.1	830 nm and 780 nm Laser ($E_{laser} = 1.49$ eV and 1.59 eV)	153
6.5.3.2	632 nm Laser ($E_{laser} = 1.96$ eV)	157
6.5.4	Structure Assignments Based on the TB3 Model	158
6.5.5	Structure Assignments Based on the Experimental E_{ii} Values	164
6.6	Conclusions	170

7 Effect of Residual Stresses Upon the RBMs of Nanotubes in Epoxy Composites	173
7.1 Introduction	173
7.2 Experimental	174
7.3 Results	175
7.4 Determination of the Thermal Expansion Coefficient of the Epoxy Matrix	184
7.5 Conclusions	185
8 Conclusions	186
8.1 Raman Spectroscopy on SWNTs	186
8.2 Effect of Uniaxial Deformation on the Intensity of the Raman RBMs of Nanotubes	186
8.3 Tight-Binding Calculations on the electronic DOS of Nanotubes	187
8.4 Structure Assignments by Raman Spectroscopy ...	188
8.5 Effect of Residual Stresses Upon the RBMs of Nanotubes in Epoxy Composites	189
9 Suggestions for Future Work	190
9.1 Different Laser Wavelengths and Polymer Matrices	190
9.2 Different Nanotube Sources	190
9.3 Pressure	191
9.4 Isolated Carbon Nanotubes	191

Appendix I: Electronic Band Structure Calculations	193
I.1 The TB1 Model	193
I.1.1 Procedure	193
I.1.2 C/C++ Code	193
I.1.3 Convergence	196
I.1.4 Resolution in Energy	197
I.1.5 Computation Time	199
I.2 The TB3 Model	200
I.2.1 Procedure	200
I.2.2 C/C++ Code	200
I.2.3 Convergence	205
I.2.4 Resolution in Energy	206
I.2.5 Computation Time	206
Appendix II: Heating Effects on the Band Position	208
II.1 Laser Power Effect on the Band Position	208
II.1.1 D, G and G' Bands	208
II.1.2 RBMs	211
II.2 Focus Effect on the Band Position	217
II.2.1 D, G and G' Bands	218
II.2.2 RBMs	221
II.3 Hot Stage Experiments	234
II.4 Discussion	243
References	245

Acknowledgments

First, I would like to acknowledge Professor Young for offering me the opportunity to undertake a Ph.D. course in Manchester on carbon nanotubes. I also thank him for his guidance, patience, unconditional support and encouragement. This work was supported through the European Union Thematic Network CNT-NET and partially funded by the EPSRC.

During the past three years, I have learned so much about science and even more about life in general. It is difficult to believe that all of this was made possible with a simple e-mail sent about three years ago. I would like to acknowledge S.T. and D.L. for their support and for encouraging me to look for a Ph.D. project abroad.

I would like to thank Neil Wilson and Dr. Julie MacPherson of the University of Warwick for the supply of individual nanotubes that were used in this work and our fruitful discussions. I also have to acknowledge Dr. Day and his group for their support and our valuable discussions.

I am grateful for the assistance of the Materials Science Centre staff, especially Mike Faulkner and Andy Forrest for their help on the SEM and AFM, respectively. And I would like to thank in particular Neil Wardman for his assistance for the Raman spectroscopy equipment and our valuable discussions.

Finally, I would like to thank my colleagues and friends, in the Raman group and outside the university, for making the past three years so fun and enjoyable.

List of Symbols

a_0	Length of the vectors \vec{a}_1 and \vec{a}_2
\vec{a}_1	First lattice vector of a graphite sheet
\vec{a}_2	Second lattice vector of a graphite sheet
α	Polarizability
α_i	Angle between the incident laser beam polarization and the nanotube axis
\hat{c}	Unit vector along the nanotube circumference
\vec{C}_h	Chiral vector defining the nanotube circumference
d	Diameter of the nanotube
\vec{E}	Electric field
E	Energy
E_{laser}	Laser excitation energy
E_{ii}	Energy separation between the i th pair of van Hove singularities for nanotubes
E_{11}^M	Energy separation between the first pair of van Hove singularities for metallic nanotubes
E_{11}^S	Energy separation between the first pair of van Hove singularities for semiconducting nanotubes
E_{22}^S	Energy separation between the second pair of van Hove singularities for semiconducting nanotubes
ε_{2p}	Site energy for π orbitals
ε	Strain
ε_c	Strain along the nanotube circumference
ε_t	Strain along the nanotube axis
ξ_m	Thermal expansion coefficient of the epoxy matrix
ξ_n	Thermal expansion coefficient of nanotubes along their axis
γ	Hopping parameter
Γ	Half width of the Breit-Wigner-Fano peak

$\gcd(n,m)$	Greatest common divisor of the two integers n and m
h	Planck's constant
H	Hamiltonian
I	Intensity of the Raman signal
k	Boltzmann's constant
\vec{k}	Wave vector
k_c	Wave vector component along the circumference
k_t	Wave vector component along the nanotube axis
λ	Wavelength
(n,m)	Indexes defining the nanotube structure
ν	Frequency
N	Number of unit cells
N_{hex}	Number of hexagons
ω	Raman wave number
$\Delta\omega$	Full width at half maximum
p	Integer nearest to $(n-m)$ divided by 3
P	Pressure
\vec{P}	Induced dipole moment
ψ	Wave function
φ	Wave function
q	Remainder of $(n-m)$ divided by 3
Q	Measure of the interaction between phonons and electrons
Q_j	Normal vibrational mode
\vec{r}	Location vector
S	Overlap integral
t	Time
T	Temperature
T_g	Glass transition temperature
\vec{T}	Translational vector along the nanotube axis
\vec{t}_1	\vec{T} component along \vec{a}_1
\vec{t}_2	\vec{T} component along \vec{a}_2

\hat{t}	Unit vector along the nanotube axis
θ	Nanotube chiral angle
X	Wave function

List of Abbreviations

Å	Ångström
AFM	Atomic Force Microscope
BWF	Breit-Wigner-Fano
°C	Celsius degree
CCD	Charge Coupled Device
cm ⁻¹	Raman wave number
CVD	Chemical Vapor Deposition
DOS	Density of States
eV	Electron-Volt
GPa	Gigapascal
JDOS	Joint Density of States
K	Kelvin degree
kbar	Kilobar
µm	Micrometer
µW	Microwatt
mm	Millimeter
meV	Milli-electron-Volt
mW	Milliwatt
MWNT	Multi-Walled Carbon Nanotubes
nm	Nanometer
PMMA	Poly (Methyl Methacrylate)
PVA	Poly (Vinyl Alcohol)
RBM	Radial Breathing Mode
STM	Scanning Tunneling Microscopy
STS	Scanning Tunneling Spectroscopy
SWNT	Single-Wall Carbon Nanotubes
TB1	Tight-Binding model including only the interactions with the nearest-neighboring carbon atoms in the hexagonal lattice
TB3	Tight-Binding model that includes the interactions with up to the third-nearest neighboring carbon atoms

TEM	Transmission Electron Microscopy
TPa	Terapascal
vHs	Van Hove singularity
W	Watt
wt.%	Weight %

Abstract

The intensity variations of the Raman Radial Breathing Modes (RBMs) of Single-Wall Carbon Nanotubes (SWNTs) in epoxy/SWNT composites and Poly(Vinyl Alcohol) PVA/SWNT films were investigated as a function of strain using three different lasers of wavelengths 830, 780 and 632 nm. Variations of between 10% and 200% in the RBM intensities were observed over a range of strain between -0.6% and 0.7%. The trend (increase or decrease) as well as the magnitude of the intensity variations depends on the nanotube diameter and its chirality. Using tight-binding calculations, these intensity variations can be explained entirely by resonance theory. The electronic band structure of SWNTs is predicted to vary significantly with uniaxial strain. Electronic density of states calculations confirm that the energy of the electronic transitions shifts with strain, becoming closer or further away from the laser excitation energy depending on the nanotube structure. The nanotubes are thus moved closer or further away from resonance, causing the intensity variations. It is demonstrated that through the use of resonance theory, a tentative chirality can be assigned to each type of SWNT from knowledge of its RBM position and the effect of strain upon the RBM intensity, thus determining its entire structure.

Declaration

No portion of the work referred to in the thesis has been submitted in support of an application for another degree or qualification of this or any other university or other institute of learning.

Copyright Statement

Copyright in text of this thesis rests with the Author. Copies (by any process) either in full, or of extracts, may be made only in accordance with instructions given by the Author and lodged in the John Rylands University Library of Manchester. Details may be obtained from the Librarian. This page must form part of any such copies made. Further copies (by any process) of copies made in accordance with such instructions may not be made without the permission (in writing) of the Author.

The ownership of any intellectual property rights which may be described in this thesis is vested in The University of Manchester, subject to any prior agreement to the contrary, and may not be made available for use by third parties without the written permission of the University, which will prescribe the terms and conditions of any such agreement.

Further information on the conditions under which disclosures and exploitation may take place is available from the Head of School of Materials.

Chapter 1

General Introduction

Since their discovery more than a decade ago, Single-Wall Carbon Nanotubes (SWNTs) have received considerable attention, due to their exceptional properties and their potential applications. These large molecules made only of carbon atoms have a tubular structure with a diameter down to several Ångströms and a length up to several microns. Their extremely high tensile modulus makes them one of the stiffest materials ever discovered. They are expected to be used in many potential applications, such as electronic components, reinforcement in composite materials, hydrogen or chemical storage. However, a major difficulty has to be overcome: the control over the nanotube structure during the synthesis. Despite the recent advances in the synthesis methods, only limited amounts of nanotubes are available and the nanotube materials produced contain generally a broad range of nanotube diameters and chiralities. The determination of the (n,m) indexes defining the entire structure of the SWNTs remains a challenge and is essential for both large-scale applications and scientific studies.

Several research groups are currently trying to develop new electronic components at the nanoscale level using carbon nanotubes. Others are developing new conductive composite materials with carbon nanotubes. In these samples, the carbon nanotubes are subject to external strains due to the interaction with the substrate or with the polymer matrix surrounding them, which might change their electronic properties. Controlling the nanotube structure and their properties during the synthesis is a major challenge, and assuring that these desired properties are conserved in real devices is another one.

Resonant Raman spectroscopy has proven to be a powerful and non-destructive tool for the study of carbon nanotubes. It is widely used to characterize raw nanotube samples, but it can also be used to study their electronic properties, their deformation under strain and recently to determine

their structure. This work has two main purposes:

- to study the effect of strain on the electronic properties of the carbon nanotubes by Raman spectroscopy.
- to develop a new and more reliable way to determine the carbon nanotube structure using Raman spectroscopy.

Chapter 2 is a brief introduction on carbon nanotubes. Their structure, synthesis methods, properties and potential applications are reviewed. Chapter 3 is a review of some experimental results obtained by Raman spectroscopy from carbon nanotubes. The main features of a typical Raman spectrum are presented and the resonant Raman scattering process is introduced. Chapter 4 is a review of the different techniques used to determine the atomic structure of nanotubes. Two models based on the tight-binding approximation are introduced in Chapter 5 to calculate the nanotube electronic band structure and density of states and study their behavior under strain. Deformation test results on epoxy/nanotube composites and PVA/nanotube films are showed in Chapter 6, where a new and more reliable way to determine the nanotube structure is introduced. Finally, in Chapter 7, the effect of residual stresses on the low-frequency Raman spectrum is investigated in epoxy/ nanotube composites.

Chapter 2

Carbon Nanotubes

The SWNTs were discovered simultaneously by D.S. Bethune *et al.* in the United States and by S. Iijima *et al.* in Japan in 1993 [1,2], two years after the discovery of the Multi-Walled Carbon Nanotubes (MWNTs). SWNTs were observed for the first time in the soot produced by the arc-discharge technique, using catalyst particles such as iron or cobalt. Following this discovery, several synthesis processes were developed: laser vaporization, chemical vapor deposition, gas phase catalytic growth...

Even though the synthesis parameters were all optimized, several challenges remain: the reaction yield, the purity of the resulting product and also the control over the nanotube structure. The large-scale synthesis of carbon nanotubes is essential to future applications, especially for mechanical reinforcement. Also, the nanotubes produced are generally mixed with other byproducts like graphitic particles, catalyst particles, other fullerenes... Finally, since the properties of SWNTs depend heavily on their structure, the synthesis of nanotubes with a single chirality or with a fine diameter distribution is highly desirable. In this section, the structure of the nanotube and the main synthesis methods are described. Their properties and their potential applications are also presented.

2.1 Structure

A SWNT can be considered as a rolled graphene sheet, capped with fullerene-like hemispheres at its extremities. These cylinder-shaped carbon molecules have a very high aspect ratio, with lengths up to several tens of micrometers and diameters as small as several Ångströms [3].

The carbon atoms are arranged on a hexagonal network (honeycomb structure) (Figure 2.1) and each of them have three neighbors with which it forms strong sp^2 -structure bonds. The nanotube structure is usually described

by its 1D unit cell, defined by the chiral vector \vec{C}_h along its circumference and \vec{T} the translational vector along the nanotube axis.

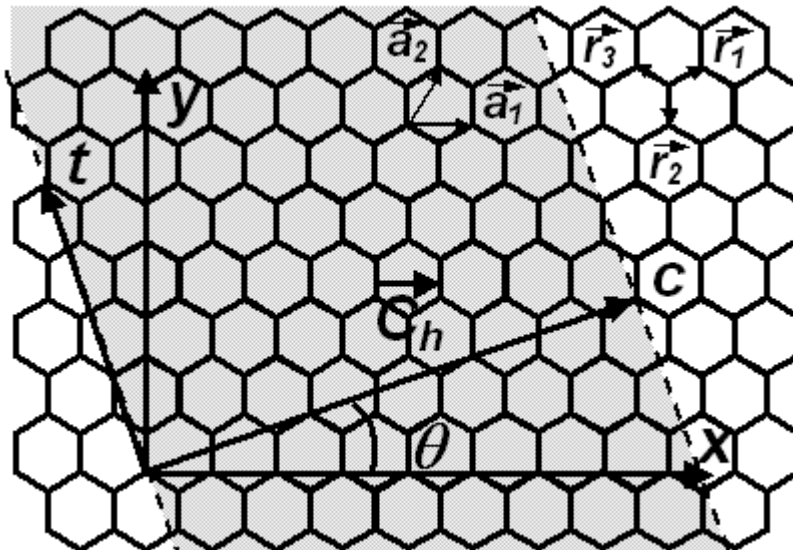


Figure 2.1: Structure of a graphene sheet.

The entire nanotube structure is given by two integers (n,m) which define the components of the chiral vector along the two lattice vectors of the graphite sheet:

$$\vec{C}_h = n \vec{a}_1 + m \vec{a}_2 \quad (2.1)$$

The length of the chiral vector is the circumference of the nanotube:

$$C_h = \sqrt{n^2 + m^2 + nm} \ a_0 \quad (2.2)$$

where a_0 is the length of the lattice vectors $|\vec{a}_1| = |\vec{a}_2| = a_0 = 0.249 \text{ nm}$. The translational vector characterizes the periodicity of the nanotube structure along its axis.

$$\vec{T} = \vec{t}_1 + \vec{t}_2 = t_1 \vec{a}_1 + t_2 \vec{a}_2 \text{ with } \gcd(t_1, t_2) = 1 \quad (2.3)$$

$$t_1 = \frac{2m+n}{\gcd(2n+m, 2m+n)}; \quad t_2 = -\frac{2n+m}{\gcd(2n+m, 2m+n)} \quad (2.4)$$

$$T = |\vec{T}| = \frac{\sqrt{3(n^2 + m^2 + nm)}}{\gcd(2n+m, 2m+n)} a_0 \quad (2.5)$$

where $\gcd(n,m)$ is the greatest common divisor of the two integers n and m .

The chiral angle θ is the angle between the chiral vector and the zigzag direction along \hat{x} . It is given by:

$$\theta = \tan^{-1} \left[\frac{\sqrt{3} n}{2m+n} \right] \quad (2.6)$$

Depending on the (n,m) indexes and the resulting chiral angle, three different types of nanotubes can be distinguished:

- Armchair nanotubes: $n = m$ and $\theta = 30^\circ$.
- Zigzag nanotubes: $m = 0$ and $\theta = 0^\circ$.
- Chiral nanotubes: $n \neq m \neq 0$ with $0^\circ < \theta < 30^\circ$.

MWNTs are made of many coaxial single-walled nanotubes. The distance separating the different walls is similar to the interplane distance of 3.34Å in graphite and the different nanotubes have usually different chiralities.

2.2 Synthesis Methods

2.2.1 Arc-Discharge Method

The arc-discharge method is an inexpensive way to produce, both SWNTs and MWNTs. Two graphite electrodes are contained in a reaction chamber filled with an inert gas (helium). Carbon atoms are evaporated when high currents flow through the electrodes. At the end of the reaction, the black soot inside the chamber is collected. It usually contains fullerenes, MWNTs, SWNTs (if catalyst particles such as nickel, yttrium, cobalt are used) and also graphitic particles. The reaction yield depends on the current, the nature and the pressure of the gas inside the chamber, the catalysts used and also the distance between the electrodes.

2.2.2 Laser Vaporization

The synthesis of SWNTs by pulsed laser vaporization was developed by Guo *et al.* [4], and then improved by Thess *et al.* in 1996 [5]. Large quantities of nanotubes can be produced with this technique, with a fine diameter distribution around 1.4 nm, a better control over the growth conditions than the arc-discharge technique and a lower concentration of amorphous carbon in the

resulting product. However, the technique cannot be upscaled due to its high cost.

In this process, an intense laser beam vaporizes a graphite rod containing a small amount of nickel and cobalt catalyst particles. The vaporized material is carried to a water-cooled collector by an inert gas flow, where the nanotube soot is formed. The growth conditions are controlled by the gas nature, pressure and flow, the intensity of the laser beam, and the relative concentration of catalyst particles.

2.2.3 Chemical Vapor Deposition (CVD)

Chemical Vapor Deposition (CVD) methods have been widely used to produce carbon fibers and other carbon materials. Yacaman *et al.* synthesized MWNTs by the catalytic decomposition of acetylene over iron particles [6].

In this process, catalyst particles are heated in a furnace at high temperatures and in the flow of a hydrocarbon gas. The nanotube material grown on the particles are collected when the furnace is cooled down to room temperature. The main synthesis parameters are the hydrocarbon gas, the temperature of the furnace, the catalyst particles and the substrate on which they are placed, the size of the particles and the reaction time.

Chemical vapor deposition is an easy and inexpensive way to produce nanotube in large quantities. However, the main drawback of these methods is the high density of defects along the nanotube walls.

2.2.4 Gas Phase Catalytic Growth

In 1999, Nikolaev *et al.* [7] developed a gas phase catalytic process to produce large quantities of SWNTs (HiPco process). This is a low-cost technique, which can be used continuously since metal particles are introduced in a gas phase.

A flow of carbon monoxide mixed with iron pentacarbonyl passes through a heated furnace. Iron particles are produced in-situ by the decomposition of iron pentacarbonyl molecules and are used as catalysts for the decomposition of carbon monoxide. The nanotubes produced have diameters as small as

0.7 nm and few amorphous carbon materials are produced. Iron particles remain but they can be removed by acid treatments.

2.3 Properties

2.3.1 Electronic Properties

Tight-binding calculations predicted that the nanotubes would be metallic or semiconducting, depending on their diameter and their structure [8]. All armchair nanotubes are predicted to be metallic, while the zigzag and chiral nanotubes are metallic if the difference $n - m$ is a multiple of 3, and semiconducting otherwise. For the semiconducting nanotubes, the band gap is inversely proportional to their diameter.

Wildoer *et al.* [9] have resolved the atomic structure and probed the electronic density of states of carbon nanotubes simultaneously using Scanning Tunneling Microscopy (STM) and Scanning Tunneling Spectroscopy (STS). Their STS results confirmed that the nanotube electronic properties depend on its structure and were consistent with the tight-binding calculations. Odom *et al.* [10] using the same techniques showed that the band gap of semiconducting nanotubes decreases with increasing diameter.

The electronic band structure and density of states of carbon nanotubes are predicted to be extremely sensitive to strain [11-14] and deformation [15-21]. Their behavior upon deformation depends on the structure of the nanotubes and also on the deformation mode. Using several numerical methods [11-14], band gaps for semiconducting nanotubes were found to vary with uniaxial strain along the nanotube axis. They increase or decrease depending on the nanotube chirality. Uniaxial strain along the nanotube axis also opens a band gap in non-armchair metallic nanotubes, whereas the armchair nanotubes remain metallic. This is due to the variations of orientation of the carbon-carbon bonds with respect to the nanotube axis with chirality. Torsional strain (strain along the circumferential direction) also induces band gap changes, but the chirality dependence of these variations is dramatically different [12,13]. The band structures of armchair nanotubes are sensitive to torsional strain, while the zigzag nanotubes are not affected.

Structural distortions such as bending and twisting of the nanotubes also lead to changes in the electronic band structure [16,18]. Depending on the bending and twisting angle, these deformations can induce the opening of a band gap in armchair metallic nanotubes. Interactions between electrons in σ -state (in-plane orbital) and π -state (out-of-plane orbital), which are generally neglected in straight nanotubes, become significant with increased curvature via bending and twisting.

Radial deformations of the nanotubes when they are dispersed on a substrate [22] or "polygonization" of their cross section under pressure [15] also effect their band structure due to the interaction of σ states and π states. Using local-density approximation calculations, Charlier *et al.* [15] determined the electronic band structure of a (12,0) nanotube with various cross sections. The round, triangular and square cross sections generate metallic nanotubes, while the nanotube with an hexagonal cross section is semiconducting and has a 0.5 eV band gap. Sluitera *et al.* [21] found that the band gap variations depend on the symmetries of armchair nanotubes: polygonization under pressure of bundles of (12,12) nanotubes (with a three-fold symmetry) leads to the opening of a band gap which increases with pressure, but polygonized bundles of (10,10) nanotubes (without a three-fold symmetry) remain metallic.

Using a generalized gradient approximation and tight-binding calculations, Park *et al.* [17] discovered that the flattening of (5,5) and (9,0) nanotubes opens a band gap in these normally metallic nanotubes. Kilic *et al.* [19] predicted and Gulseren *et al.* [20] later confirmed that the band gap generally decreases with the flattening. The magnitude of the electronic band structure changes is sometimes high enough to induce metal-semiconducting transitions [23-25] and leads to noticeable variations in conductance [26].

Few experimental reports have confirmed these theoretical predictions. Paulson *et al.* [27] measured the resistance of a MWNT while applying strain with the tip of an Atomic Force Microscope (AFM). No resistance variation was detected until the nanotube broke. Tombler *et al.* [28] used the same technique on a SWNT suspended over a trench and observed the decrease of the

conductance by two orders of magnitude when the nanotube was deflected by 14°.

Several research groups reported resistance variations in carbon nanotubes under pressure [29-31]. The resistance generally drops slightly until the pressure reaches a critical value between 1.5 and 2.0 GPa. A discontinuity then appears in the resistance value that is usually associated with a phase transition during which the cross section of the nanotube is deformed and turns into a polyhedron.

Recently, Minot *et al.* measured band gap variations with SWNT stretching, using an AFM tip [32]. The SWNT was suspended over a trench with its extremities attached by gold electrodes. Using the AFM tip, strain and a gate voltage were applied simultaneously, enabling the measurement of the band gap as a function of strain. It was proved possible to open a band gap in a metallic nanotube (diameter around 3 nm) and to change the band gap of a semiconducting nanotube (diameter around 4 nm) with strain.

Separately, Cao *et al.* [33] found a way to apply a more uniform uniaxial strain along the nanotube using an AFM tip. They observed resistance variations under uniaxial strain on metallic and semiconducting nanotubes and found that zigzag nanotubes are the most sensitive to uniaxial strain, while the armchair nanotubes are the least sensitive. Tight-binding calculations on the nanotube band structure predict that armchair nanotubes are not sensitive to uniaxial strain [13], while density-functional theory predicts the opening and enlargement of a band gap with uniaxial strain [34].

2.3.2 Mechanical Properties

Carbon nanotubes are strong and flexible at the same time. Due to the very high strength of the sp^2 carbon-carbon bond, carbon nanotubes are predicted to have a tensile modulus between 0.5 and 5.5 TPa [3]. For comparison, the tensile modulus of steel is around 200 GPa. Early experimental values were between 1.0 and 1.8 TPa. Krishnan *et al.* [35] measured the tensile modulus of 27 nanotubes by looking at the thermal vibration amplitudes in a transmission electron microscope. They obtained an average value of 1.25 TPa.

Another remarkable characteristic is their resiliency. Carbon nanotubes can sustain large deformations, such as bending, torsion or flattening of the walls, without irreversible modifications of their atomic structure. At large strains, the nanotubes are subject to buckling and kink forming, without bond breaking.

2.3.3 Chemical Properties

Functional groups, such as -COOH, -CO, or -COH, can be added to carbon nanotubes around open ends or defects along the walls [36]. Using these functional groups, carbon nanotubes can be functionalized with a wide variety of molecules. Chemical functionalization can improve the solubilization of carbon nanotubes in aqueous or organic solutions [37].

2.4 Applications

2.4.1 Nanoelectronics

In 1998, Martel *et al.* showed that a nanotube placed on top of a silicon substrate with electrodes deposited at both ends behaves like a field-effect transistor [22]. The conductance of the nanotube can be modulated by varying the gate voltage. All these transistors prepared in air were p-type transistors (transport dominated by holes). N-type transistors can also be prepared by chemical doping using for example potassium. Derycke *et al.* [38] discovered that n-type transistors can be obtained by annealing the p-type transistors at 700 K for 10 minutes. Its characteristics are preserved in air by coating the device with a PMMA film.

Using these techniques, a voltage inverter (logic gate NO) was prepared using a single nanotube bundle. The nanotube bundle was deposited on top of three electrodes. One half was used as a p-type transistor while the other half was doped with potassium to become an n-type transistor.

Considering the size of these devices, carbon nanotubes could potentially replace the silicon technology to continue the miniaturization of electronic components. However, two challenges remain before any commercial applications: the control over the nanotube growth and the large-scale

production of these nanodevices.

2.4.2 Composite Reinforcement

One possible application of the carbon nanotubes mechanical properties is the reinforcement in composite materials. They combine strength, flexibility, high aspect ratio and a low density. Several research groups have reported that the composite tensile modulus increases with the nanotube concentration. For example, Allaoui *et al.* [39] reported a 290% increase in tensile modulus in epoxy/MWNTs with 4 wt.% of MWNT. Kearns *et al.* [40] reported an increase of 55% in tensile modulus and a 40% increase in tensile strength in polypropylene fibers reinforced with 1 wt.% of MWNTs.

However, several obstacles subsist such as preparing a well-bonded interface to have a good load transfer. A well-bonded interface can be expected with a large surface area, but the surface of the nanotubes is relatively smooth, and the SWNTs are generally assembled into bundles and into aggregates. A poor dispersion of nanotubes in the polymer matrix not only reduces the quality of the polymer-nanotube interface, but the composite tensile strength can also be reduced due to slippage, since the nanotubes in the bundles are maintained together only by weak van der Waals forces. One way to improve the interfacial bonding and the dispersion of nanotubes in the polymer matrix is the covalent chemical functionalization of nanotubes. The reinforcement of elastomers by covalently functionalized nanotubes improves the tensile modulus and strength of the composite, while keeping the elongation at break constant [41].

Moreover, the exceptional mechanical properties of carbon nanotubes cannot be exploited to their full potential if the nanotubes are dispersed isotropically in the composite. Haggenmueller *et al.* [42] and Vigolo *et al.* [43] reported an improvement in mechanical properties with nanotube alignment in PMMA/SWNT melt spun fibers and PVA/SWNT fibers respectively.

2.4.3 Field Emission

Field emission is the emission of electrons by a tunnel effect when a sufficiently high enough electric field is applied [3]. For commercial use, the

electron emissive material must have a low threshold electric field and high stability.

Carbon nanotubes have all the right characteristics for field emission. They can sustain high currents without serious damage and due to their high aspect ratio the threshold electric field is lower than the conventional materials used so far. With this important property, carbon nanotubes can not only be used for flat panel displays, but also as tips for transmission electron microscopy [44].

2.4.4 Hydrogen storage

Hydrogen appears to be a clean energy source that could replace the fossil fuels used for automobiles. However, low storage capacities have prevented hydrogen to be a viable alternative. Considering the tubular structure and the high surface-to-volume ratio of carbon nanotubes, an intense research activity has been generated [3].

Early results indicate that the maximum storage capacity is between 1 and 10 wt.% of H₂. But so far, there is some controversy about the storage capacity of carbon nanotubes due to the lack of reproducibility of the results. Moreover, the mechanism of hydrogen storage is still unclear [45].

2.4.5 Nanosensors

The electrical conductance of carbon nanotubes was thought to be dramatically affected by the adsorption of gas molecules on its surface. Collins *et al.* [46] reported that the conductance through nanotube-based field effect transistors can be reversibly tuned by the adsorption of small amounts of gas molecules, resulting in the chemical doping of nanotubes. Using this principle, biosensors were developed and were able to detect traces of proteins [47]. However, later it was found that a charge transfer from the adsorbed oxygen to the nanotube cannot explain the change in electrical conductance [38]. Instead, the adsorbed molecules affect mostly the conductance between the metallic contacts and the nanotube [48].

Modi *et al.* [49] fabricated a gas ionization sensor using a film of aligned MWNTs as an anode. When a potential is applied between this anode and an aluminum sheet, a discharge can be created between them and the threshold potential to create this discharge is characteristic of the gas detected.

Resonant Raman spectroscopy has proven to be a powerful tool to probe simultaneously the structural properties of SWNTs [50], and the local strains in epoxy/SWNTs composites [51]. The position of several Raman bands shifts with strain, due to the expansion or contraction of the carbon bonds. Using a fine laser spot, accurate strain mappings could be obtained with nanotubes as strain sensors.

Chapter 3

Raman Spectroscopy

Raman spectroscopy is a widely used technique to probe the vibrational states of gases, liquids and solids. The Raman effect was discovered in 1928 by Sir Chandrasekhara Venkata Raman [52]. When light passes through a sample of a given chemical compound, most of it is transmitted without wavelength change. However, a small amount of it is scattered inelastically (wavelength variation) in directions different from the one of the incoming beam. This phenomenon is called the Raman effect.

Soon after the discovery of the SWNTs, Raman spectroscopy was proven to be a powerful and non-destructive technique to characterize the raw nanotube samples. In this chapter, an explanation of the Raman effect is given and the most obvious Raman bands from carbon nanotubes are described. A review of experimental results from carbon nanotubes is presented.

3.1 Theory

3.1.1 Classical Description

When monochromatic light of energy encounters a molecule or matter in general (gas, solid, or liquid), the oscillating electric field of the incoming light interacts with the electric charges in the material, inducing a dipole moment [53]. This induced dipole moment \vec{P} is proportional to the amplitude of the incident electric field \vec{E} :

$$\vec{P} = \alpha \vec{E} \quad (3.1)$$

where α is the polarizability, which depends on the molecule chemical composition and structure.

This induced dipole then radiates scattered light [53]:

- **Elastically:** The wavelength of the scattered light is the same as the incident light. This scattering process is the Rayleigh scattering.

- **Inelastically:** The wavelength of the scattered light is different from the incident light. This process is the Raman scattering.

The Raman effect can be explained by a classical theory, based on the effect of molecular vibrations on the polarizability. The incident electric field is given by:

$$\vec{E} = \vec{E}_0 \cos 2\pi\nu_0 t \quad (3.2)$$

where ν_0 is the frequency of the incident light. The interacting molecule has molecular vibrations composed of normal modes:

$$Q_i = Q_i^0 \cos 2\pi\nu_i t \quad (3.3)$$

where ν_i is the frequency of the i th normal mode. The polarizability of the electrons in the molecule is affected by molecular vibrations:

$$\alpha = \alpha_0 + \left(\frac{\delta\alpha}{\delta Q_j} \right) Q_j + \dots \quad (3.4)$$

Limiting the expansion to the second order terms, the combination of Equations 3.1- 3.4 leads to:

$$\vec{P} = \alpha_0 \vec{E}_0 \cos 2\pi\nu_0 t + \vec{E}_0 Q_i^0 \left(\frac{\delta\alpha}{\delta Q_i} \right) \frac{\cos 2\pi(\nu_0 + \nu_i)t + \cos 2\pi(\nu_0 - \nu_i)t}{2} \quad (3.5)$$

From this Equation 3.5, three processes are predicted:

- The first term corresponds to the Rayleigh scattering. The scattered and incident light have the same frequency ν_0 .
- The second term is the anti-Stokes Raman scattering. The scattered light frequency is the sum of the incident light frequency and the frequency of the vibration mode.
- The third term is the Stokes Raman scattering. The scattered light frequency is the difference between the incident light frequency and the frequency of the vibration mode.

Equation 3.5 also explains the main difference between infrared spectroscopy and Raman spectroscopy. Infrared and Raman spectroscopy are two techniques widely used to probe the vibrational modes of molecules. In contrast to infrared spectroscopy which is sensitive to dipole moment variations, a molecule is Raman active only if polarizability variations are involved. For

example, the polarizability of the C=C bond changes dramatically with stretching, so the Raman scattering is strong, while the infrared absorption is weak.

3.1.2 Quantum Mechanical Description

The classical description cannot explain all the experimental results and additional selection rules from quantum mechanics are needed. The interaction between the electrons in the molecule and the incident laser light is described by electronic transitions between the ground state and an excited vibrational state [53].

In infrared spectroscopy, the electrons absorb the incident photons with an energy equal to the difference of energy between the ground state and the excited vibrational state.

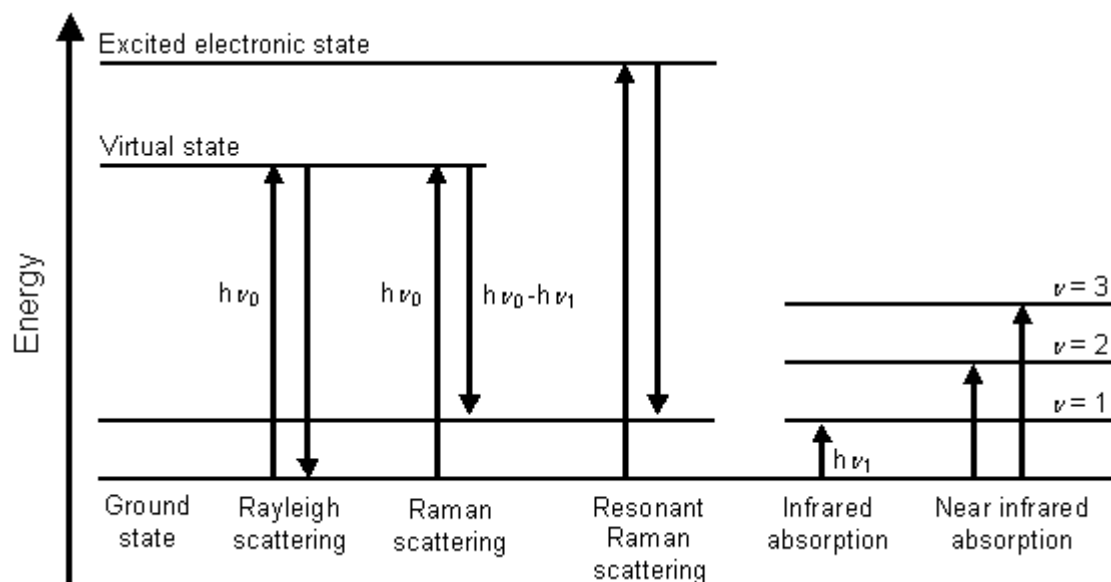


Figure 3.1: Diagram of spectroscopic transitions involved in different types of vibrational spectroscopy. ν_0 indicates the laser frequency, ν_1 indicates the scattered or the absorbed light frequency, while ν is the vibrational quantum number.

In Raman spectroscopy, the electrons are first excited to an electronic state. The latter is usually a "virtual state", which is the result of the distortion of the electronic cloud around the atoms due to the electric field of the incident

light. The electrons then relax with the emission of a photon. Depending on the transition, several processes are expected (Figure 3.1) [53]:

- The final state is the same as the initial state (ground state). The incident light is scattered elastically: this is the Rayleigh scattering.
- The initial state is the ground state, the final state is an excited vibrational state and the intermediate state is a virtual electronic state. The scattered light has a lower frequency than the incident light. The electron in the molecule gains an energy quantum (with the creation of a phonon). This is the typical Stokes Raman scattering.
- The initial state is an excited vibrational state, the final state is the ground state or a lower excited vibrational state, and the intermediate state is a virtual state. The scattered light has a higher frequency than the incident light. The electron in the molecule loses an energy quantum (with the annihilation of a phonon). This is the typical anti-Stokes Raman scattering.
- The Stokes and anti-Stokes Raman scattering can involve an intermediate state, which is a real electronic state. In this particular case, the Raman scattering is termed resonant. The Raman signal is then significantly enhanced.

In all these scattering processes, selection rules exist due to energy and momentum conservation, and also the symmetries in the molecule.

3.1.3 Anti-Stokes/Stokes Intensity Ratio

The anti-Stokes Raman intensity depends on the population of the first excited vibrational state, thus its intensity is usually much weaker than the Stokes intensity. The anti-Stokes/Stokes intensity ratio depends on the temperature and is proportional to the Boltzmann factor [53]:

$$\frac{I_{(\nu_0 + \nu_i)}}{I_{(\nu_0 - \nu_i)}} = \frac{(\nu_0 + \nu_i)^4}{(\nu_0 - \nu_i)^4} \exp\left(\frac{-h\nu_i}{kT}\right) \quad (3.6)$$

where $I_{(\nu_0 + \nu_i)}$ and $I_{(\nu_0 - \nu_i)}$ are the anti-Stokes and Stokes Raman intensity functions respectively, T is the temperature, h and k are Planck's and Boltzmann's constants respectively.

3.2 Raman Spectroscopy on Carbon Nanotubes

The typical Raman spectrum of SWNTs consists of four main features the G band (around 1600 cm^{-1}), the D band (around 1300 cm^{-1}), the G' band (2600 cm^{-1}) and the low-frequency Radial Breathing Modes (RBMs) [51,54,55].

3.2.1 G Band

The G band (for a laser line of wavelength 785 nm) is fitted with 4 Lorentzian lines: a strong peak at around 1590 cm^{-1} with three weaker ones appearing as shoulders around 1540 cm^{-1} , 1560 cm^{-1} and 1605 cm^{-1} . This band is also observed in other sp^2 carbon materials, such as highly oriented pyrolytic graphite, or glassy carbon [56].

The strongest band is actually a triplet of unresolved vibrational modes of symmetry A_{1g} , E_{1g} and E_{2g} . They are associated with vibrations of neighboring carbon atoms in opposite directions along the nanotube axis and its circumference. The band position is independent of the diameter of the nanotube [57]. The lower component around 1560 cm^{-1} is diameter dependent and the splitting between this component and the strongest one at 1590 cm^{-1} is different for metallic and semiconducting nanotubes. The splitting decreases with increasing diameter and becomes zero when the diameter is infinite (or extremely large).

3.2.2 D Band

The D band is located around 1300 cm^{-1} and is usually associated with sp^3 carbon states, defects along the nanotube axis (atom substitution, vacancies, grain boundaries for example), the presence of graphitic particles or crystallites of finite size of several nanometers. It is observed in disordered sp^2 carbon materials but not in highly oriented pyrolytic graphite [56]. The ratio of the intensities of the D and G bands is used to estimate the purity of nanotube synthesis products, the efficiency of purification processes [58], and also to characterize the chemical functionalization of nanotubes [59].

The D band position shows a large dispersion depending on the excitation laser energy. It shows a linear dependence on the excitation laser

energy E_{laser} with a slope of $60 \text{ cm}^{-1}/\text{eV}$, superimposed by an oscillatory behavior [60]. The D band position depends on the nanotube chirality [61] and on its diameter [62]. The examination of raw nanotube material should yield several values of the D band position close to each other, since a large range of chiralities and diameter is expected to be in resonance simultaneously. An analysis of the D band of isolated nanotubes ($E_{laser} = 2.41 \text{ eV}$) showed that its position ω_D and the diameter d of the nanotube are related by the following equation:

$$\omega_D (\text{cm}^{-1}) = 1354.8 - \frac{16.5}{d (\text{nm})} \quad (3.7)$$

This relationship is valid for metallic nanotubes as well as semiconducting nanotubes, isolated or in bundles [62].

3.2.3 G' Band

The G' band is known to be an overtone of the D band. Its position in frequency is twice that of the D band. However, in highly crystalline graphite, the G' band is also present while the D band is absent [56].

The average G' band position shows a linear dependence on the excitation laser energy, like in other sp^2 materials [63], superimposed by an oscillatory behavior. The G'-band linear behavior in isolated SWNTs is similar to that observed in SWNT bundles and is given by:

$$\overline{\omega_{G'}} (\text{cm}^{-1}) = 2420 + 106 E_{laser} (\text{eV}) \quad (3.8)$$

where $\overline{\omega_{G'}}$ is the average G' band position in cm^{-1} over many nanotubes [64] and E_{laser} is expressed in eV.

The G' band position (cm^{-1}) $\omega_{G'}$ exhibit a similar diameter dependence as the D band. An analysis of the G' band positions from isolated nanotubes yield a linear relationship with the inverse diameter $1/d (\text{nm}^{-1})$, as follows:

$$\omega_{G'} (\text{cm}^{-1}) = 2708.1 - \frac{35.4}{d (\text{nm})} \quad (3.9)$$

The values for $1/d \rightarrow 0$ and the slope are nearly the double of the corresponding values for the D band [62].

3.2.4 Radial Breathing Modes (RBMs)

The Radial Breathing Mode (RBM) is a vibrational mode in which all the carbon atoms move radially, perpendicular to the nanotube axis. The RBM is sensitive to the nanotube diameter and is widely used to estimate the diameter distribution in raw nanotube samples [54]. Each nanotube has a distinctive RBM with its position ω_{RBM} related to its diameter:

$$\omega_{RBM} = \frac{A}{d} + B \quad (3.10)$$

where A and B are the constants used to fit the experimental values. B is generally used to describe the interaction between nanotubes in a bundle [65] and values between 6.5 and 16 cm⁻¹ were reported [66-68]. For A, values between 222 and 248 cm⁻¹.nm were reported [68-70]. The value 248 cm⁻¹.nm was reported for isolated carbon nanotubes, while the lower values were for nanotube bundles.

3.2.5 Intermediate Range Peaks

Several unassigned weaker and broader features also appear in the Raman spectra of carbon nanotubes. They are in the following ranges:

- 300-700 cm⁻¹: The second harmonic of the RBM appears as a very weak feature at the frequency 2 ω_{RBM} [71].
- 700-1000 cm⁻¹: A weak peak appears around 860 cm⁻¹ and its position is independent of the excitation laser energy. Above and below this peak, the presence of two bands was reported and their positions was found to depend linearly with the excitation laser energy [72].
- 1700-2000 cm⁻¹: Two features around 1750 cm⁻¹ and another around 1950 cm⁻¹ were reported [71,73] in nanotube bundles and isolated carbon nanotubes. The first two features were assigned to overtones of the infrared-active out-of-plane mode at 867 cm⁻¹. The band around 1950 cm⁻¹ is identified as a combination mode of the in-plane transverse optic and longitudinal acoustic modes.

- Over 3000 cm^{-1} : A broad feature appears at twice the frequency of the G band and is generally assigned to the second harmonic of the tangential modes [71,74].

3.3 Resonant Raman Spectroscopy

The intensity of the Raman bands depends on the laser excitation energy (E_{laser}) according to resonance theory [67,72,75-77]. It becomes extremely strong when the incident or the scattered laser light energy is close to the energy E_{ii} of an electronic transition. Due to their one-dimensionality, each SWNT has a set of van Hove singularities (vHs) in the electronic density of states spectrum at specific energies. E^M_{11} is the energy separation between the first pair of vHs for metallic nanotubes. E^S_{11} and E^S_{22} are the energy separation between the first and second pair of vHs for semiconducting nanotubes, respectively. For each E_{laser} value, a resonance window can be defined as the energy range $E_{laser} \pm 0.1\text{ eV}$. A nanotube is resonant with the laser, if any of the E_{ii} values (E^M_{11} , E^S_{11} or E^S_{22} for example) is in the resonance window.

3.3.1 G Band

Raman spectra of the G band were collected from nanotubes produced by the laser vaporization technique (range of diameters between 1.0 and 1.6 nm) with different excitation laser energy E_{laser} between 0.94 eV and 3.05 eV [75]. The spectrum collected with $E_{laser} = 1.92\text{ eV}$ is particularly different from the others. While in the other spectra, the data can be fit with the same set of Lorentzian lines, a broad and strong asymmetric peak appears around 1540 cm^{-1} for $E_{laser} = 1.92\text{ eV}$. This enhancement is only observed in metallic nanotubes and is due to the coupling of phonons and a continuum of collective excitations of electrons (plasmons), which gives it a Breit-Wigner-Fano (BWF) shape [78,79]:

$$I(\omega) = I_0 \frac{(1 + (\omega - \omega_{BWF})/Q\Gamma)^2}{1 + [(\omega - \omega_{BWF})/\Gamma]^2} \quad (3.11)$$

where $1/Q$ is a measure of the interaction between phonons and a continuum of plasmons, ω_{BWF} is the BWF peak frequency at maximum intensity I_0 , and Γ is the half width of the BWF peak.

The E_{laser} value is consistent with the E_{ii}^M values between 1.6 eV and 2.2 eV calculated for nanotubes with a diameter range of 1.0-1.6 nm. This energy range around 1.9 eV in which the metallic nanotubes are in resonance is called the "metallic window" and its position and extent depend on the diameter distribution of the nanotube sample, as predicted by the calculated E_{ii} values.

Rafailov *et al.* [80] collected spectra of the G band and measured the intensity of the peak associated with metallic nanotubes as a function of E_{laser} . The resonance window was found to shift to lower energies when the mean diameter of the nanotube sample increases, and smaller nanotubes were found to have a sharper resonance window.

3.3.2 Radial Breathing Modes (RBMs)

Raman spectra of the RBMs were collected from nanotubes synthesized with the laser vaporization technique using six different laser lines: 1.17, 1.59, 1.92, 2.41, 2.54 and 2.71 eV. The experimental data were fitted with Lorentzian lines with the same linewidth of 8.4 cm^{-1} . Even though the spectra were collected on the sample, the RBM band profile is particularly dependent on E_{laser} : the number, the intensity and the position of the different RBMs change dramatically with E_{laser} [75].

The position of the RBMs was found to be inversely proportional to the diameter of the nanotube. Using the relation $\omega_{RBM} = 223.75/d$ [75], the nanotubes observed with Raman spectroscopy have a diameter in the range of 1.1-1.5 nm which is compatible with the diameter range obtained by Transmission Electron Microscopy (TEM). These experimental results can be explained with the resonant Raman theory. For each E_{laser} value, a different set of nanotubes with their E_{ii} values close to E_{laser} appears. The relative intensities of the RBMs depend on how close E_{ii} is to E_{laser} and also on the nanotube population in the sample.

Using a tunable laser, Jorio *et al.* [81] measured the intensity of an RBM

located at 173.6 cm^{-1} from an individual nanotube, as a function of E_{laser} . The RBM intensity reaches a maximum when the electronic transition energy E_{ii} is equal to E_{laser} (incident light) or $E_{laser} \pm E_{ph}$ (scattered light, E_{ph} is the energy of the phonon involved in the process).

3.3.3 G' Band

Generally, the G' band has a single Lorentzian line profile in SWNT bundles and most of the individual SWNTs. However, for some individual nanotubes, a two-peak structure was reported [82]. From the analysis of the RBM, the (n,m) indexes were determined and using the tight-binding calculations of the electronic density of states, it was found that this two-peak structure was due to a double resonance process. While in most cases the incident light or the scattered light is in resonance with one electronic transition (thus the one-peak profile), in these specific cases, the incident light is in resonance with one transition and the scattered light with another one.

3.3.4 Stokes, Anti-Stokes Spectra

When the temperature of the sample is controlled by the laser power, the intensity of a specific Raman peak can be used to determine *in situ* the temperature of the carbon nanotubes, assuming that the anti-Stokes/Stokes intensity ratio is proportional to the Boltzmann factor. Huong *et al.* [83] used a low-frequency line at 120 cm^{-1} associated with the nanotubes, while Huang *et al.* [84] and Li *et al.* [85] calculated an average temperature value using several peaks in the Raman spectra. Using this procedure, reasonable temperature values between 300 K and 700 K were obtained.

However, a large distribution of intensity ratios can be observed on the same sample irradiated by the same laser. Yu *et al.* collected the Stokes and anti-Stokes Raman spectra of RBMs for a thin nanotube bundle [68]. One RBM at 199 cm^{-1} appears in the Stokes spectrum but is totally suppressed in the anti-Stokes spectrum. Another RBM at 184 cm^{-1} is present in both anti-Stokes and Stokes spectra, but the anti-Stokes RBM is stronger than its symmetric one in the Stokes spectra. Temperature and the Boltzmann factor alone cannot explain

these results, since the temperature value obtained from the 184 cm^{-1} RBM would be negative. Then enhancement from resonance effects has to be taken into account [68,81,86,87].

The Raman signal is significantly enhanced when E_{ii} is equal to E_{laser} or $E_{laser} \pm E_{ph}$. E_{ph} is small compared to E_{laser} for RBMs: it is about 25 meV for a 200 cm^{-1} RBM. Nevertheless, this small difference induces different resonance conditions for the Stokes and anti-Stokes spectra. The anti-Stokes RBM intensity reaches its maximum at a lower E_{laser} value (around $E_{laser} - E_{ph}$) than the Stokes RBM intensity. Using resonant Raman theory, the E_{ii} values can be determined from the anti-Stokes/Stokes intensity ratio [87].

This resonance enhancement is particularly obvious for the G band, where $E_{ph} \approx 0.20\text{ eV}$ becomes significant compared to E_{laser} [88]. Brown *et al.* collected the Stokes and anti-Stokes spectra of the G band using four different values of E_{laser} : 1.49, 1.58, 1.92 and 2.19 eV. A broad peak around 1540 cm^{-1} is associated with metallic nanotubes and appears only in the resonance window. The resonance window was found shifted to lower energy values for the anti-Stokes scattering process. For $E_{laser} = 1.49\text{ eV}$, the metallic nanotubes are in resonance by the anti-Stokes process, but not by the Stokes process. For $E_{laser} = 1.58\text{ eV}$, metallic nanotubes appear in both spectra. For $E_{laser} = 1.92\text{ eV}$, the metallic nanotubes contributes to the Stokes spectrum but not to the anti-Stokes spectrum. And for $E_{laser} = 2.19\text{ eV}$, only semiconducting nanotubes are detected.

The Raman band intensity should not be used to determine the temperature of raw nanotube samples like powders since different types of nanotubes are probed in the Stokes and anti-Stokes spectrum. The relation between the Stokes and anti-Stokes intensity should only be used in non-resonant cases [86,89].

The different resonance conditions for the Stokes and anti-Stokes processes might induce an apparent upshift of 2 - 3 cm^{-1} in the Stokes spectrum, since nanotubes with slightly different diameters appear in these spectra [90]. However, reports on nanotube bundles [91], or isolated nanotubes

[81,87] do not show a shift or only a small one within the resolution of the Raman spectrometer.

3.4 Polarized Raman Spectroscopy

Polarized Raman spectroscopic studies on aligned nanotubes [78,92-95] or on individual nanotubes [96,97] have showed that the intensity of the Raman bands depend on the angle α_i between the incident laser beam polarization and the nanotube axis. The intensity of the main features of the SWNT spectra, like the RBMs, reaches its maximum when the incident laser polarization is parallel to the nanotube axis.

Gommans *et al.* [92] and Hwang *et al.* [95] observed this phenomenon on aligned SWNT fibers made by the electrophoretic attraction of the nanotubes to a positively charged carbon fiber and PMMA fibers reinforced with 1 wt.% of SWNTs: the intensity of Raman bands decreases dramatically when the incident laser polarization is perpendicular to the nanotube axis. Rao *et al.* [93] also observed an intensity loss over the entire Raman spectra, when the incident laser polarization is not parallel to the nanotube axis, however they report a minimum in intensity for $\alpha_i = 55^\circ$ and not 90° in the configuration where the incident and the scattered light polarizations are parallel.

Jorio *et al.* [94] studied a rope of aligned SWNTs synthesized with the arc-discharge technique by polarized Raman spectroscopy and assigned the symmetry groups of the different components of the G band for semiconducting nanotubes: 1549 cm^{-1} (E_{2g}), 1567 cm^{-1} ($A_{1g} + E_{1g}$), 1590 cm^{-1} ($A_{1g}+E_{1g}$) and 1607 cm^{-1} (E_{2g}).

Duesberg *et al.* [96] collected Raman spectra of the RBMs, D and G bands of a thin SWNT bundle produced by the arc-discharge method, with different angles between the laser polarization and the bundle axis, in the configuration where the polarization of the incident and scattered lights are parallel. The incident and the scattered light polarizations were parallel. All the bands reach their maximum in intensity when the polarization is parallel to the nanotube axis, and they disappear when the polarization is perpendicular.

3.5 Effect of Deformation on the Raman Spectra

The Raman spectrum from carbon nanotubes varies in peak intensities and positions when the sample is under strain. The RBMs, G and G' band shift at different rates depending on the strain applied. Lourie *et al.* [98] observed the shift of the G' band to higher wave numbers when the nanotubes are cooled from room temperature to 81 K. The 4 cm^{-1} upshift was explained by the contraction of the carbon-carbon bonds and was used to estimate the tensile modulus of SWNTs around 3 TPa. The same experiments were performed on carbon nanotubes embedded in an epoxy matrix: a noticeable upshift of 15 cm^{-1} of the G' band was observed with the embedment and was attributed to the contraction of the carbon-carbon bonds induced by the volume reduction of the epoxy matrix after polymerization. Cooling the epoxy composite led to a further upshift of 21 cm^{-1} .

Much smaller shifts were obtained by Schadler *et al.* [99] and Ajayan *et al.* [100] in compression and tension tests. Nanotubes (at a relatively high concentration of 5 wt.%) were embedded in an epoxy matrix in both experiments. In the first case, the G' band was upshifted by 6 cm^{-1} at 1% strain in compression and also slightly upshifted at 1% in tension. In the second experiment, no shift of the G' band was detected in compression and only a small downshift (less than 1 cm^{-1} , within experimental error) was observed in tension even at 1.2% strain.

Two explanations are possible for these differences: the poor bonding between the nanotubes and the epoxy matrix, and the poor dispersion of nanotubes. A poor interface between the nanotubes and the matrix limits the load transfer to the nanotubes and induces the debonding of the nanotubes at high strain values. The poor dispersion means that the nanotube bundles are still aggregated into small particles. This not only restricts the interface between the nanotubes and the matrix but leads to the slippage inside the nanotube bundles at high strain values, since the nanotubes are only maintained together by weak van der Waals forces.

Cooper *et al.* [51] demonstrated that Raman spectroscopy can be used as a way to monitor the deformation of nanotubes under tensile strain and

pressure. The G' band shifts to higher wave numbers in compression and to lower wave numbers in tension. The G' band shift rate at slow tensile strain values was measured by four-point bending tests for nanotubes produced by the arc discharge technique ($-1.3 \text{ cm}^{-1}/\% \text{ strain}$) and by the pulsed laser vaporization technique ($-15 \text{ cm}^{-1}/\% \text{ strain}$) embedded in an epoxy matrix. Comparing these band shift rates to those obtained from carbon fibers with different tensile modulus, the tensile modulus of carbon nanotubes was found to be of the order of 1 TPa.

The band shift rate of the G' band depends on the orientation of the nanotubes inside the composite material and the polarization of the incident laser [101], since only the nanotubes parallel to the polarization are supposed to be probed. Polarized Raman spectroscopy was performed on films of polyurethane acrylate reinforced with unoriented SWNTs. When the polarization of the incident laser was parallel to the direction along which the strain was applied, the G' band shifts to lower wave numbers, since the matrix is in tension in this direction. However, when the polarization is perpendicular to the strain axis, the nanotubes probed are in compression, and thus the G' band shifts slightly to higher wave numbers [101].

Hadjiev *et al.* reported similar results on the G band for nanotubes embedded in an epoxy composite. The G band shifts to higher wave numbers by 3 cm^{-1} when the composite is in compression ($-0.45\% \text{ strain}$) and the incident polarization is parallel to the strain axis. When the incident polarization is perpendicular to the strain axis, the Raman spectrum is nearly identical to the one from the unstressed sample. It is noted that in this report the RBM does not shift in position and that its intensity remains constant within the resolution of the spectrometer when in compression [102].

The peak positions are also sensitive to hydrostatic pressure. One simple way to observe this effect is to immerse the nanotubes in various liquids [103]. Carbon nanotubes are subject to hydrostatic pressure when they are immersed in a liquid, which leads to an upshift of the G' band. The RBMs and the G band were also predicted and found to shift to higher wave numbers with pressure [51,90,103-109]. A phase transition occurs for a pressure value between 1.5

and 2.0 GPa, where the cross section is deformed (flattening or polygonization) [90,105,108,109]. The upshift rate of the RBM position ω_{RBM} ranges from 7 to 10 cm⁻¹/GPa, depending on ω_{RBM} . The experimental values for the normalized pressure-induced upshift rates were fitted reasonably well with the following equation:

$$\frac{1}{\omega_{RBM}} \frac{d\omega_{RBM}}{dP} = \frac{A}{\omega_{RBM}^{-2.2}} \quad (3.12)$$

where A is a constant and P the pressure [110].

Variations in the absolute RBM intensities were reported and their overall decrease as a function of pressure was explained by the faceting of the nanotubes in the bundles [90]. However, the variations in the relative RBM intensities at low pressure values were not commented upon.

These relative RBM intensity variations may be the result of pressure-induced shift of the electronic transition energies E_{ii} , and therefore the result of modifications of the resonance conditions. Optical absorption spectroscopy on films of nanotube bundles [111] and suspensions of debundled nanotubes [112] under pressure indicate that all electronic transition energies E_{ii} shift to lower energies with increasing pressure. This result is in contradiction with tight-binding and local-density approximation calculations that predict that the band gap variation trend with strain depends on the nanotube (n,m) indexes [113].

The absorption peaks all decrease in intensity, before vanishing at high pressures. Those at energies between 0.9 and 1.3 eV correspond to the E_{11}^S values of semiconducting nanotubes and shift with variable magnitudes depending on the nanotube diameter. The E_{11}^S values of the larger diameter nanotubes are more sensitive to hydrostatic pressure than the ones with a smaller diameter. The peaks at higher energies (between 1.2 and 2.8 eV) correspond to the E_{22}^S values of semiconducting nanotubes and are much less sensitive to pressure. Also, the shift rates of the E_{22}^S values are independent of the nanotube diameter [112]. The reported values of the E_{22}^S shift rates, between 10 and 20 meV/GPa may be important enough to induce the variation of the relative RBM intensities observed in Reference 90.

3.6 Effect of Chemical Treatments on the Raman Spectra

The D band is commonly associated with defects and sp^3 carbon states along the nanotube sidewalls. Its intensity increases compared to the G band intensity when defects are introduced by heating the nanotubes above 1500°C [114]. The intensity ratio between the D and G bands is used to monitor the efficiency of acid-based purification methods [114-116]. The D band intensity of HiPco SWNTs increases in intensity with longer acid treatment times, due to the introduction of defects and disorder [115,116]. Using a 780 nm laser, Ziegler *et al.* compared the RBMs from acid-treated HiPco SWNTs with different reaction times. The 267 cm^{-1} RBM decreases significantly in intensity, compared to the other RBMs, with increasing reaction times. It was concluded that smaller diameter nanotubes are more reactive due to their higher curvature [116]. Wiltshire *et al.* also observed the preferential oxidation of smaller diameter nanotubes using a 514 nm laser [115].

Defects such as vacancies are potential active sites for covalent chemical functionalization. The attachment of functional groups to the nanotube sidewall can be indicated by a variation of the D/G band intensity ratio. Khare *et al.* also observed a 9 cm^{-1} downshift of the G band in HiPco SWNTs functionalized with ammonia, compared to the pristine nanotube material. RBM position shifts and the decrease in relative RBM intensity of the smaller diameter nanotubes were reported in the same study [117].

Charge transfer from the adsorption of chemical species on the nanotube sidewall also leads to modifications of the Raman spectra, such as the shift of the band positions [62]. The Raman bands of SWNTs synthesized by the laser vaporization technique shift to lower or higher wave numbers depending on the dopant. Only a little modification was observed for I₂ doping: the 186 cm^{-1} RBM shifts to 188 cm^{-1} and the G band from 1593 cm^{-1} to 1590 cm^{-1} . The doping by bromine Br₂ (electron acceptor) leads to an upshift of the 186 cm^{-1} RBM and the G band by 74 cm^{-1} and 24 cm^{-1} , respectively; while the doping by rubidium Rb and potassium K (electron donor) leads to a downshift of the G band and the disappearance of the RBM. The G band of the Rb- and K-doped SWNTs

exhibits the BWF lineshape characteristic of metallic nanotubes [118]. Position shifts of the D and G' bands, and intensity variations of the RBM and G band were reported for boron-doped SWNTs. The intensity variations were attributed to modifications of the resonance conditions in the boron-doped nanotubes [119].

The electrochemical modifications of the nanotube Raman spectra were studied using various electrolyte solutions. Varying the potential of an electrode made of a SWNT film immersed in an electrolyte solution is a way to control the doping level of nanotubes. The RBMs, D, G and G' bands were found to shift with charge transfer [120-126]. The position shift can be explained by the intercalation of nanotubes by the adsorbed dopants [120,121]. While the G band shift rate does not depend on the incident laser wavelength, the G' band shift rate depends significantly on the incident laser wavelength. The G' band does not shift with the doping level when the lasers of wavelength 477 nm and 488 nm are used to collect the Raman spectra, but the G' band shift rate is not zero and increases with the incident laser wavelength, for wavelengths 514 nm and above [125].

The intensity of the RBMs and G band varies significantly when the applied potential is changed [120-126]. A drop in overall Raman intensity is observed when the applied potential value is higher than 1 V (anodic or cathodic). The BWF feature characteristic of metallic nanotubes decreases in intensity with an increasing anodic potential and eventually disappears [122,124]. Most of the band shifts and intensity variations are reversible at low voltages, however at high voltages, oxidation reactions occur, leading to the formation of C-O bonds and the introduction of disorder along the nanotube sidewalls [126].

These intensity variations are explained by the electrochemical doping of nanotubes, which induces variations of the electron populations. An anodic potential applied to the SWNT electrode depletes the valence band of the nanotubes, while a cathodic potential fills the conduction band [122,123]. Resonant Raman scattering in nanotubes involves electronic transitions between vHs. The removal of electrons in the vHs in the valence band, or the

filling of the vHs in the conduction band modifies the resonance conditions [124]. The electron removal or filling can be monitored by optical absorption spectroscopy. Increasing the applied potential leads to the disappearance of the absorption peaks that correspond to transitions between vHs [123]. Electrochemical doping is only expected to change the populations of the valence and conduction bands, however, Corio et al. suggested that applying a potential also induces the shift of the vHs in metallic nanotubes [124].

3.7 Effect of Temperature on the Raman Spectra

The position of the main Raman bands from the nanotubes depends on the temperature of the sample. The RBMs, the D, G and G' bands were found to shift to lower wave numbers with increasing temperatures [83-85,127,128]. The peak positions were found to vary linearly with temperature with slopes between -10^{-2} to $-4.10^{-2} \text{ cm}^{-1}/\text{K}$. In these experiments, the temperature of the nanotubes was controlled using a cryostat and a heating stage, or by setting the incident laser power used for Raman spectroscopy.

This shift was assigned to the expansion of the C-C bonds in the carbon nanotube with increasing temperature [83-85,128]. However, the C-C bond length in a graphite plane was found to contract up to 673 K, then expand at higher temperatures [129]. An X-ray diffraction study of SWNT bundles revealed that the thermal expansion coefficient of the SWNT diameter is negative between 300K and 950K [130], in apparent contradiction with the downshift of the RBMs at high temperatures. Theoretical studies confirmed that the thermal expansion coefficient of the nanotube diameter and length is negative at room temperature, remains negative under a critical temperature between 400K [131] and 900K [132], then becomes positive at higher temperatures. Also, the thermal expansion coefficients of $-1.5 \times 10^{-6} \text{ K}^{-1}$ reported for the nanotube diameter [130] and $-13.0 \times 10^{-6} \text{ }^{\circ}\text{C}^{-1}$ for the in-plane C-C bonds [133] are too small to explain the magnitude of RBM position shifts.

In general, the change of Raman band position is the result of the combination of a pure volume effect associated with the thermal expansion of the sample and a pure temperature effect. The pure temperature effect is partly

due to the anharmonicity in the interatomic potential. The harmonic potential is symmetric in tension and in compression and therefore the average atomic positions remain unchanged with temperature. This is not true for an anharmonic potential [131]. Raravikar *et al.* concluded that thermal expansion only plays a minor role in the downshift of the RBM positions and that the main contributions to this effect are the anharmonicities of the intra- and intertube potentials [134].

The downshift rate of the Raman bands depends on the nanotube material and its purity. It was found to be inversely proportional to the thermal conductivity of the nanotube sample. Purified nanotube samples such as the purified HiPco nanotubes used in this study exhibit a low downshift rate, while higher shift rates were obtained from nanotube materials containing amorphous carbon [135].

Apart from the Raman band downshift, heating nanotube materials to high temperatures also leads to irreversible effects on the peak intensities. The laser irradiation effect on the intensity of the G band was studied on a nanotube bundle treated with $\text{H}_2\text{SO}_4/\text{H}_2\text{O}_2$. After laser irradiation a broad band centered at 1540 cm^{-1} characteristic of metallic nanotubes appeared on the Raman spectra and this new feature remained after the laser power was lowered again. This observation was attributed to the degassing of adsorbed oxidizing molecules at high temperatures that are responsible for the modifications of the electronic properties [136].

Corio *et al.* observed the irreversible decrease of the D band intensity with increasing laser power and attributed this result to the thermal annealing of defects along the nanotube sidewalls and in the amorphous carbon particles. Also, the G' band shifts to lower wave numbers with increasing laser power. However, the opposite occurred when the laser power was increased from 50 to $100 \mu\text{W}/\mu\text{m}^2$ and it was explained by the destruction of the smaller diameter nanotubes [89].

Further evidence of these irreversible effects is given by the low-frequency Raman spectra of the RBMs. Four RBMs located at 191, 218, 257, and 280 cm^{-1} are observed in the original spectrum collected at $10 \mu\text{W}/\mu\text{m}^2$

laser power by Corio *et al.* [89]. When the laser power is increased to 100 $\mu\text{W}/\mu\text{m}^2$, only two RBMs centered at 190 and 215 cm^{-1} remain observable. The RBM at 280 cm^{-1} corresponding to a smaller diameter nanotube is irreversibly lost, when the laser is decreased to the original value, while the one at 257 cm^{-1} is barely visible. The destruction of smaller diameter nanotubes was attributed by their lower heat capacity or higher structural stress. Similar results were reported for nanotubes treated by acids and confirmed by electron microscopy [137-139].

Another explanation for the variations of the relative RBM intensities is the modification of the resonance conditions with temperature. To study the variation of the electronic transition energies E_{ii} with temperature, Fantini *et al.* measured their values by recording their Raman excitation profiles, while varying the laser power. The E_{ii} values were found to vary with temperature with various magnitudes and trends depending on the nanotube structure. Shifts in E_{ii} energy values between 20 and 50 meV were observed when the laser power was increased from 18 μW to 5 mW [140].

It is unclear by how much the temperature increased in the sample, but the E_{ii} shifts are much larger than the ones reported by Lefebvre *et al.* [141], large enough to induce significant relative RBM intensity variations. In a study based on photoluminescence and photoluminescence excitation spectroscopy between 5 K and 300 K, the E_{ii} values exhibit only a very weak temperature dependence (shift of less than 10 meV), which depends on the nanotube structure [141].

Chapter 4

Structure Determination and Chirality Assignment

4.1 Control over the Structure of Synthesis Products

The nanotube chirality and the uniformity of the synthesis products play a key role in nanotube-based devices, especially in the development of electronic components. However, despite the recent advances, synthesis products generally contain a large range of nanotube diameters and chiralities.

In 1996, Thess *et al.* reported the synthesis of metallic SWNT bundles, uniform in diameter, and mainly comprising (10,10) nanotubes [5]. Later, it was found that these bundles also contain SWNTs with other chiralities [142]. It is possible to control the mean diameter of the synthesis products by varying the different synthesis parameters, such as temperature, pressure, the composition and the size of the catalyst particles. Kataura *et al.* observed that the mean diameter (estimated by Raman spectroscopy) increases when the temperature of the laser furnace increases, but the synthesis method still yielded a broad diameter range [143].

One way to narrow the diameter distribution is to grow nanotubes on catalyst particles of uniform size. Cheung *et al.* managed to control the diameter and limit the broadness of the diameter distribution by using nearly monodisperse iron catalyst particles, but nanotubes with larger diameters were also present due to the agglomeration of the particles [144]. To avoid this problem, Han *et al.* used instead binary arrays of monodisperse zirconia particles and monodisperse iron oxide particles and relatively narrow diameter distribution were obtained with the mean diameter close to the one of the catalyst particles [145].

Since it is still impossible to produce on a large scale nanotubes of a specific diameter and chirality, methods to selectively destroy some nanotubes

from the synthesis products were developed. Yudasaka *et al.* oxidized SWNTs in a H₂O₂ solution under monochromatic light. It was observed by Raman spectroscopy that the nanotubes with an E_{ii} value close to the energy of the monochromatic light are preferentially destroyed [146].

Collins *et al.* developed a technique to selectively destroy metallic nanotubes in bundles and produce arrays of carbon nanotube field-effect transistor [147]. A bundle is deposited on electrodes printed on an oxidized silicon substrate. By applying an appropriate potential on the silicon substrate, the semiconducting nanotubes are made insulators. A high current is then run through the metallic nanotubes and eventually destroys them, while the semiconducting nanotubes remain intact.

In the experiments cited above, little is known about the characteristics of the nanotubes used, except for an approximate value of their diameter and whether they are metallic or semiconducting. The determination of the (n,m) indexes giving the entire structure of the SWNTs remains a challenge but is essential for both scientific studies and possible large-scale applications. In the following sections, the different techniques available to determine the atomic structure of nanotubes are presented.

4.2 Scanning Tunneling Microscopy (STM)

Scanning Tunneling Spectroscopy (STS) and Scanning Tunneling Microscopy (STM) are two techniques that have been used to characterize the topography of surfaces at the atomic level and to probe the local electronic DOS. In a STM, a bias voltage is applied to a fine tip (usually made of tungsten) which scans the sample surface. At each point on the surface, the tunneling current between the tip and the sample is measured and a feedback system maintains this current constant by moving the tip up and down with a piezo-electric scanner, resulting in the topography of the sample. STS measurements are obtained by varying the bias voltage at a particular location [148].

Wildöer *et al.* obtained simultaneously the atomic structure and the electronic DOS of 27 types of isolated nanotubes [9], including semiconducting and metallic nanotubes. The band gaps were measured by STS and found to

depend on the nanotube chirality. The results matched reasonably well the theoretical predictions of the tight-binding calculations [8]. Odom *et al.* analyzed by STM and STS samples synthesized by the laser vaporization process of Thess *et al.* [5] and confirmed that the bundles contain nanotubes with a wide range of chiralities other than (10,10) without a dominant one [149].

STM and STS are also two useful tools to study locally the effect of deformation on the electronic properties of nanotubes. Clauss *et al.* observed a twisted armchair nanotube in a bundle and explained the low conductivity of some isolated nanotubes or even macroscopic nanotube material by twist and shear deformations [150]. Odom *et al.* measured the electronic DOS at several points around a kink in a bent nanotube. He assigned the same chirality to both sides of the kink and discovered new low-energy features that were attributed to the presence of the kink [151].

Also, Ouyang *et al.* characterized for the first time by STM and STS metal-metal and metal-semiconductor intramolecular junctions of two nanotubes of different chiralities [152,153]. The key role of defects along nanotubes on their electronic properties was demonstrated.

4.3 Electron Diffraction

Electron diffraction is a useful tool to probe the local structure of nanotubes, but diffraction patterns are obtained only in optimum conditions: near-perfect periodicity, absence of defects, nanotube oriented perpendicular to the electron beam, no distortion. Most electron diffraction results were obtained from bundles of SWNTs, because of the low scattering power of individual SWNTs.

The chirality assignment is made by comparing the diffraction patterns with the simulated ones from nanotubes with a specific chirality. The diffraction patterns exhibit first- and second-order reflections which are diffuse arcs, indicating that the bundles are composed of nanotubes of different chiralities without a dominant type [142,154,155]. The diffraction intensity along these arcs is not constant and therefore they could not be explained by the presence of amorphous material [142].

4.4 Raman Spectroscopy

Resonant Raman spectroscopy has proven to be a powerful tool for the structure determination of individual SWNTs [70,156]. The RBM position provides an approximate value of the diameter, but several nanotubes of different chiralities have close diameter values. Duesberg *et al.* limited the number of possible candidates for a particular RBM by examining the shape of the G band. An asymmetrical Breit-Wigner-Fano shape of the G band indicates that the nanotube is metallic. Therefore only the possible candidates with (n,m) indexes satisfying:

$$\frac{n-m}{3} = p \quad (4.1)$$

where p is an integer were considered. But even with this restriction, several candidates remain and this method would not be useful for semiconducting nanotubes [156].

Using the RBM positions and resonance theory, Jorio *et al.* were able to characterize 13 metallic and 4 semiconducting isolated nanotubes. When several possible candidates existed for a particular RBM, the RBM was assigned to the nanotube with the E_{ii} value which is the closest to E_{laser} . The trigonal warping effect, which induces the splitting of the vHs of non-armchair metallic nanotubes, restricts even further the number of possibilities for metallic nanotubes. The RBM is then preferentially assigned to the nanotube with the electronic DOS that exhibits the smallest split of its singularities [70].

The use of several lasers of different wavelengths and the development of tunable lasers allowed the measurement of the RBM intensity as a function of the laser excitation energy and revealed the resonance effect on the Raman spectrum [81,157-159]. The RBM intensity reaches a maximum for a particular laser energy that is consistent with the results of the tight-binding calculations of the electronic DOS for most nanotubes. These more accurate measurements allowed the complete characterization of a wide range of nanotubes, metallic [157,158] and semiconducting [159].

Another method to determine the nanotube structure is by the measurement of the anti-Stokes/Stokes Raman intensity ratios. In non-resonant

conditions, the anti-Stokes/Stokes intensity ratio is proportional to the temperature-dependent Boltzmann factor. In resonant conditions, the Stokes and anti-Stokes RBM intensities do not reach their maximum at the same laser excitation energy E_{laser} because the scattered photon has not the same energy in the Stokes process as in the anti-Stokes process. Combining the experimental intensity ratios and the theoretical Stokes and anti-Stokes excitation profiles, a chirality can be tentatively assigned to the RBM [68,81,87].

4.5 Other Spectroscopic Techniques

Ohno *et al.* recently reported the determination of the structure of an isolated nanotube using micro-photocurrent spectroscopy. Nanotubes were synthesized by CVD and were assembled into field-effect transistors with electrodes. The photocurrent from the isolated nanotube was measured as a function of the excitation energy of a tunable Ti/sapphire laser. A maximum in the photocurrent spectrum corresponding to a specific transition between vHs was observed at 1.73 eV. Combining the peak position with the AFM measurement of the nanotube diameter and using tight-binding calculations of their electronic DOS, the nanotube was assigned an (18,10) chirality [160].

Hagen *et al.* combined high-resolution absorption spectroscopy from the ultraviolet to the infrared range with tight-binding calculations to assign chiralities to individual SWNTs isolated in micelles using surfactants. The tight-binding model was slightly modified to introduce a second adjustable parameter to take into account intertube interactions, hydrostatic pressure, asymmetries in the electronic band structure and other effects. Chiralities were assigned to 14 different types of nanotube and a mean diameter value of 1.05 nm was obtained from HiPco nanotubes, which is consistent with previous studies [161].

A major advance is the discovery of fluorescence emission from individual nanotubes dispersed in water using surfactants and illuminated by a monochromatic light. This phenomenon was previously unnoticed because of the surrounding metallic nanotubes in a bundle [162]. Comparing the theoretical electronic DOS of SWNTs, the emission and excitation radiation wavelengths from the fluorescence spectroscopic measurements, Bachilo *et al.* assigned the

chiralities and (n,m) indexes to 33 different types of semiconducting nanotubes [66].

Li *et al.* assigned chiralities to suspended semiconducting HiPco nanotubes by analyzing their photoluminescence spectra and their modification with strain. Compressive uniaxial strain estimated at 0.2% and torsional strain were applied by lowering the temperature of the surrounding D₂O ice from 260K to 80K or by drying the polymer (polyvinylpyrrolidone) wrapped around the nanotubes. The band gap shift trend with temperature provides the value of the parameter p , the remainder of $(n-m)$ divided by 3 [163].

Unfortunately, in contrast to Raman spectroscopy, fluorescence spectroscopy cannot be used to characterize metallic nanotubes, solid particles, bulk samples or nanotubes dispersed in an organic solvent [164]. The major advantage of these spectroscopic methods, including Raman spectroscopy, is that they enable the characterization of synthesis products on a much larger scale than STM or electron diffraction.

4.6 Accuracy of the Chirality Assignment

4.6.1 Reliability of the Different Spectroscopic Techniques

First of all, the interpretation of STM images is a delicate task. The measure of the diameter of an isolated nanotube on a flat substrate should be possible with a linear scan across it. However, during the scan the STM tip applies forces that flatten the nanotube, so the nanotube diameter, which is estimated from its height relative to the substrate, may be underestimated.

The geometry of the STM tip and the nanotube also leads to the apparent widening of the nanotube in the direction perpendicular to its axis and therefore the overestimation of the chiral angle [165]. Curvature and the ensuing reorientation of the π -orbitals cause the distortion of the STM image as well [166].

The electron diffraction reflections are mainly diffuse arcs and bright streaks, instead of sharp spots, because of the nanotube curvature and of the finite size of the nanotube in the circumferential direction. The uncertainty of the

reflection positions results in the uncertainty of the measured diameter and chiral angle values [167]. So several pairs of indexes (n,m) could correspond to a diffraction pattern.

The fluorescence spectroscopic measurements do not provide a diameter value, and therefore a reliable chirality assignment obtained from Raman spectroscopy was necessary to assign all the fluorescence peaks to specific types of nanotube. The first assignment was chosen so that the other assignments would yield a linear relationship between the inverse diameter and the corresponding RBM position of these nanotubes. Depending on the first assignment made, different sets of chiralities could be obtained [164].

4.6.2 Theoretical Values of the E_{ii} Values

The chirality assignments from Raman spectroscopy are heavily dependent on the theoretical E_{ii} values. Nanotubes within the same diameter range can have very close E_{ii} values, which means that the (n,m) assignments are sometimes not unique. First of all, the value of the adjustable hopping parameter used in the tight-binding calculations remains unclear. Even small variations can result in a different assignment. Values obtained from STS measurements range from 2.4 [10] to 2.7 [9] and those from optical methods are between 2.65 and 3.0 eV [161]. A value of 2.9 eV is usually used in Raman spectroscopy [70].

Second, the hopping parameter can be modified to take into account curvature effects. These effects lead to the decrease of the hopping parameter, especially for the smaller nanotubes with a diameter under 1 nm [168]. Curvature is predicted to open a small band gap in the metallic zigzag nanotubes [169] and this effect was later demonstrated by STM and STS measurements [170]. According to calculations based on density functional theory, nanotubes with a diameter of less than 0.7 nm are expected to behave differently from the larger diameter nanotubes, because of curvature. Their diameter is larger than the one predicted by the model involving the folding of a graphene sheet. Their band gaps and E_{ii} values are lower than those from tight-binding calculations and some nanotubes expected to be semiconducting are in

fact metallic. Their RBM positions deviate from the $1/d$ relationship and the expected softening depends significantly on the nanotube chirality [171]. Measurements of the E_{ii} values by Raman spectroscopy based on the anti-Stokes/Stokes intensity ratio confirmed that they are lower than predicted by tight-binding calculations, but the deviations are less than 0.2 eV for nanotubes with a diameter larger than 0.83 nm [172].

Furthermore, discrepancies exist between the different theoretical methods and the experimental E_{ii} values. Depending on the model used, *ab initio* or zone-folding, E_{ii} values can differ by 0.1 eV [14,173,174]. Density functional theory yields different E_{ii} values depending on the parameters and how the electronic interactions were taken into account [175,176]. The theoretical predictions match the STS measurements below the Fermi level, but it is not the case above it. The band gaps from density functional theory are systematically lower, especially for the smaller diameter nanotubes and such discrepancies are attributed to curvature effects, which would affect the conduction bands more than the valence bands [176-178]. Experimental E_{ii} values from fluorescence spectroscopy were found to be higher and much more dependent on the chirality, especially for nanotubes with a diameter smaller than 1 nm [164,179].

4.6.3 Effect of Environment

It is unclear how much the packing of nanotubes into bundles affects their properties, since it is difficult to obtain experimental results on the effect of intertube interactions. The incorporation of intertube interactions (van der Waals forces) in the theoretical study of the vibrational modes of nanotube bundles leads to an upshift of 5 to 15% of the RBM positions [105,106,180]. Venkateswaran *et al.* reported an upshift of 8% (14 cm^{-1}) of the RBM position of a (9,9) nanotube packed in a bundle [105]. Henrard *et al.* calculated the RBM position upshift for a wide range of nanotube diameters from 7 to 17 Å and reported that the relative upshift increases from 4.8% for the smaller (6,4) nanotube to 14.4% for the larger (12,12) nanotube [180]. These calculations were performed on infinitely large bundles, so the RBM positions are expected

to depend on the bundle size. The RBM position converges towards its "infinite-bundle" value, as the bundle size increases [181].

The electronic properties of nanotubes in bundles are also predicted to change from the isolated nanotubes. The armchair (10,10) nanotubes should be metallic according to tight-binding calculations, but results from density functional theory indicate that intertube interactions open a 0.1 eV wide pseudogap (decrease of the electronic DOS at the Fermi level) in (10,10) nanotubes packed in bundles [182]. Other theoretical studies found that intertube interactions in bundles result in the broadening of vHs and a shift by as much as 0.25 eV of their position [174,183].

Rao *et al.* reported an downshift of 10 cm⁻¹ from the isolated nanotubes to the nanotube bundles. It was suggested that the E_{ii} values shift to lower energies in bundles and therefore different nanotubes are in resonance in the raw solid material and in solution, resulting in an apparent shift of the RBM position [184]. O'Connell *et al.* compared the Raman excitation profile of raw HiPco nanotubes and the same nanotubes isolated in solution and confirmed that the E_{ii} values shift to lower energies by an average value of 86 meV and the resonance window is broadened by an average factor of 2.4 in bundles, compared to the same nanotubes in solution. No significant difference of the RBM position was found between the isolated nanotubes and the bundles [185].

O'Connell *et al.* concurred that the RBM shift in bundles is only an apparent shift, due to different nanotube types being in resonance [185]. A comparison between HiPco nanotube bundles and individual HiPco nanotubes prepared by capillary electrophoresis also revealed no significant change in RBM positions [186]. A Raman spectroscopic study of HiPco nanotubes suspended in solution using various surfactants and polymers found that the Raman band positions (RBMs and G band) are independent of the solution content [187]. Chou *et al.* compared the RBM positions from as-produced SWNTs with those from SWNTs wrapped with DNA or surfactants, and found that they do not depend on the wrapping agent around the SWNTs [188].

The comparison of optical absorption spectroscopy measurements between micelles of individual HiPco nanotubes and bundles from the raw

material revealed that the position of the optical bands are shifted down by 50 meV and broadened by about 80 meV in the bundles [161]. The magnitude of the shifts depends on the wrapping agent used to fractionate the nanotubes [188]. These shifts would be significant enough to induce relative RBM intensity variations, as observed by Heller *et al.* on HiPco nanotubes in different aggregation states [189].

A simultaneous study by fluorescence and Raman spectroscopy by Hartschuh *et al.* revealed that even though two isolated nanotubes have identical RBMs, their corresponding fluorescence emission spectra can be dramatically different. These differences were attributed to perturbations of the electronic DOS by defects and different local environments [190]. Another combined Raman and fluorescence spectroscopic study of nanotubes suspended in water with various surfactants and polymers showed that the fluorescence peak positions depend on the chemical composition and structure of the surfactant or polymer, while the RBMs and G band remained the same. The magnitude of the shift, which can reach 25 meV for some polymers, appears to depend on the ability of the surfactant or polymer to shield the nanotubes from water [187].

After a comparison between the experimental E_{ii} values from Raman spectroscopy and fluorescence spectroscopy [66], it was concluded that each nanotube sample may have its own set of E_{ii} values and parameters to determine d from the RBM positions, reflecting the particularity of the experimental conditions and the interactions between the nanotubes and their environment [172,191].

The uncertainty on the E_{ii} values and RBM positions means that additional information is needed to determine the nanotube chirality. The behavior of the SWNT DOS under strain, investigated by Raman spectroscopy can be an additional criterion for their identification and the determination of SWNT structure.

Chapter 5

Electronic Structure and Density of States

The electronic band structure of SWNTs was calculated using several techniques such as tight-binding calculations or density-functional theory (see Chapter 2). It is predicted to vary significantly upon strain and deformation of the nanotube. In this chapter, the technique developed by L. Yang *et al.* [12,13] is first reviewed in detail. This is an extension of a technique previously developed by Saito *et al.* [8,177], which is based on a tight-binding approximation. In the second part, an improved tight-binding model previously developed by Reich *et al.* [192] is presented and extended to take into account the effect of deformation.

5.1 Tight-Binding Model Including Only Nearest-Neighbor Interactions (TB1)

5.1.1 Theoretical Approach

The 1D electronic density of states (DOS) of carbon nanotubes can be obtained using the tight-binding approximation, based on the zone-folding scheme, following the method developed by Saito *et al.* [8,168,177]. Recently, Yang *et al.* [12,13] extended this method to nanotubes deformed by uniaxial and torsional strains. Following is a description of their generalized method applied to nanotubes under uniaxial strain along their axis.

In these calculations, the ends of the carbon nanotube are neglected. The carbon nanotube is considered as a rolled graphite sheet, with translational symmetry along the nanotube axis. First, the electronic structure of the unrolled graphene sheet is determined [193] and then the periodic boundary condition is applied along the nanotube circumference.

A carbon atom has four valence electrons, three of which are involved in strong C=C bonds in the graphite plane. These three electrons are in the 2s and

$2p$ states. The fourth electron is in the $2p_z$ state with the axis of the corresponding wave function perpendicular to the graphite plane. In this model, only one electron per carbon atom is supposed to contribute to the electronic conductivity, the one in the $2p_z$ state (π orbital).

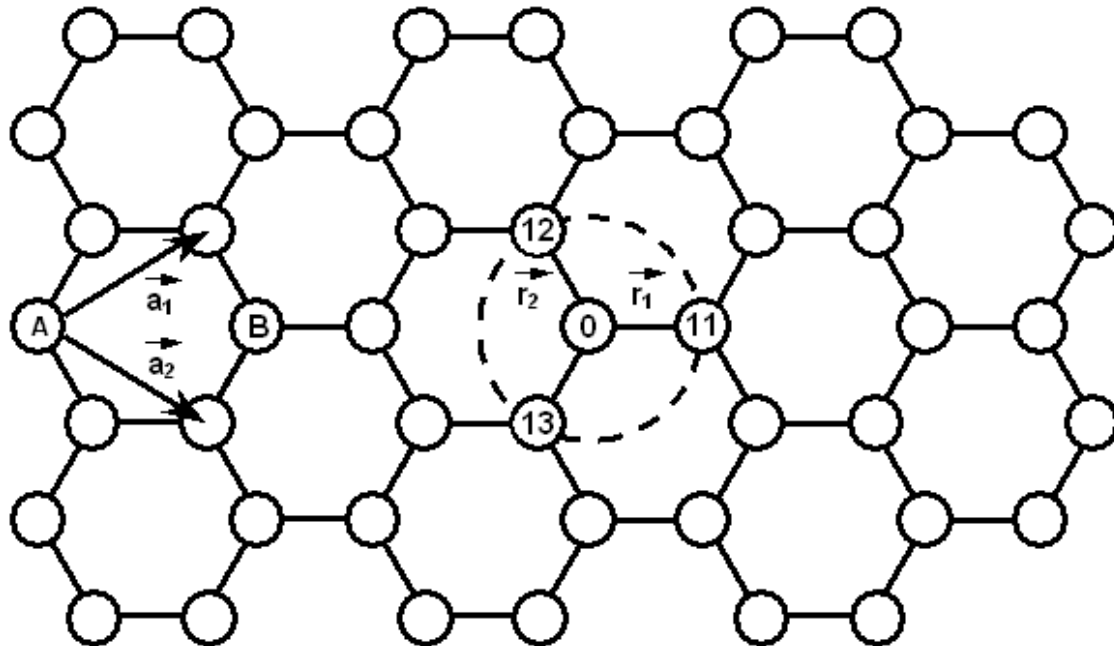


Figure 5.1: Graphite hexagonal lattice. The atom A0 has 3 nearest-neighbors.

The graphite unit cell contains two atoms, A and B (Figure 5.1), and the entire graphite plane is generated by translating this unit cell along the two lattice vectors \vec{a}_1 and \vec{a}_2 .

In the tight-binding approximation, the wave function ψ used has the following form:

$$\psi = \varphi_1 + \beta \varphi_2 \quad (5.1)$$

where β is a constant, φ_1 the sum of the $2p_z$ orbitals from all the A atoms generated by primitive lattice translations:

$$\varphi_1 = \sum_A \exp(i\vec{k} \cdot \vec{r}_A) X(\vec{r} - \vec{r}_A) \quad (5.2)$$

$X(\vec{r})$ being the wave function of a normalized orbital $2p_z$ for an isolated carbon atom located at \vec{r} , and φ_2 the sum of the $2p_z$ orbitals from all the B atoms generated by primitive lattice translations:

$$\varphi_2 = \sum_B \exp(i\vec{k} \cdot \vec{r}_B) X(\vec{r} - \vec{r}_B) \quad (5.3)$$

Any curvature effect is neglected.

The electronic energy dispersion relations for 2D graphite as a function of the wave vector \vec{k} are determined by finding the eigenvalues of the (2x2) Hamiltonian H :

$$H\psi = E\psi \quad (5.4)$$

$$H\varphi_1 + \beta H\varphi_2 = E\varphi_1 + \beta E\varphi_2 \quad (5.5)$$

Equation 5.5 is then multiplied then by φ_1^* and φ_2^* respectively,

$$\left. \begin{aligned} \varphi_1^* H\varphi_1 + \beta \varphi_1^* H\varphi_2 &= E\varphi_1^*\varphi_1 + \beta E\varphi_1^*\varphi_2 \\ \varphi_2^* H\varphi_1 + \beta \varphi_2^* H\varphi_2 &= E\varphi_2^*\varphi_1 + \beta E\varphi_2^*\varphi_2 \end{aligned} \right\} \quad (5.6)$$

integrated over the entire graphite plane,

$$\left. \begin{aligned} \int \varphi_1^* H\varphi_1 d\tau + \beta \int \varphi_1^* H\varphi_2 d\tau &= E \int \varphi_1^* \varphi_1 d\tau + \beta E \int \varphi_1^* \varphi_2 d\tau \\ \int \varphi_2^* H\varphi_1 d\tau + \beta \int \varphi_2^* H\varphi_2 d\tau &= E \int \varphi_2^* \varphi_1 d\tau + \beta E \int \varphi_2^* \varphi_2 d\tau \end{aligned} \right\} \quad (5.7)$$

The overlap of the p_z wave functions centered on different atoms is neglected:

$$\int X^*(\vec{r} - \vec{r}_A) X(\vec{r} - \vec{r}_B) d\tau = 0 \quad (5.8)$$

and all the site energies are set at zero:

$$H_{11} = \int \varphi_1^* H\varphi_1 d\tau = 0 \quad (5.9)$$

$$H_{22} = \int \varphi_2^* H\varphi_2 d\tau = 0 \quad (5.10)$$

This leads to:

$$\left. \begin{aligned} H_{11} + \beta H_{12} &= ES \\ H_{21} + \beta H_{22} &= \beta ES \end{aligned} \right\} \quad (5.11)$$

where:

$$H_{12} = H_{21}^* = \int \varphi_1^* H\varphi_2 d\tau \quad (5.12)$$

$$\text{and } S = \int \varphi_1^* \varphi_1 d\tau = \int \varphi_2^* \varphi_2 d\tau \quad (5.13)$$

Eliminating β the following equation is obtained:

$$\begin{vmatrix} -ES & H_{12} \\ H_{21} & -ES \end{vmatrix} = 0 \quad (5.14)$$

$$E^2 S^2 - H_{21} H_{12} = 0 \quad (5.15)$$

$$E^2 S^2 - |H_{12}|^2 = 0 \quad (5.16)$$

Since the overlap integrals are neglected, $S=N$, the number of unit cells in the graphite plane. And thus:

$$E = \pm \frac{1}{N} |H_{12}| \quad (5.17)$$

To calculate $|H_{12}|$, only the interactions between the nearest neighbors are considered: all A atoms have three neighboring B atoms and all B atoms have three neighboring A atoms. For the undeformed graphene sheet, writing:

$$-\gamma_0 = \int X^*(\vec{r} - \overrightarrow{AB}) H X(\vec{r}) d\tau > 0 \quad (5.18)$$

H_{12} becomes:

$$H_{12} = \sum_{A,B} \exp(-i \vec{k} \cdot (\vec{r}_A - \vec{r}_B)) \int X^*(\vec{r} - \overrightarrow{AB}) H X(\vec{r}) d\tau \quad (5.19)$$

$$H_{12} = \sum_{\substack{N \\ \text{unit}}} \sum_{\substack{A's \\ \text{nearest} \\ \text{cells neighbors}}} \exp(-i \vec{k} \cdot (\vec{r}_A - \vec{r}_B)) (-\gamma_0) \quad (5.20)$$

However, when the nanotube is under uniaxial strain along the nanotube axis, the C=C bond vectors \vec{r}_1 , \vec{r}_2 and \vec{r}_3 are strained in a different way depending on the nanotube chirality. They can be expressed in the chirality-dependent (c,t) coordinate system (see Figure 2.1) (\hat{c} and \hat{t} are the unit vectors along the nanotube circumference and axis, respectively.), as follows:

$$\vec{r}_1 = \frac{(n+m)}{2 C_h} \mathbf{a}_0 (1 + \varepsilon_c) \hat{c} - \frac{(n-m)}{2\sqrt{3} C_h} \mathbf{a}_0 (1 + \varepsilon_t) \hat{t} \quad (5.21)$$

$$\vec{r}_2 = -\frac{m}{2 C_h} \mathbf{a}_0 (1 + \varepsilon_c) \hat{c} + \frac{(2n+m)}{2\sqrt{3} C_h} \mathbf{a}_0 (1 + \varepsilon_t) \hat{t} \quad (5.22)$$

$$\vec{r}_3 = -(\vec{r}_1 + \vec{r}_2) = -\frac{n}{2 C_h} \mathbf{a}_0 (1 + \varepsilon_c) \hat{c} - \frac{(n+2m)}{2\sqrt{3} C_h} \mathbf{a}_0 (1 + \varepsilon_t) \hat{t} \quad (5.23)$$

where C_h is the circumference of the nanotube in units of unstrained lattice vector length $|\vec{a}_1| = |\vec{a}_2| = a_0 = 0.249\text{nm}$, and ε_c , ε_t are the uniaxial strains along the nanotube circumference and axis, respectively. The 1D unit cell length $|\vec{T}|$ of the deformed nanotube is given by:

$$|\vec{T}| = (1 + \varepsilon_t) \frac{\sqrt{3} C_h a_0}{\gcd(2n+m, n+2m)} \quad (5.24)$$

where $\gcd(2n+m, n+2m)$ is the greatest common divisor of $(2n+m)$ and $(n+2m)$.

Due to the bond length changes, the hopping parameter γ_0 between carbon atoms for the unstrained graphite sheet must be rescaled with bond length. Three hopping parameters, one for each bond length, are introduced:

$$\gamma_i = \gamma_0 (r_0 / r_i)^2 \quad (i = 1, 2, 3) \quad (5.25)$$

The γ_0 value used in these calculations is 2.9 eV and the unstrained bond length r_0 is 0.144 nm. This leads to:

$$H_{12} = -[\gamma_1 \exp(-i\vec{k} \cdot \vec{r}_1) + \gamma_2 \exp(-i\vec{k} \cdot \vec{r}_2) + \gamma_3 \exp(-i\vec{k} \cdot \vec{r}_3)] \quad (5.26)$$

The eigenvalues of the Hamiltonian are thus given by:

$$E(\vec{k}) = \pm \left[\gamma_1^2 + \gamma_2^2 + \gamma_3^2 + 2 \gamma_1 \gamma_2 \cos(\vec{k} \cdot (\vec{r}_1 - \vec{r}_2)) + 2 \gamma_1 \gamma_3 \cos(\vec{k} \cdot (\vec{r}_3 - \vec{r}_1)) + 2 \gamma_2 \gamma_3 \cos(\vec{k} \cdot (\vec{r}_2 - \vec{r}_3)) \right]^{\frac{1}{2}} \quad (5.27)$$

Using the equations of the bond vectors and the periodic boundary condition around the circumference:

$$k_c (1 + \varepsilon_c) C_h a_0 = 2\pi j \quad (5.28)$$

$E(\vec{k})$ is rewritten as:

$$E_j(k_t) = \pm \left[\gamma_1^2 + \gamma_2^2 + \gamma_3^2 + 2 \gamma_1 \gamma_2 \cos\left(\pi j \frac{(n+2m)}{C_h^2} - \frac{\sqrt{3} n}{2 C_h} a_0 (1 + \varepsilon_t) k_t\right) + 2 \gamma_1 \gamma_3 \cos\left(\pi j \frac{(n-m)}{C_h^2} + \frac{\sqrt{3} (n+m)}{2 C_h} a_0 (1 + \varepsilon_t) k_t\right) + 2 \gamma_2 \gamma_3 \cos\left(\pi j \frac{(2n+m)}{C_h^2} + \frac{\sqrt{3} m}{2 C_h} a_0 (1 + \varepsilon_t) k_t\right) \right]^{\frac{1}{2}} \quad (5.29)$$

where j is an integer, k_c the wave vector component along the circumference direction, and k_t is the wave vector component along the nanotube axis. k_t is included in the interval $-\frac{\pi}{|\vec{T}|} < k_t < \frac{\pi}{|\vec{T}|}$ and $j = 1, 2, \dots, N_{hex}$, where N_{hex} is the number of hexagons in the 1D unit cell and is given by:

$$N_{hex} = \frac{2(n^2 + m^2 + nm)}{\gcd(2n+m, 2m+n)} \quad (5.30)$$

The electronic DOS of the (n,m) nanotube is calculated using:

$$\text{DOS}(E) = \frac{2}{N_{hex}} \sum_{j=1}^{N_{hex}} \int \left| \frac{1}{\frac{dE_j(k_t)}{dk_t}} \right| \delta(E_j(k_t) - E) dE \quad (5.31)$$

5.1.2 Results

The electronic band structure and DOS of an armchair $(5,5)$ nanotube, a zigzag $(9,0)$ nanotube and a chiral $(10,5)$ nanotube are showed on Figures 5.2-5.4, respectively (The computation method and the program C/C++ code are given in Appendix I.). $E = 0$ in the band structure represents the Fermi level. Below it (negative energy values), the electronic bands constitute the valence band, and those above it constitute the conduction band. The electronic DOS is obtained from the band structure by calculating the slopes $dE_j(k_t)/dk_t$ of each band, and thus becomes large when the slope is small (especially around $k_t = 0$). VHs appear when the slope $dE_j(k_t)/dk_t$ is zero at the edges of an energy band.

There should be twice as many electronic bands as the number of hexagons N_{hex} in the 1D unit cell, however due to symmetries (for the armchair and zigzag nanotubes for example) some of these bands are doubly degenerate. For the $(5,5)$ nanotube, $N_{hex} = 10$ but only 6 bands and their symmetrical equivalents appear in the valence band since 4 of them are doubly degenerate.

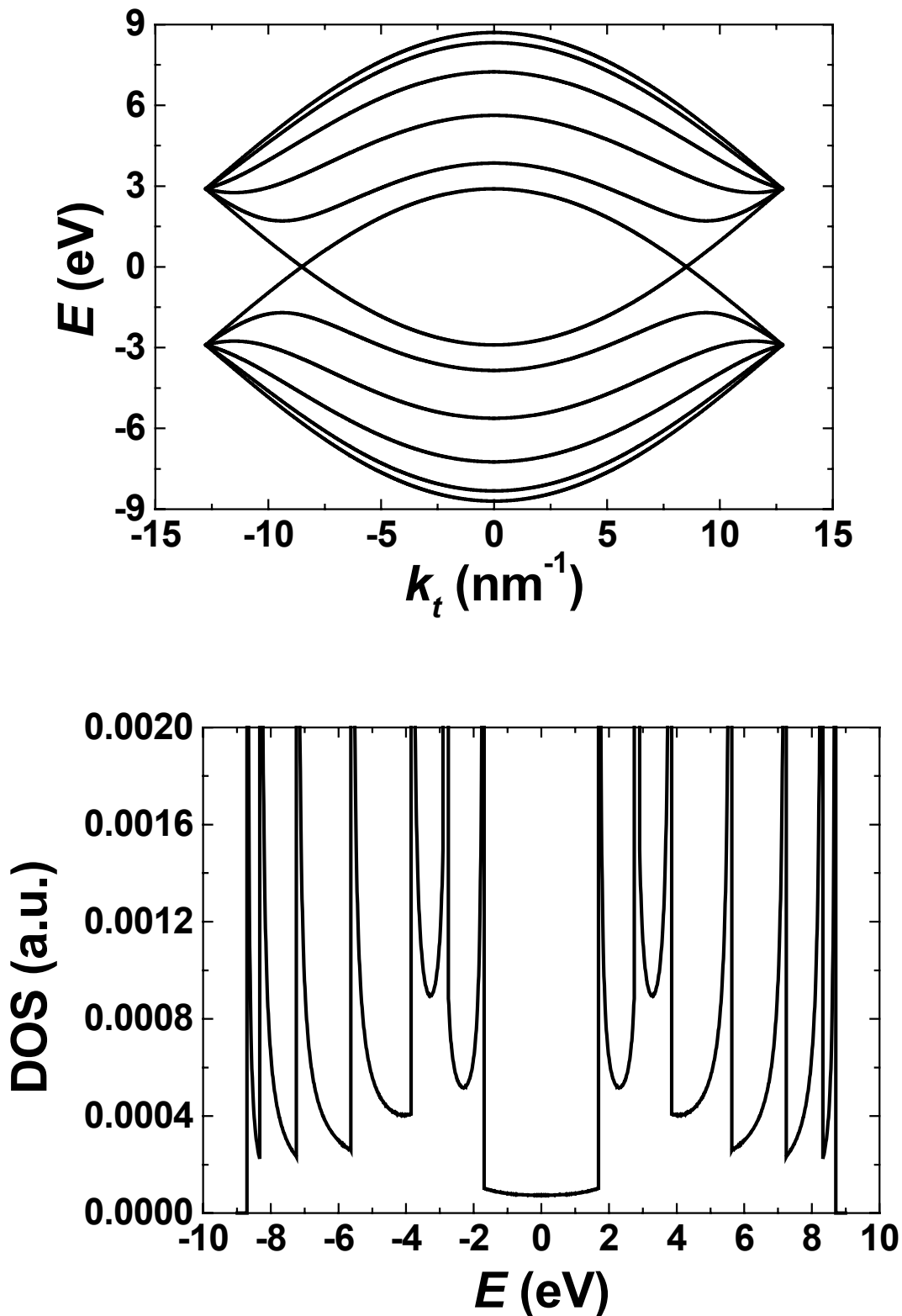


Figure 5.2: Electronic band structure (top) and DOS (bottom) of a (5,5) nanotube, calculated with the TB1 model.

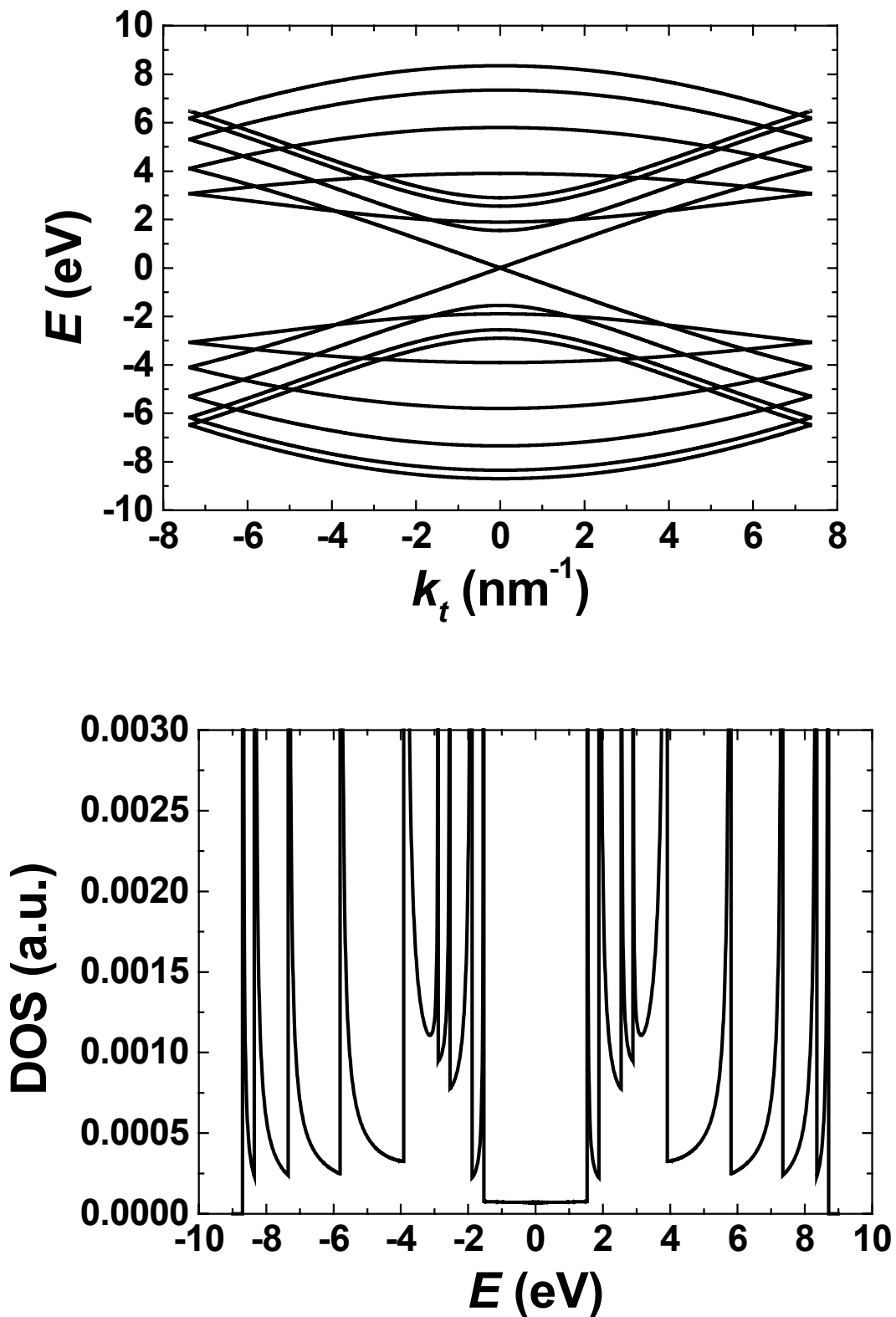


Figure 5.3: Electronic band structure (top) and DOS (bottom) of a (9,0) nanotube, calculated with the TB1 model.

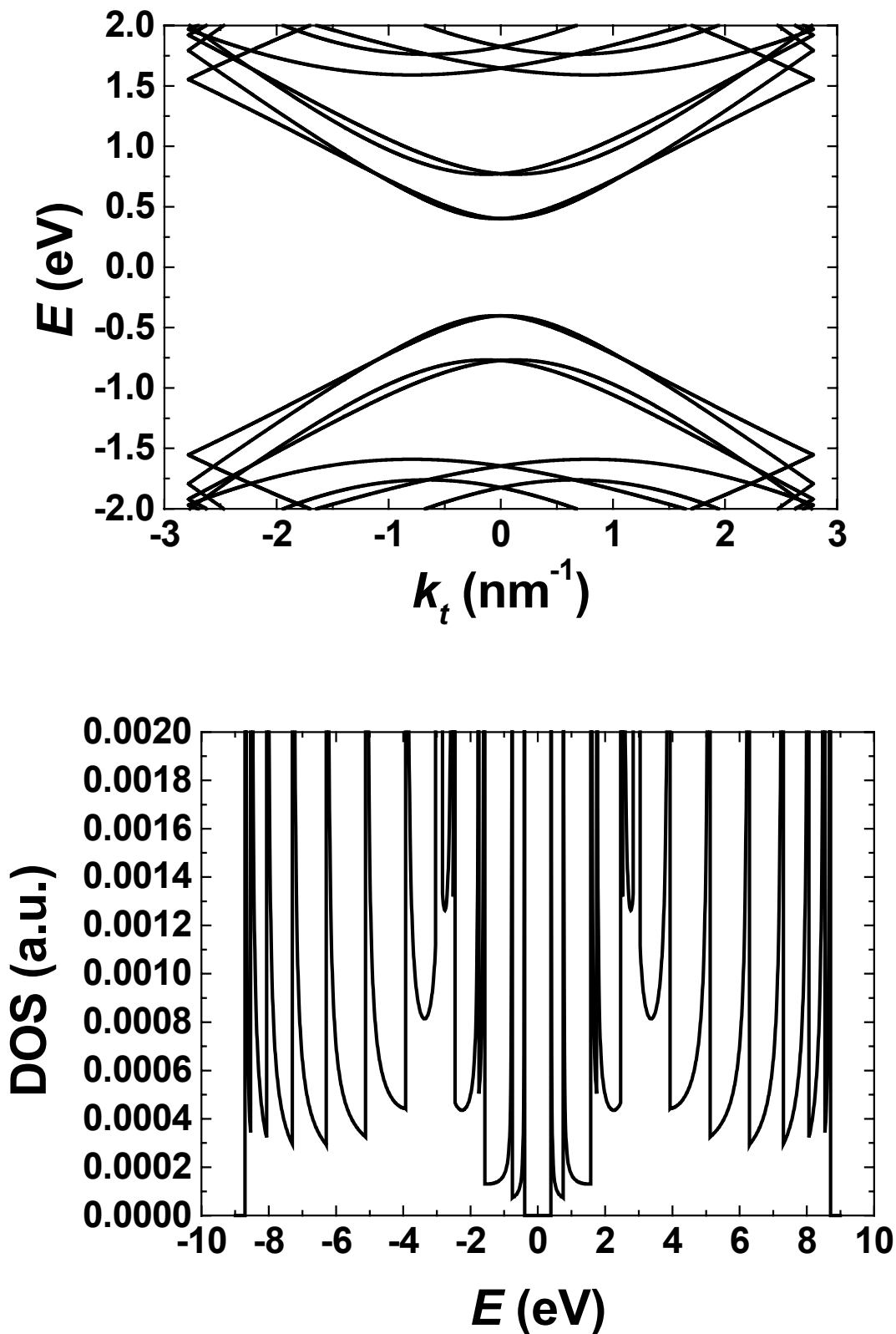


Figure 5.4: Electronic band structure (top) and DOS (bottom) of a (10,5) nanotube, calculated with the TB1 model.

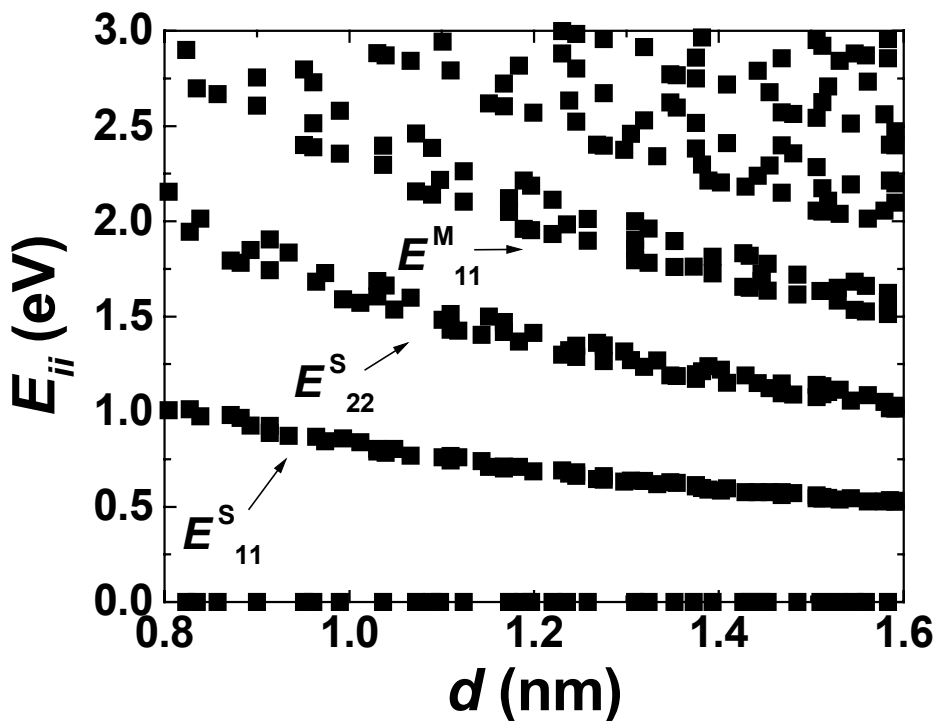


Figure 5.5: Energy separations E_{ii} between the i th pair of vHs in the electronic DOS for nanotubes with a diameter between 0.8 and 1.6 nm, calculated with the TB1 model.

From these figures, the nature of these nanotubes and their electronic band gap can be easily determined. For the (5,5) and (9,0) nanotubes, some electronic bands reach $E = 0$ and the DOS around the Fermi level has a finite value. Their band gap is zero and they are metallic. For the (10,5) nanotube, no band is present for energies between -0.40 eV and 0.40 eV, and the DOS around the Fermi level is zero. It is thus a semiconducting nanotube with a band gap of 0.80 eV. The band gap of semiconducting nanotubes is given by the energy difference E^S_{11} between the first pair of vHs. In this model, since the overlap of π orbitals centered on different atoms is neglected, the conduction and the valence bands are perfectly symmetrical. Thus, the energy difference E_{ii} between the i th pair of symmetrical vHs is simply twice the position of the vHs in the conduction band.

The energy difference E_{ii} between the i th pair of symmetrical vHs was calculated for all the nanotubes with a diameter between 0.8 nm and 1.6 nm

(Figure 5.5). Their values are inversely proportional to the diameter of the nanotube. The points corresponding to $E_{ii} = 0$ come from metallic nanotubes. The first two non-zero E_{ii} values come from semiconducting nanotubes, and are somewhat spread around trend lines given by [168]:

$$E_{11}^S = \frac{2 a_0 \gamma_0}{\sqrt{3} d} ; E_{22}^S = \frac{4 a_0 \gamma_0}{\sqrt{3} d} \quad (5.32)$$

The energy separation between the first pair of vHs for metallic nanotubes has higher values E_{11}^M and are spread around a trend line given by:

$$E_{11}^M = \frac{6 a_0 \gamma_0}{\sqrt{3} d} \quad (5.33)$$

The spreading of the E_{ii} values is minimum for E_{11}^S and becomes wider for the higher-energy peaks.

5.1.3 Effect of Deformation

In Figure 5.6, the electronic DOS of the semiconducting (9,4) nanotube is plotted for different axial strain values. Strain induces changes in the DOS and the shift of the vHs position. The position of the first vHs located around 0.46 eV shifts to lower energies in tension and to higher energies in compression. The position of the second vHs located at 0.87 eV follows the opposite trend: higher energies in tension and lower energies in compression.

From Figure 5.7, the E_{ii} shift trend and magnitude depend on the nanotube structure. The trend can be predicted by determining the two integers p and q , defined by:

$$n - m = 3 q + p \quad (5.34)$$

If $p = 1$, as it is the case for the (10,6), (11,4) and (13,0) nanotubes, the nanotube is semiconducting and the energy separation E_{22}^S between the second pair of vHs decreases in tension. For the (14,0), (12,4), (10,5) and (9,7), $p = -1$, which means they are also semiconducting but in this case E_{22}^S increases in tension.

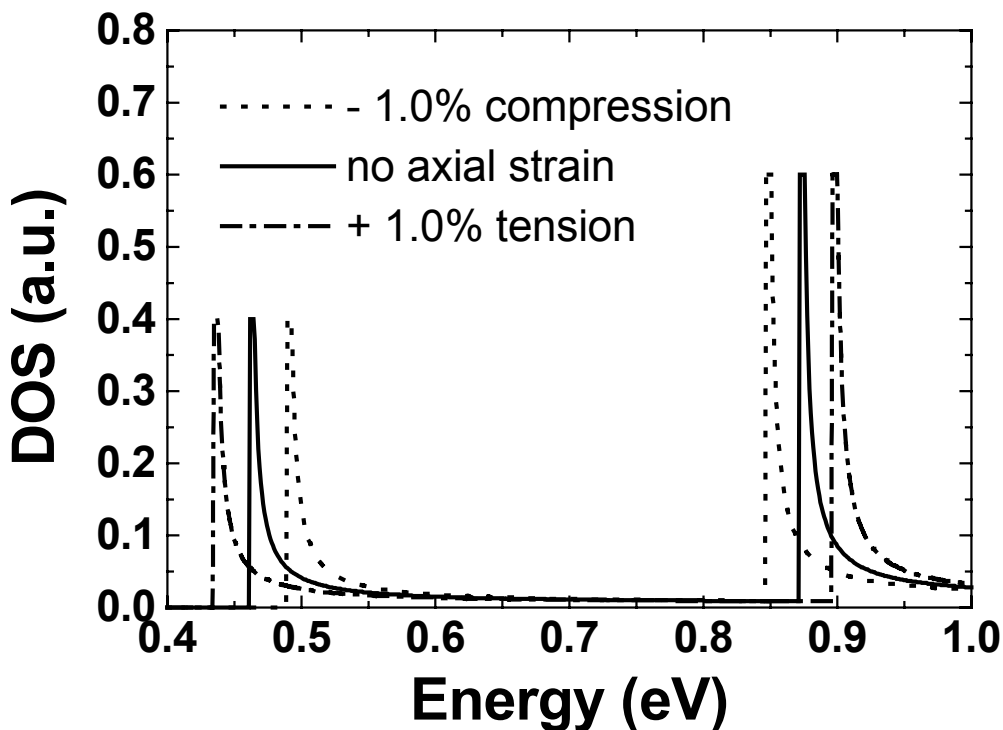


Figure 5.6: DOS of the (9,4) nanotube for different axial strain values, calculated with the TB1 model.

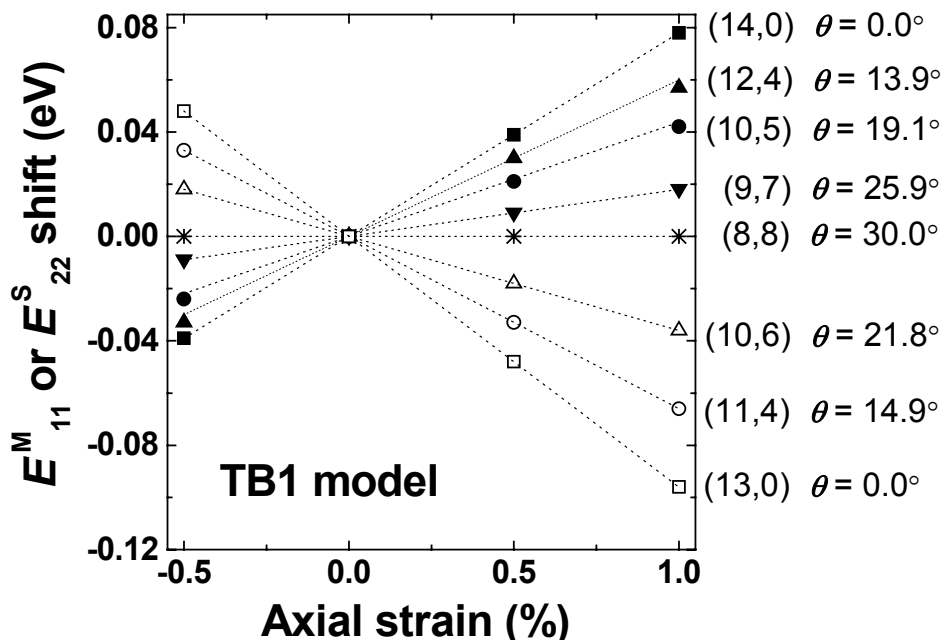


Figure 5.7: The shift of the E^M_{11} value for the metallic (8,8) nanotube and the shift of the E^S_{22} values for the semiconducting (14,0), (12,4), (10,5), (9,7), (10,6), (11,4) and (13,0) nanotubes, as a function of axial strain. The chiral angle θ is given for each nanotube.

For metallic SWNTs ($p = 0$), two types of nanotubes must be distinguished. The DOS of armchair metallic nanotubes is insensitive to uniaxial strain. The energy separation E_{11}^M between the first pair of vHs remains constant with strain. As for non-armchair metallic nanotubes, the vHs are split due to the trigonal warping effect [63,168,194]. The lower energy component shifts to higher energies in tension, while the upper energy component shifts to lower energies in tension.

As for the shift magnitude, the absolute value of the slope of the E_{ii} shift as a function of strain varies with the chiral angle and the (n,m) indexes. It decreases when the chiral angle increases: it is maximum for zigzag nanotubes ($\theta = 0^\circ$) and reaches zero for armchair metallic nanotubes ($\theta = 30^\circ$) (Figure 5.7). It also depends on the (n,m) indexes: the $(13,0)$ and $(14,0)$ tubes have opposite p values and the same chirality, but since their (n,m) indexes are different, the absolute value of the slope of the E_{ii} shift is higher for the $(13,0)$ tube.

5.2 Tight-Binding Model Including Interactions with Third Nearest-Neighbor (TB3)

5.2.1 Theoretical Approach

The model described above neglected the overlap between wave functions and only considered the interactions between nearest neighbors. This model fits generally poorly the STS measurements and *ab initio* calculations over the whole k_t range, except around the point $k_t = \pi / |\vec{T}|$. Recently, an improved tight-binding model was introduced, including overlap and interactions with second- and third nearest-neighbors [192]. The introduction of overlap results in the asymmetry between the conduction and the valence band. This asymmetry is predicted by *ab initio* calculations [173] and was seen experimentally in STS measurements [178]. This improved tight-binding model is presented in the following section and extended to include the effect of strain.

To solve Equation 5.7, while taking into account overlap, the following equation has to be solved:

$$\begin{vmatrix} H_{11} - ES_{11} & H_{12} - ES_{12} \\ H_{12}^* - ES_{12}^* & H_{11} - ES_{11} \end{vmatrix} = 0 \quad (5.35)$$

where the site energies H_{11} and H_{22} , defined by Equations 5.9 and 5.10 are equal but are not zero and:

$$S_{11} = \int \varphi_1^* \varphi_1 d\tau = \int \varphi_2^* \varphi_2 d\tau \quad (5.36)$$

$$S_{12} = \int \varphi_1^* \varphi_2 d\tau$$

Equation 5.14 is a simplification of Equation 5.35, where the site energies are set to zero and overlap is neglected. The general solution of Equation 5.35 is:

$$E = \frac{-(-2E_0 + E_1) \pm \sqrt{(-2E_0 + E_1)^2 - 4E_2 E_3}}{2E_3} \quad (5.37)$$

where:

$$E_0 = H_{11} S_{11} \quad (5.38)$$

$$E_1 = S_{12} H_{12}^* + H_{12} S_{12}^* \quad (5.39)$$

$$E_2 = H_{11}^2 - H_{12} H_{12}^* \quad (5.40)$$

$$E_3 = S_{11}^2 - S_{12} S_{12}^* \quad (5.41)$$

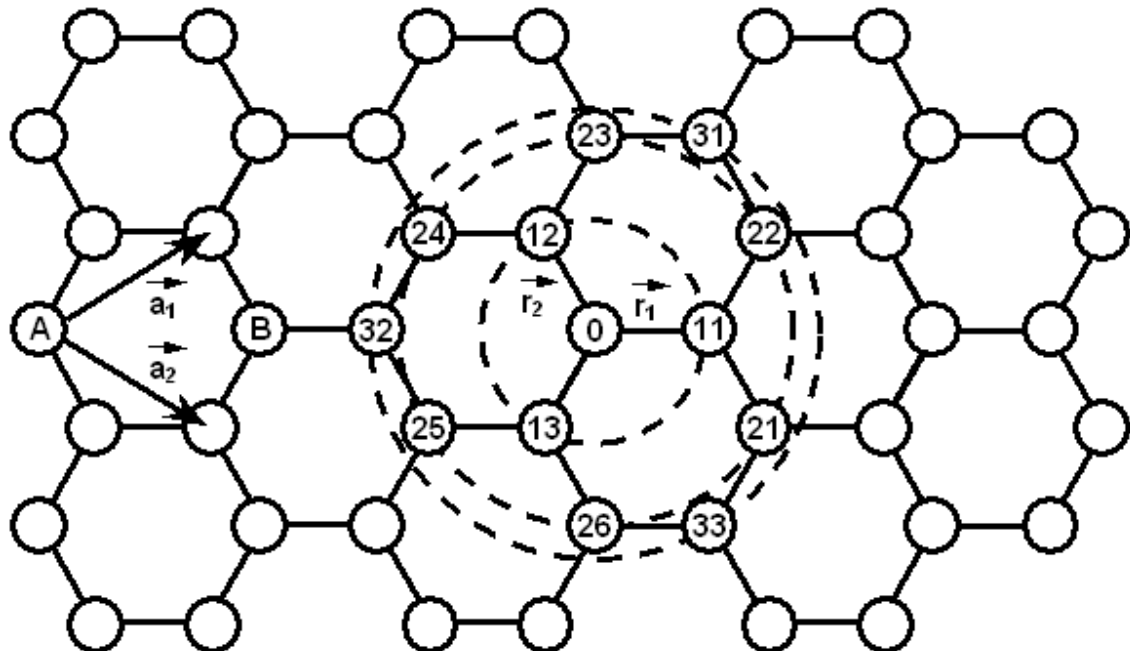


Figure 5.8: Graphite hexagonal lattice. The atom A0 has 6 A second-nearest neighbors and 3 B third-nearest neighbors.

The calculation of H_{11} , H_{12} , S_{11} and S_{12} requires the introduction of the interactions with the second- and third-nearest neighbors which are showed in Figure 5.8. The atomic positions of the neighbors expressed in the basis set of bond vectors \vec{r}_1 and \vec{r}_2 are given in Table 5.1. Each A atom has 3 B nearest-neighbors B_{1i} ($i=1,2,3$), 6 A second-nearest neighbors A_{2i} ($i=1,2,\dots,6$), and 3 B third-nearest neighbors B_{3i} ($i=1,2,3$).

Table 5.1: Position vectors of the nearest neighbors expressed in the basis set of bond vectors \vec{r}_1 and \vec{r}_2 .

Carbon atom	Position	Carbon atom	Position
B11	\vec{r}_1	A24	$\vec{r}_2 - \vec{r}_1$
B12	\vec{r}_2	A25	$-2\vec{r}_1 - \vec{r}_2$
B13	$-\vec{r}_1 - \vec{r}_2$	A26	$-\vec{r}_1 - 2\vec{r}_2$
A21	$\vec{r}_1 - \vec{r}_2$	B31	$2(\vec{r}_1 + \vec{r}_2)$
A22	$2\vec{r}_1 + \vec{r}_2$	B32	$-2\vec{r}_1$
A23	$\vec{r}_1 + 2\vec{r}_2$	B33	$-2\vec{r}_2$

The site energy ε_{2p} , the interactions energies γ_0 , γ_1 , γ_2 , between nearest-, second-nearest- and third-nearest-neighbors respectively, and the corresponding overlap s_1 and s_2 are defined as follows:

$$\varepsilon_{2p} = \int X^*(\vec{r} - \vec{R}_A) H X(\vec{r} - \vec{R}_A) d\tau \quad (5.42)$$

$$\gamma_0 = \int X^*(\vec{r} - \vec{R}_{1i}) H X(\vec{r}) d\tau \quad (i = 1,2,3) \quad (5.43)$$

$$\gamma_1 = \int X^*(\vec{r} - \vec{R}_{2i}) H X(\vec{r}) d\tau \quad (i = 1,2,\dots,6) \quad (5.44)$$

$$\gamma_2 = \int X^*(\vec{r} - \vec{R}_{3i}) H X(\vec{r}) d\tau \quad (i = 1,2,3) \quad (5.45)$$

$$s_0 = \int X^*(\vec{r} - \vec{R}_{1i}) X(\vec{r}) d\tau \quad (i = 1,2,3) \quad (5.46)$$

$$s_1 = \int X^*(\vec{r} - \vec{R}_{2i}) X(\vec{r}) d\tau \quad (i = 1,2,\dots,6) \quad (5.47)$$

$$s_2 = \int X^*(\vec{r} - \vec{R}_{3i}) X(\vec{r}) d\tau \quad (i = 1,2,3) \quad (5.48)$$

where \vec{R}_{1i} , \vec{R}_{2i} , and \vec{R}_{3i} are the vectors defined between the atom C_0 and the atoms C_{1i} (nearest neighbors), C_{2i} (second-nearest neighbors), and C_{3i} (third-

nearest neighbors), respectively.

Using Equations 5.42 to 5.48, H_{11} , H_{12} , S_{11} and S_{12} can be expressed as follows:

$$H_{11} = \int \varphi_1^* H \varphi_1 d\tau = \sum_{A, A' \text{ atoms}} \exp(-i \vec{k} \cdot (\vec{r}_A - \vec{r}_{A'})) \int X^*(\vec{r} - \vec{r}_A) H X(\vec{r} - \vec{r}_{A'}) d\tau \quad (5.49)$$

$$\begin{aligned} H_{11} = & \varepsilon_{2p} + 2\gamma_1(|\vec{r}_1 - \vec{r}_2|) \cos(\vec{k} \cdot (\vec{r}_1 - \vec{r}_2)) + 2\gamma_1(|2\vec{r}_1 + \vec{r}_2|) \cos(\vec{k} \cdot (2\vec{r}_1 + \vec{r}_2)) \\ & + 2\gamma_1(|\vec{r}_1 + 2\vec{r}_2|) \cos(\vec{k} \cdot (\vec{r}_1 + 2\vec{r}_2)) \end{aligned} \quad (5.50)$$

$$S_{11} = \int \varphi_1^* \varphi_1 d\tau = \sum_{A, A' \text{ atoms}} \exp(-i \vec{k} \cdot (\vec{r}_A - \vec{r}_{A'})) \int X^*(\vec{r} - \vec{r}_A) X(\vec{r} - \vec{r}_{A'}) d\tau \quad (5.51)$$

$$\begin{aligned} S_{11} = & 1 + 2 s_1(|\vec{r}_1 - \vec{r}_2|) \cos(\vec{k} \cdot (\vec{r}_1 - \vec{r}_2)) + 2 s_1(|2\vec{r}_1 + \vec{r}_2|) \cos(\vec{k} \cdot (2\vec{r}_1 + \vec{r}_2)) \\ & + 2 s_1(|\vec{r}_1 + 2\vec{r}_2|) \cos(\vec{k} \cdot (\vec{r}_1 + 2\vec{r}_2)) \end{aligned} \quad (5.52)$$

$$H_{12} = \int \varphi_1^* H \varphi_2 d\tau = \sum_{A, B \text{ atoms}} \exp(-i \vec{k} \cdot (\vec{r}_A - \vec{r}_B)) \int X^*(\vec{r} - \vec{r}_A) H X(\vec{r} - \vec{r}_B) d\tau \quad (5.53)$$

$$\begin{aligned} H_{12} = & \gamma_0(|\vec{r}_1|) \exp(i \vec{k} \cdot \vec{r}_1) + \gamma_0(|\vec{r}_2|) \exp(i \vec{k} \cdot \vec{r}_2) + \gamma_0(|\vec{r}_1 + \vec{r}_2|) \exp(-i \vec{k} \cdot (\vec{r}_1 + \vec{r}_2)) \\ & + \gamma_2(|2\vec{r}_1 + \vec{r}_2|) \exp(i 2 \vec{k} \cdot (\vec{r}_1 + \vec{r}_2)) + \gamma_2(|2\vec{r}_1|) \exp(-i 2 \vec{k} \cdot \vec{r}_1) \\ & + \gamma_2(|2\vec{r}_2|) \exp(-i 2 \vec{k} \cdot \vec{r}_2) \end{aligned} \quad (5.54)$$

$$S_{12} = \int \varphi_1^* \varphi_2 d\tau = \sum_{A, B \text{ atoms}} \exp(-i \vec{k} \cdot (\vec{r}_A - \vec{r}_B)) \int X^*(\vec{r} - \vec{r}_A) X(\vec{r} - \vec{r}_B) d\tau \quad (5.55)$$

$$\begin{aligned} S_{12} = & s_0(|\vec{r}_1|) \exp(i \vec{k} \cdot \vec{r}_1) + s_0(|\vec{r}_2|) \exp(i \vec{k} \cdot \vec{r}_2) + s_0(|\vec{r}_1 + \vec{r}_2|) \exp(-i \vec{k} \cdot (\vec{r}_1 + \vec{r}_2)) \\ & + s_2(|2\vec{r}_1 + \vec{r}_2|) \exp(i 2 \vec{k} \cdot (\vec{r}_1 + \vec{r}_2)) + s_2(|2\vec{r}_1|) \exp(-i 2 \vec{k} \cdot \vec{r}_1) \\ & + s_2(|2\vec{r}_2|) \exp(-i 2 \vec{k} \cdot \vec{r}_2) \end{aligned} \quad (5.56)$$

When the graphite lattice is deformed under uniaxial strain, the distance between carbon atoms varies anisotropically, and therefore the parameters defined in Equations 5.42 to 5.48 are rescaled accordingly [195]. If the new bond vectors are \vec{r}_1' and \vec{r}_2' , the new parameters are defined as follows:

$$\gamma_{01} = \gamma_0 \left(\frac{|\vec{r}_1|}{|\vec{r}_1'|} \right)^2 \quad (5.57)$$

$$\gamma_{02} = \gamma_0 \left(\frac{|\vec{r}_2|}{|\vec{r}_2'|} \right)^2 \quad (5.58)$$

$$\gamma_{03} = \gamma_0 \left(\frac{|\vec{r}_1 + \vec{r}_2|}{|\vec{r}_1' + \vec{r}_2'|} \right)^2 \quad (5.59)$$

$$\gamma_{11} = \gamma_1 \left(\frac{|\vec{r}_1 - \vec{r}_2|}{|\vec{r}_1' - \vec{r}_2'|} \right)^2 \quad (5.60)$$

$$\gamma_{12} = \gamma_1 \left(\frac{|2\vec{r}_1 + \vec{r}_2|}{|2\vec{r}_1' + \vec{r}_2'|} \right)^2 \quad (5.61)$$

$$\gamma_{13} = \gamma_1 \left(\frac{|\vec{r}_1 + 2\vec{r}_2|}{|\vec{r}_1' + 2\vec{r}_2'|} \right)^2 \quad (5.62)$$

$$\gamma_{21} = \gamma_2 \left(\frac{|\vec{r}_1 + \vec{r}_2|}{|\vec{r}_1' + \vec{r}_2'|} \right)^2 \quad (5.63)$$

$$\gamma_{22} = \gamma_2 \left(\frac{|\vec{r}_1|}{|\vec{r}_1'|} \right)^2 \quad (5.64)$$

$$\gamma_{23} = \gamma_2 \left(\frac{|\vec{r}_2|}{|\vec{r}_2'|} \right)^2 \quad (5.65)$$

$$s_{01} = s_0 \left(\frac{|\vec{r}_1|}{|\vec{r}_1'|} \right)^2 \quad (5.66)$$

$$s_{02} = s_0 \left(\frac{|\vec{r}_2|}{|\vec{r}_2'|} \right)^2 \quad (5.67)$$

$$s_{03} = s_0 \left(\frac{|\vec{r}_1 + \vec{r}_2|}{|\vec{r}_1' + \vec{r}_2'|} \right)^2 \quad (5.68)$$

$$s_{11} = s_1 \left(\frac{|\vec{r}_1 - \vec{r}_2|}{|\vec{r}_1' - \vec{r}_2'|} \right)^2 \quad (5.69)$$

$$s_{12} = s_1 \left(\frac{|2\vec{r}_1 + \vec{r}_2|}{|2\vec{r}_1' + \vec{r}_2'|} \right)^2 \quad (5.70)$$

$$s_{13} = s_1 \left(\frac{|\vec{r}_1 + 2\vec{r}_2|}{|\vec{r}_1' + 2\vec{r}_2'|} \right)^2 \quad (5.71)$$

$$s_{21} = s_2 \left(\frac{|\vec{r}_1 + \vec{r}_2|}{|\vec{r}_1' + \vec{r}_2'|} \right)^2 \quad (5.72)$$

$$s_{22} = s_2 \left(\frac{|\vec{r}_1|}{|\vec{r}_1'|} \right)^2 \quad (5.73)$$

$$s_{23} = s_2 \left(\frac{|\vec{r}_2|}{|\vec{r}_2'|} \right)^2 \quad (5.74)$$

Using the new parameters, Equations 5.38 to 5.41 are rewritten as follows:

$$E_0 = \left[\begin{array}{l} \varepsilon_{2p} + 2\gamma_{11} \cos(\vec{k} \cdot (\vec{r}_1 - \vec{r}_2)) + 2\gamma_{12} \cos(\vec{k} \cdot (2\vec{r}_1 + \vec{r}_2)) \\ + 2\gamma_{13} \cos(\vec{k} \cdot (\vec{r}_1 + 2\vec{r}_2)) \end{array} \right] \quad (5.75)$$

$$\times \left[\begin{array}{l} 1 + 2s_{11} \cos(\vec{k} \cdot (\vec{r}_1 - \vec{r}_2)) + 2s_{12} \cos(\vec{k} \cdot (2\vec{r}_1 + \vec{r}_2)) \\ 2s_{13} \cos(\vec{k} \cdot (\vec{r}_1 + 2\vec{r}_2)) \end{array} \right]$$

$$\begin{aligned} E_1 = & 2[s_{01}\gamma_{01} + s_{02}\gamma_{02} + s_{03}\gamma_{03} + s_{21}\gamma_{21} + s_{22}\gamma_{22} + s_{23}\gamma_{23}] \\ & + 2\cos(\vec{k} \cdot (\vec{r}_1 - \vec{r}_2))[s_{01}\gamma_{02} + s_{02}\gamma_{01} + s_{03}\gamma_{22} + s_{03}\gamma_{23} + s_{22}\gamma_{03} + s_{23}\gamma_{03}] \\ & + 2\cos(\vec{k} \cdot (2\vec{r}_1 + \vec{r}_2))[s_{01}\gamma_{03} + s_{02}\gamma_{22} + s_{03}\gamma_{01} + s_{22}\gamma_{02} + s_{02}\gamma_{21} + s_{21}\gamma_{02}] \\ & + 2\cos(\vec{k} \cdot (\vec{r}_1 + 2\vec{r}_2))[s_{01}\gamma_{21} + s_{01}\gamma_{23} + s_{02}\gamma_{03} + s_{03}\gamma_{02} + s_{21}\gamma_{01} + s_{23}\gamma_{01}] \\ & + 2\cos(3\vec{k} \cdot \vec{r}_1)[s_{01}\gamma_{22} + s_{22}\gamma_{01}] + 2\cos(3\vec{k} \cdot \vec{r}_2)[s_{02}\gamma_{23} + s_{23}\gamma_{02}] \quad (5.76) \\ & + 2\cos(3\vec{k} \cdot (\vec{r}_1 + \vec{r}_2))[s_{03}\gamma_{21} + s_{21}\gamma_{03}] \\ & + 2\cos(2\vec{k} \cdot (2\vec{r}_1 + \vec{r}_2))[s_{21}\gamma_{22} + s_{22}\gamma_{21}] \\ & + 2\cos(2\vec{k} \cdot (\vec{r}_1 + 2\vec{r}_2))[s_{21}\gamma_{23} + s_{23}\gamma_{21}] \\ & + 2\cos(2\vec{k} \cdot (\vec{r}_1 - \vec{r}_2))[s_{22}\gamma_{23} + s_{23}\gamma_{22}] \end{aligned}$$

$$\begin{aligned} E_2 = & \left[\begin{array}{l} \varepsilon_{2p} + 2\gamma_{11} \cos(\vec{k} \cdot (\vec{r}_1 - \vec{r}_2)) + 2\gamma_{12} \cos(\vec{k} \cdot (2\vec{r}_1 + \vec{r}_2)) \\ + 2\gamma_{13} \cos(\vec{k} \cdot (\vec{r}_1 + 2\vec{r}_2)) \end{array} \right]^2 \\ & - [(\gamma_{01})^2 + (\gamma_{02})^2 + (\gamma_{03})^2 + (\gamma_{21})^2 + (\gamma_{22})^2 + (\gamma_{23})^2] \\ & - 2\cos(\vec{k} \cdot (\vec{r}_1 - \vec{r}_2))[\gamma_{01}\gamma_{02} + \gamma_{03}\gamma_{22} + \gamma_{03}\gamma_{23}] \\ & - 2\cos(\vec{k} \cdot (2\vec{r}_1 + \vec{r}_2))[\gamma_{01}\gamma_{03} + \gamma_{02}\gamma_{21} + \gamma_{02}\gamma_{22}] \quad (5.77) \\ & - 2\cos(\vec{k} \cdot (\vec{r}_1 + 2\vec{r}_2))[\gamma_{01}\gamma_{21} + \gamma_{01}\gamma_{23} + \gamma_{02}\gamma_{03}] \\ & - 2\gamma_{01}\gamma_{22} \cos(3\vec{k} \cdot \vec{r}_1) - 2\gamma_{02}\gamma_{23} \cos(3\vec{k} \cdot \vec{r}_2) \\ & - 2\gamma_{03}\gamma_{21} \cos(3\vec{k} \cdot (\vec{r}_1 + \vec{r}_2)) - 2\gamma_{21}\gamma_{22} \cos(2\vec{k} \cdot (2\vec{r}_1 + \vec{r}_2)) \\ & - 2\gamma_{23}\gamma_{21} \cos(2\vec{k} \cdot (\vec{r}_1 + 2\vec{r}_2)) - 2\gamma_{22}\gamma_{23} \cos(2\vec{k} \cdot (\vec{r}_1 - \vec{r}_2)) \end{aligned}$$

$$\begin{aligned}
 E_3 = & \left[1 + 2s_{11} \cos(\vec{k} \cdot (\vec{r}_1 - \vec{r}_2)) + 2s_{12} \cos(\vec{k} \cdot (2\vec{r}_1 + \vec{r}_2)) + 2s_{13} \cos(\vec{k} \cdot (\vec{r}_1 + 2\vec{r}_2)) \right]^2 \\
 & - \left[(s_{01})^2 + (s_{02})^2 + (s_{03})^2 + (s_{21})^2 + (s_{22})^2 + (s_{23})^2 \right] \\
 & - 2 \cos(\vec{k} \cdot (\vec{r}_1 - \vec{r}_2)) [s_{01} s_{02} + s_{03} s_{22} + s_{03} s_{23}] \\
 & - 2 \cos(\vec{k} \cdot (2\vec{r}_1 + \vec{r}_2)) [s_{01} s_{03} + s_{02} s_{21} + s_{02} s_{22}] - 2 s_{01} s_{22} \cos(3\vec{k} \cdot \vec{r}_1) \quad (5.78) \\
 & - 2 \cos(\vec{k} \cdot (\vec{r}_1 + 2\vec{r}_2)) [s_{01} s_{21} + s_{01} s_{23} + s_{02} s_{03}] - 2 s_{02} s_{23} \cos(3\vec{k} \cdot \vec{r}_2) \\
 & - 2 s_{03} s_{21} \cos(3\vec{k} \cdot (\vec{r}_1 + \vec{r}_2)) - 2 s_{21} s_{22} \cos(2\vec{k} \cdot (2\vec{r}_1 + \vec{r}_2)) \\
 & - 2 s_{23} s_{21} \cos(2\vec{k} \cdot (\vec{r}_1 + 2\vec{r}_2)) - 2 s_{22} s_{23} \cos(2\vec{k} \cdot (\vec{r}_1 - \vec{r}_2))
 \end{aligned}$$

The products $\vec{k} \cdot \vec{r}_1$ and $\vec{k} \cdot \vec{r}_2$ are calculated using Equations 5.21, 5.22 and the boundary condition expressed in Equation 5.28.

5.2.2 Results

The electronic band structure and DOS of an armchair (5,5) nanotube, a zigzag (9,0) nanotube and a chiral (10,5) nanotube obtained with the improved tight-binding model are showed on Figures 5.9-5.11, respectively. The seven parameters of the model are: $\varepsilon_{2p} = -2.03$ eV, $\gamma_0 = -2.79$ eV, $\gamma_1 = -0.68$ eV, $\gamma_2 = -0.30$ eV, $s_0 = 0.30$ eV, $s_1 = 0.046$ eV, and $s_2 = 0.039$ eV [192]. The electronic DOS is calculated using Equation 5.31 (see Appendix I).

The most striking difference between Figures 5.2 and 5.9 is the asymmetry between the valence band and the conduction band. This is particularly obvious in the DOS spectrum, where the electronic states in the valence band are much more compact and closer to the Fermi level ($E = 0$ eV). The conduction band is less compact than the valence band and spreads further away from the Fermi level. For example, the maximum energy in the conduction band is around 9 eV in Figure 5.2 and above 12 eV in Figure 5.9. Also in Figure 5.9, the degeneracy of the electronic bands is partially lifted around $k_t = \pi / |\vec{T}|$.

Because of this asymmetry between the valence and the conduction bands, the determination of the electronic transition energies is more delicate.

According to the TB3 model, the nanotubes are still predicted to be metallic if $(n-m)$ is a multiple of 3. Because of the momentum conservation principle, the transitions between electronic bands of same k_c are favored.

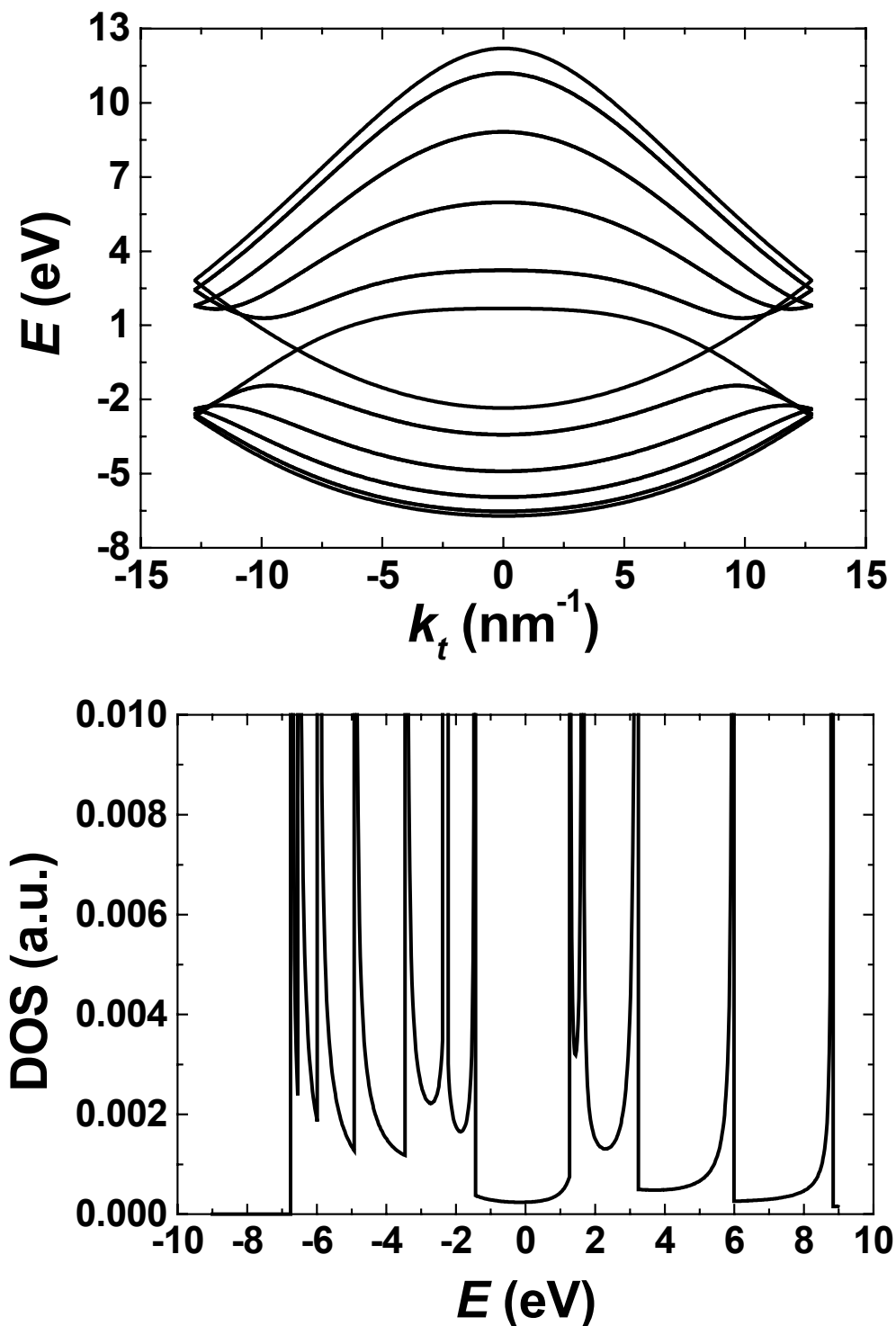


Figure 5.9: Electronic band structure (top) and DOS (bottom) of a (5,5) nanotube, calculated with the TB3 model.

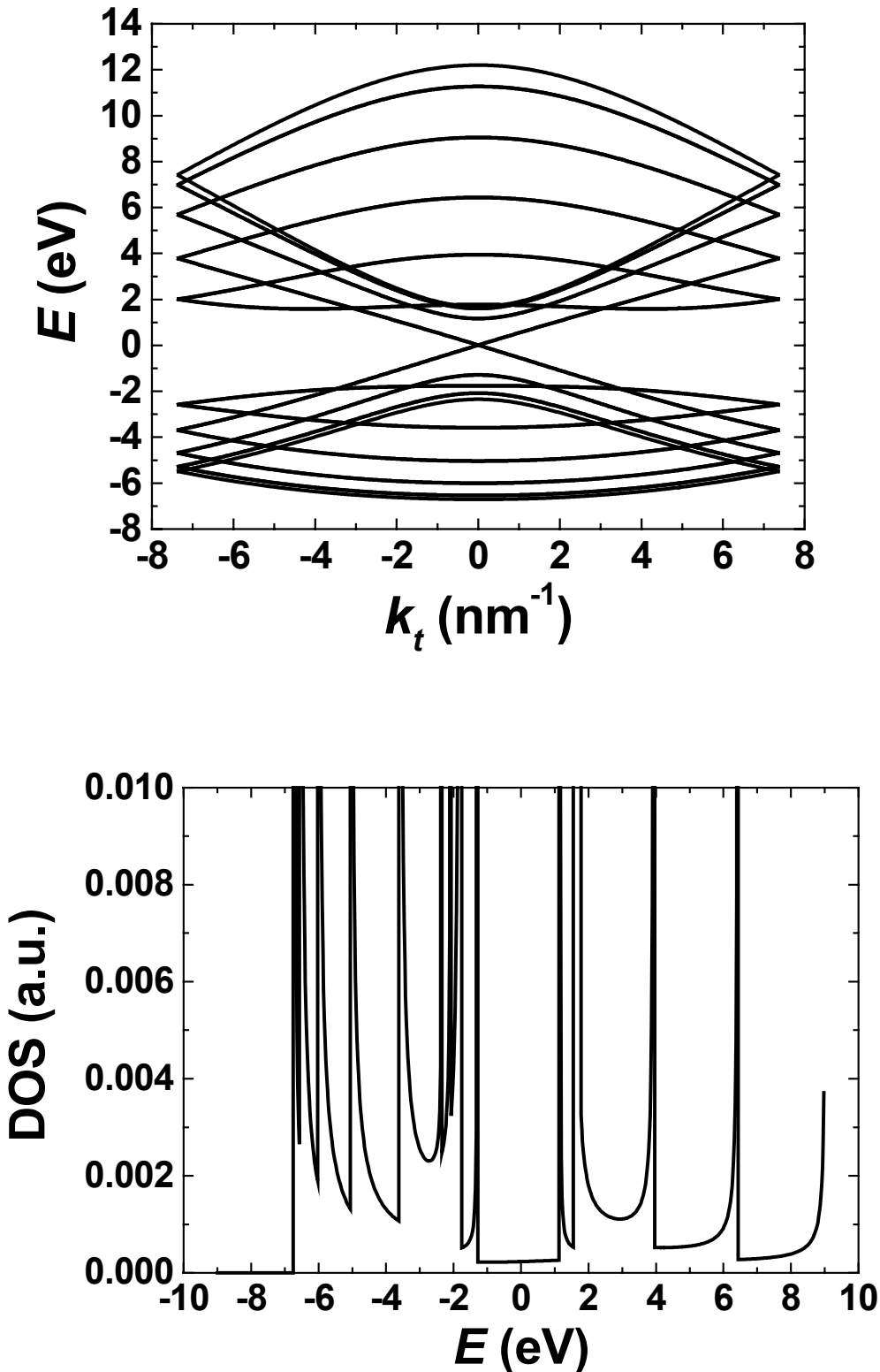


Figure 5.10: Electronic band structure (top) and DOS (bottom) of a (9,0) nanotube, calculated with the TB3 model.

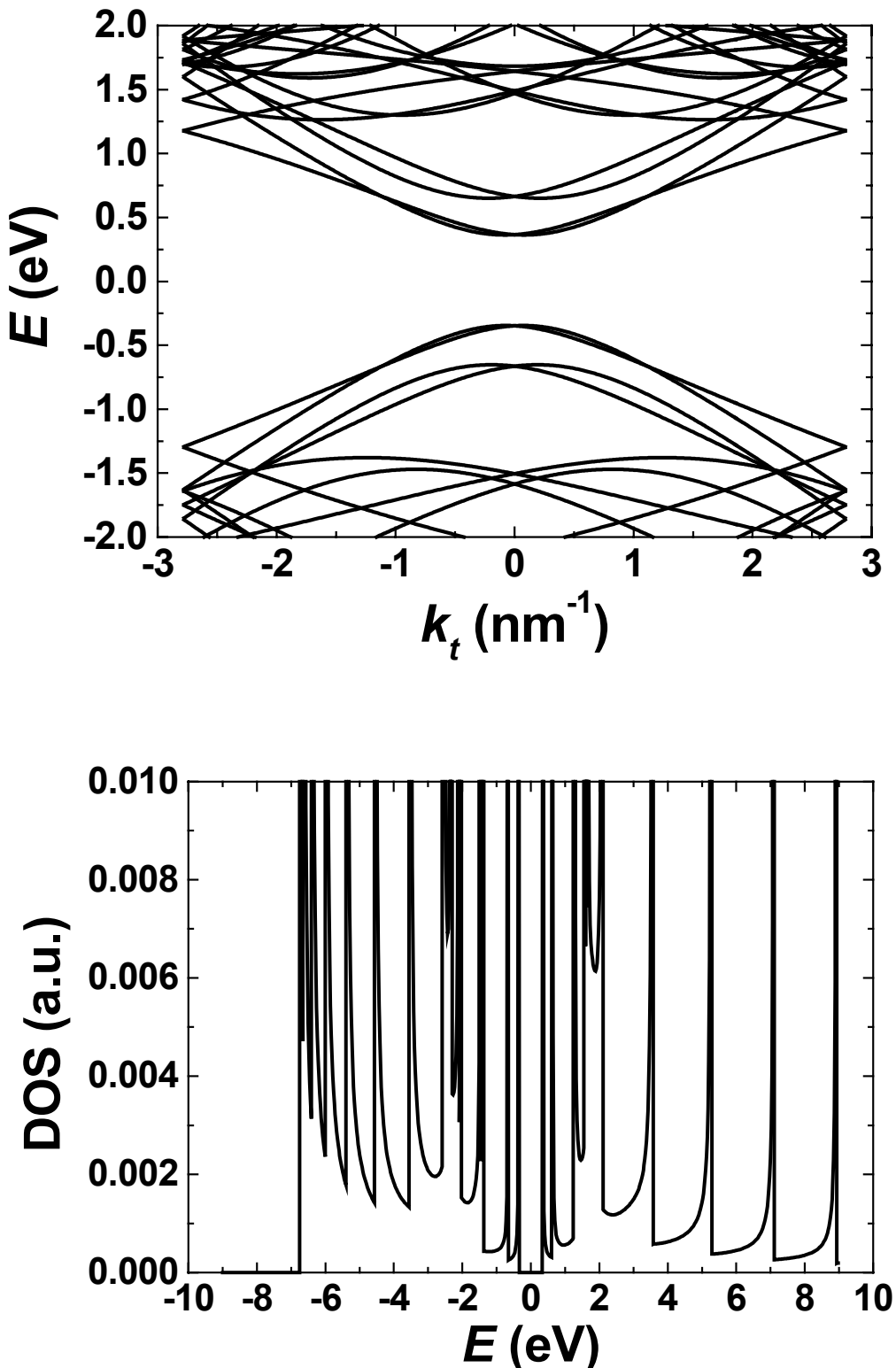


Figure 5.11: Electronic band structure (top) and DOS (bottom) of a (10,5) nanotube, calculated with the TB3 model.

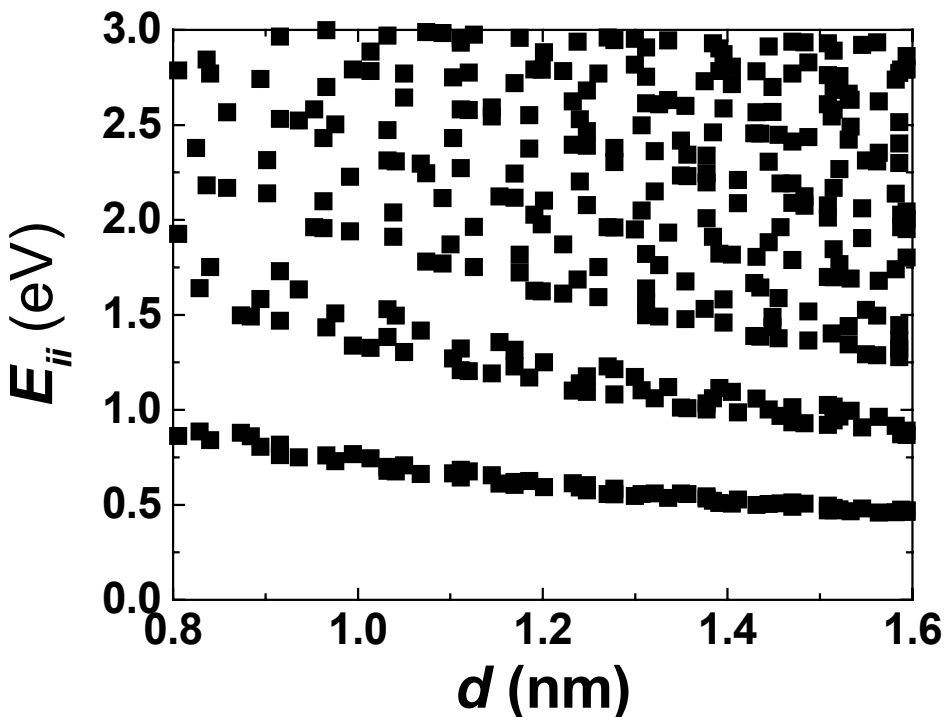


Figure 5.12: Energy separations E_{ii} between the i th pair of vHs in the electronic DOS for nanotubes with a diameter between 0.8 and 1.6 nm, calculated with the TB3 model.

In the symmetric case, these bands are in the same order in the valence and conduction bands, but in the asymmetric case, bands mix differently above and below the Fermi level. This is especially true for achiral nanotubes and $|E| \geq 1.5$ eV (Figure 5.11). For transition energies below 3 eV, the transitions are still between the i th pair of vHs in the DOS.

The electronic transition energies were calculated for all nanotubes in a diameter range between 0.8 and 1.6 nm (Figure 5.12). Their values are still approximately inversely proportional to the nanotube diameter, but compared to Figure 5.5, Figure 5.12 exhibits a much larger dependence on the nanotube chirality, especially for transitions of energies above 1.5 eV. To better compare the data from the two models, the E_{22}^S and E_{11}^M values are plotted against the diameter in Figures 5.13 and 5.14 respectively. The results from the TB3 model are systematically lower than those from the TB1 model, and the difference is larger for smaller diameter nanotubes. The data can be fitted with Equations 5.32 and 5.33, with only one adjustable parameter γ_0 . In the diameter range between 0.8 nm and 1.6 nm, the E_{22}^S values from the TB1 model can be fitted

with $\gamma_0 = 2.88 \text{ eV}$, while those from the TB3 model can be fitted with $\gamma_0 = 2.50 \text{ eV}$. As for the E_{11}^M values, $\gamma_0 = 2.84 \text{ eV}$ for the TB1 model and $\gamma_0 = 2.43 \text{ eV}$ for the TB3 model. The TB3 model was developed to obtain the optical transition values from *ab initio* calculations, and those are known to be systematically lower than the values from experiments or other models [192].

To quantify the dispersion of the data, and thus the dependence of E_{ii} on the nanotube chirality, the following quantity was calculated:

$$\text{Chi}^2 = \frac{1}{N} \sum_{k=1}^N (x_{\text{data}} - x_{\text{fit}})^2 \quad (5.79)$$

where x_{data} are the data points, x_{fit} the corresponding results from the fitting equation, and N the total number of data points. The Chi^2 values were 0.0022 and 0.0053 for the E_{22}^S values obtained from the TB1 and the TB3 models respectively. As for the E_{11}^M values, they were 0.0099 and 0.0246, respectively.

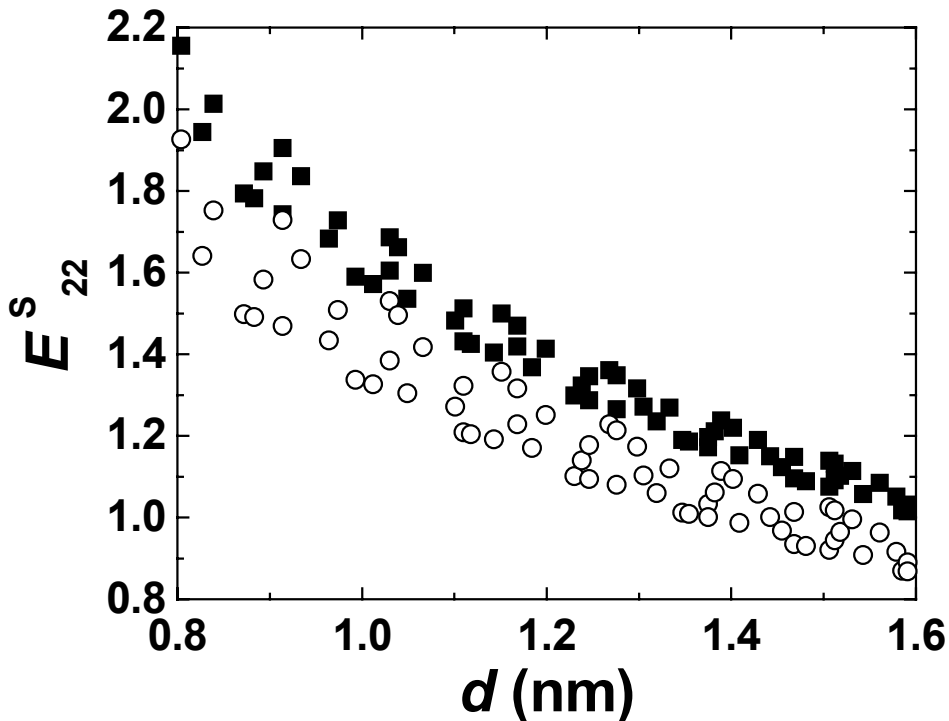


Figure 5.13: Comparison between the E_{22}^S values calculated with the TB1 model (solid squares) and the TB3 model (open circles).

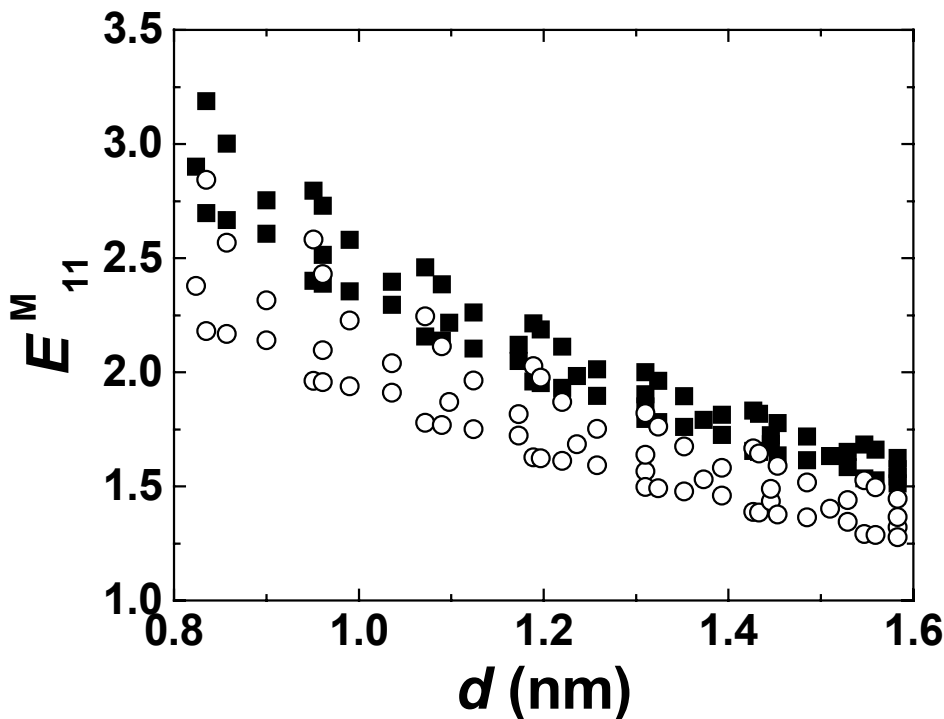


Figure 5.14: Comparison between the $E_M^M_{11}$ values calculated with the TB1 model (solid squares) and the TB3 model (open circles).

5.2.3 Effect of Deformation

The effect of uniaxial deformation was studied on all nanotubes with diameters between 0.8 and 1.6 nm. The E_{ii} values were computed for all of them for a strain value of 0.5% in tension and in compression. The results for the (14,0), (12,4), (10,5), (9,7), (8,8), (10,6), (11,4) and (13,0) nanotubes are presented in Figure 5.15. The E_{ii} values for the same nanotubes were previously computed with the TB1 model and presented in Figure 5.7.

The shift trend and magnitude depend on the nanotube structure. The trend for all semiconducting nanotubes is identical to the trend predicted by the TB1 model. The $p = 1$ nanotubes have their E_{22}^S values shift to lower energies in tension and to higher energies in compression. The $p = -1$ nanotubes have the opposite behavior: their E_{22}^S values shift to higher energies in tension and to lower energies in compression.

The zigzag nanotubes also have the same behavior as the behavior predicted by the TB1 model. The two components of E_{11}^M shifts closer to each other in tension. The only difference between the two models is for armchair

nanotubes: they become sensitive to uniaxial strain. Their unique E_{11}^M value shifts to higher energies in tension and to lower energies in compression.

The shift magnitude is found to decrease with the chiral angle, concurring with the results from the TB1 model. It is maximum for zigzag nanotubes and minimum for armchair nanotubes. The shift magnitudes from the TB3 model are systematically larger than those from the TB1 model.

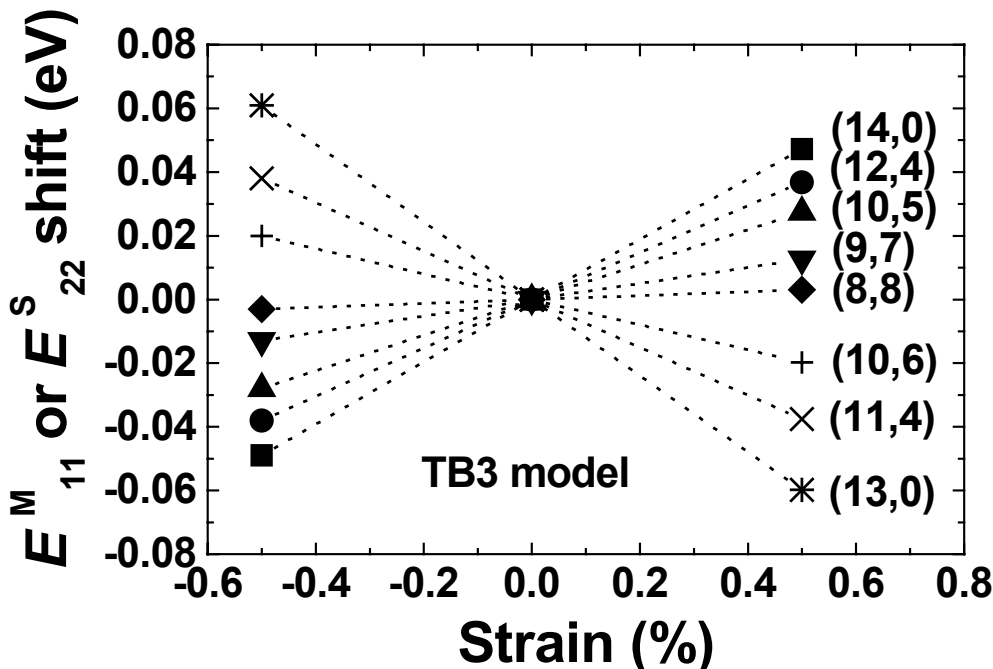


Figure 5.15: The shift of the E_{11}^M value for the metallic (8,8) nanotube and the shift of the E_{22}^S values for the semiconducting (14,0), (12,4), (10,5), (9,7), (10,6), (11,4) and (13,0) nanotubes, as a function of strain.

5.3 Comparison with Experimental Results for Semiconducting Nanotubes

The chirality assignments from Raman spectroscopy are heavily dependent on the theoretical E_{ii} values. A difference of several tens of meV for the E_{ii} values can lead to the assignment of a different structure to a RBM. In order to check the accuracy of the results from the tight-binding models, the theoretical E_{11}^S and E_{22}^S values are compared to those previously tabulated in Reference 179 by Weisman *et al.* obtained from photoluminescence spectroscopic measurements on individual semiconducting nanotubes

suspended in water with surfactants (Figure 5.16). Depending on the value of the parameter p , these experimental E_{ii} values were fitted with the following equations:

$$E_{11}^S (p = -1) = \frac{1241.45 \text{ eV}}{157.5 + 1066.9 d} + 0.0431 \text{ eV} \frac{(\cos(3\theta))^{0.886}}{d^{2.129}} \quad (5.80)$$

$$E_{11}^S (p = 1) = \frac{1241.45 \text{ eV}}{157.5 + 1066.9 d} - 0.0957 \text{ eV} \frac{(\cos(3\theta))^{1.374}}{d^{2.272}} \quad (5.81)$$

$$E_{22}^S (p = -1) = \frac{1241.45 \text{ eV}}{145.6 + 575.7 d} - 0.1764 \text{ eV} \frac{(\cos(3\theta))^{1.110}}{d^{2.497}} \quad (5.82)$$

$$E_{22}^S (p = 1) = \frac{1241.45 \text{ eV}}{145.6 + 575.7 d} + 0.1646 \text{ eV} \frac{(\cos(3\theta))^{0.828}}{d^{1.809}} \quad (5.83)$$

where d is the nanotube diameter and θ the chiral angle.

The E_{22}^S values from photoluminescence measurements follow a general trend that is inversely proportional to the nanotube diameter, but exhibit a larger chirality dependence than predicted by the tight-binding models (Figures 5.17 and 5.18). The tight-binding models generally underestimate the experimental values from photoluminescence spectroscopy, except for the results from the TB1 model on the smaller diameter nanotubes.

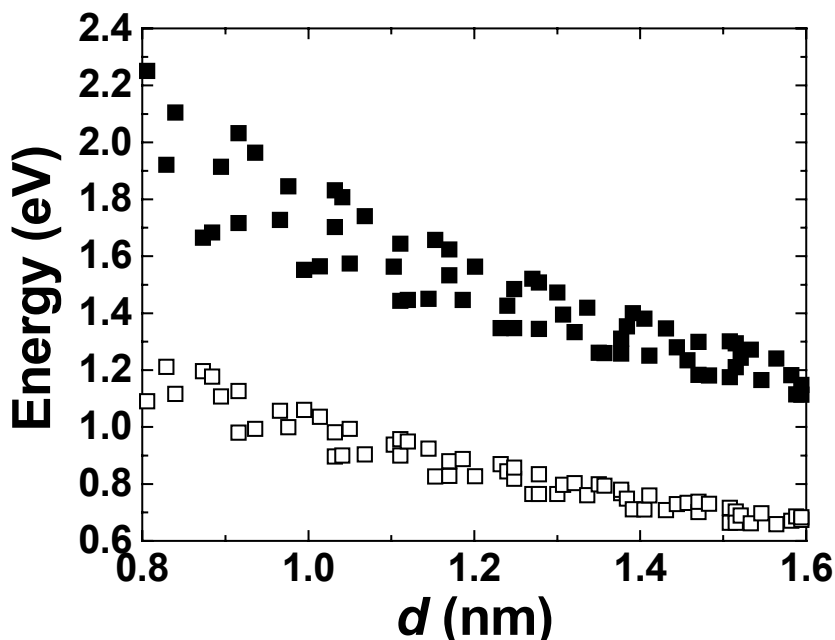


Figure 5.16: Experimental E_{11}^S (open squares) and E_{22}^S (solid squares) values from photoluminescence spectroscopy [179] for nanotubes with a diameter between 0.8 and 1.6 nm.

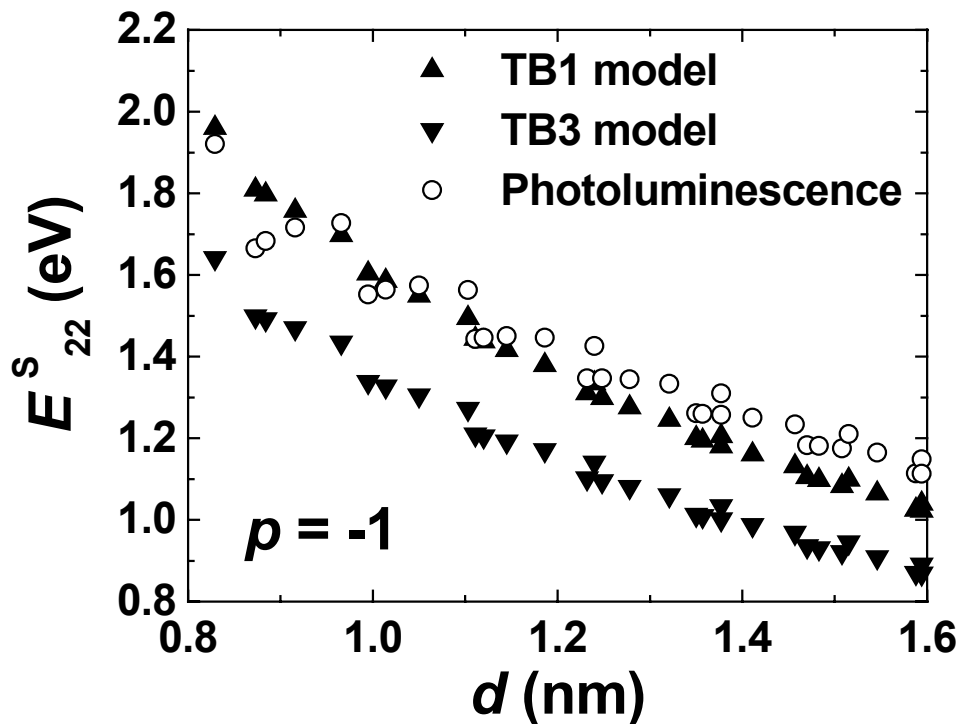


Figure 5.17: Comparison between the E_s^{22} values for $p=-1$ nanotubes from the TB1 tight-binding model (up triangles), the TB3 model (down triangles) and from photoluminescence spectroscopy [179].

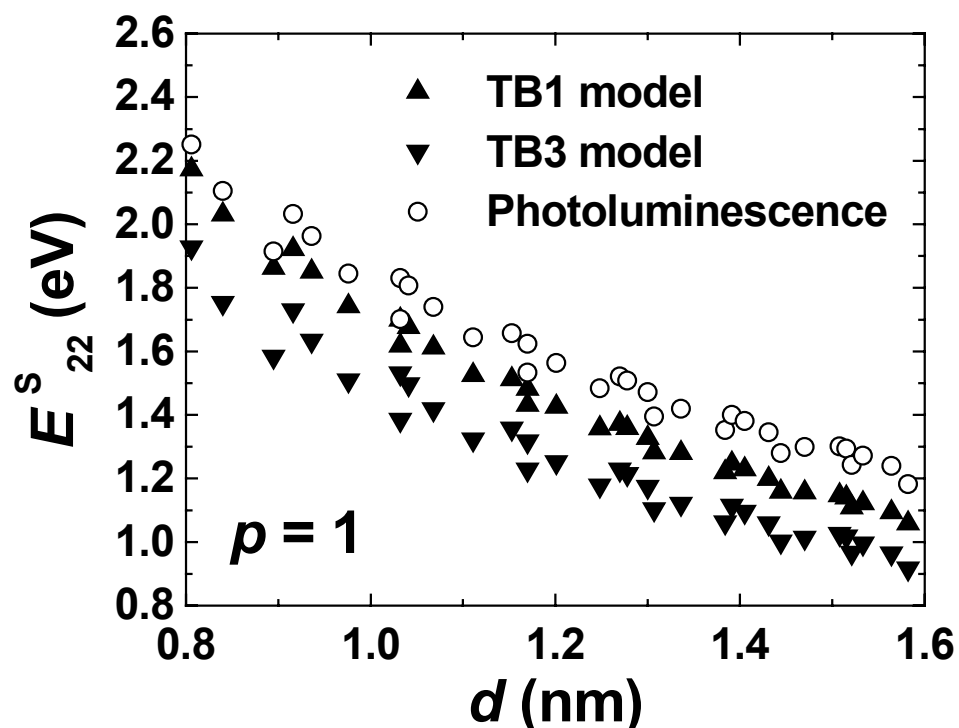


Figure 5.18: Comparison between the E_s^{22} values for $p=1$ nanotubes from the TB1 tight-binding model (up triangles), the TB3 model (down triangles) and from photoluminescence spectroscopy [179].

The ratio between the E_{22}^S values from photoluminescence spectroscopic measurements ($E_{22\text{ PL}}^S$) and the tight-binding models ($E_{22\text{ TB}}^S$), TB1 and TB3, is plotted against the nanotube diameter in Figures 5.19 and 5.20. The theoretical values cannot be corrected by a simple adjustment of the tight-binding parameters to fit the photoluminescence data, due to their large chirality dependence.

The ratios were fitted successfully with the following function:

$$\frac{E_{22\text{ PL}}^S(p)}{E_{22\text{ TB}}^S(p)} = A + \frac{B}{d} + C \frac{(\cos(3\theta))^D}{d^E} \quad (5.84)$$

where A, B, C, D, E are five adjustable parameters (see Table 5.2).

Table 5.2: Fit results of the E_{22}^S value ratios with Equation 5.84. There are only 4 significant digits, the others are added to avoid rounding errors.

Model	p	A	B	C	D	E
TB1	-1	1.24546	-0.21307	-0.06387	1.50042	1.88052
	1	1.27324	-0.31634	0.11788	0.13746	1.32874
TB3	-1	1.42342	-0.21037	-0.05072	2.03415	2.74792
	1	1.39795	-0.17032	-0.03424	4.63259	1.46966

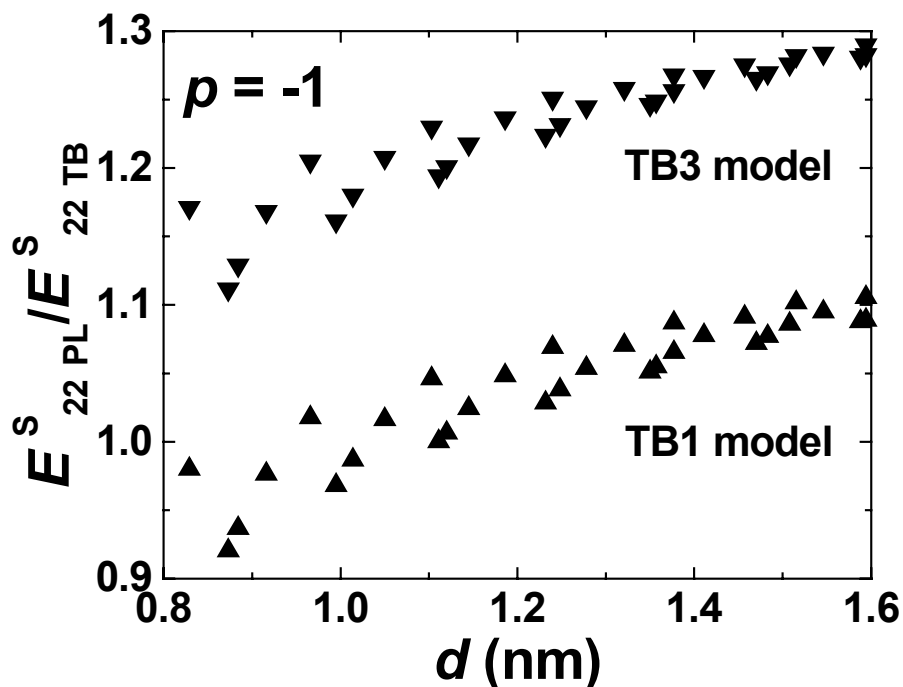


Figure 5.19: Ratio between the E_{22}^S values for $p=-1$ nanotubes from the photoluminescence spectroscopy [179] and the tight-binding models TB1 (up triangles) and TB3 (down triangles).

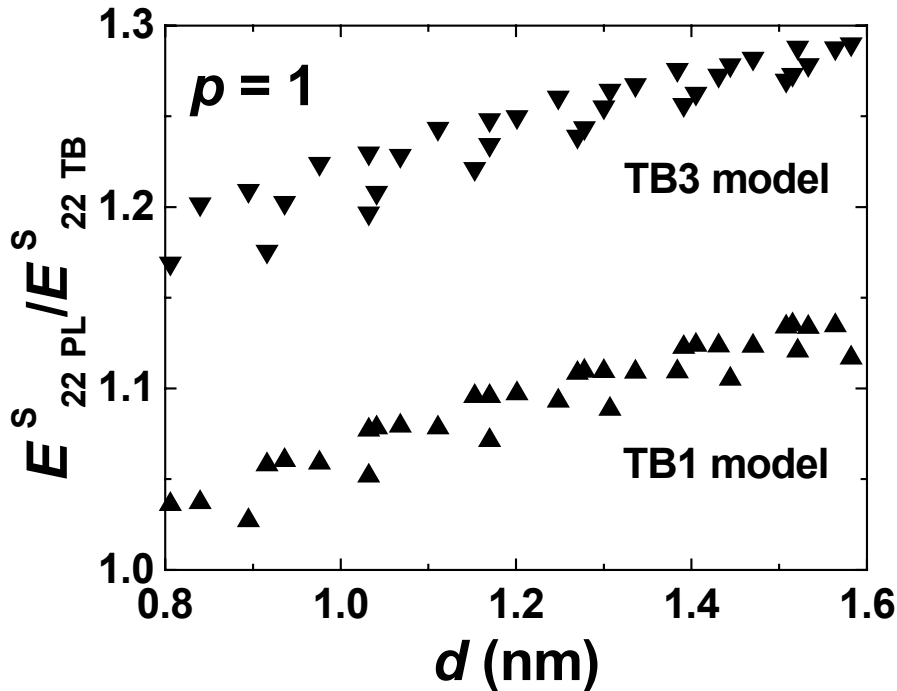


Figure 5.20: Ratio between the E_{22}^S values for $p=1$ nanotubes from the photoluminescence spectroscopy [179] and the tight-binding models TB1 (up triangles) and TB3 (down triangles).

The mean errors of the fit are 2 meV and 3 meV for the TB1 model and the TB3 model, with maximum differences of 11 and 15 meV, respectively. The five adjustable parameters have no simple physical meaning and will only be used to predict the strain-induced shifts of the experimental E_{22}^S values.

5.4 Comparison with Experimental Results for Metallic Nanotubes

The E_{11}^M values were previously measured experimentally using a tunable laser, by recording the Raman RBM excitation profile from individual metallic nanotubes suspended in water with surfactants [196]. These experimental values are compared to those from the tight-binding models in Figures 5.21 and 5.22. For each nanotube, two values of E_{11}^M are given, due to the trigonal warping effect [168]. The experimental values of the two components of E_{11}^M are between the values predicted by the two models. The chirality dependence of E_{11}^M is well reproduced by the two models for the lower-energy component, but is overestimated for the higher-energy component.

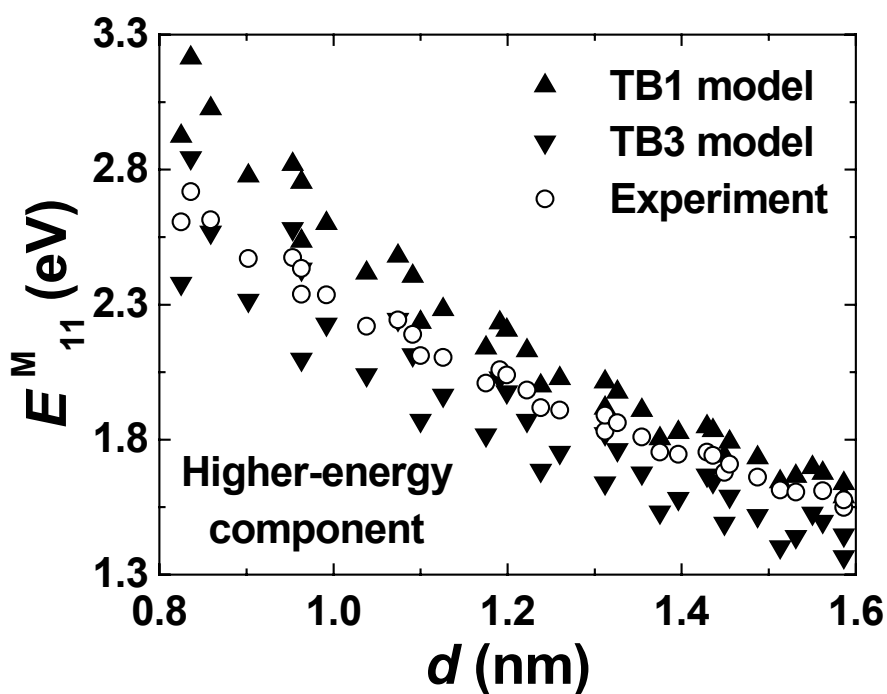
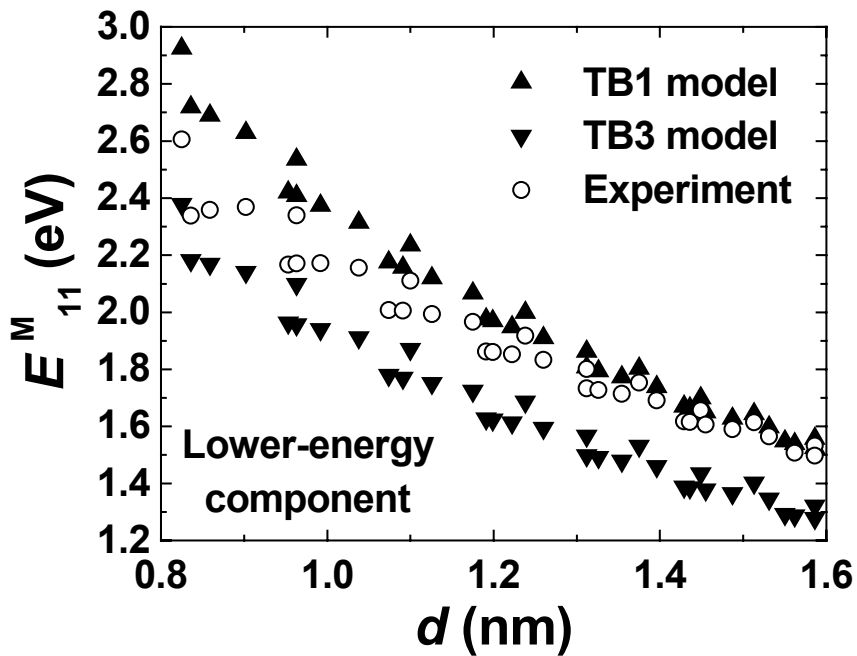


Figure 5.21: Comparison between the E_{11}^M values (lower-energy component) from the TB1 tight-binding model (up triangles), the TB3 model (down triangles) and from Raman excitation profiles [196].

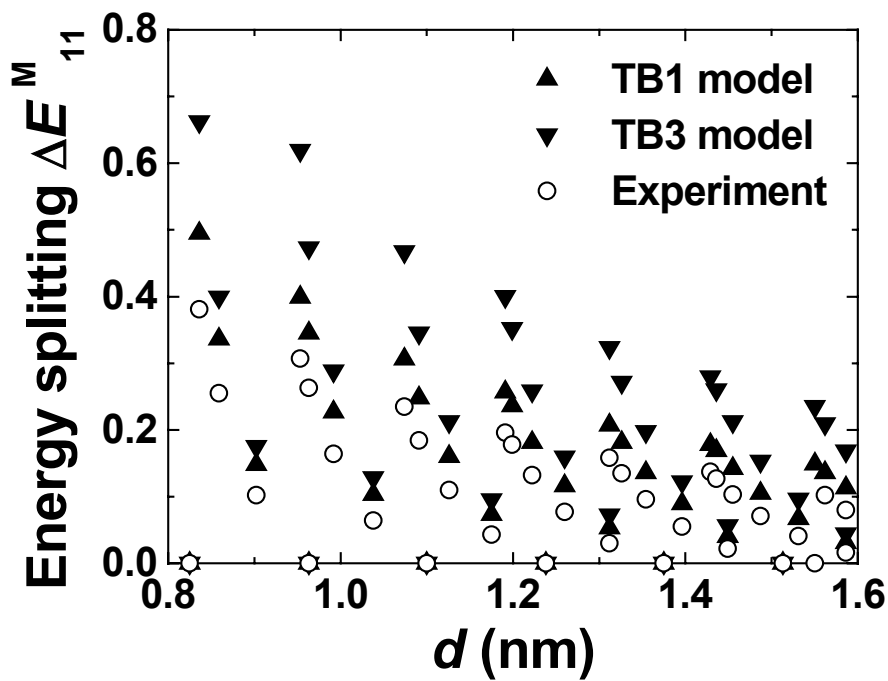


Figure 5.23: Comparison between the energy splitting ΔE_{11}^M values (between the two components of E_{11}^M) from the TB1 tight-binding model (up triangles), the TB3 model (down triangles) and from Raman excitation profiles [196].

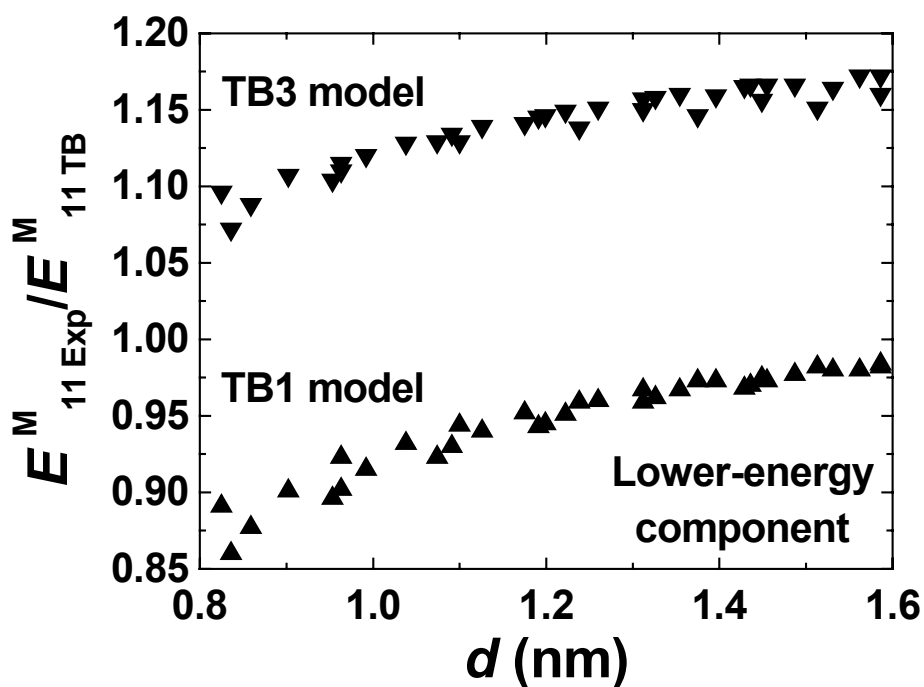


Figure 5.24: Ratio between the E_{11}^M values (lower-energy component) from Raman spectroscopy [196] and the tight-binding models TB1 (up triangles) and TB3 (down triangles).

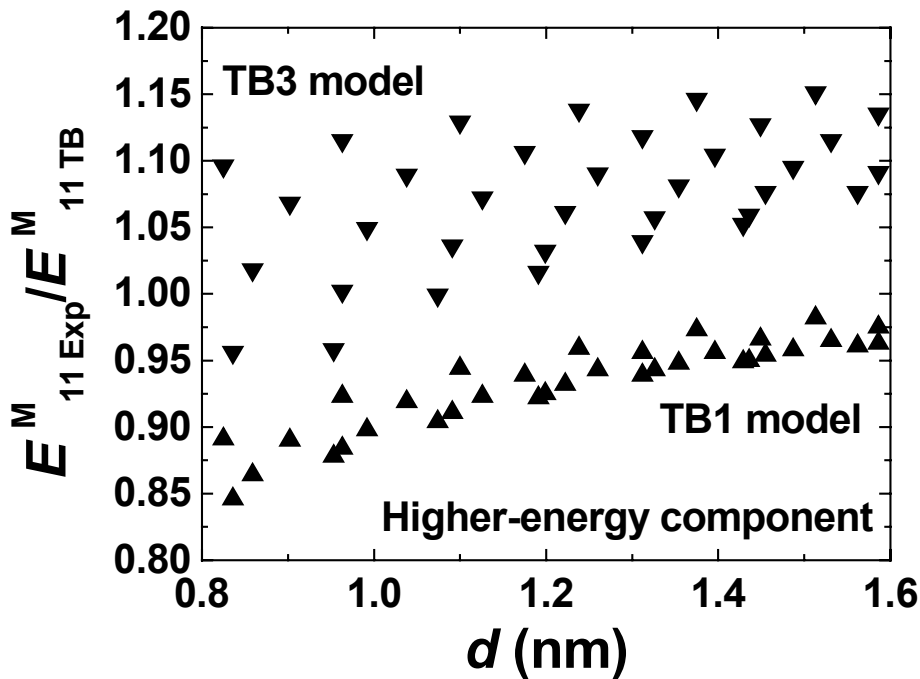


Figure 5.25: Ratio between the E^M_{11} values (higher-energy component) from Raman spectroscopy [196] and the tight-binding models TB1 (up triangles) and TB3 (down triangles).

The energy splitting ΔE^M_{11} between the lower- and higher-energy components vary with the chiral angle and diameter of the nanotube: it is maximum for zigzag nanotubes, zero for armchair nanotubes, and decreases with increasing diameter. The energy splitting ΔE^M_{11} is systematically overestimated by the tight-binding models over the diameter range between 0.8 and 1.6 nm (Figure 5.23).

The ratio between the experimental values $E^M_{11 \text{ Exp.}}$ and those from the tight-binding models ($E^M_{11 \text{ TB}}$) is showed as a function of the diameter in Figures 5.24 and 5.25. The results for the lower-energy component mainly depend on the nanotube diameter and only weakly on the chiral angle. As for the higher-energy component, the chirality dependence is much stronger, especially for the E^M_{11} values from the TB3 model.

The data in Figures 5.24 and 5.25 can be fitted using a function similar to Equation 5.84. Since $\theta = 30^\circ$ for armchair nanotubes, the data for armchair nanotubes had to be fitted first to have suitable initial values for A and B .

parameters. The best values for the parameters A , B , C , D and E for metallic nanotubes are given in Table 5.3.

Table 5.3: Fit results of the E_{11}^M value ratios with Equation 5.84. There are only 4 significant digits, the others are added to avoid rounding errors.

Model	Component	A	B	C	D	E
TB1	Lower	1.08916	-0.16156	-0.01981	1.26697	3.62663
	Higher	1.08916	-0.16156	-0.03886	0.71767	0.98675
TB3	Lower	1.24728	-0.12201	-0.00782	1.70829	7.96174
	Higher	1.21616	-0.09781	-0.13013	1.37609	0.79756

The mean errors of the fit are 4 meV and 7 meV for the TB1 model and the TB3 model, with maximum differences of 15 and 51 meV, respectively. Again, the five adjustable parameters have no simple physical meaning and will only be used to predict the strain-induced shifts of the E_{11}^M values.

5.5 Conclusions

Two models based on the tight-binding approximation, previously developed by Yang *et al.* and Reich *et al.*, were presented to calculate the nanotube electronic band structure and DOS, and their modifications under uniaxial strain: one includes only the interactions with the nearest-neighboring carbon atoms in the hexagonal lattice (TB1 model), the other includes the interactions with up to the third-nearest neighboring carbon atoms (TB3 model). The electronic transition energies E_{ii} obtained by the TB3 model are systematically lower than those from the TB1 model. The E_{ii} values are found to vary with strain by the two models. The variation trends and magnitudes depend strongly on the nanotube structure. The variation trends predicted by the two models are identical, except for the armchair nanotubes which are sensitive to uniaxial strain according to the TB3 model. Also, the magnitude of the shift predicted by the TB3 model is systematically higher than those from the TB1 model.

The chirality assignments from Raman spectroscopy are heavily dependent on the theoretical E_{ii} values. A difference of several tens of meV for the E_{ii} values can lead to the assignment of a different structure to a RBM. In

order to check the accuracy of the results from the tight-binding models, the E_{ii} values obtained by the tight-binding models were compared to experimental values from photoluminescence spectroscopy (semiconducting nanotubes) and Raman excitation profiles (metallic nanotubes). For the semiconducting nanotubes, the theoretical E_{22}^S values are generally lower than the experimental ones. For the metallic nanotubes, the experimental E_{11}^M values are between the two sets of theoretical values. The ratio between the experimental and theoretical E_{ii} values for the semiconducting and metallic nanotubes was fitted successfully with functions of the nanotube diameter and chiral angle, with mean errors of several meV in the diameter range between 0.8 and 1.6 nm. These fit functions can now be used to predict the strain-induced shifts of the experimental values.

Chapter 6

Deformations of SWNTs Composites

Raman spectroscopy has been used to study the deformation of carbon nanotubes (see Chapter 3 for review). The G' band was found to shift to lower wave numbers when the nanotubes are in tension and to higher wave numbers in compression. Similar effects were found for the D and G band but at a smaller extent. When deformed, the electronic band structure and DOS are expected to change according to the tight-binding calculations of Chapter 5. According to resonance theory, some nanotubes are expected to become closer to resonance and others further away from resonance, therefore modifying the Raman spectrum. In this chapter, Raman spectra of nanotubes in epoxy composites and PVA films are presented using three laser excitation energies. It is showed how the Raman spectrum varies when the nanotubes are under uniaxial strain along their axis during the four-point bending tests. (Note: The results about the deformation tests on epoxy/SWNT composites were reported in the following publication: M. Lucas and R.J. Young, Physical Review B **69**, 85405 (2004))

6.1 Experimental Procedures

6.1.1 Nanotube Samples

Two types of SWNTs were studied: the purified HiPco and Elicarb nanotubes. The purified HiPco nanotubes were obtained from Carbon Nanotechnologies Inc. (USA) and produced by disproportionation of carbon monoxide. Their mean diameter is about 1 nm [7]. The raw HiPco nanotube material was purified using a two-step process to remove the metallic catalyst particles and the amorphous carbon: the powder is first oxidized in a wet Ar/O₂ environment at low temperatures (less than 400°C), then sonicated and stirred overnight in a concentrated acid solution [197]. The purified Elicarb SWNTs from Thomas Swan & Co Ltd. (UK) were produced by CVD. They have a mean diameter of less than 2 nm and are several microns long.

6.1.2 Epoxy Composite Preparation

A dispersion of nanotubes in ethanol was first sonicated for 2 hours before the addition of 50 parts of Araldite epoxy resin LY5052 (matrix). The mixture was then sonicated for another 2 hours and left in a vacuum oven overnight. After the addition of 19 parts of Araldite iso-4-one hardener HY5052, it was stirred for 5 minutes and cast on a flat and square metal frame. The resulting SWNT weight fraction was 0.025%. The 3 mm thick film was left at room temperature in air for 7 days. Strips of dimensions 60 mm x 10 mm were cut and their sides were ground using SiC grinding papers (grade 600) using water as a lubricant.

6.1.3 PVA Film Preparation

A poly(vinyl alcohol)(PVA)-nanotube suspension was prepared by adding 10 mg of nanotubes into 10 mL of a 1 wt.% PVA (BHD Ltd., approximate molecular weight of 22,000) solution. The suspension was sonicated for an hour and left overnight to settle. Epoxy beams (60x10x2 mm) were prepared by cold-curing a mixture of 50 parts of Araldite epoxy resin LY5052 and 19 parts of Araldite iso-4-one hardener HY5052 on a metal frame for 7 days. Several drops of the PVA-nanotube suspension were placed on an epoxy beam and allowed to dry, leaving a thin film.

6.1.4 Raman Spectroscopy

The Raman spectra were collected using a Renishaw 1000 Raman microprobe system connected to an optical microscope (Figure 6.1). Three different laser lines were used:

- A near-infrared laser of wavelength $\lambda = 830$ nm ($E_{laser} = 1.49$ eV).
- A near-infrared laser of wavelength $\lambda = 780$ nm ($E_{laser} = 1.59$ eV).
- An He-Ne laser of wavelength $\lambda = 632$ nm ($E_{laser} = 1.96$ eV).

The polarized laser beam passes first through a pinhole and lenses to be focused spatially, and then through holographic notch filters, which split the laser beam. During the four-point bending tests, the incident laser was polarized parallel to the composite beam, the direction along which the strain was applied.

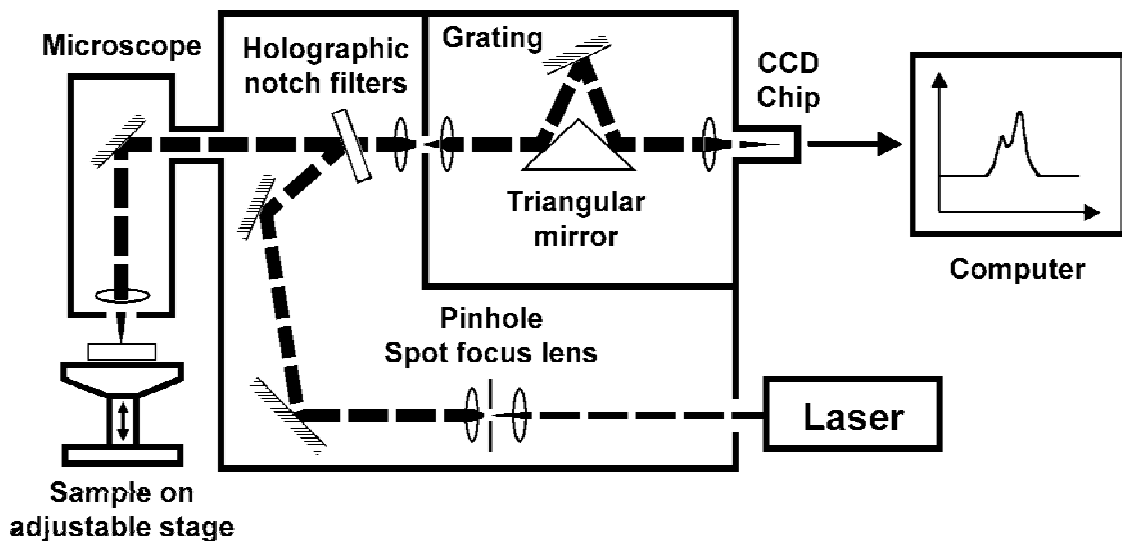


Figure 6.1 : Diagram of the Raman spectroscopy experimental setup.

The sample is mounted on an adjustable microscope stage and the laser beam is focused on the sample surface with a $\times 50$ objective lens. The laser spot diameter is about $2 \mu\text{m}$. The laser power on the sample is 0.25 mW, 3.0 mW and 0.3 mW for the lasers of wavelength 632 nm, 780 nm and 830 nm, respectively. The scattered light from the surface of the sample is collected in the backscattering geometry, passes through the holographic notch filters, which filter out the incident laser line, and processed by a spectrometer. The different Raman lines and the incident laser line are separated by a diffraction grating and a triangular mirror. Once processed by the spectrometer, the light is collected by a Charge Coupled Device (CCD) camera. Photons of the scattered light generate charges inside the CCD chip, which are collected with electrodes. The current measured is proportional to the number of photons detected and thus to the intensity of the scattered light. The intensity of the light is collected as a function of its wavelength (the difference with the incident light wavelength is expressed in Raman wave number in cm^{-1}), processed and stored on the computer. The resolution of the spectrometer is about 1 cm^{-1} .

The peaks on the Raman spectra were fitted with Lorentzian functions:

$$I = \frac{I_0}{\left(1 + 4 \frac{(\omega - \omega_c)^2}{\Delta\omega^2}\right)} \quad (6.1)$$

where ω is the Raman wave number, ω_c the center, I_0 the maximum intensity ($\omega = \omega_c$) and $\Delta\omega$ the full width at half maximum of the peak. Depending on the laser wavelength and the sample, different types of background were subtracted: flat, linear or exponential decay. Since the absolute RBM intensities vary depending on the position of the laser spot, the RBM intensity values were normalized, divided by their respective values at zero strain.

The epoxy/Hipco SWNT composite samples were studied only with the 780 nm laser. The RBMs from Hipco SWNTs have a significantly higher intensity using the 780 nm laser, compared to the other lasers, and compared to the RBMs from Elicarb SWNTs. In order to collect RBMs with higher intensities without considerably increasing the amount of SWNTs used, thin PVA/Hipco SWNT films were studied with the 830 nm and 632 nm lasers, and PVA/Elicarb SWNT films were studied with the three lasers.

6.1.5 Strain Gauge

Strain measurement is usually undertaken with an electrical resistance strain gauge (Figure 6.2). The strain gauge is composed of one long electrically conductive strip forming a zigzag, backed by a thin (30 microns) and flexible polyimide film. The entire device is 11 mm long and 4 mm wide, with 10 parallel metal bands.

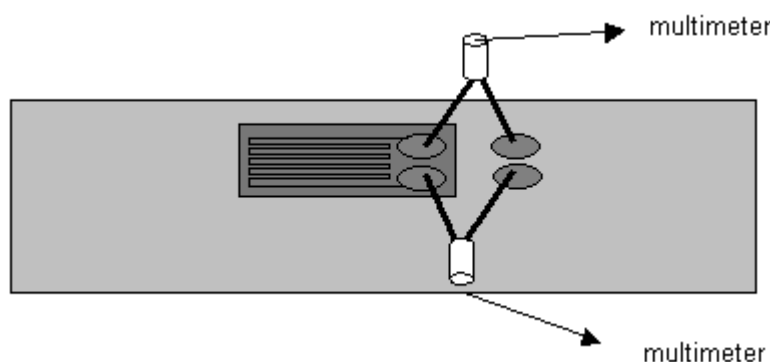


Figure 6.2: Diagram of the strain gauge glued on the composite sample. Wires are soldered onto it and connected to a multimeter.

When the strain gauge is stretched the wires become longer, and thinner. The electrical resistance therefore increases. The strain value ε_m is

obtained from the resistance value given by a multimeter using the following equation:

$$\varepsilon_m = \frac{(RS_i - RS_0)}{2.06 RS_0} \times 100\% \quad (6.2)$$

where RS_i is the multimeter reading at a given strain value and RS_0 the multimeter reading at zero strain. 2.06 is called the "gauge factor" and is provided by the strain gauge manufacturer (Measurements Group, Inc., USA).

6.1.6 Four-Point Bending Tests

The epoxy beam was deformed step-wise with 0.05% strain intervals using a four-point bending rig. Depending on the way the composite beam is inserted in the rig and bent, the nanotubes near the top surface of the sample are in tension (bent downward) or in compression (bent upward) (Figure 6.3). The strain value was measured with a strain gauge of gauge factor 2.06, glued on the top surface of the sample using cyanoacrylate adhesive. The strain value given by the strain gauge has an accuracy better than 0.005%.

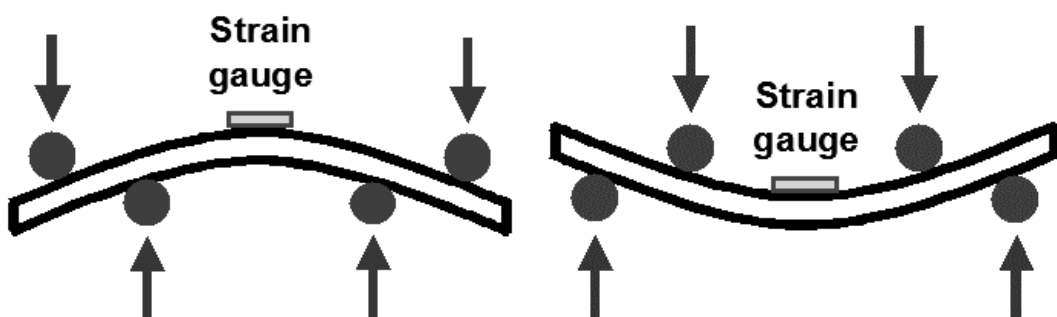


Figure 6.3: Diagram of the four-point bending test. The top surface of the sample is in tension when it is bent upward (left) or in compression when it is bent downward (right).

The strain applied on the SWNTs was monitored by the shift of the G or G' band. Both the G and G' bands shift to lower wave numbers in tension and to higher wave numbers in compression. The G' band is preferred over the G band to monitor the stress transfer since it is more sensitive to deformation [198]. However, the G' band was found to be very weak and broad using the $\lambda = 830$ nm laser. This study was limited to low-strains (less than 0.7%) in tension

and compression, where the G or G' bands still shift linearly with strain, which is an indicator of an effective stress transfer to the nanotubes [51].

For the epoxy composite samples, five low-frequency Raman spectra were collected at each strain value with an exposure time of one minute. For the PVA films, three low-frequency Raman spectra were collected at each strain value with an exposure time of four minutes. The results presented in the following sections are the average over these spectra. The tension and compression test results were obtained separately from different samples.

6.2 Raman Spectroscopy on Carbon Nanotube Powder Before Deformation

6.2.1 HiPco Nanotubes

Figures 6.4 to 6.6 are typical Raman spectra collected from the HiPco nanotube powder with lasers of three different wavelengths: 830 nm (Figure 6.4), 780 nm (Figure 6.5), and 632 nm (Figure 6.6) which correspond to laser excitation energies of 1.49 eV, 1.59 eV and 1.96 eV respectively. All three spectra consist of four main bands: the RBMs, the D, G and G' bands. However, their relative intensities depend on the laser wavelength. Compared to the most intense peak (the G band), the RBMs are very strong, while the G' band is very weak with the near-infrared laser of wavelength 830 nm. With the 632 nm laser, the RBMs are weak, while the G' band is strong. Other bands are also present depending on the laser used between 500 and 1000 cm⁻¹ (especially for the 830 nm laser) and between 1600 and 2000 cm⁻¹.

The most remarkable fact is the dependence of the low-frequency spectra on the laser excitation energy. Figures 6.7 to 6.9 are the low-frequency spectra from the HiPco nanotube powder corresponding to the RBMs, collected with three different laser excitation energies. Depending on the laser excitation energy, different peaks appear with different relative intensities. The $E_{laser} = 1.49$ eV spectrum is fitted with 6 Lorentzian lines centered at 183, 205, 214, 227, 235, and 265 cm⁻¹, the $E_{laser} = 1.59$ eV spectrum with 6 centered at

206, 214, 226, 234, 267, and 272 cm^{-1} , and the $E_{\text{laser}} = 1.96 \text{ eV}$ spectrum with 5 centered at 197, 220, 256, 283, and 297 cm^{-1} .

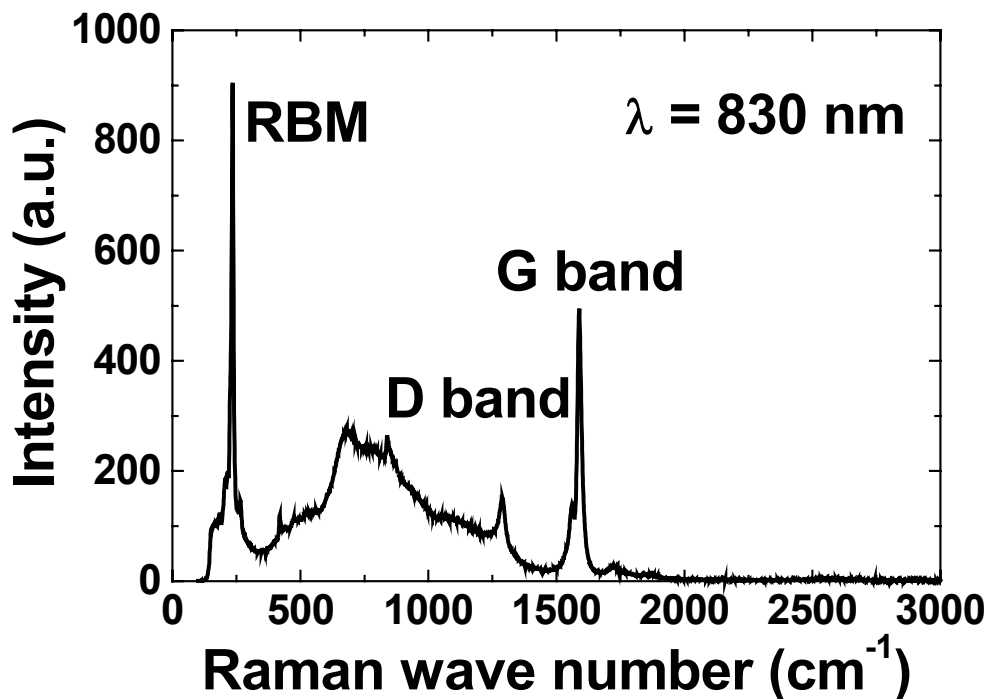


Figure 6.4: Raman spectrum of the HiPco nanotube powder using the near-infrared laser of wavelength 830 nm.

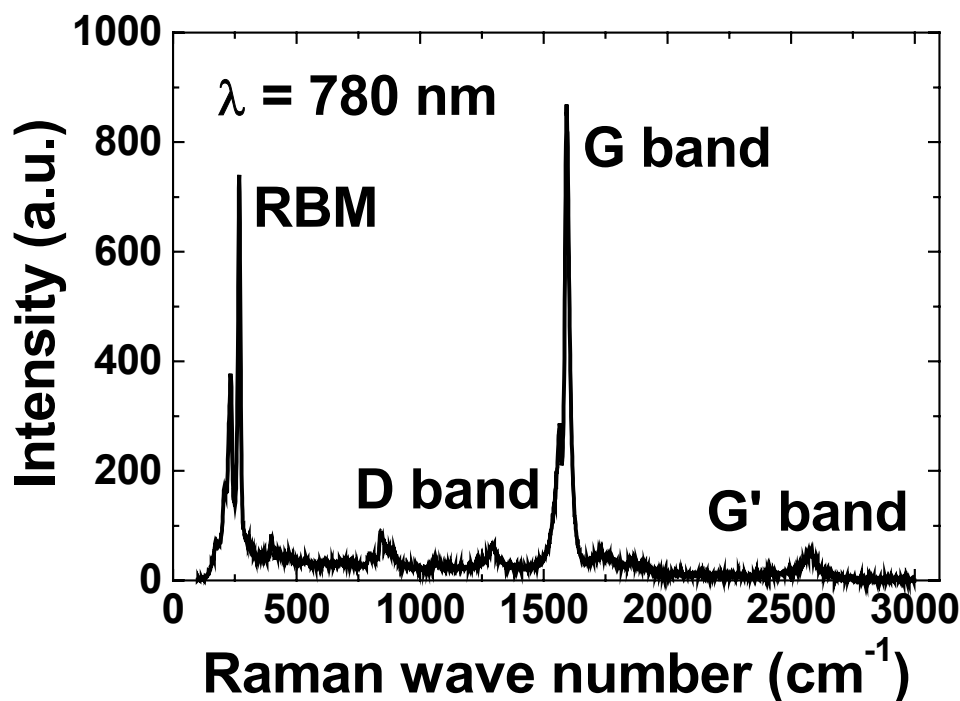


Figure 6.5: Raman spectrum of the HiPco nanotube powder using the near-infrared laser of wavelength 780 nm.

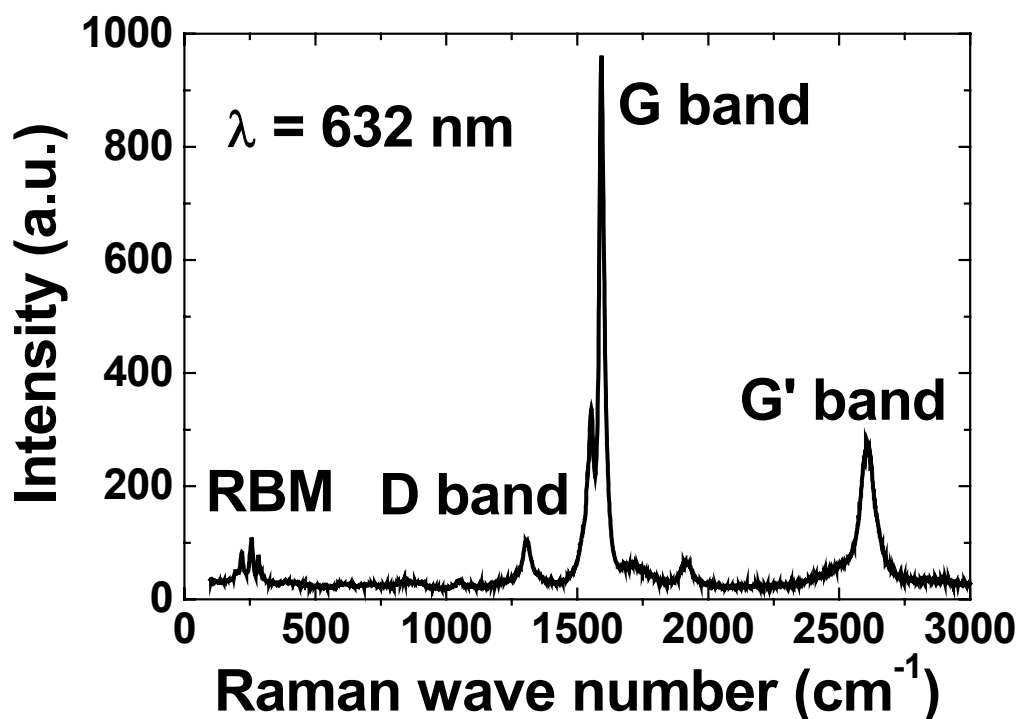


Figure 6.6: Raman spectrum of the HiPco nanotube powder using the He-Ne laser of wavelength 632 nm.

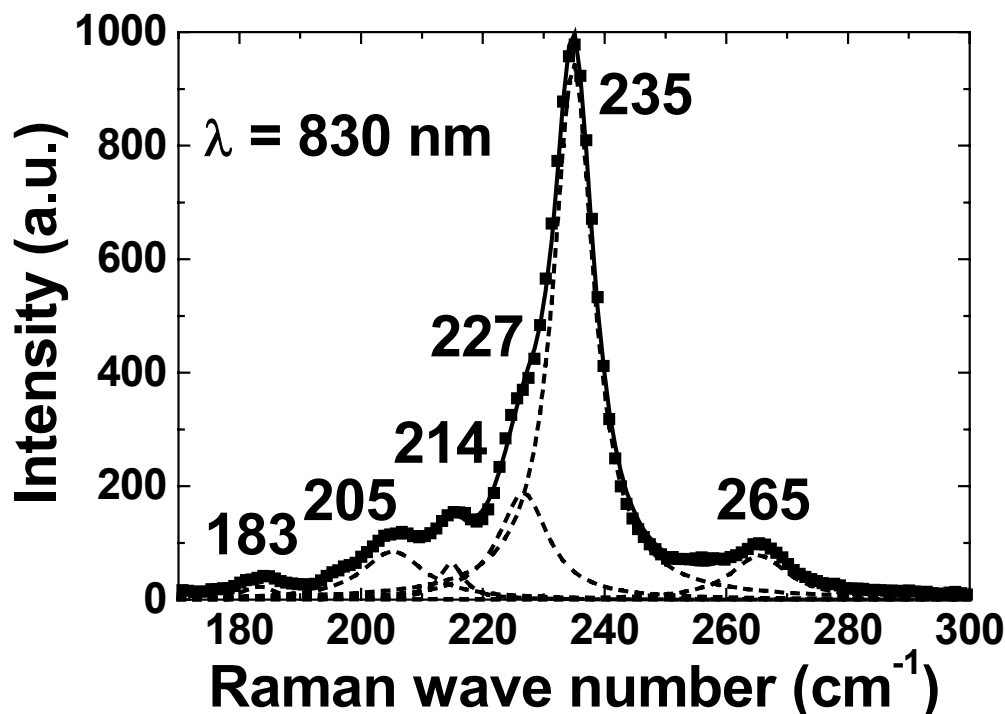


Figure 6.7: Raman spectrum of the RBMs with a laser of wavelength 830 nm (squares). The spectrum is fitted (solid line) with 6 different Lorentzian lines (dashed lines). The peak positions are indicated in Raman wave number (cm^{-1}).

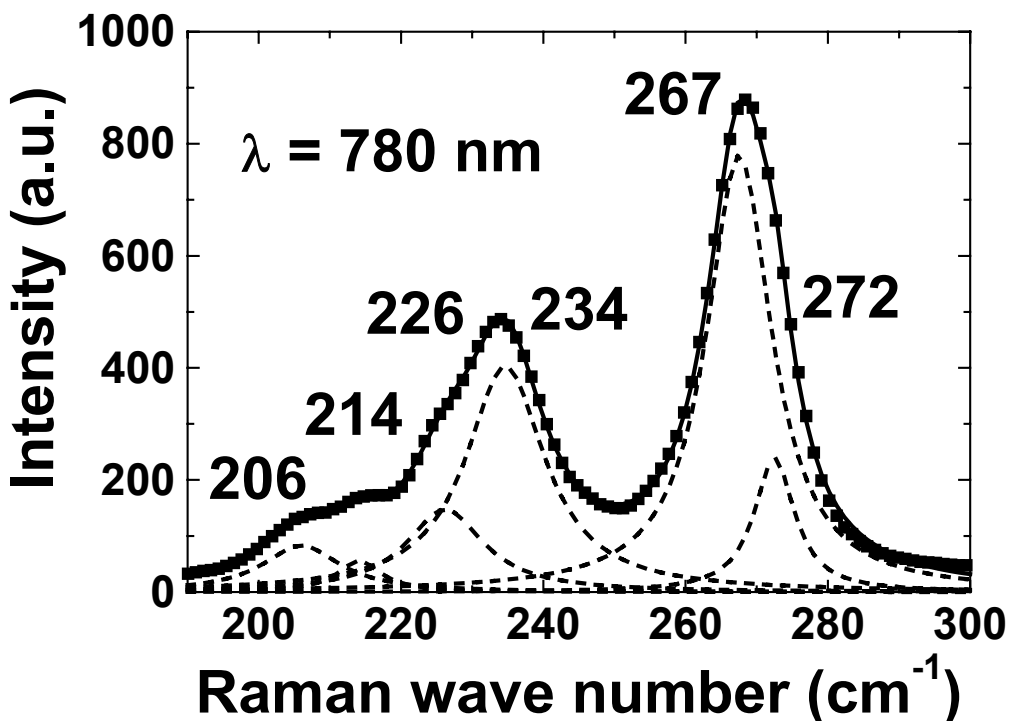


Figure 6.8: Raman spectrum of the RBMs with a laser of wavelength 780 nm (squares). The spectrum is fitted (solid line) with 5 different Lorentzian lines (dashed lines). The peak positions are indicated in Raman wave number (cm^{-1}).

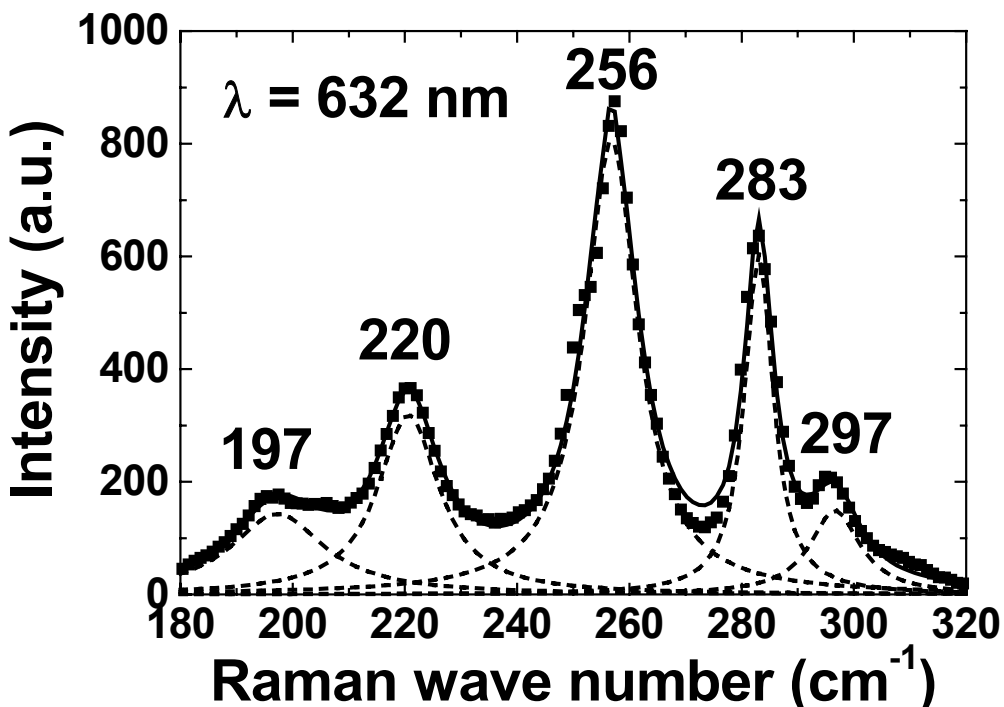


Figure 6.9: Raman spectrum of the RBMs with a laser of wavelength 632 nm (squares). The spectrum is fitted (solid line) with 5 different Lorentzian lines (dashed lines). The peak positions are indicated in Raman wave number (cm^{-1}).

Each of these RBMs corresponds to one type of nanotube with a distinctive diameter and structure. Their positions are known to be inversely proportional to their diameter. Their intensities depend on the nanotube diameter distribution in the sample, the orientation of the nanotubes with respect to the polarization of the incident laser and also on their electronic DOS. Considering the diameter range and the laser excitation energies, both metallic and semiconducting nanotubes are expected.

6.2.2 Elicarb Nanotubes

Figures 6.10 to 6.12 are typical Raman spectra collected from the Elicarb nanotube powder with lasers of three different wavelengths: 830 nm (Figure 6.10), 780 nm (Figure 6.11), and 632 nm (Figure 6.12). The four main bands are also visible on the three spectra except for the G' band in the 830 nm spectrum. In contrast to the HiPco material, the G band does not have a shoulder on the lower wave number side around 1560 cm^{-1} . Also the D band/G band intensity ratio is slightly higher for the Elicarb nanotubes, possibly reflecting a higher concentration of defects along the nanotube sidewalls.

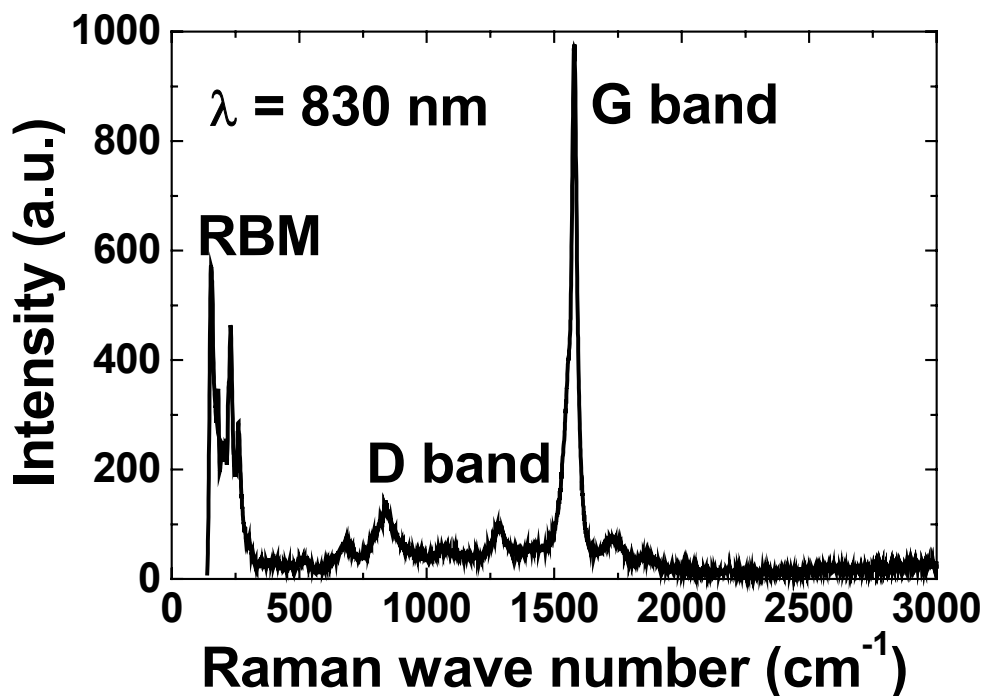


Figure 6.10: Raman spectrum of the Elicarb nanotube powder using the near-infrared laser of wavelength 830 nm.

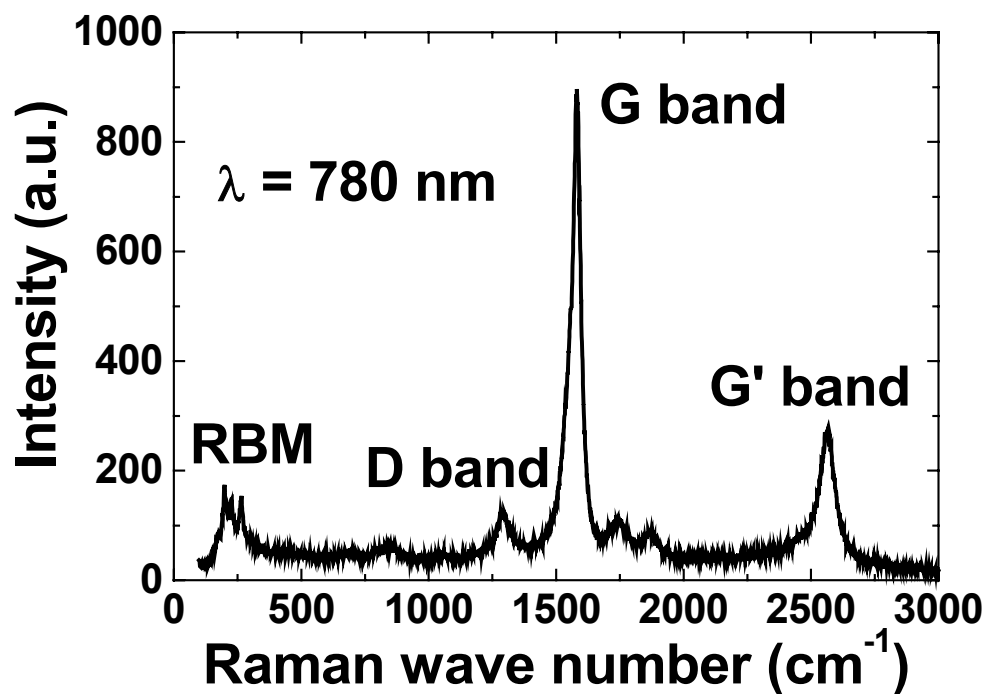


Figure 6.11: Raman spectrum of the Elicarb nanotube powder using the near-infrared laser of wavelength 780 nm.

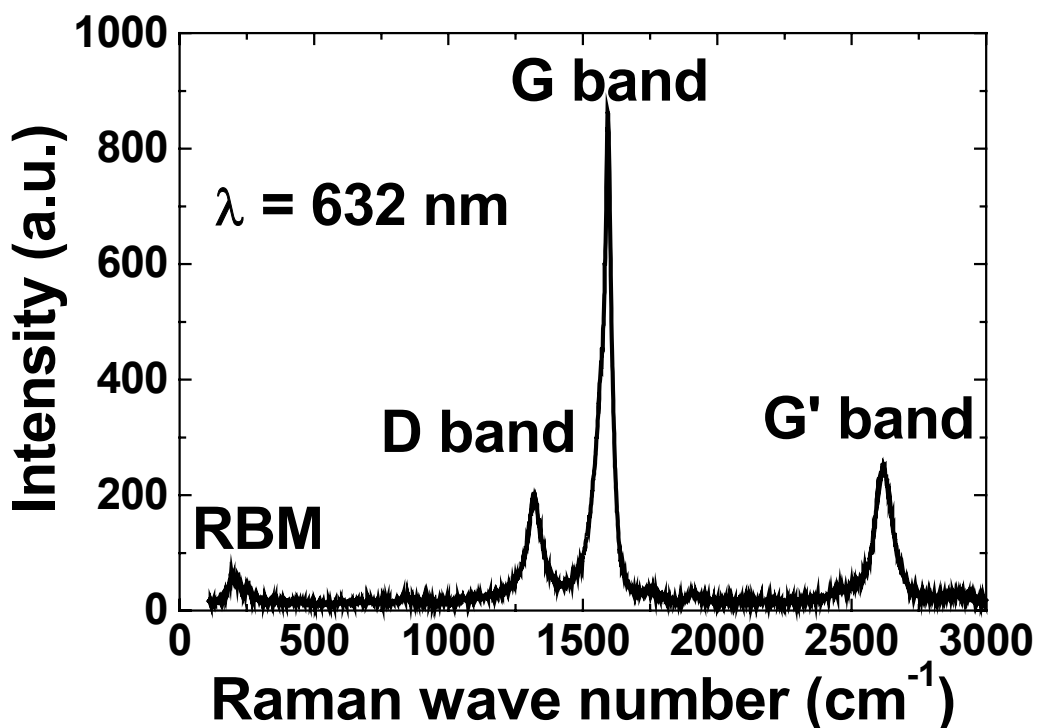


Figure 6.12: Raman spectrum of the Elicarb nanotube powder using the He-Ne laser of wavelength 632 nm.

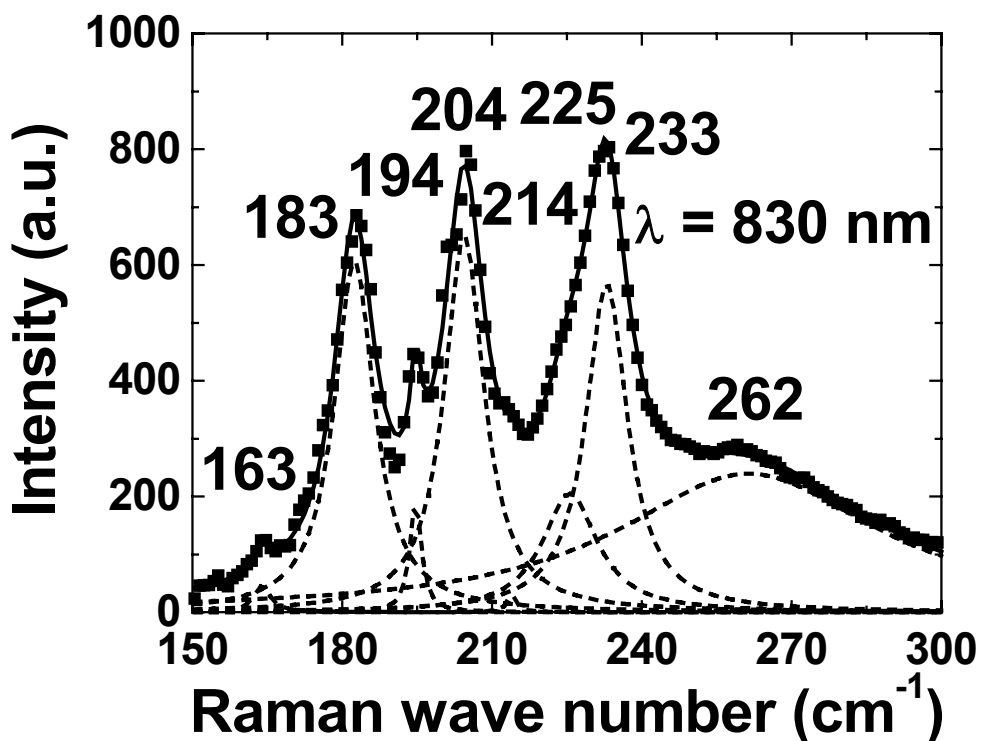


Figure 6.13: Raman spectrum of the RBMs with a laser of wavelength 830 nm (squares). The spectrum is fitted (solid line) with 8 different Lorentzian lines (dashed lines). The peak positions are indicated in Raman wave number (cm^{-1}).

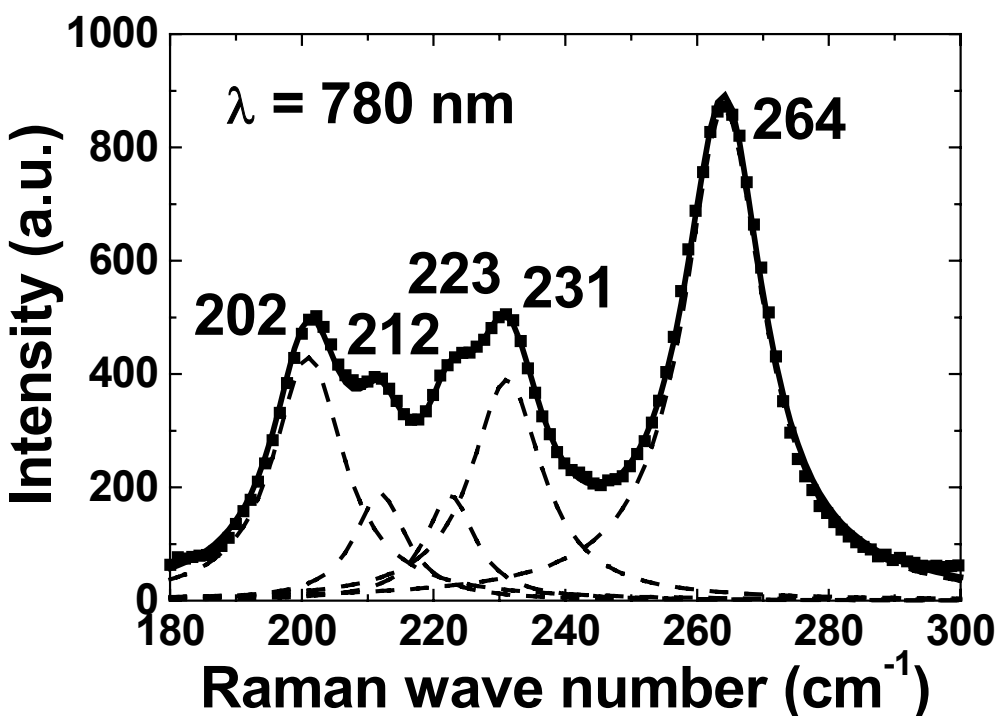


Figure 6.14: Raman spectrum of the RBMs with a laser of wavelength 780 nm (squares). The spectrum is fitted (solid line) with 5 different Lorentzian lines (dashed lines). The peak positions are indicated in Raman wave number (cm^{-1}).

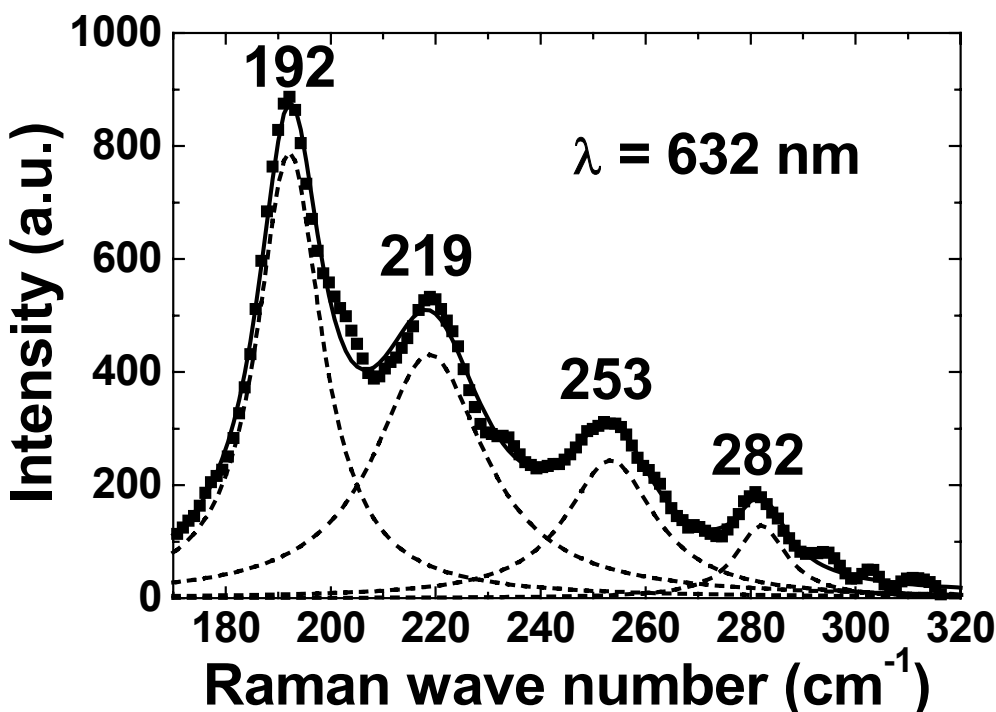


Figure 6.15: Raman spectrum of the RBMs with a laser of wavelength 632 nm (squares). The spectrum is fitted (solid line) with 4 different Lorentzian lines (dashed lines). The peak positions are indicated in Raman wave number (cm^{-1}).

Figures 6.13 to 6.15 are the low-frequency spectra from the Elicarb nanotube powder collected with the three different laser wavelengths. The number of visible RBMs on the Elicarb nanotube spectra differs from the HiPco nanotube spectra but both nanotube samples exhibit several common RBMs. The $E_{\text{laser}} = 1.49 \text{ eV}$ spectrum is fitted with 8 Lorentzian lines centered at 163, 183, 194, 204, 214, 225, 233, and 262 cm^{-1} , the $E_{\text{laser}} = 1.59 \text{ eV}$ spectrum with 5 centered at 202, 212, 223, 231, and 264 cm^{-1} , and the $E_{\text{laser}} = 1.96 \text{ eV}$ spectrum with 4 centered at 192, 219, 253, and 282 cm^{-1} .

Also the relative RBM intensities on the Elicarb nanotube spectra are different from the HiPco nanotube spectra: the lower wave number RBMs (below 220 cm^{-1}) have a higher intensity compared to the higher wave number RBMs. This is consistent with a larger mean diameter of the Elicarb nanotubes. The relative RBM intensities vary significantly for the Elicarb material depending on the location of the laser spot, while they remain fairly constant for the HiPco material, indicating the HiPco material is more uniform.

6.3 Raman Spectroscopy on Epoxy/SWNTs Composites

6.3.1 HiPco Nanotube Composites

Figures 6.16 to 6.18 are typical Raman spectra collected from HiPco nanotubes embedded in an epoxy composite (Figure 6.17, 780 nm laser) and in a PVA film (Figures 6.16 and 6.18, 830 nm and 632 nm laser respectively). Several weak RBMs in the powder spectra disappear or appear only as weak shoulders which cannot be analyzed. The $E_{\text{laser}} = 1.49$ eV spectrum is fitted with 5 Lorentzian lines centered at 207, 217, 227, 237, and 266 cm^{-1} (Figure 6.16), the $E_{\text{laser}} = 1.59$ eV spectrum with 5 centered at 210, 232, 238, 268, and 272 cm^{-1} (Figure 6.17), and the $E_{\text{laser}} = 1.96$ eV spectrum with 5 centered at 200, 221, 257, 284, and 299 cm^{-1} (Figure 6.18).

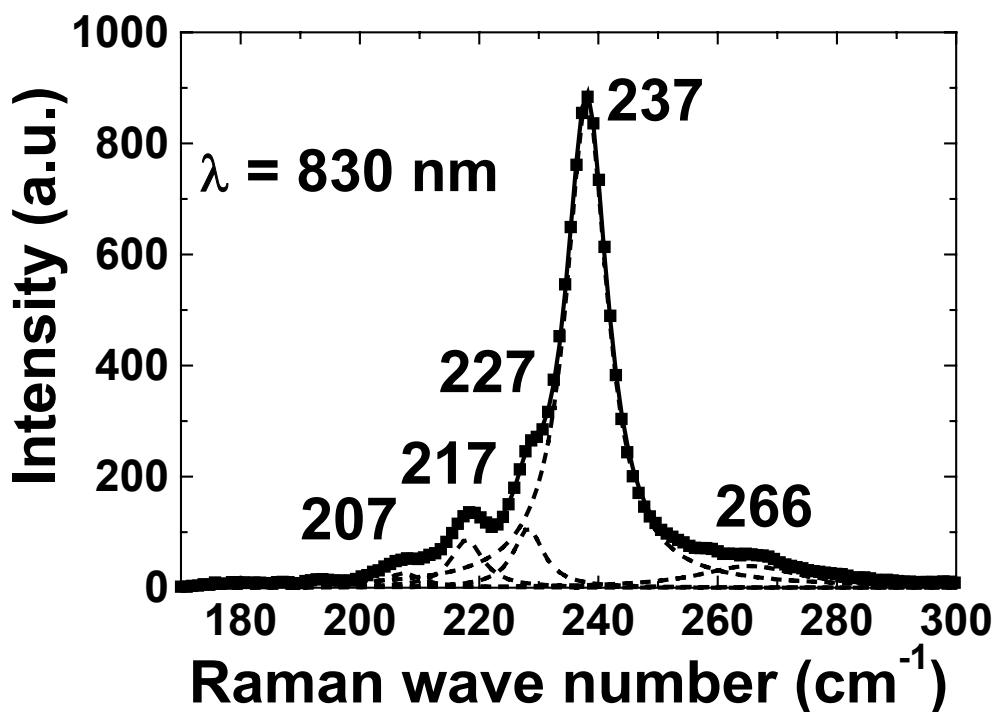


Figure 6.16: Low-frequency Raman spectrum of HiPco nanotubes in a PVA/SWNT film (solid squares) using a laser of wavelength 830 nm. The spectrum from the PVA/SWNT film was fitted (solid line) with 5 Lorentzian components (dashed lines) centered at 207, 217, 227, 237, 266 cm^{-1} .

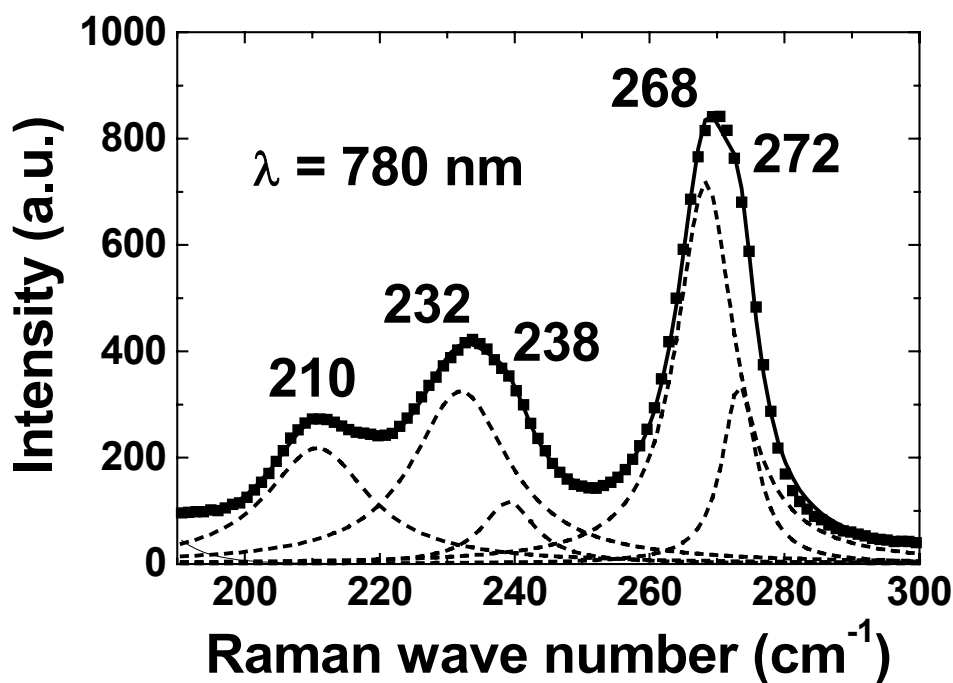


Figure 6.17: Low-frequency Raman spectrum of HiPco nanotubes in epoxy/SWNT composite (solid squares) using a laser of wavelength 780 nm. The spectrum from the epoxy/SWNT composite was fitted (solid line) with 5 Lorentzian components (dashed lines) centered at 210, 232, 238, 268, 272 cm^{-1} .

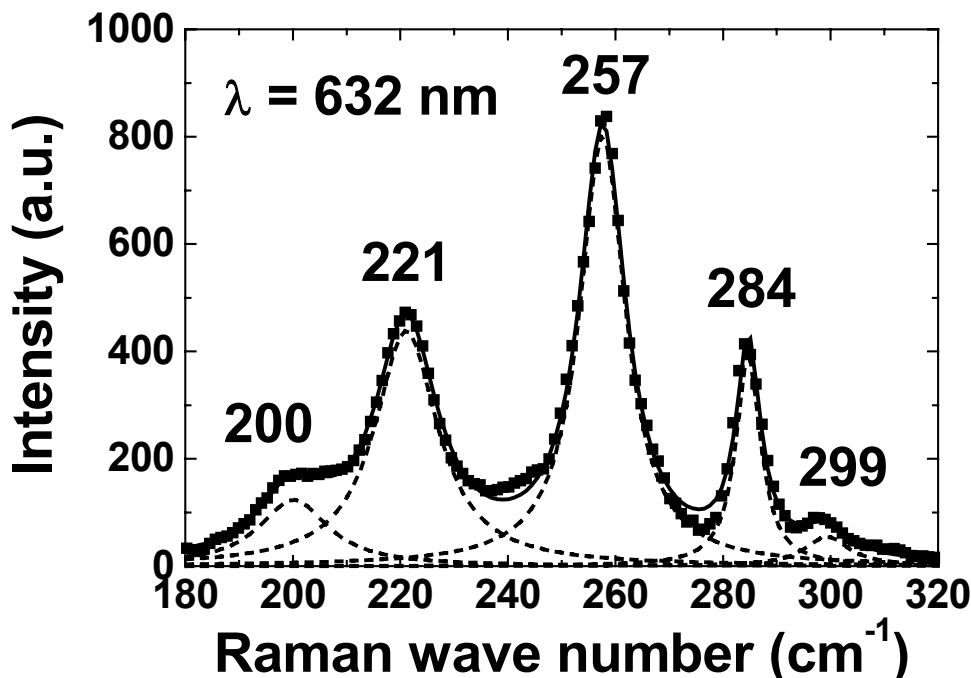


Figure 6.18: Low-frequency Raman spectrum of HiPco nanotubes in a PVA/SWNT film (solid squares) using a laser of wavelength 632 nm. The spectrum from the PVA/SWNT film was fitted (solid line) with 5 Lorentzian components (dashed lines) centered at 200, 221, 257, 284, 299 cm^{-1} .

The nanotube diameter can be estimated using the two following equations:

$$d \text{ (nm)} = \frac{223.5}{\omega_{RBM} \text{ (cm}^{-1}\text{)} - 12.5} \quad (6.3)$$

$$d \text{ (nm)} = \frac{248}{\omega_{RBM} \text{ (cm}^{-1}\text{)}} \quad (6.4)$$

These two equations give the extreme theoretical RBM values: the first equation was used for nanotubes in suspensions [66], and the second for individual nanotubes [70]. Using Equations 6.3 or 6.4, the HiPco nanotube diameters were found to be in the range of 0.8 nm to 1.2 nm. According to resonance theory [199], only the RBMs centered at 200 and 221 cm⁻¹ are metallic, the others are semiconducting.

6.3.2 Elicarb Nanotube Composites

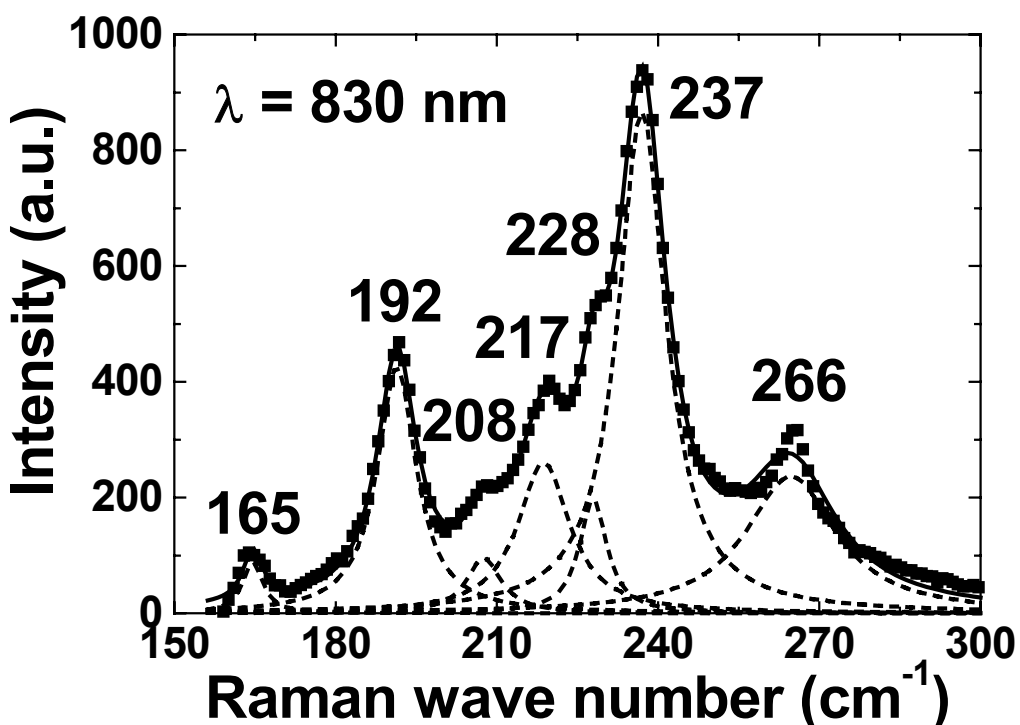


Figure 6.19: Low-frequency Raman spectrum of Elicarb nanotubes in a PVA/SWNT film (solid squares) using a laser of wavelength 830 nm. The spectrum from the PVA/SWNT film was fitted (solid line) with 7 Lorentzian components (dashed lines) centered at 165, 192, 208, 217, 228, 237, 266 cm⁻¹.

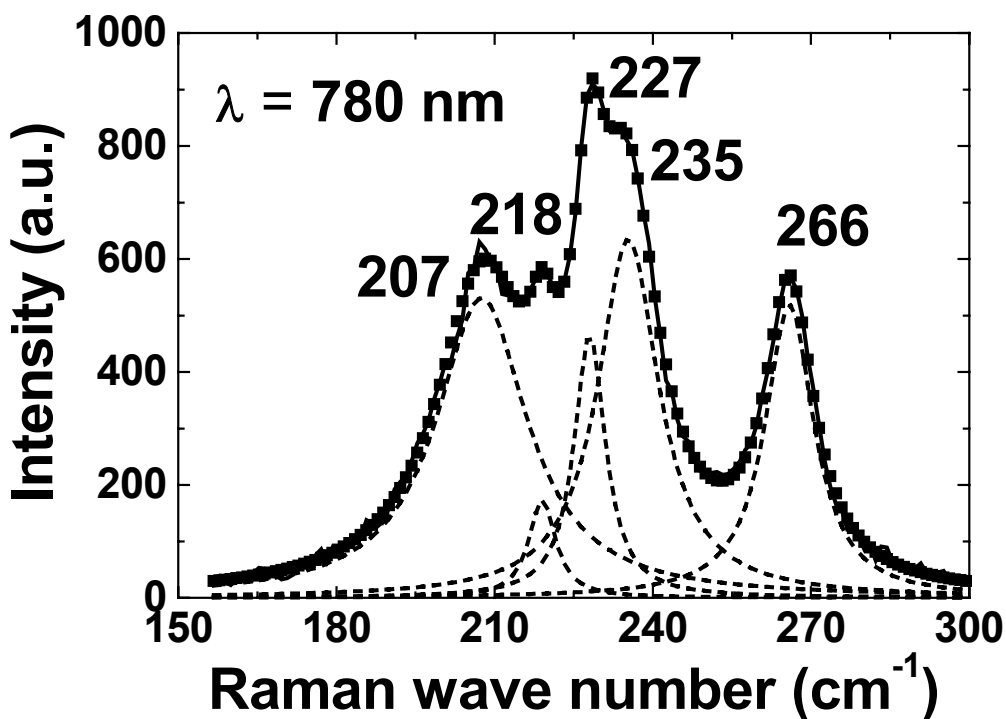


Figure 6.20: Low-frequency Raman spectrum of Elicarb nanotubes in a PVA/SWNT film (solid squares) using a laser of wavelength 780 nm. The spectrum from the PVA/SWNT film was fitted (solid line) with 5 Lorentzian components (dashed lines) centered at 207, 218, 227, 235, 266 cm^{-1} .

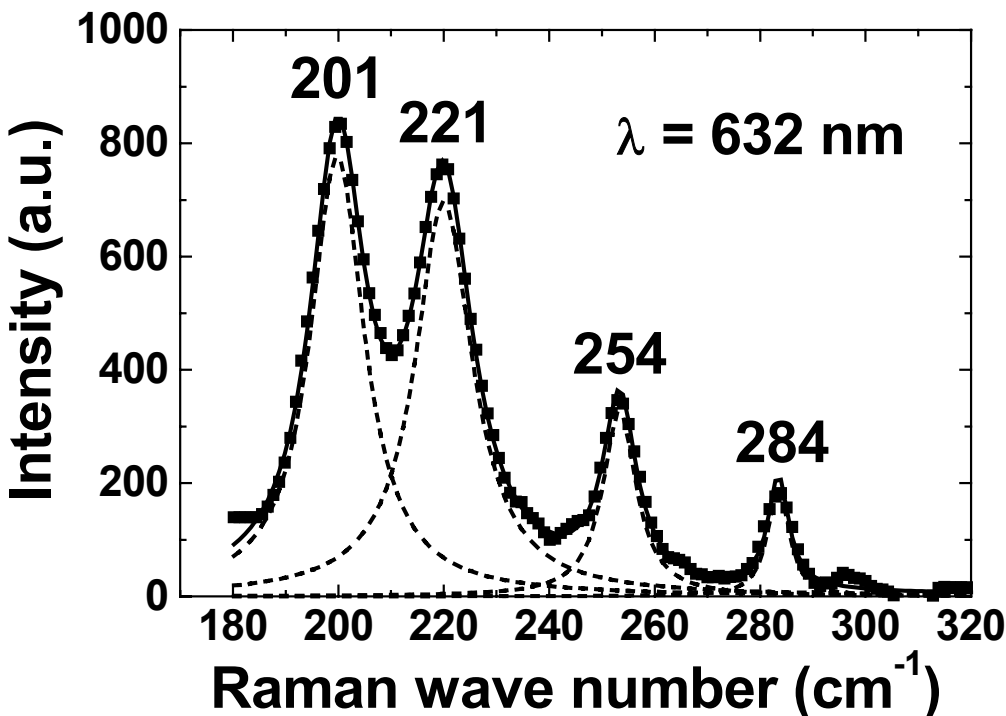


Figure 6.21: Low-frequency Raman spectrum of Elicarb nanotubes in a PVA/SWNT film (solid squares) using a laser of wavelength 632 nm. The spectrum from the PVA/SWNT film was fitted (solid line) with 4 Lorentzian components (dashed lines) centered at 201, 221, 254, 284 cm^{-1} .

Figures 6.19 to 6.21 are typical Raman spectra collected from Elicarb nanotubes embedded in a PVA film with the 3 different lasers. The $E_{laser} = 1.49$ eV spectrum is fitted with 7 Lorentzian lines centered at 165, 192, 208, 217, 228, 237, and 266 cm^{-1} (Figure 6.19), the $E_{laser} = 1.59$ eV spectrum with 5 centered at 207, 218, 227, 235, and 266 cm^{-1} (Figure 6.20), and the $E_{laser} = 1.96$ eV spectrum with 4 centered at 201, 221, 254, and 284 cm^{-1} (Figure 6.21). Using Equations 6.3 or 6.4, the nanotube diameters are in the range of 0.8 nm to 1.5 nm. Only the RBMs centered at 165, 201 and 221 cm^{-1} are expected to be metallic, the others are semiconducting.

6.3.3 Upshift of the RBM Positions in Composite

When the low-frequency spectra of nanotube powders (Figures 6.7-6.9 and 6.13-6.15) are compared to those of the nanotubes in epoxy/SWNT composite or PVA film (Figures 6.16-6.21), an upshift of the RBM positions is observed. It is different for each RBM and ranges from 1 to 9 cm^{-1} . This upshift is consistent with a report on the crystallization behavior of polypropylene reinforced with SWNTs. Valentini *et al.* reported an upshift of the RBM positions when nanotubes (with concentrations between 5% and 20% in weight) were introduced in a polypropylene matrix [200]. Chambers *et al.* reported an upshift of 3 to 7 cm^{-1} for the RBM positions and 10 cm^{-1} for the G band in gamma cyclodextrin composites [201]. However, another study where SWNTs were incorporated in a natural rubber matrix found no RBM position shift but a 10 cm^{-1} upshift of the G band from the nanotube powder to the composite [202].

This observation can be attributed to the sensitivity of the RBM position to the nanotube environment, which usually exerts compressive forces [103]. Raman studies of different nanotube samples under hydrostatic pressure, including HiPco nanotubes, revealed that the upshift rate is between 6 and $9\text{ cm}^{-1}/\text{GPa}$ for all RBMs, including the higher wave number RBMs [89,107,108,203]. This does not explain the larger difference in RBM position shift reported here. Moreover, these reported shift rates would indicate that at least some nanotubes are under a pressure of 1 GPa in the composite sample. Such a high pressure leads to a significant decrease in absolute intensities and

variations in relative RBM intensities [105]. However, this is not the case for the homogeneous HiPco material. A reduction in absolute intensity was observed, but the relative RBM intensities remain approximately the same.

This upshift is attributed to reduced heating effects under laser irradiation. High temperatures lead to the downshift of the RBM positions and nanotube heating in the composite is limited because of their low concentration in the polymer matrix. The effect of temperature on the positions of the RBMs, D, G and G' bands is studied in detail in Appendix II.

6.4 Deformation Test Results

6.4.1 HiPco Nanotube Composites

6.4.1.1 830 nm Laser ($E_{laser} = 1.49 \text{ eV}$)

Stress transfer to the nanotubes in the PVA film was monitored by measuring the G band shift as a function of uniaxial strain. It shifts to lower wave numbers in tension and to higher wave numbers in compression (Figure 6.22). A linear fit in the low strain range yields a shift rate of $-8.2 \text{ cm}^{-1}/\% \text{ strain}$. No noticeable shift of the RBM positions or increase in their widths was detected during the four-point bending tests within the limits of experimental error ($\pm 1 \text{ cm}^{-1}$) (Figure 6.23). Considering the low strain rate and a Poisson's ratio of about 0.3 [204], any RBM shift during the deformation test is expected to be within the limits of experimental error. This should be contrasted with the behavior of similar SWNTs under pressure where significant shifts of the RBMs from the HiPco material were obtained under hydrostatic pressure [89]. The state of stress on the SWNTs is different under pressure than in a deformed composite and considerably higher levels of deformation can be applied using hydrostatic pressure.

In Figure 6.24, the Raman spectra of the nanotubes in the PVA film when no strain was applied and when the sample was in compression at 0.6% are compared. The intensities of the 3 RBMs located at 217, 227 and 237 cm^{-1} clearly increase in compression. During the tension tests (Figure 6.25), the intensities of these 3 RBMs vary the opposite way.

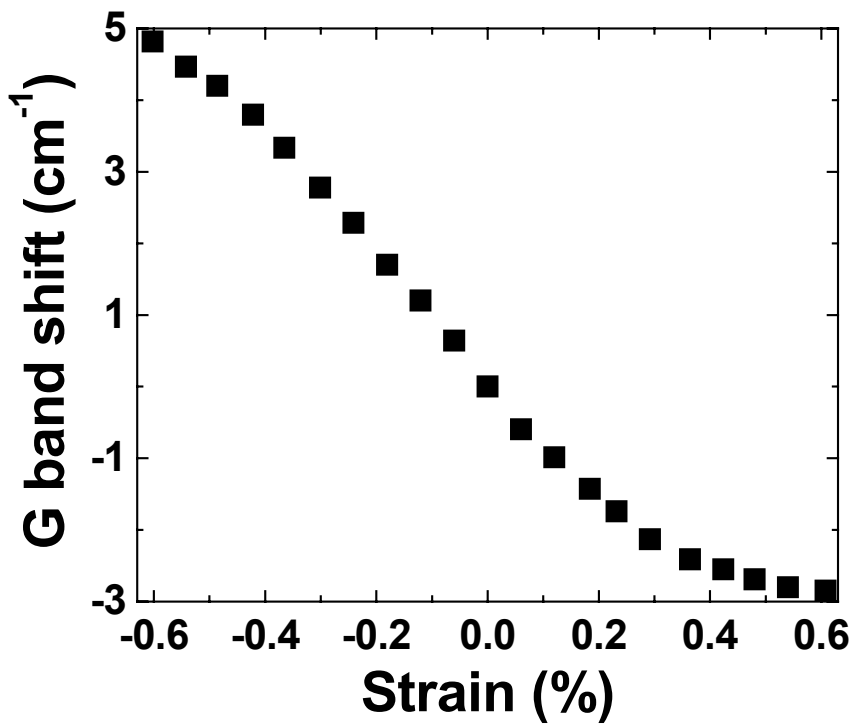


Figure 6.22: G band shift as a function of axial strain for a PVA film. The laser wavelength was 830 nm.

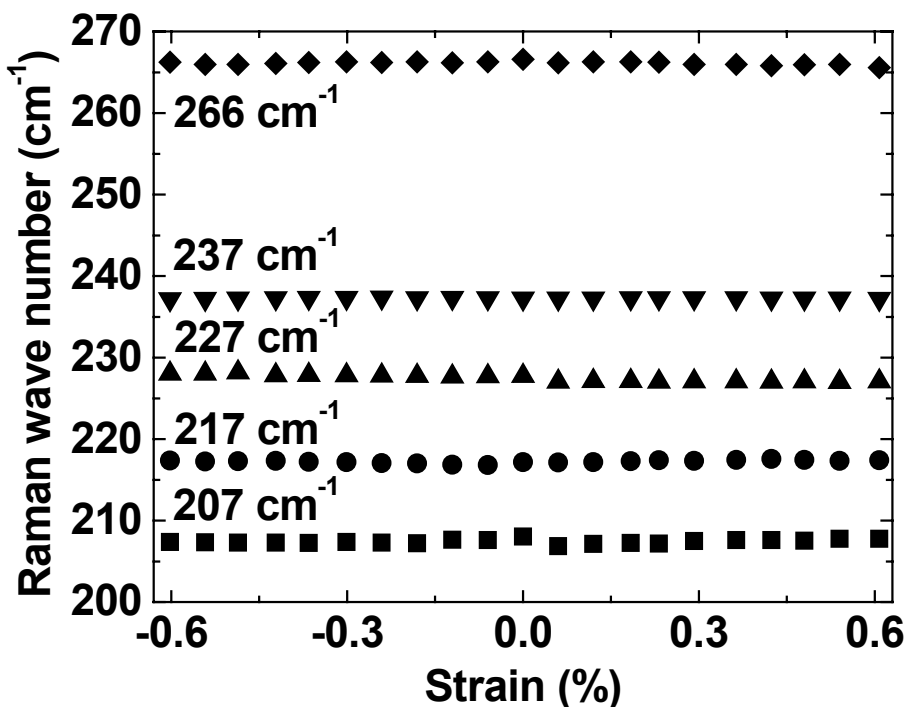


Figure 6.23: RBM position as a function of axial strain in four-point bending tests. The laser wavelength was 830 nm.

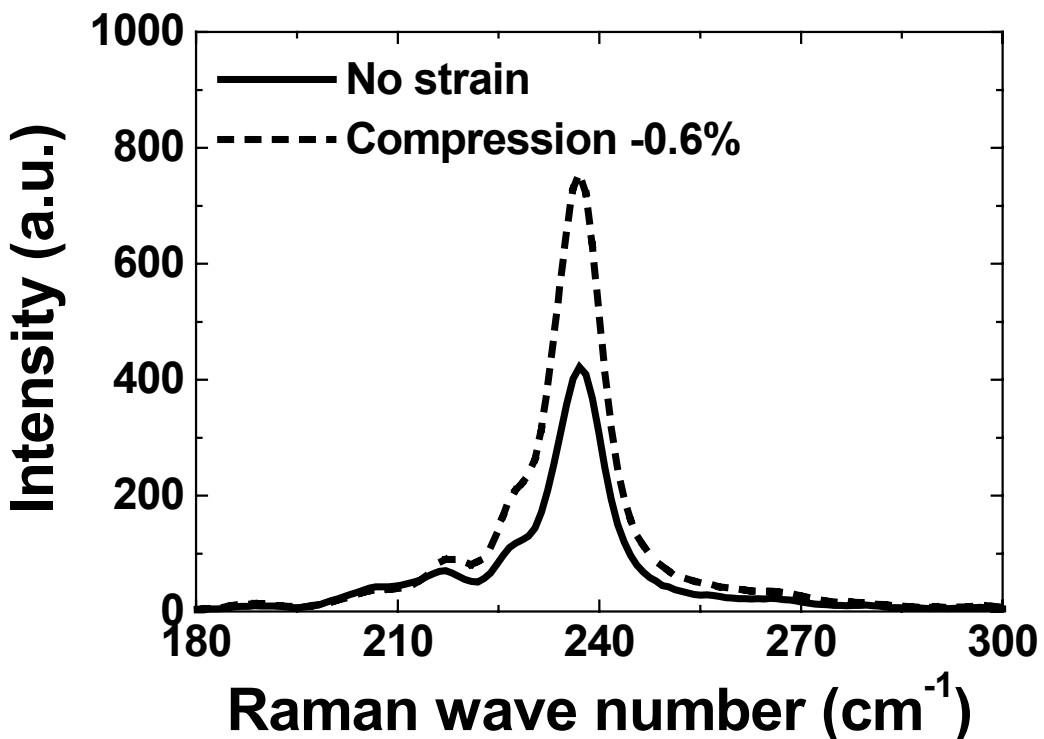


Figure 6.24: Comparison between the low-frequency Raman spectra of the HiPco nanotubes in a PVA film at zero stress (solid line) and in compression (-0.6%) (dashed line). The laser wavelength was 830 nm.

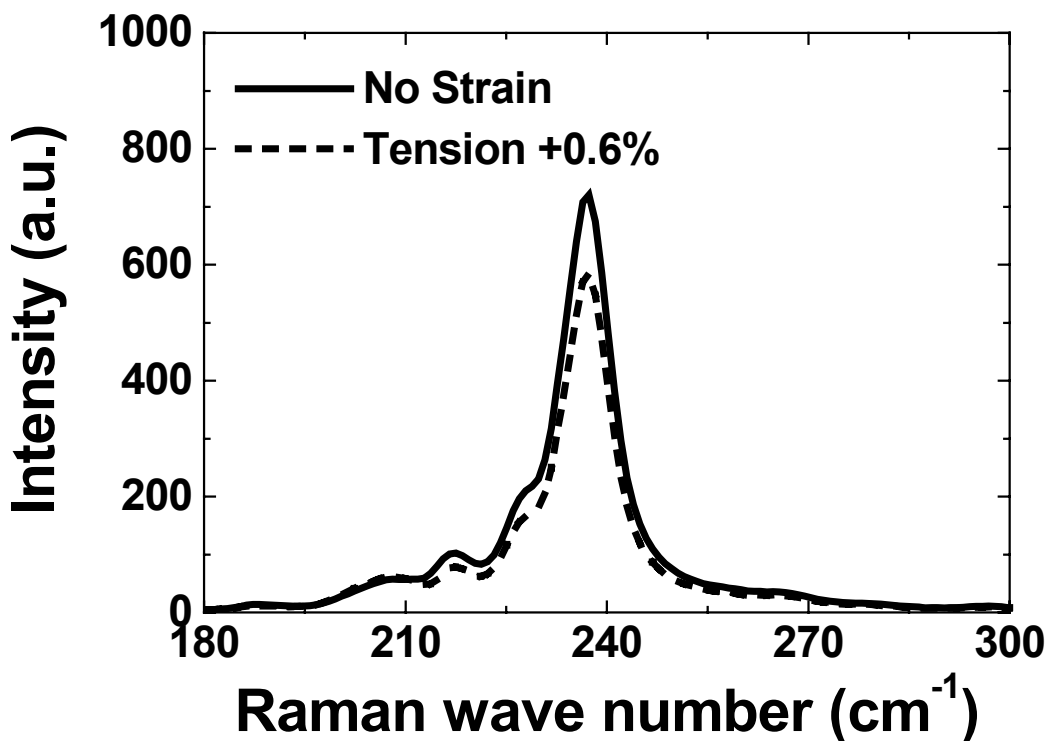


Figure 6.25: Comparison between the low-frequency Raman spectra of the HiPco nanotubes in a PVA film at zero stress (solid line) and in tension (+0.6%) (dashed line). The laser wavelength was 830 nm.

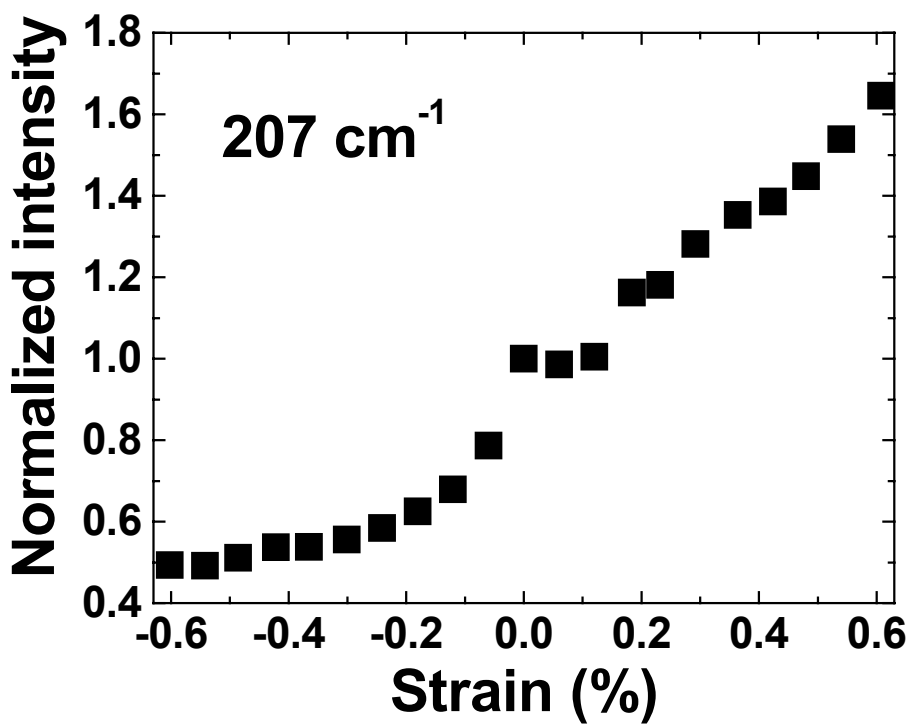


Figure 6.26: Normalized intensity (compared to the value at zero strain) for the RBM centered at 207 cm^{-1} . The laser wavelength was 830 nm.

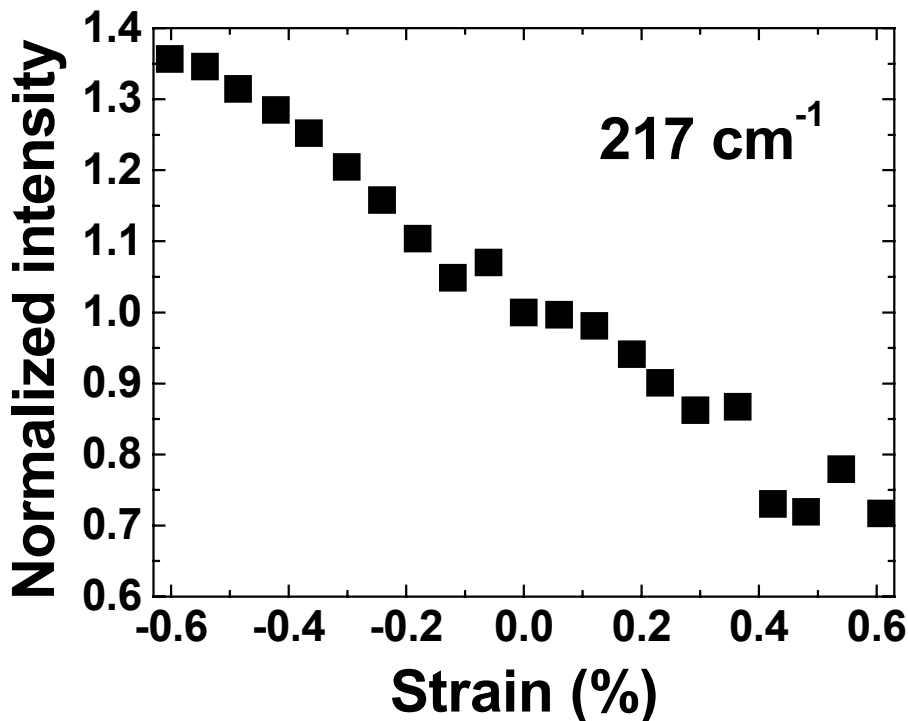


Figure 6.27: Normalized intensity (compared to the value at zero strain) for the RBM centered at 217 cm^{-1} . The laser wavelength was 830 nm.

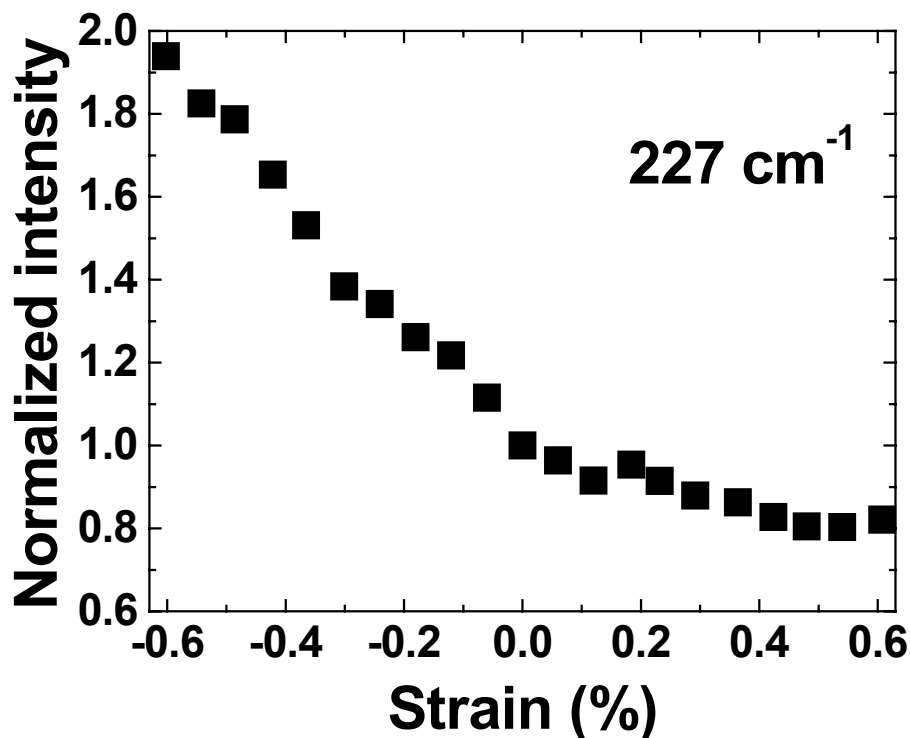


Figure 6.28: Normalized intensity (compared to the value at zero strain) for the RBM centered at 227 cm^{-1} . The laser wavelength was 830 nm.

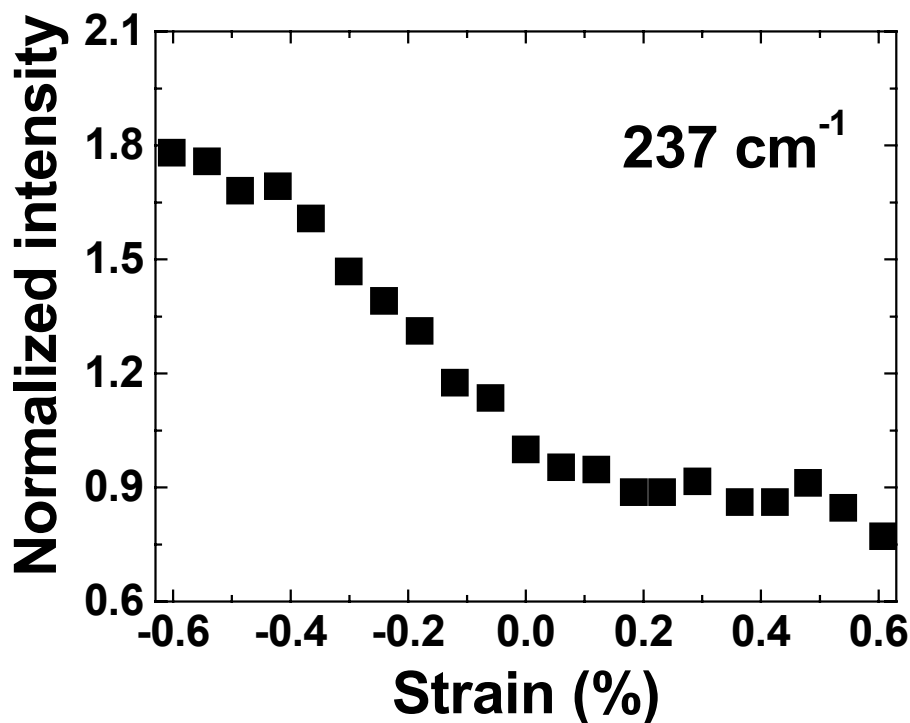


Figure 6.29: Normalized intensity (compared to the value at zero strain) for the RBM centered at 237 cm^{-1} . The laser wavelength was 830 nm.

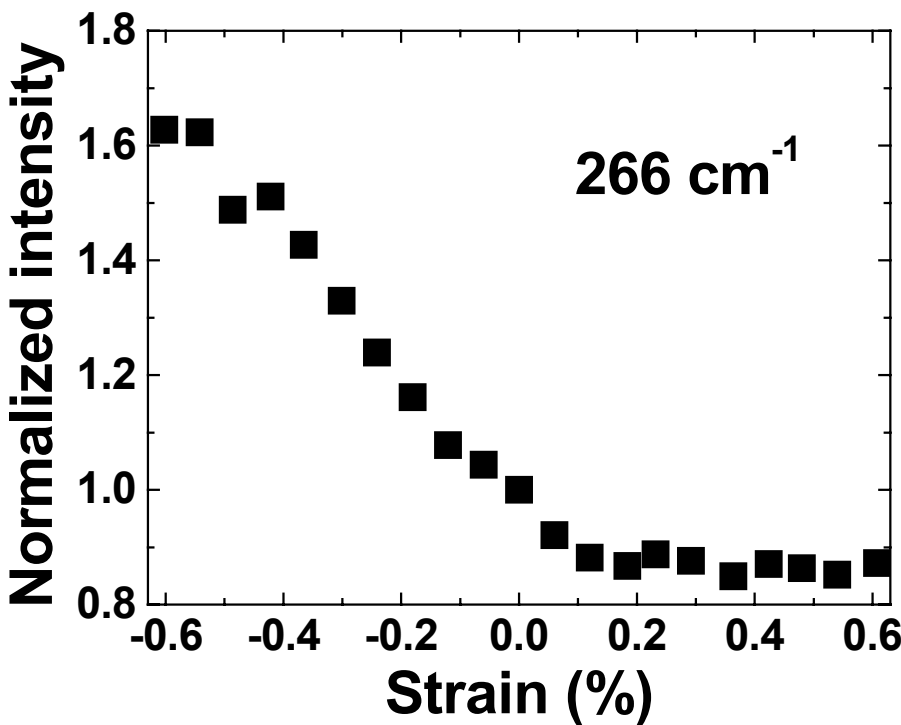


Figure 6.30: Normalized intensity (compared to the value at zero strain) for the RBM centered at 266 cm^{-1} . The laser wavelength was 830 nm.

The intensity variations of the five RBMs, including the two smaller RBMs centered at 207 and 266 cm^{-1} , are showed as a function of strain between -0.6% and 0.6% in Figures 6.26 to 6.30. The variation trend depends on the RBM considered, and therefore on the nanotube chirality and diameter. The intensity of the RBM at 207 cm^{-1} increases in tension and decreases in compression. The other four RBMs at 217 , 227 , 237 and 266 cm^{-1} behave the opposite way: their intensity decreases in tension and increases in compression. The magnitude of these variations also depends on the nanotube structure. The RBM at 217 cm^{-1} increases in intensity by 40% at -0.6% strain and decreases by 30% at 0.6% , while the one at 237 cm^{-1} increases by 80% at -0.6% strain and decreases by less than 20% in tension at 0.6% .

6.4.1.2 780 nm Laser ($E_{\text{laser}} = 1.59\text{ eV}$)

The G' band shift in the epoxy composite as a function of strain is showed in Figure 6.31. The slope in the low strain range was $-10.9\text{ cm}^{-1}/\%$ and this value is similar to the one reported in Reference 101 ($-6.3\text{ cm}^{-1}/\%$ for

unoriented nanotubes). This is higher than the value for the G band for the 830 nm laser, which is consistent with a previous report on carbon fibers, where the G' band was found more sensitive to deformation than the G band [198]. The RBM positions were found unchanged within the resolution of the spectrometer in the strain range between -0.3% and 0.7% (Figure 6.32).

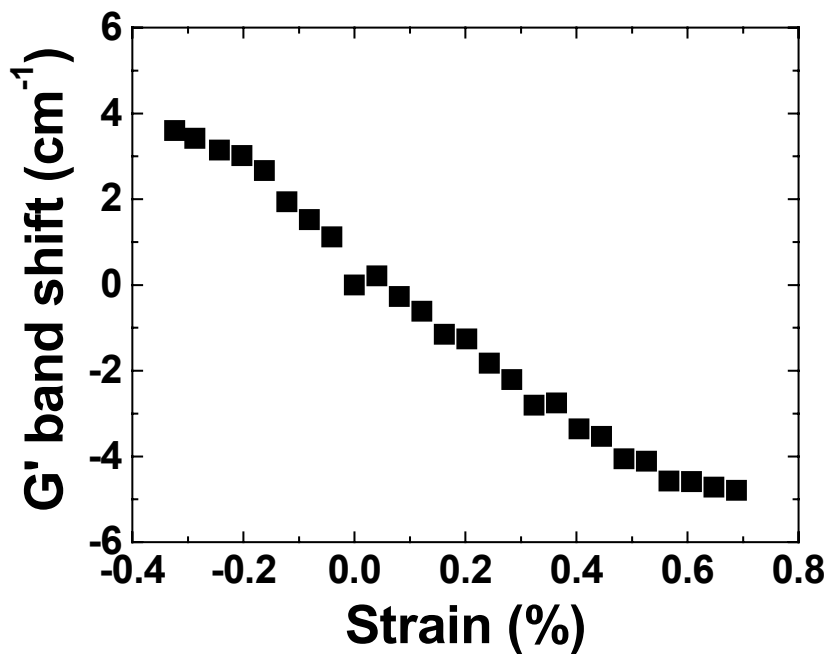


Figure 6.31: G' band shift as a function of axial strain for an epoxy/SWNT composite sample. The laser wavelength was 780 nm.

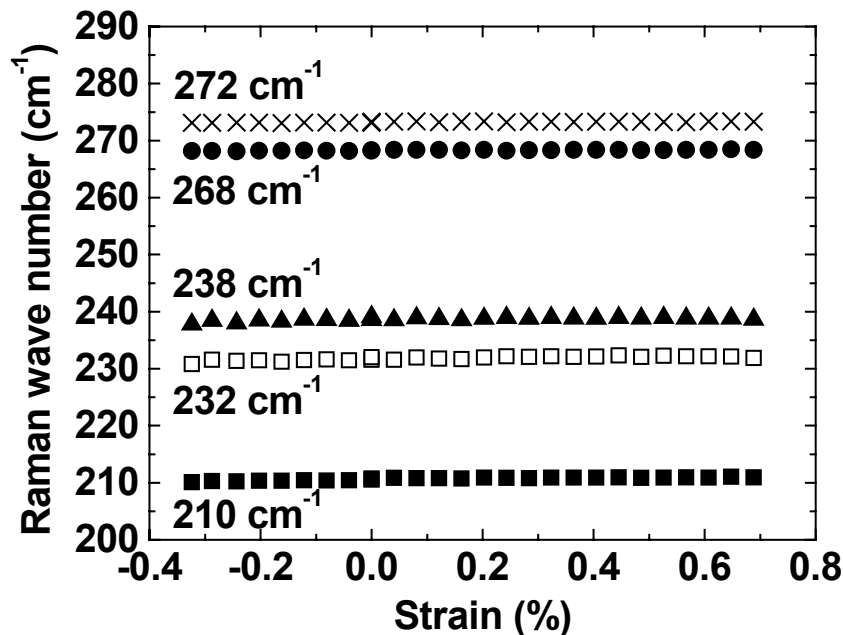


Figure 6.32: RBM position as a function of axial strain in four-point bending tests. The laser wavelength was 780 nm.

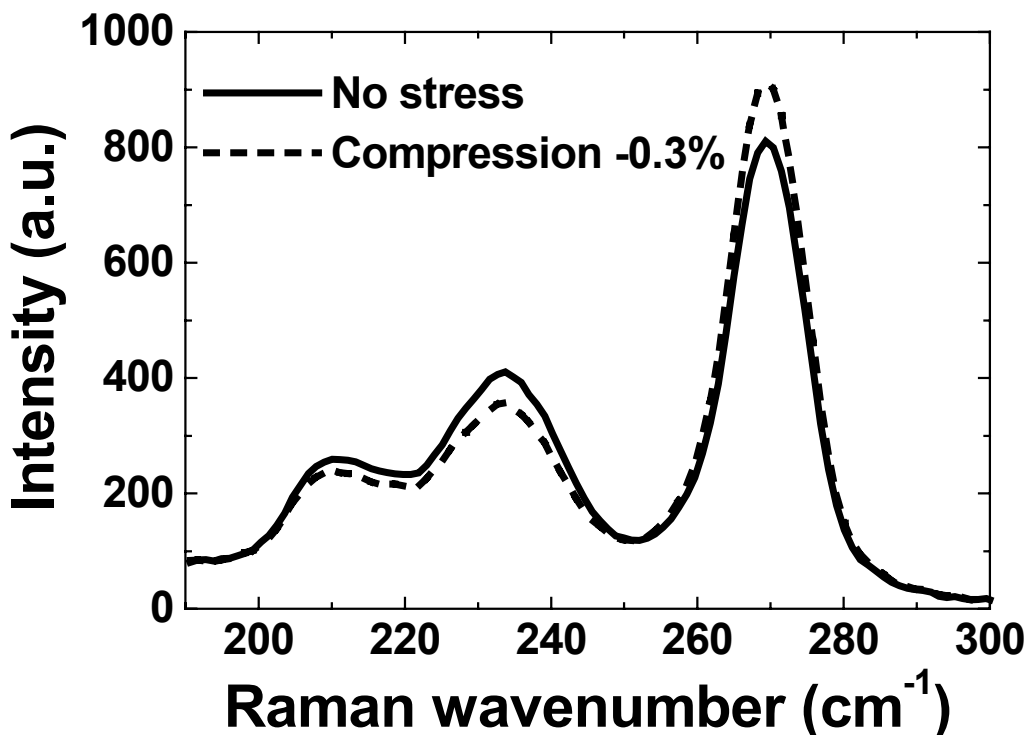


Figure 6.33: Comparison between the low-frequency Raman spectra of the HiPco nanotubes in epoxy composite at zero stress (solid line) and in compression (-0.3%). The laser wavelength was 780 nm.

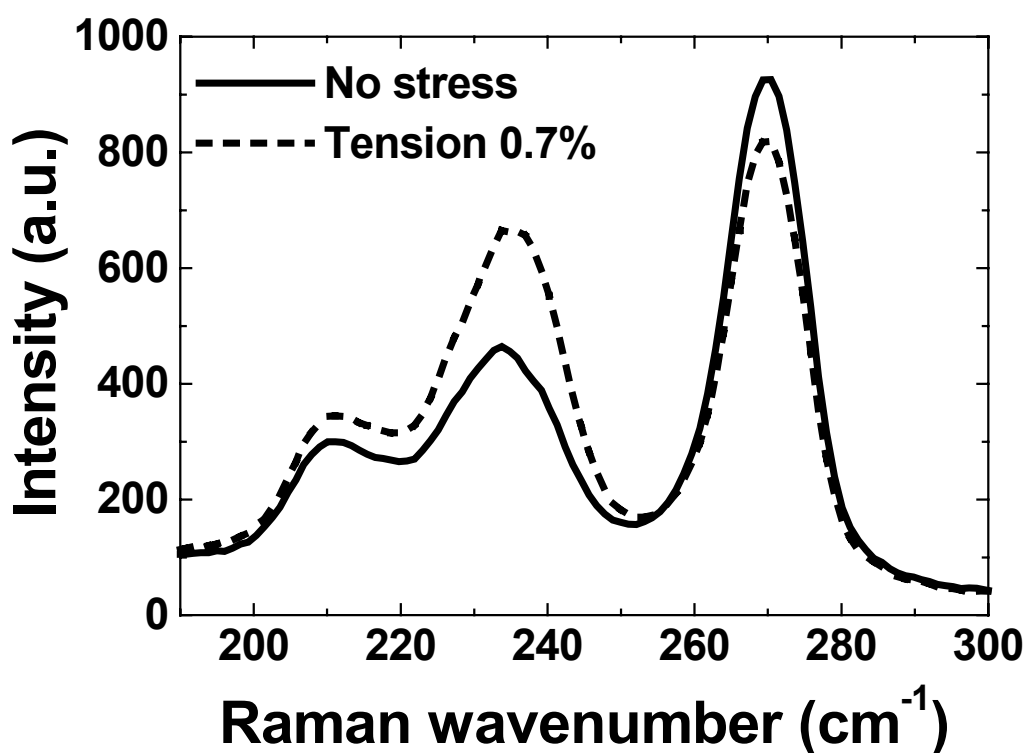


Figure 6.34: Comparison between the low-frequency Raman spectra of the HiPco nanotubes in epoxy composite at zero stress (solid line) and in tension (0.7%) (dashed line). The laser wavelength was 780 nm.

Intensities vary with strain for all 5 RBM peaks (Figures 6.33 and 6.34). The variation trend depends on the nanotube considered. The intensities of the 210 cm^{-1} , 232 cm^{-1} and 238 cm^{-1} RBMs increase in tension, while the intensities of the 268 cm^{-1} and 272 cm^{-1} RBMs decrease. During the compression tests, the RBM intensities vary the opposite way: the intensities of the 210 cm^{-1} , 232 cm^{-1} and 238 cm^{-1} RBMs decrease, while those of the 268 cm^{-1} and 272 cm^{-1} RBMs increase.

The normalized RBM intensity variations for HiPco SWNTs embedded in the epoxy matrix are showed in Figure 6.35 to 6.39. The magnitude of the intensity variations varies with the nanotube considered. For instance, the 210 cm^{-1} RBM intensity decreases by up to 10% in compression and increases by up to 20% in tension. Whereas for the 238 cm^{-1} peak, its intensity decreases by up to 30% in compression and increases by up to 150% in tension. These intensity variations are reversible. The peak intensities go back to their initial values when the strain is released.

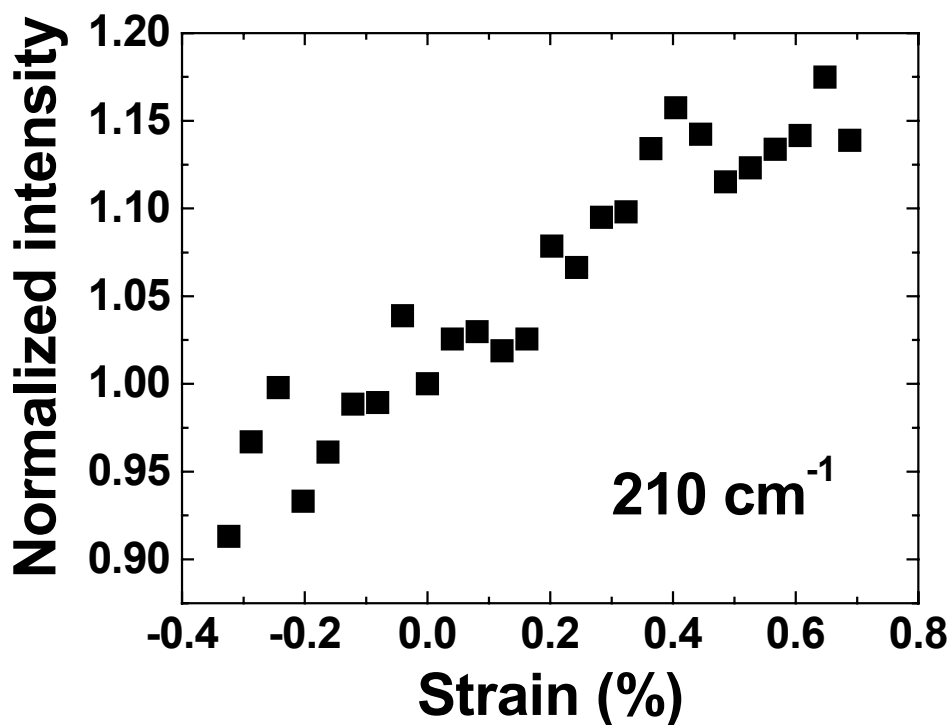


Figure 6.35: Normalized intensity (compared to the value at zero strain) for the RBM centered at 210 cm^{-1} . The laser wavelength was 780 nm.

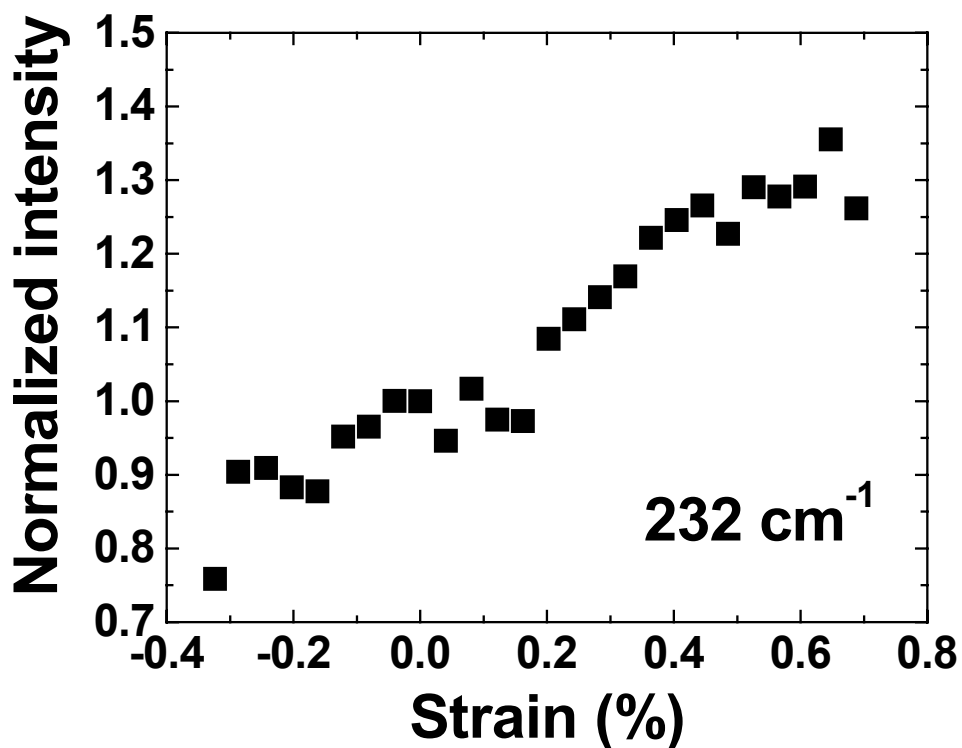


Figure 6.36: Normalized intensity (compared to the value at zero strain) for the RBM centered at 232 cm^{-1} . The laser wavelength was 780 nm.

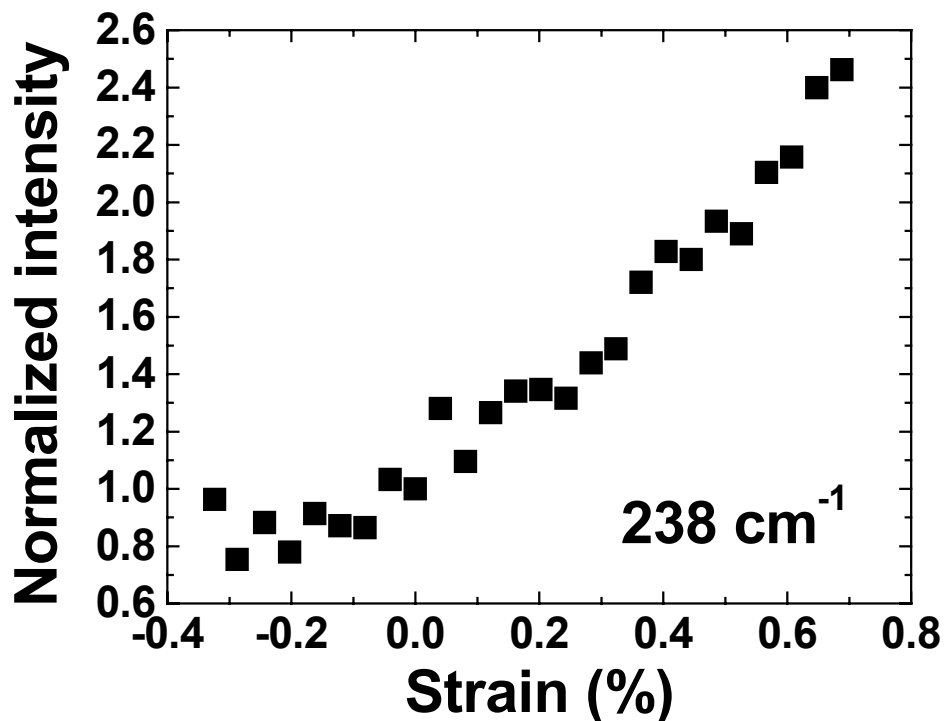


Figure 6.37: Normalized intensity (compared to the value at zero strain) for the RBM centered at 238 cm^{-1} . The laser wavelength was 780 nm.

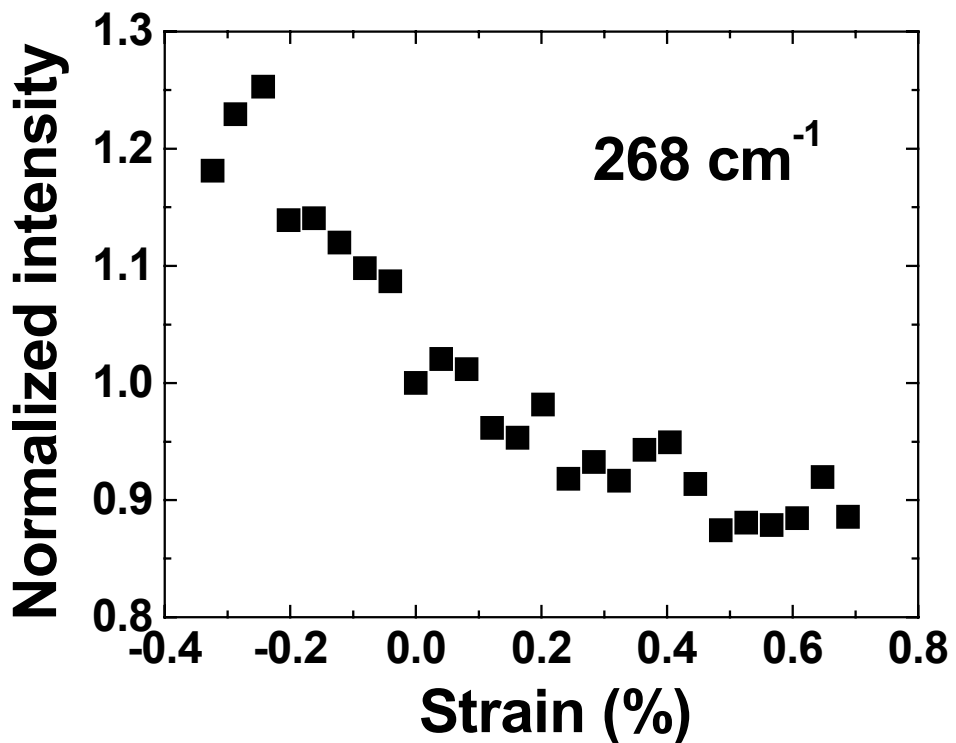


Figure 6.38: Normalized intensity (compared to the value at zero strain) for the RBM centered at 268 cm^{-1} . The laser wavelength was 780 nm.

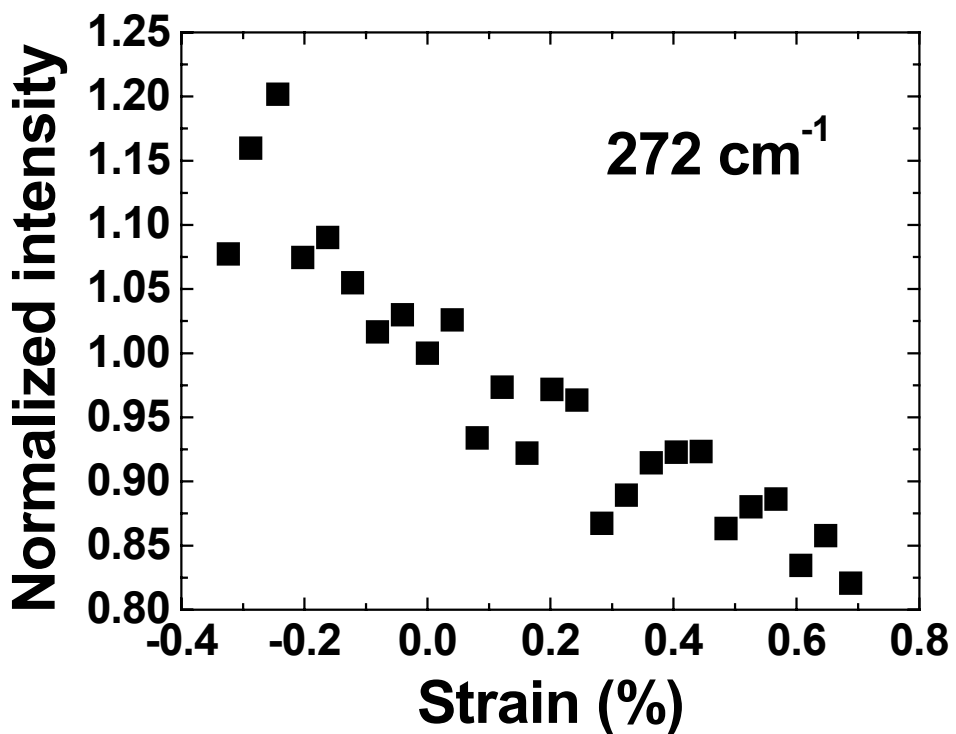


Figure 6.39: Normalized intensity (compared to the value at zero strain) for the RBM centered at 272 cm^{-1} . The laser wavelength was 780 nm.

Three RBMs are very close in position to three other RBMs observed with the 830 nm laser: the $207/210\text{ cm}^{-1}$, $237/238\text{ cm}^{-1}$ and $266/268\text{ cm}^{-1}$ RBMs. The 207 and 210 cm^{-1} RBMs have the same behavior, and so is the pair of RBMs located at 266 and 268 cm^{-1} . However, even though the 237 and 238 cm^{-1} RBMs have the same position within the resolution of the spectrometer, they have opposite behaviors: the 237 cm^{-1} decreases in intensity in tension, while the 238 cm^{-1} increases in intensity.

6.4.1.3 632 nm Laser ($E_{laser} = 1.96\text{ eV}$)

The G' band shift and the RBM positions in the PVA film as a function of axial strain are showed in Figures 6.40 and 6.41. The G' band shift rate in the low strain range was $-11.8\text{ cm}^{-1}/\%$ and the RBM positions were found unchanged.

Intensities vary with strain for all 5 RBM peaks (Figures 6.42 and 6.43). The intensities of the 200 cm^{-1} , 257 cm^{-1} and 284 cm^{-1} RBMs increase in tension, while the intensity of the 221 cm^{-1} RBMs decreases. During the compression tests, the intensities of the 200 cm^{-1} , 257 cm^{-1} and 284 cm^{-1} RBMs decrease, while the intensity of the 221 cm^{-1} RBMs increases.

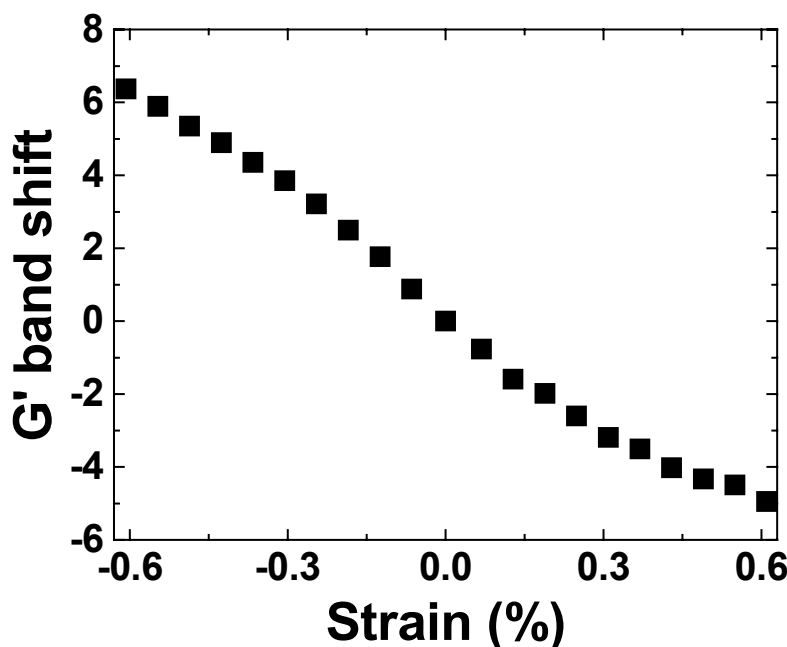


Figure 6.40: G' band shift as a function of axial strain for a PVA film. The laser wavelength was 632 nm.

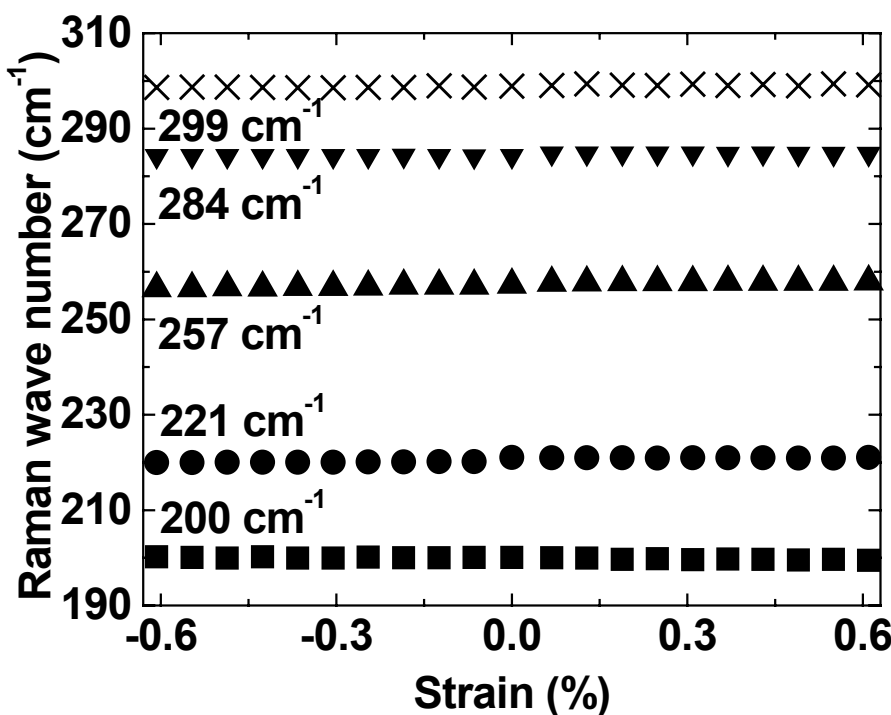


Figure 6.41: RBM position as a function of axial strain in four-point bending tests. The laser wavelength was 632 nm.

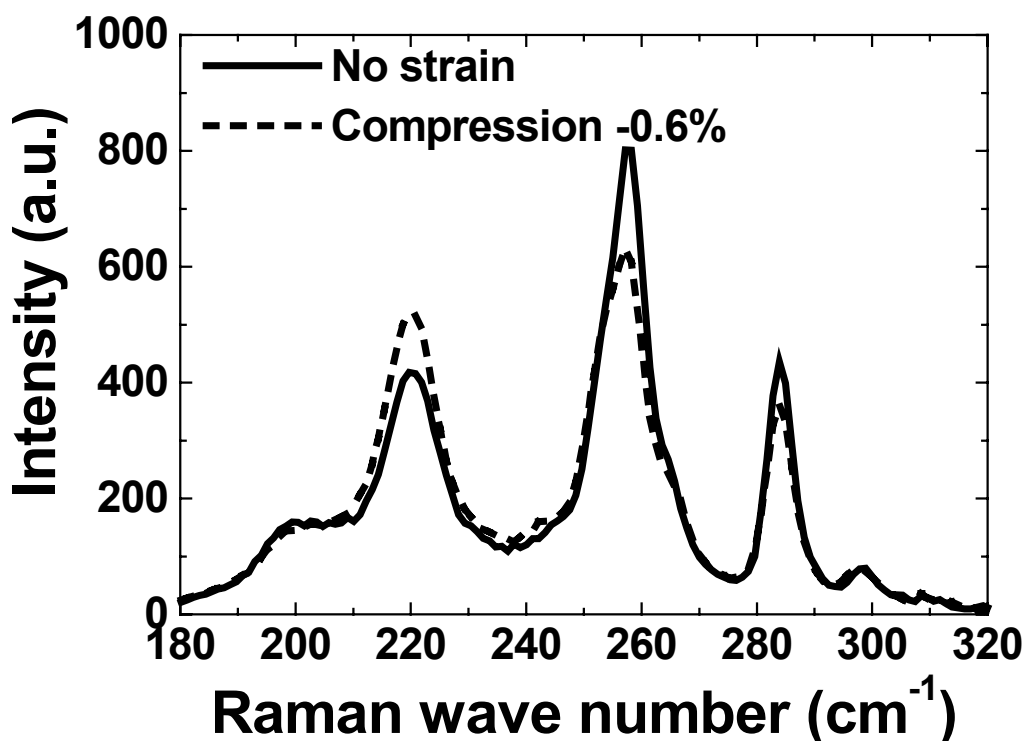


Figure 6.42: Comparison between the low-frequency Raman spectra of the HiPco nanotubes in a PVA film at zero stress (solid line) and in compression (-0.6%) (dashed line). The laser wavelength was 632 nm.

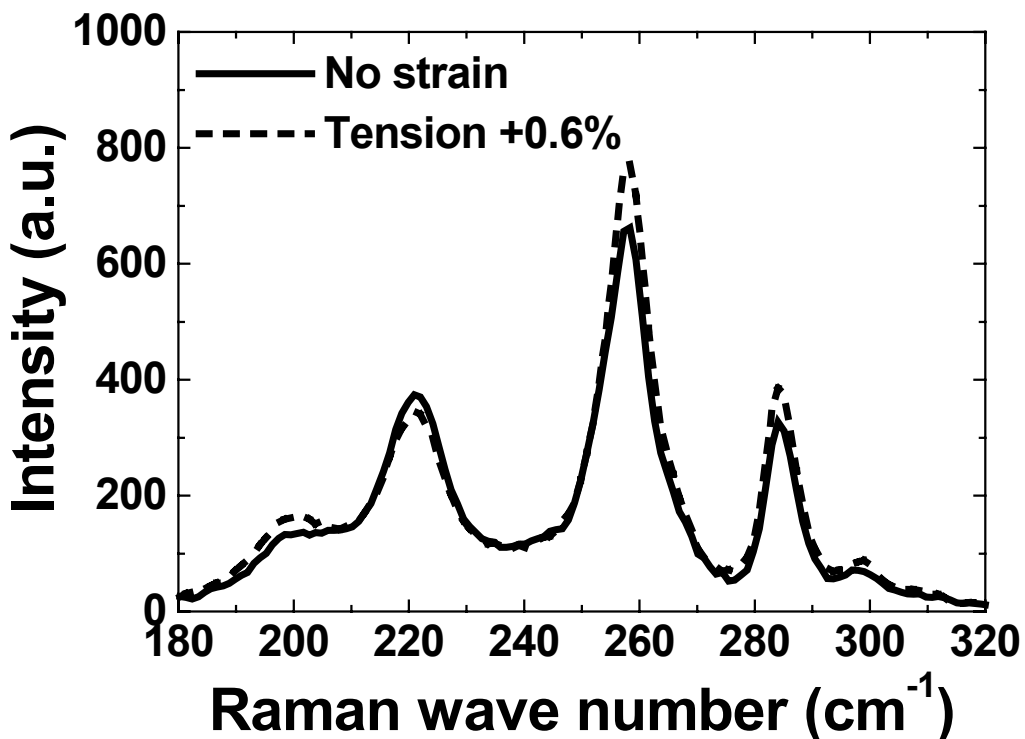


Figure 6.43: Comparison between the low-frequency Raman spectra of the HiPco nanotubes in a PVA film at zero stress (solid line) and in tension (+0.6%) (dashed line). The laser wavelength was 632 nm.

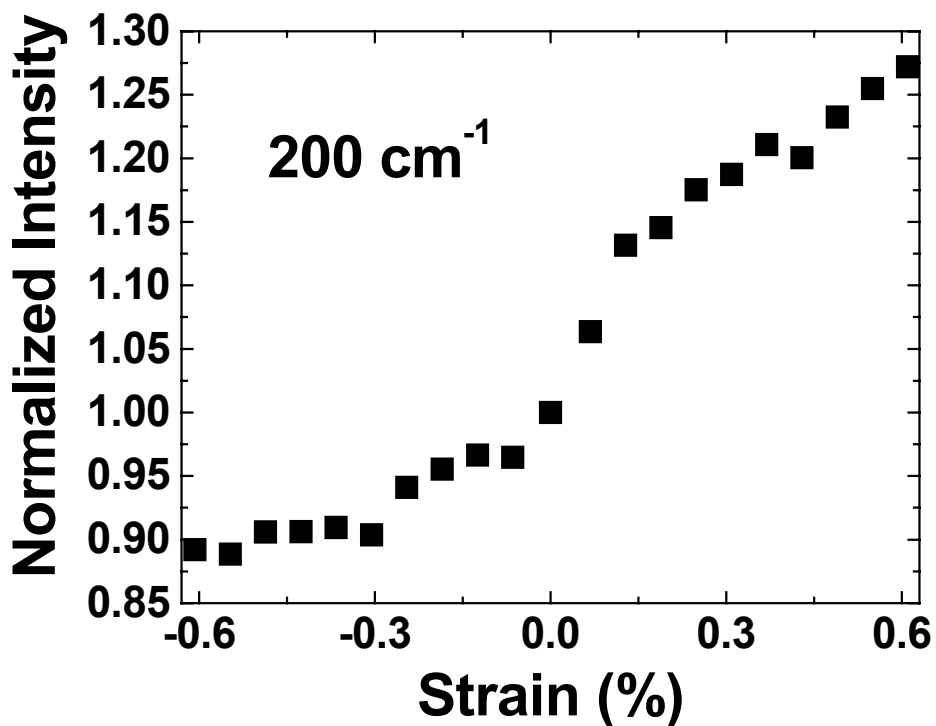


Figure 6.44: Normalized intensity (compared to the value at zero strain) for the RBM centered at 200 cm^{-1} . The laser wavelength was 632 nm.

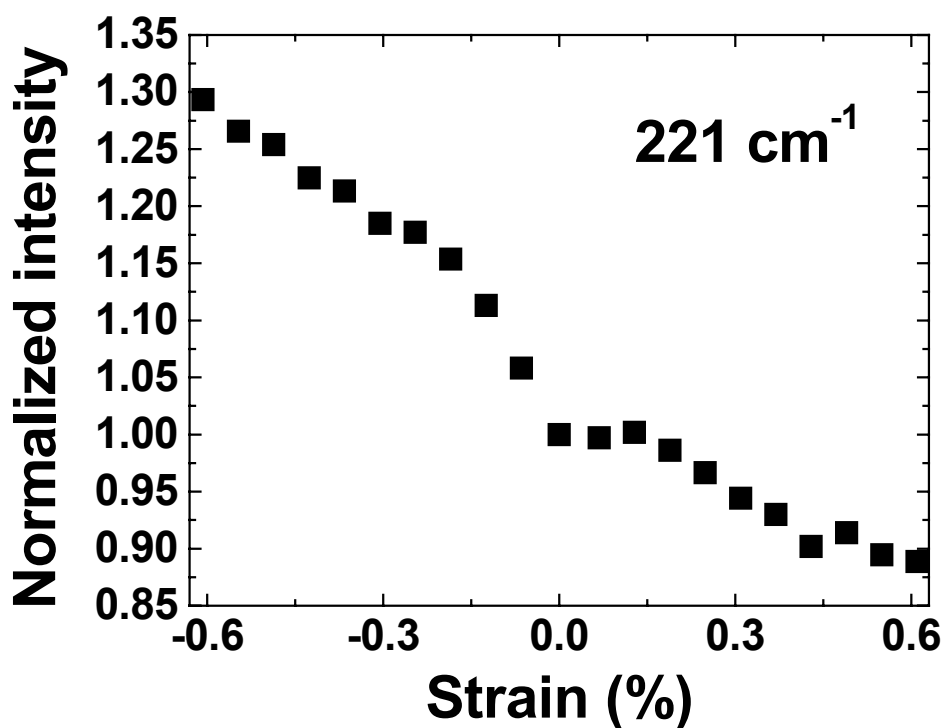


Figure 6.45: Normalized intensity (compared to the value at zero strain) for the RBM centered at 221 cm^{-1} . The laser wavelength was 632 nm.

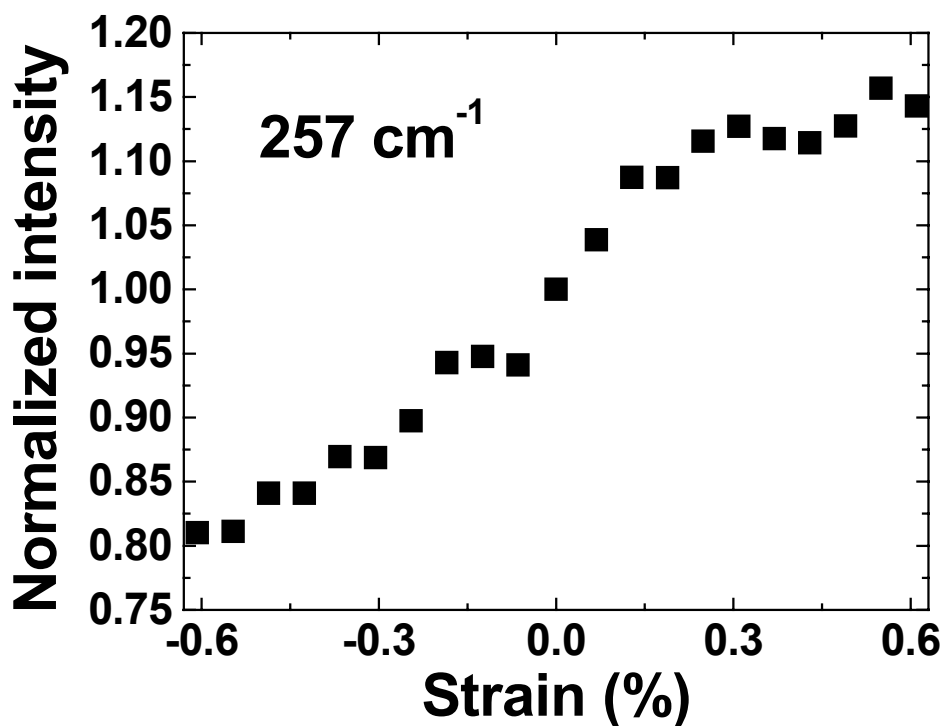


Figure 6.46: Normalized intensity (compared to the value at zero strain) for the RBM centered at 257 cm^{-1} . The laser wavelength was 632 nm.

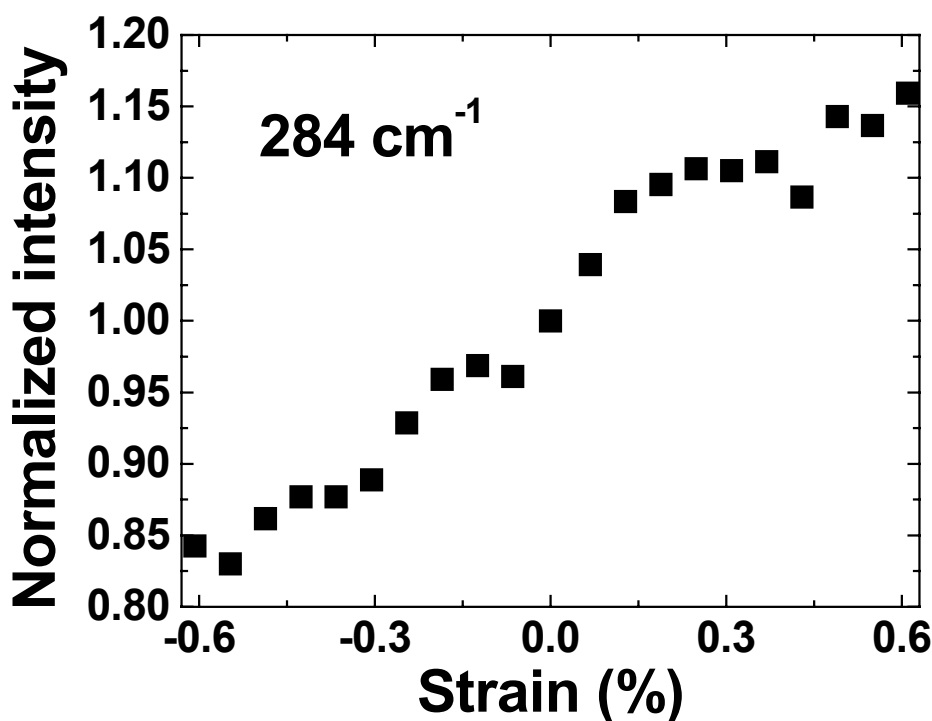


Figure 6.47: Normalized intensity (compared to the value at zero strain) for the RBM centered at 284 cm^{-1} . The laser wavelength was 632 nm.

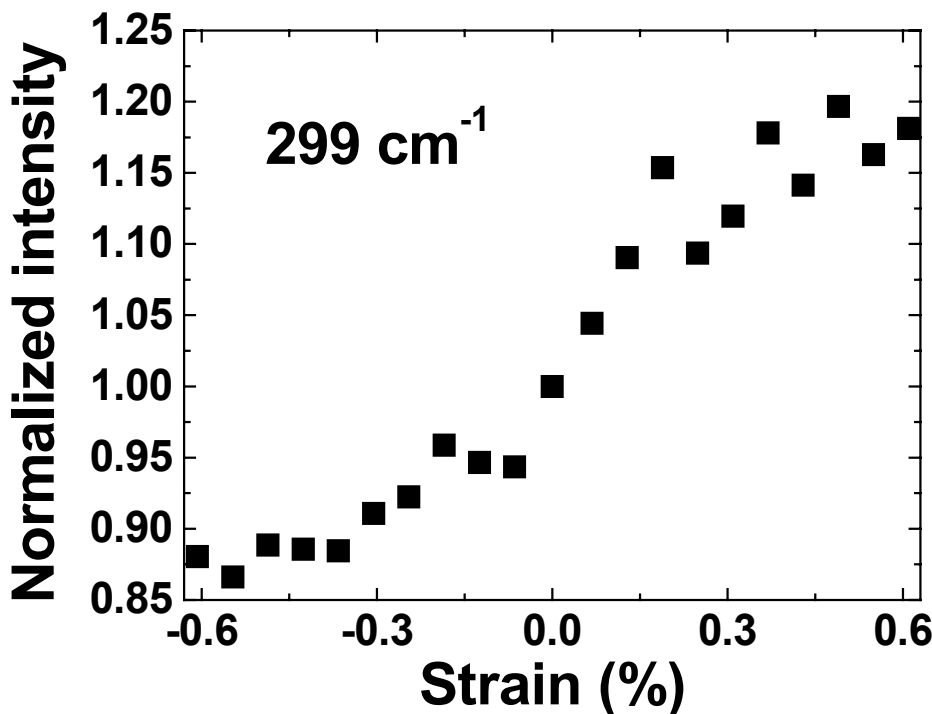


Figure 6.48: Normalized intensity (compared to the value at zero strain) for the RBM centered at 299 cm^{-1} . The laser wavelength was 632 nm.

The normalized RBM intensity variations, including the weaker 299 cm^{-1} RBM, for HiPco SWNTs in a PVA film are showed in Figures 6.44 to 6.48, within the strain range between -0.6% and 0.6%. The intensity of the RBM at 299 cm^{-1} increases in tension and decreases in compression. The magnitude of the intensity variations varies with the nanotube considered. For instance, the 200 cm^{-1} RBM intensity decreases by up to 10% in compression and increases by up to 30% in tension. Whereas for the 284 cm^{-1} peak, its intensity decreases by up to 20% in compression and increases by up to 15% in tension.

6.4.2 PVA/Elicarb Nanotube Films

6.4.2.1 830 nm Laser (1.49 eV) and 780 nm Laser (1.59 eV)

Data collected with the 830 nm laser are showed in Figures 6.49-6.59 and those collected with the 780 nm laser in Figures 6.60-6.68. The stress transfer to the nanotubes was monitored by measuring the shift of the stress-sensitive G band ($\lambda = 830\text{ nm}$) (Figure 6.49) and G' band ($\lambda = 780\text{ nm}$) (Figure 6.60) within a strain range between -0.6% and 0.6%. Linear fits in a low-strain range yield shift rates of $-6.4\text{ cm}^{-1}/\%$ for the G band and $-19.3\text{ cm}^{-1}/\%$ for the G' band.

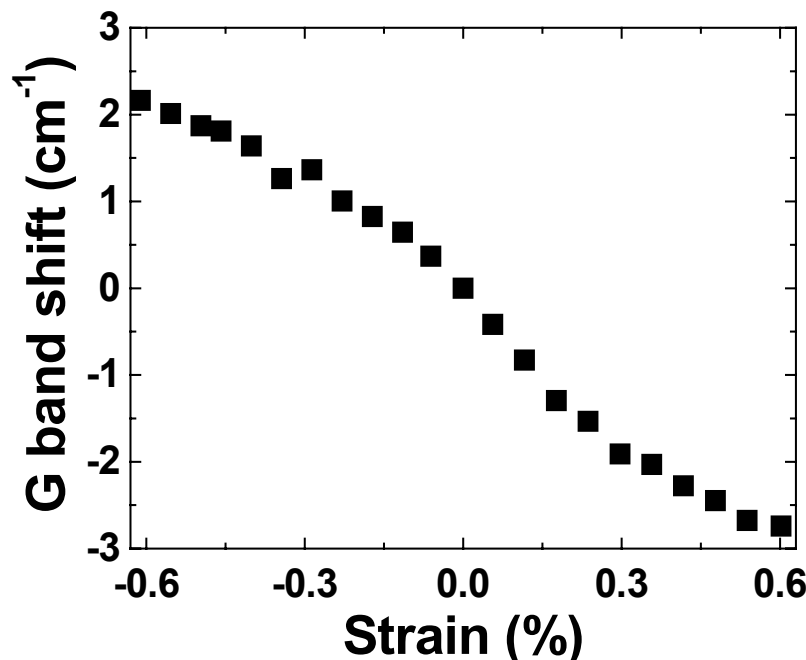


Figure 6.49: G band shift as a function of axial strain for a PVA film. The laser wavelength was 830 nm.

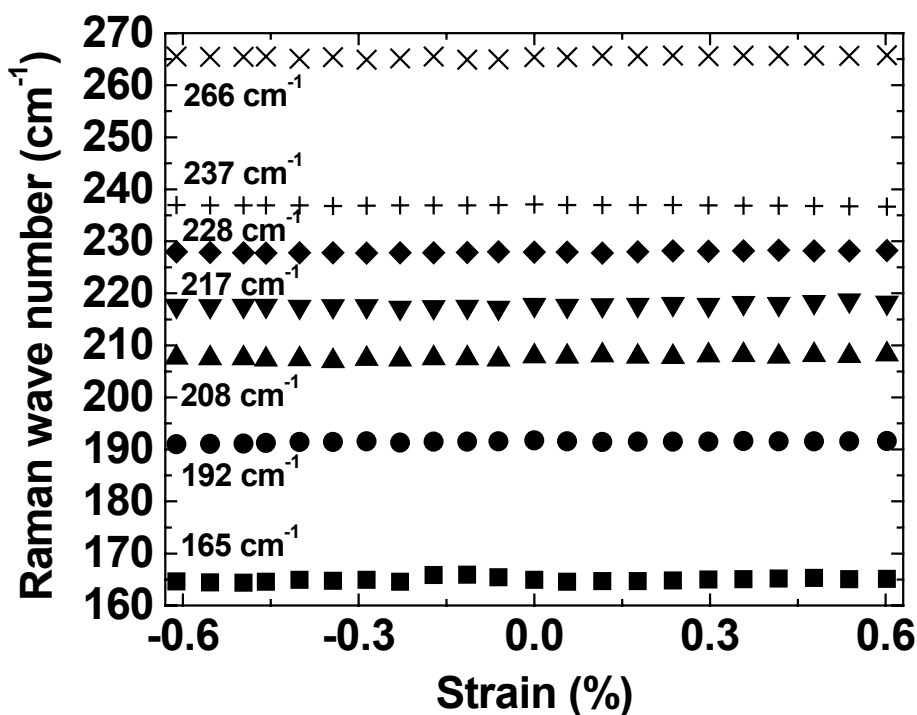


Figure 6.50: RBM position as a function of axial strain in four-point bending tests. The laser wavelength was 830 nm.

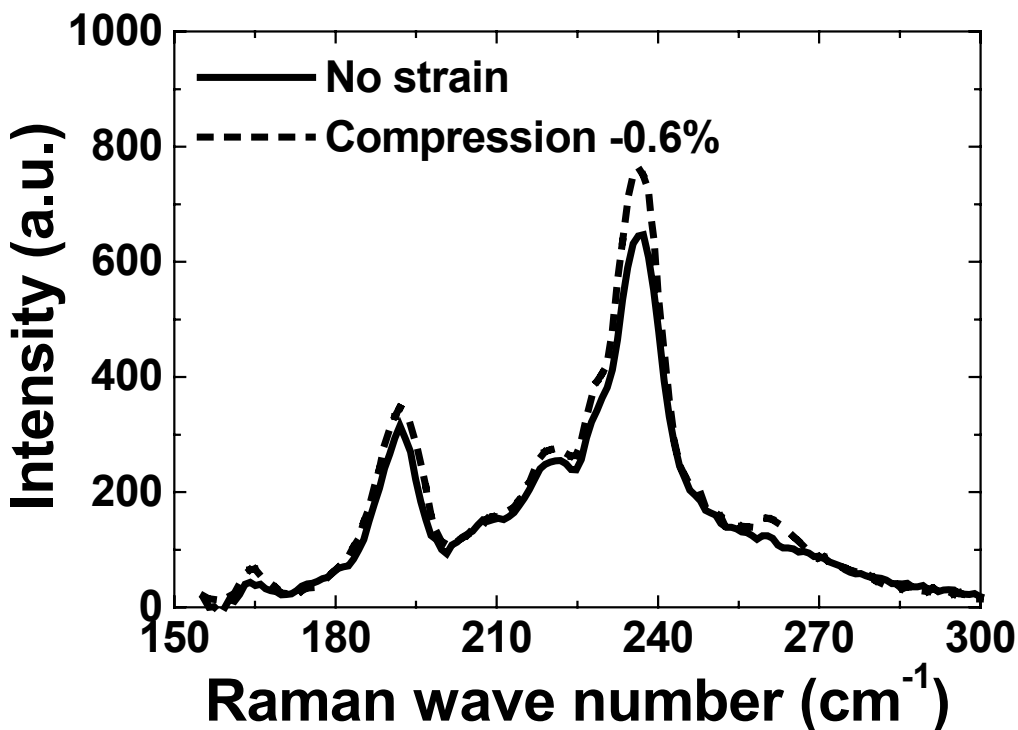


Figure 6.51: Comparison between the low-frequency Raman spectra of the Elicarb nanotubes in a PVA film at zero stress (solid line) and in compression (-0.6%) (dashed line). The laser wavelength was 830 nm.

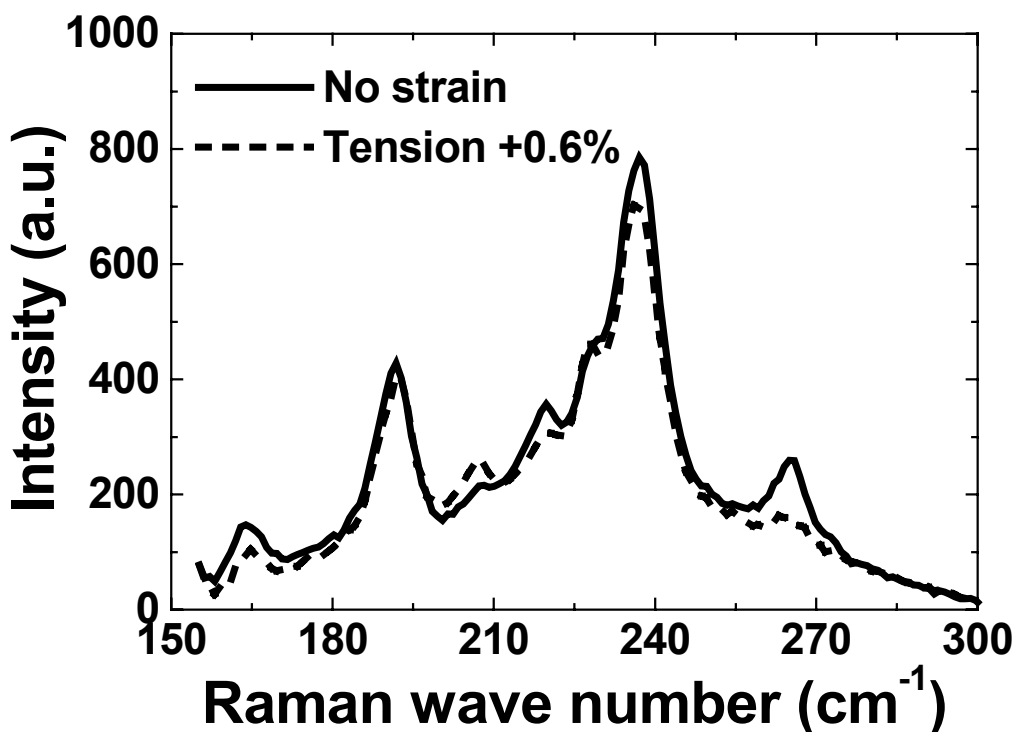


Figure 6.52: Comparison between the low-frequency Raman spectra of the Elicarb nanotubes in a PVA film at zero stress (solid line) and in tension (+0.6%) (dashed line). The laser wavelength was 830 nm.

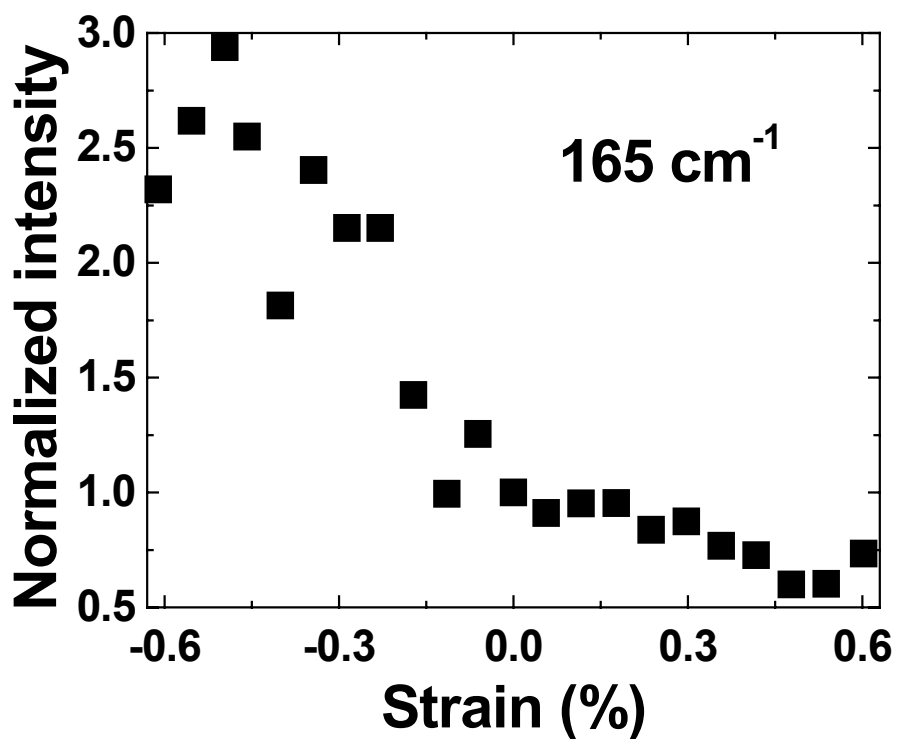


Figure 6.53: Normalized intensity (compared to the value at zero strain) for the RBM centered at 165 cm^{-1} . The laser wavelength was 830 nm.

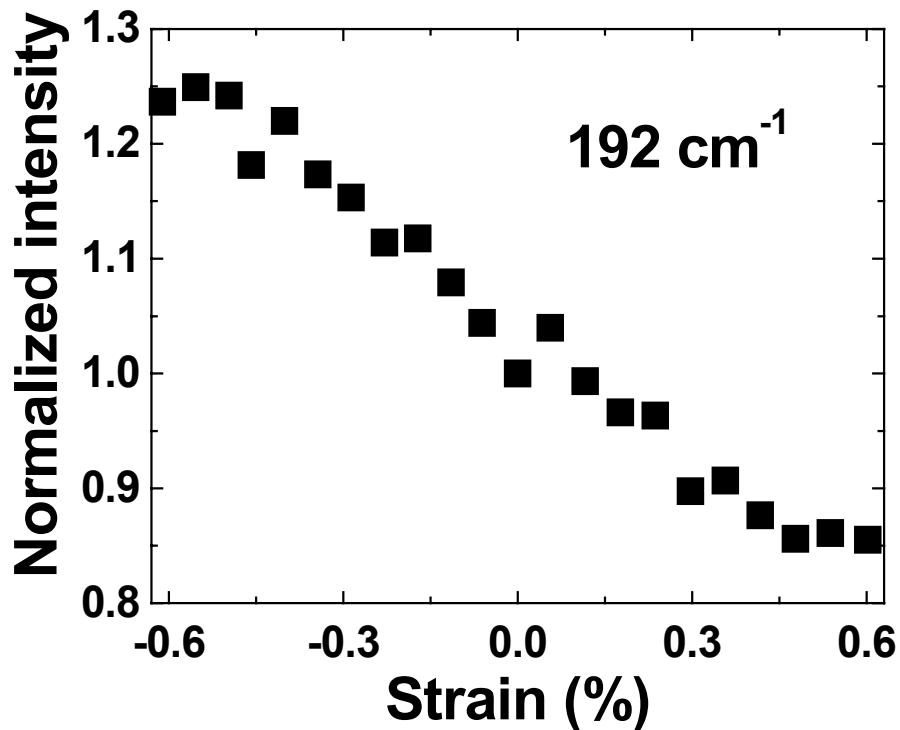


Figure 6.54: Normalized intensity (compared to the value at zero strain) for the RBM centered at 192 cm^{-1} . The laser wavelength was 830 nm.

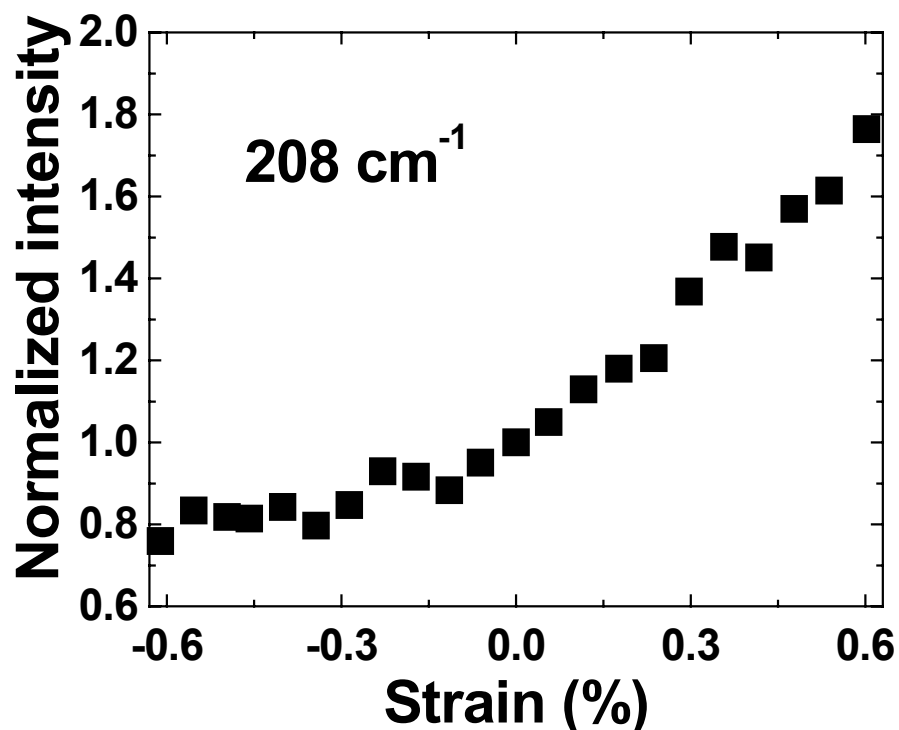


Figure 6.55: Normalized intensity (compared to the value at zero strain) for the RBM centered at 208 cm^{-1} . The laser wavelength was 830 nm.

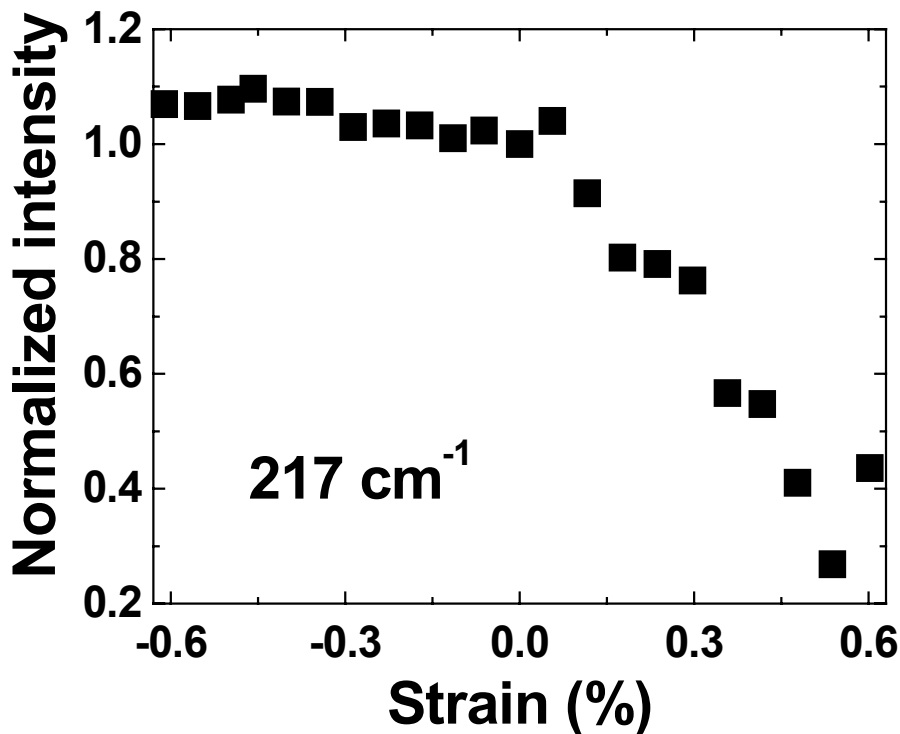


Figure 6.56: Normalized intensity (compared to the value at zero strain) for the RBM centered at 217 cm^{-1} . The laser wavelength was 830 nm.

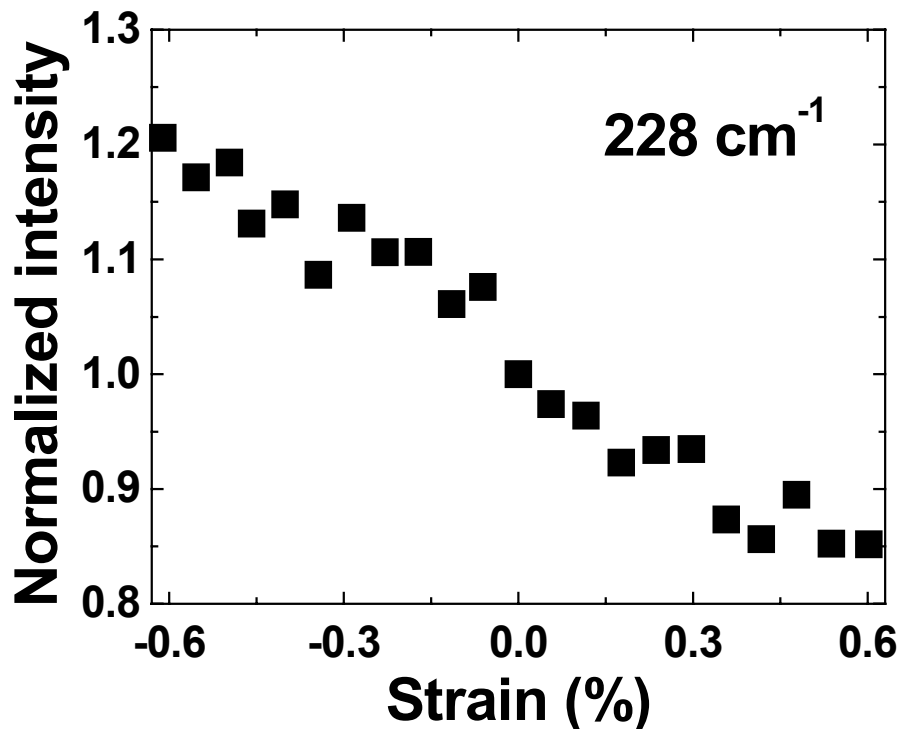


Figure 6.57: Normalized intensity (compared to the value at zero strain) for the RBM centered at 228 cm^{-1} . The laser wavelength was 830 nm.

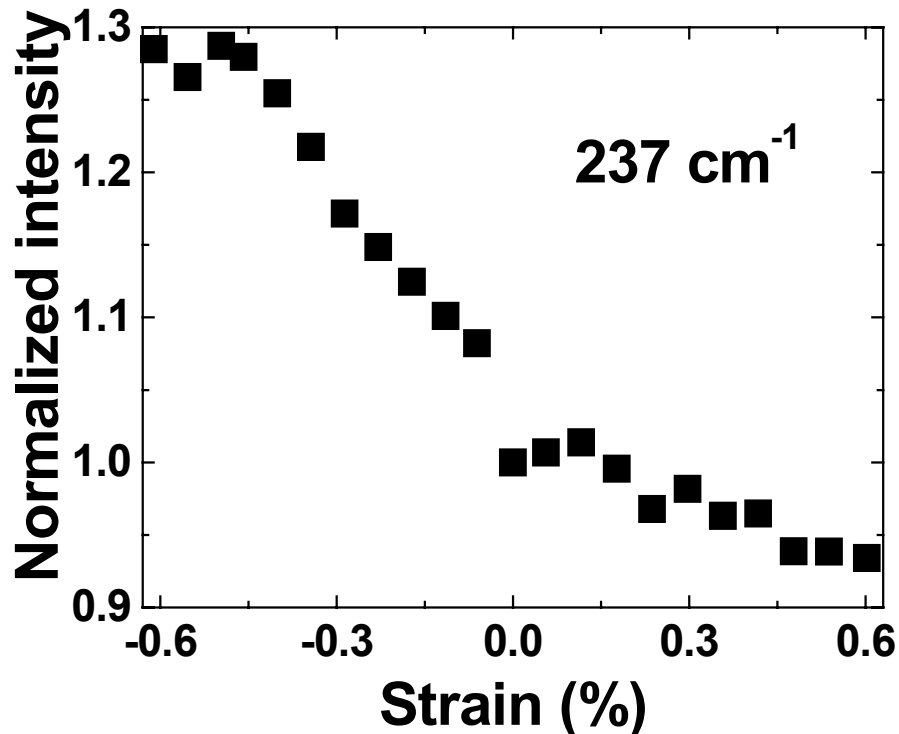


Figure 6.58: Normalized intensity (compared to the value at zero strain) for the RBM centered at 237 cm^{-1} . The laser wavelength was 830 nm.

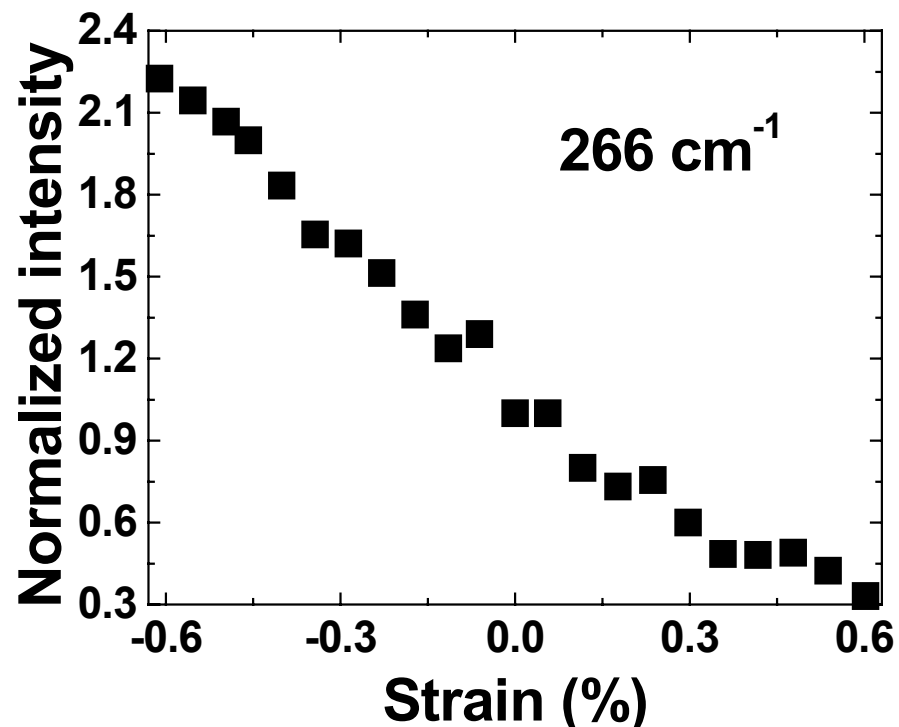


Figure 6.59: Normalized intensity (compared to the value at zero strain) for the RBM centered at 266 cm^{-1} . The laser wavelength was 830 nm.

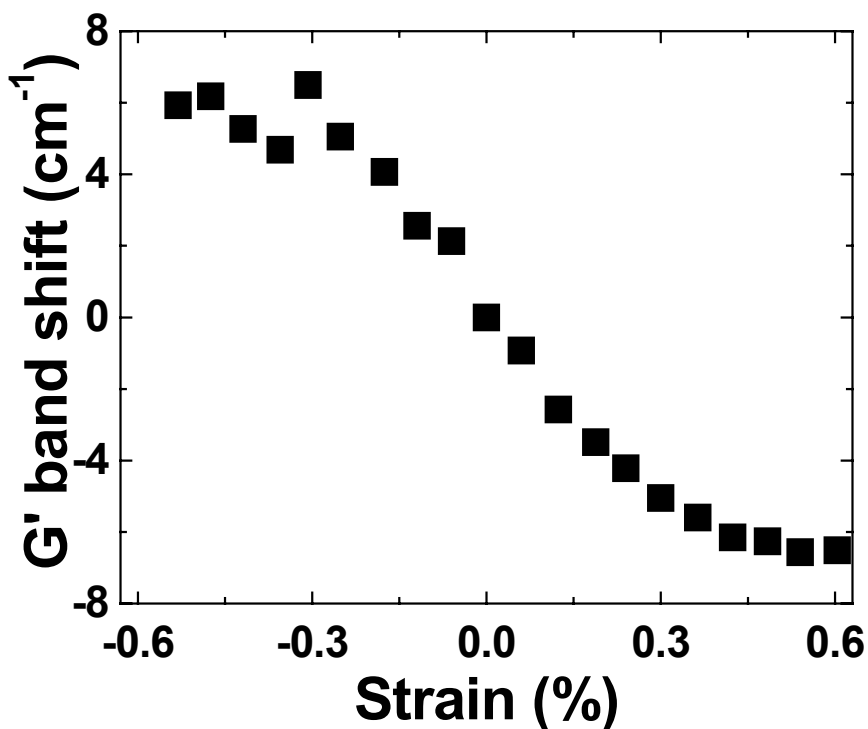


Figure 6.60: G' band shift as a function of axial strain for a PVA film. The laser wavelength was 780 nm.

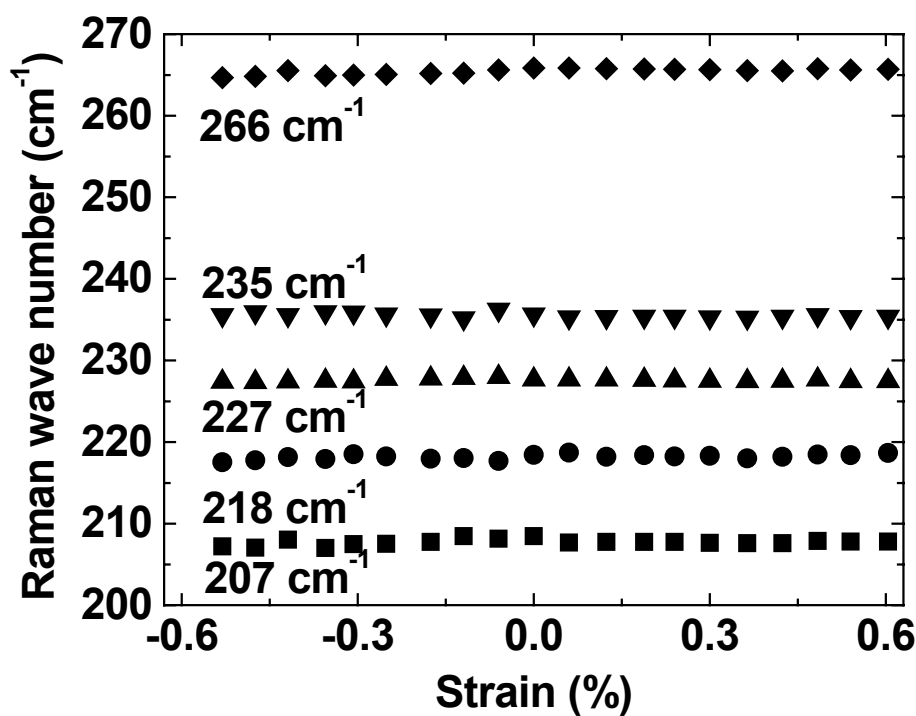


Figure 6.61: RBM position as a function of axial strain in four-point bending tests. The laser wavelength was 780 nm.

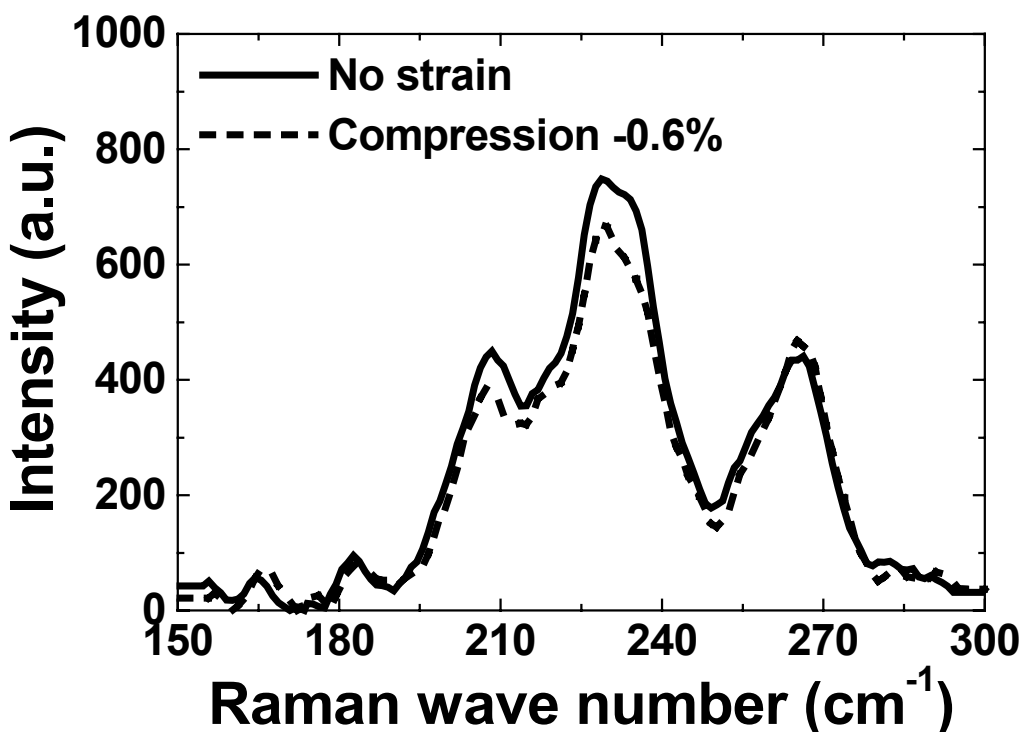


Figure 6.62: Comparison between the low-frequency Raman spectra of the Elicarb nanotubes in a PVA film at zero stress (solid line) and in compression (-0.6%) (dashed line). The laser wavelength was 780 nm.

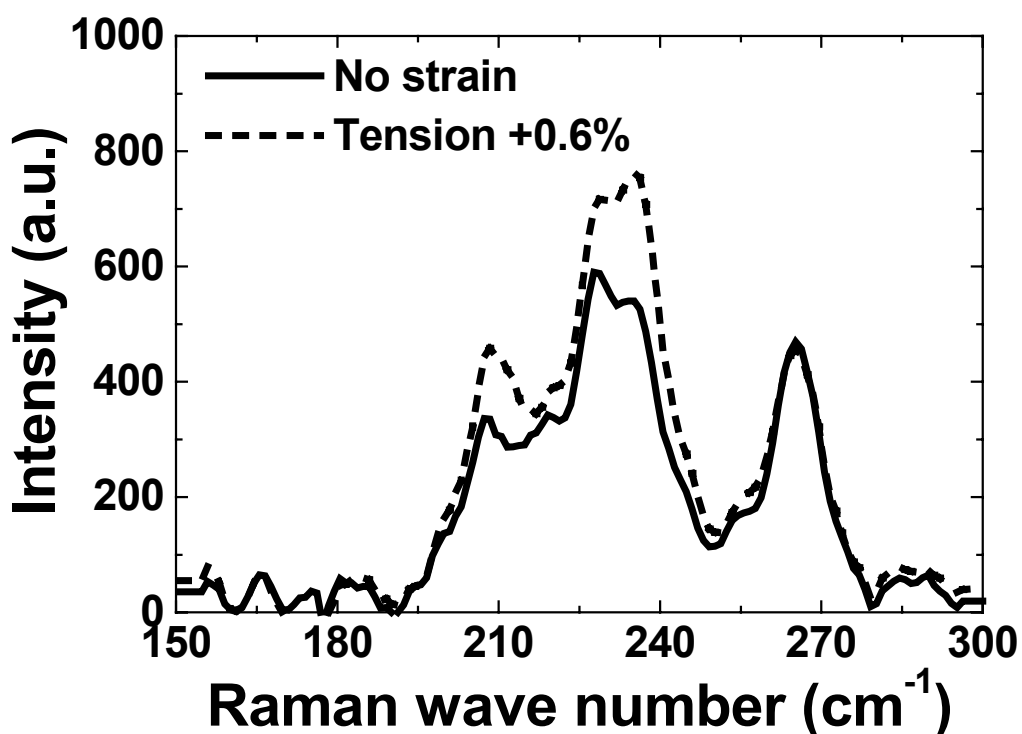


Figure 6.63: Comparison between the low-frequency Raman spectra of the Elicarb nanotubes in a PVA film at zero stress (solid line) and in tension (+0.6%) (dashed line). The laser wavelength was 780 nm.

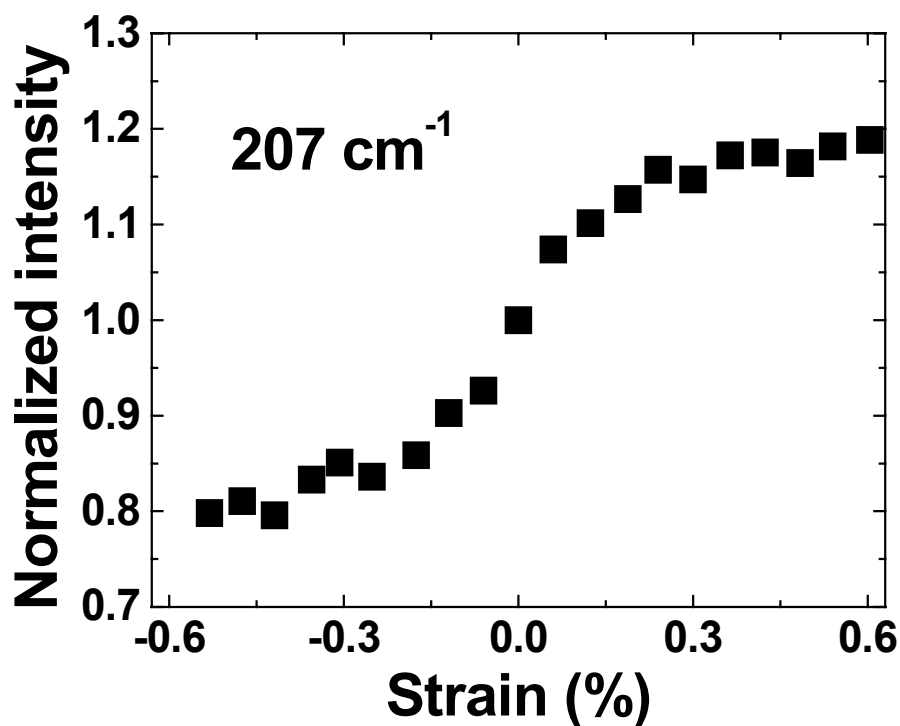


Figure 6.64: Normalized intensity (compared to the value at zero strain) for the RBM centered at 207 cm^{-1} . The laser wavelength was 780 nm.

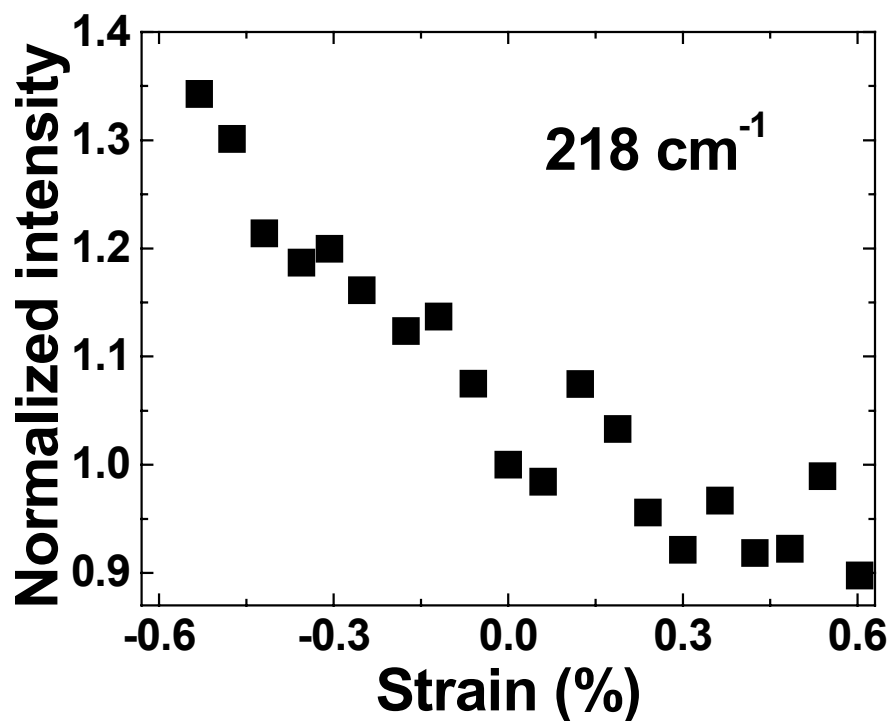


Figure 6.65: Normalized intensity (compared to the value at zero strain) for the RBM centered at 218 cm^{-1} . The laser wavelength was 780 nm.

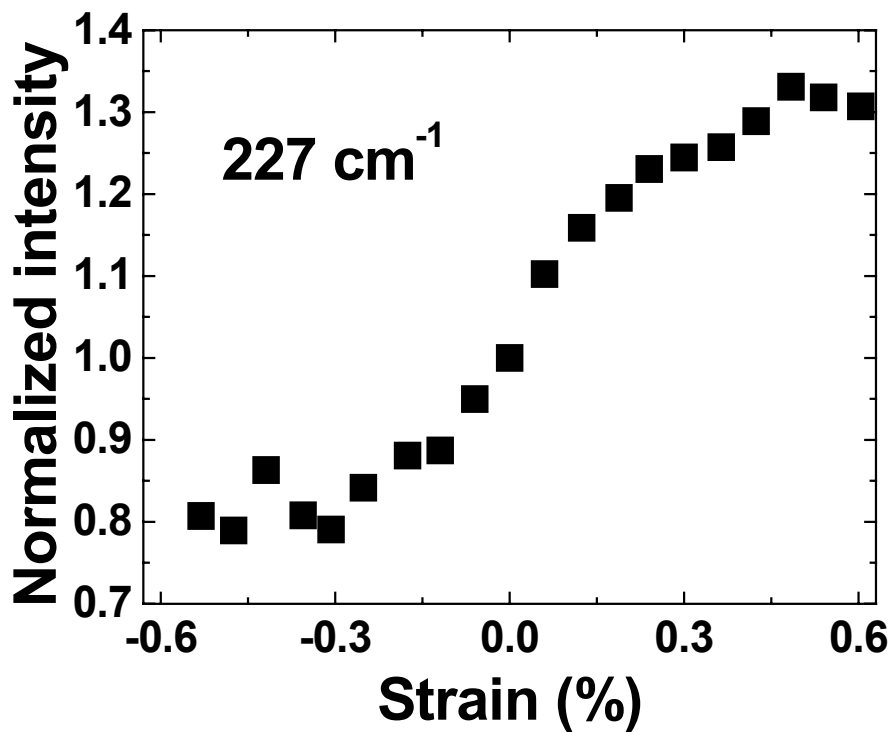


Figure 6.66: Normalized intensity (compared to the value at zero strain) for the RBM centered at 227 cm^{-1} . The laser wavelength was 780 nm.

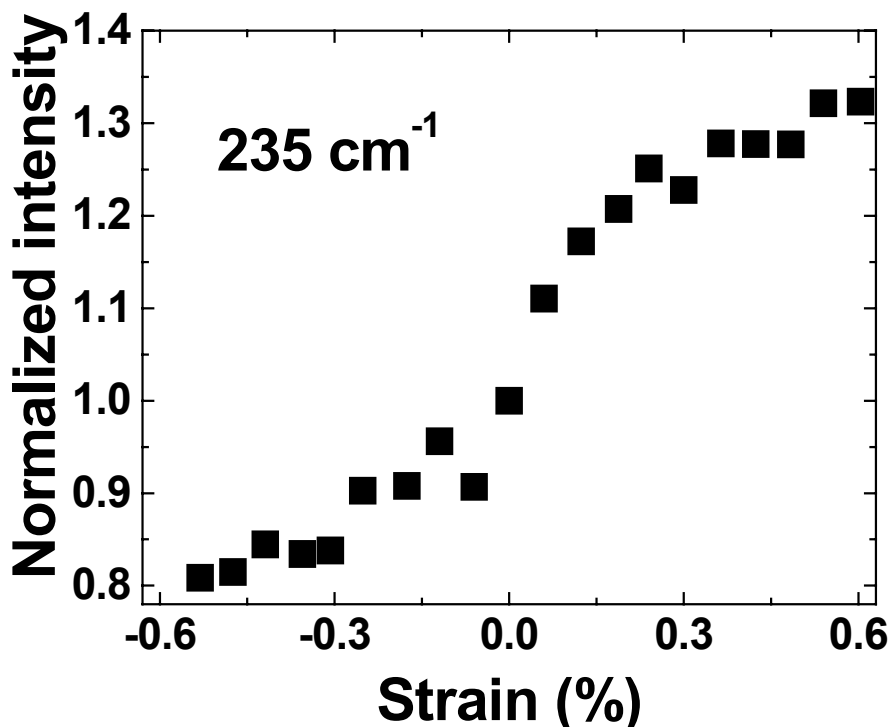


Figure 6.67: Normalized intensity (compared to the value at zero strain) for the RBM centered at 235 cm^{-1} . The laser wavelength was 780 nm.

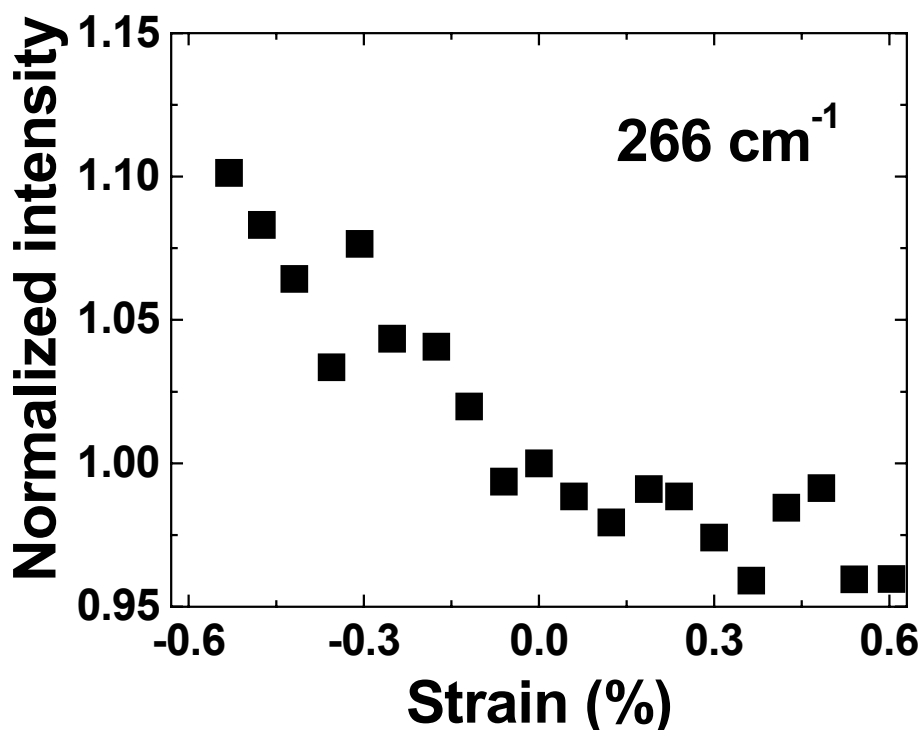


Figure 6.68: Normalized intensity (compared to the value at zero strain) for the RBM centered at 266 cm^{-1} . The laser wavelength was 780 nm.

The RBM positions are unchanged within resolution (Figures 6.50 and 6.61). Figures 6.51, 6.52, 6.62 and 6.63 show that the RBMs located at 207 , 227 , 235 cm^{-1} ($\lambda = 780\text{ nm}$) and 208 cm^{-1} ($\lambda = 830\text{ nm}$) increase in intensity in tension and decrease in compression, while the remaining RBMs show the opposite behavior.

The difference in the magnitude of the RBM intensity variation is also significant (Figures 6.53-6.59 and 6.64-6.68). The intensities of several RBMs vary linearly with a moderate magnitude (10-40% in tension or compression at 0.6% strain). Others vary considerably, such as the 165 cm^{-1} RBM in compression (Figures 6.53, +200% at -0.6% strain), and the 217 cm^{-1} RBM which nearly disappears at 0.6% in tension (Figure 6.56).

Several RBMs observed with the 780 nm laser are located very close to the RBMs observed with the 830 nm laser, but the magnitudes and trends of their intensity variations differ. The $207/208$ (Figures 6.55 and 6.64), $217/218$ (Figures 6.56 and 6.65), and $266/266\text{ cm}^{-1}$ (Figures 6.59 and 6.68) pairs of RBMs behave the same way in tension and compression but with different

magnitudes. As to the pairs of RBMs at 227/228 (Figures 6.57 and 6.66) and 235/237 cm^{-1} (Figure 6.58 and 6.67), the RBMs show opposite behaviors. Any difference in their positions is close to the resolution of the spectrometer ($\pm 1 \text{ cm}^{-1}$) so it is impossible to assign these pairs of RBMs to the same nanotube, based only on their position and the energy of their electronic transitions.

6.4.2.2 632 nm Laser ($E_{\text{laser}} = 1.96 \text{ eV}$)

The G' band shift and the RBM positions in the PVA film as a function of axial strain are showed in Figures 6.69 and 6.70. The G' band shift rate in the low strain range was $-18.2 \text{ cm}^{-1}/\%$ and the RBM positions were found unchanged. The G and G' band shift rates are higher for the Elicarb nanotube composites than for the HiPco nanotube composites. The intensities of the four RBMs, centered at 200 cm^{-1} , 221 cm^{-1} , 257 cm^{-1} and 284 cm^{-1} , from the sample under strain are compared to the same RBMs from the unstrained sample in Figures 6.71 and 6.72.

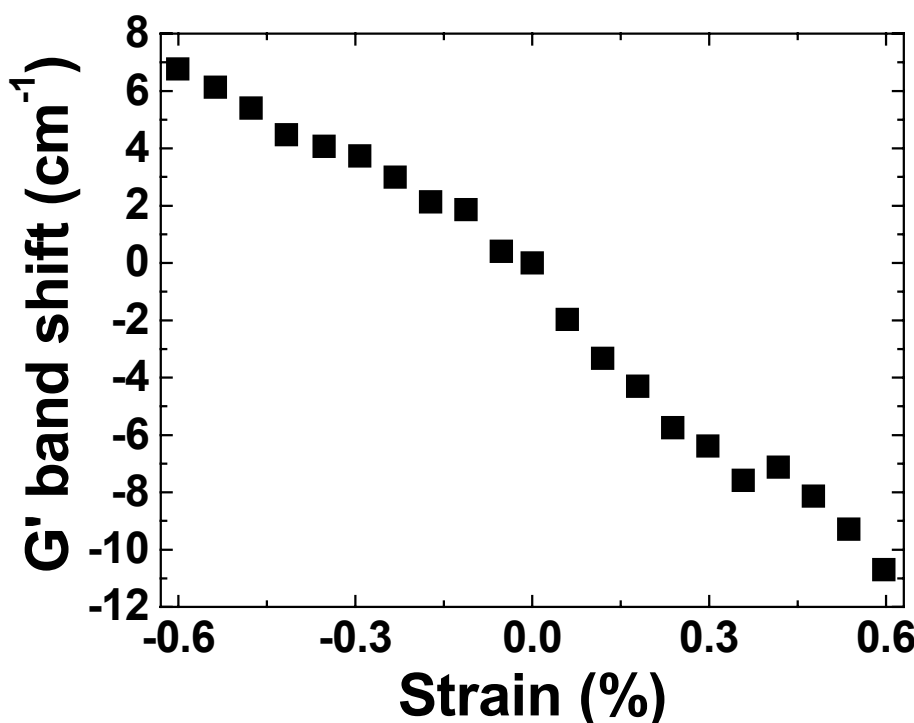


Figure 6.69: G' band shift as a function of axial strain for a PVA film. The laser wavelength was 632 nm.

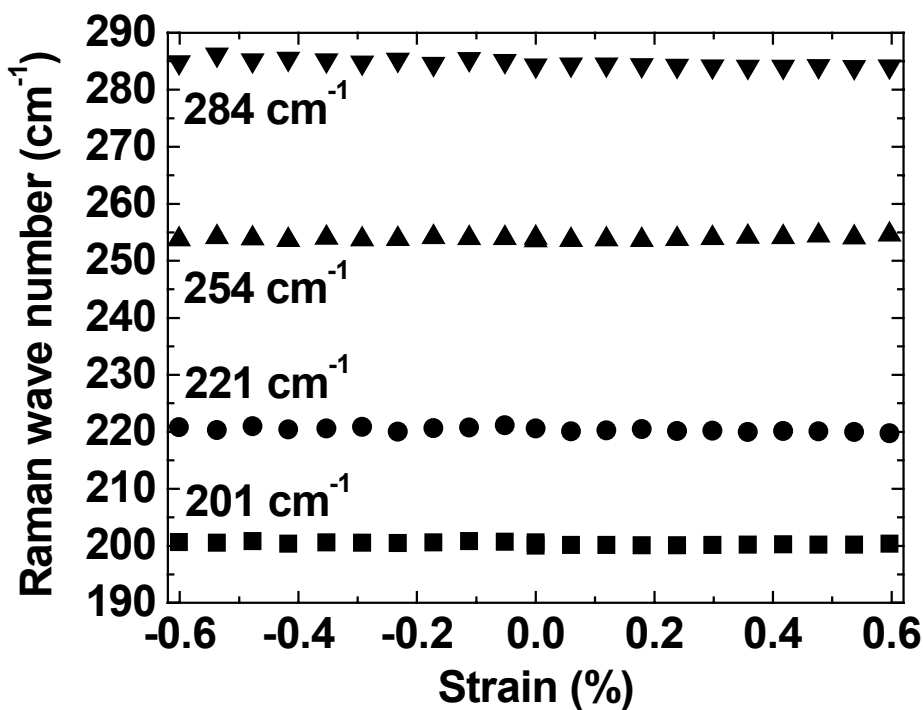


Figure 6.70: RBM position as a function of axial strain in four-point bending tests. The laser wavelength was 632 nm.

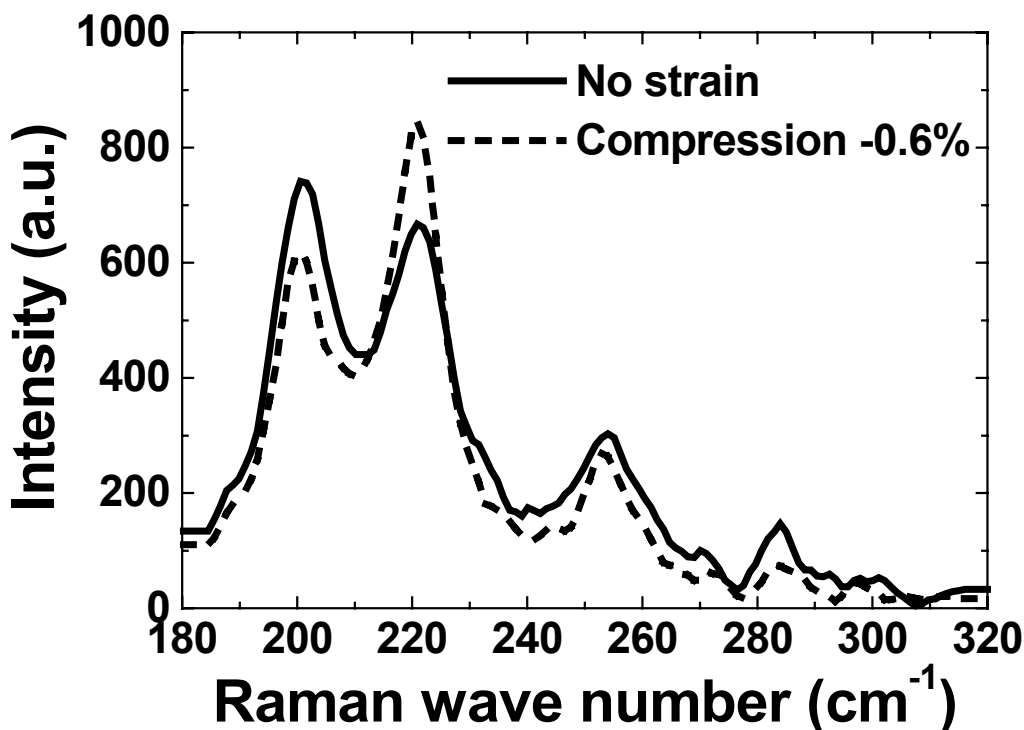


Figure 6.71: Comparison between the low-frequency Raman spectra of the Elicarb nanotubes in a PVA film at zero stress (solid line) and in compression (-0.6%) (dashed line). The laser wavelength was 632 nm.

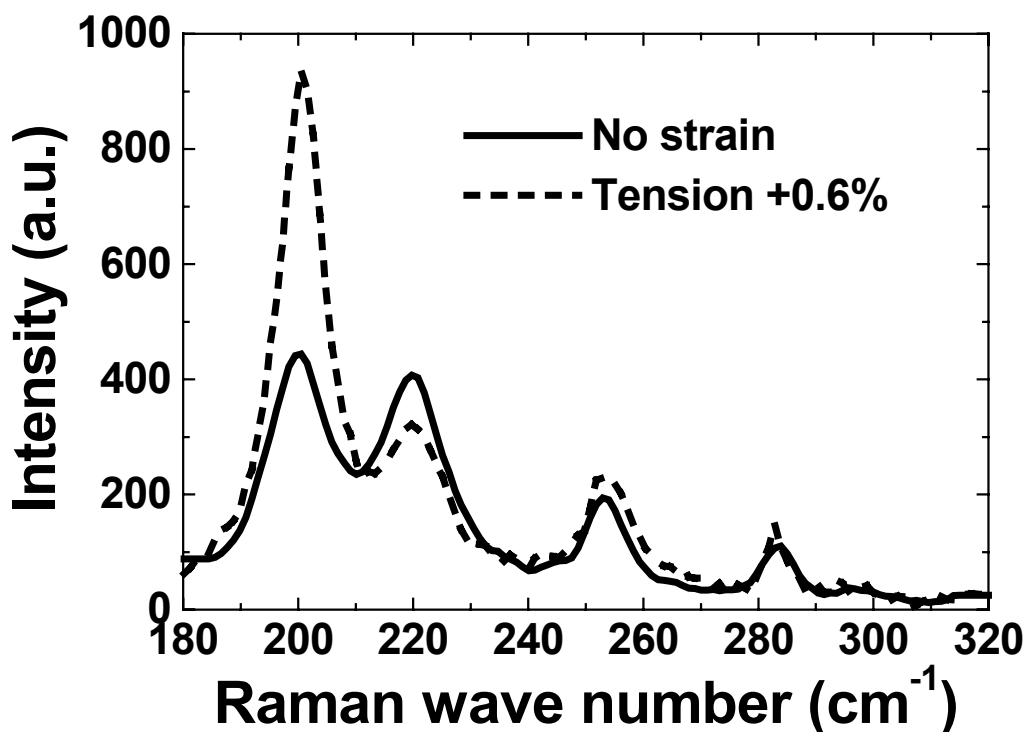


Figure 6.72: Comparison between the low-frequency Raman spectra of the Elicarb nanotubes in a PVA film at zero stress (solid line) and in tension (+0.6%) (dashed line). The laser wavelength was 632 nm.

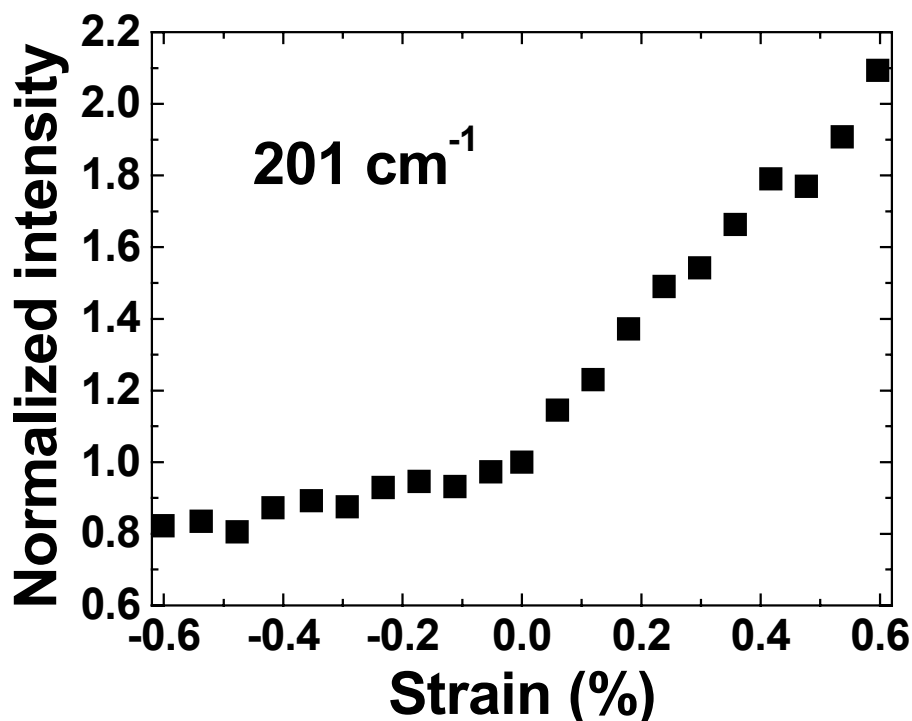


Figure 6.73: Normalized intensity (compared to the value at zero strain) for the RBM centered at 201 cm^{-1} . The laser wavelength was 632 nm.

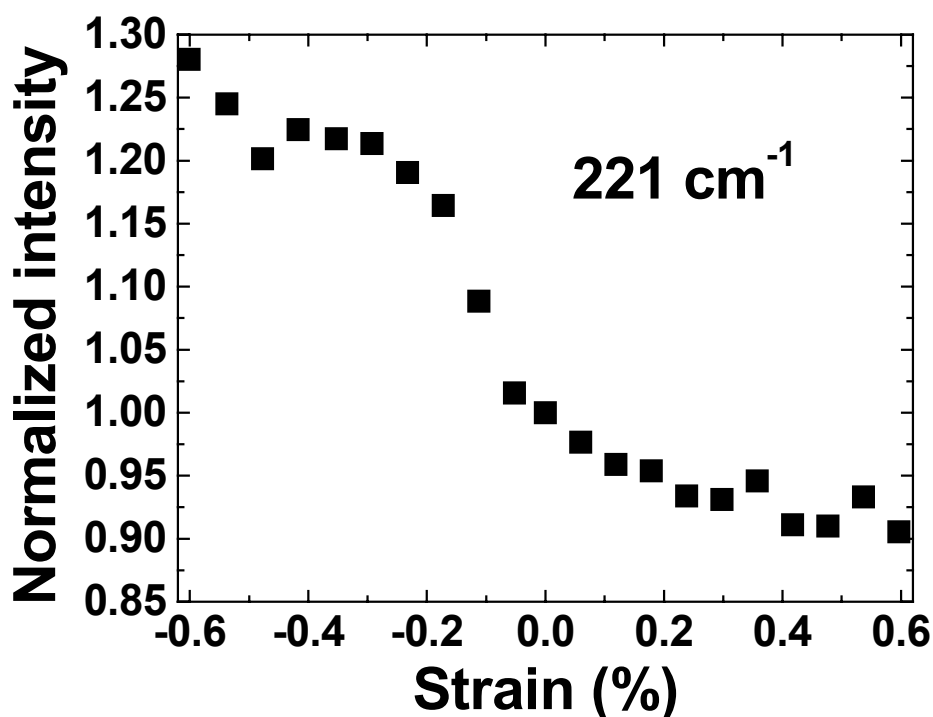


Figure 6.74: Normalized intensity (compared to the value at zero strain) for the RBM centered at 221 cm^{-1} . The laser wavelength was 632 nm.

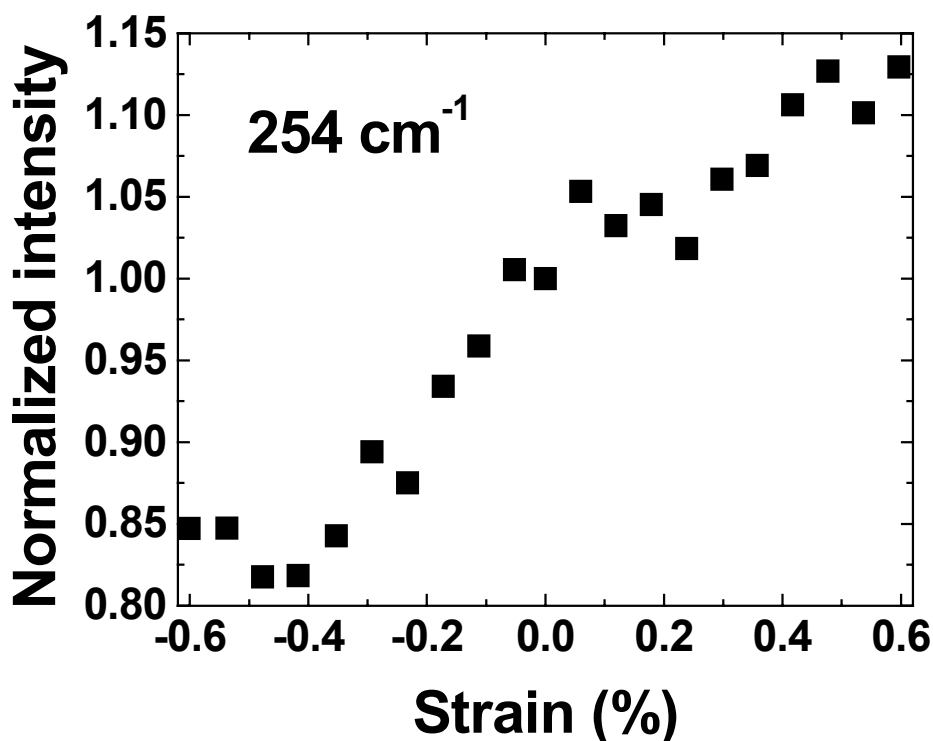


Figure 6.75: Normalized intensity (compared to the value at zero strain) for the RBM centered at 254 cm^{-1} . The laser wavelength was 632 nm.

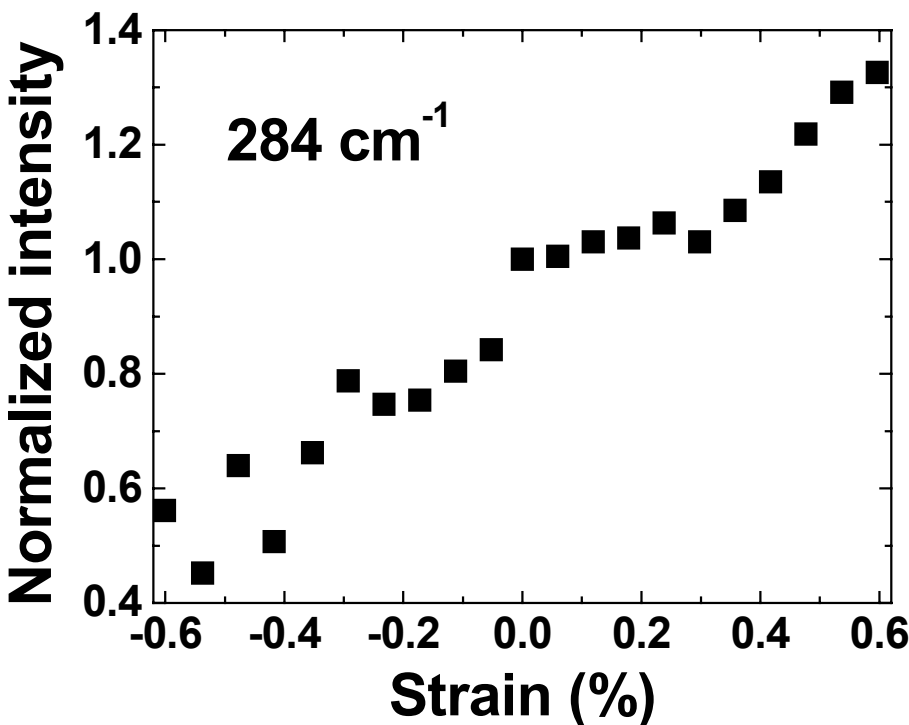


Figure 6.76: Normalized intensity (compared to the value at zero strain) for the RBM centered at 284 cm^{-1} . The laser wavelength was 632 nm.

The intensities of the 200 cm^{-1} , 257 cm^{-1} and 284 cm^{-1} RBMs increase in tension, while the intensity of the 221 cm^{-1} RBM decreases. During the compression tests, the intensities of the 200 cm^{-1} , 257 cm^{-1} and 284 cm^{-1} RBMs decrease, while the intensity of the 221 cm^{-1} RBM increases. Figures 6.73-6.76 show the intensity variations of all four RBMs within a strain range between -0.6% and 0.6%. The four RBMs are close in position to those in the HiPco nanotube composite and they behave the same way.

6.4.3 Discussion

The changes in intensity caused by deformation exceed the range of experimental error. The two main sources of error are the position of the laser spot and the fitting procedure. Due to the large width of some peaks, a significant error from the Lorentzian fit was expected, but in this study it never exceeded 5%. These large variations are not due to an inhomogeneous SWNT density in the sample, since all the spectra were collected in the same area on the sample. The results presented in this study came from a selected

homogeneous area. Before the experiments, several Raman spectra were collected in the vicinity of the selected area to check the local homogeneity in nanotube density. Small variations of less than 5% were seen but the RBM profile and the relative intensities remained approximately identical. The focused laser beam probes only the first few μm near the top surface of the sample, so the interaction volume remains approximately the same. The same intensity variation trends were observed in other areas (homogeneous and inhomogeneous nanotube density) and on other samples.

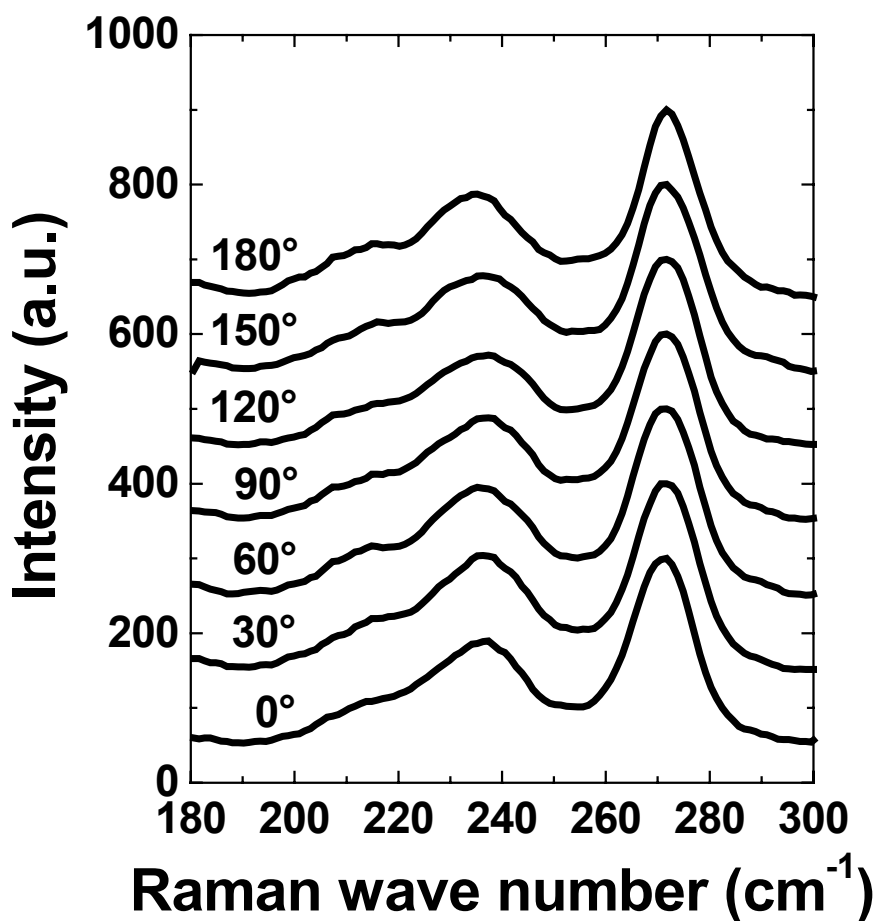


Figure 6.77: Low-frequency Raman spectra collected with different sample orientation with respect to the direction of incident laser polarization from an epoxy/Hipco SWNT composite sample using a laser of wavelength 780 nm. The spectra are offset vertically for clarity.

Any orientation effects from the four-point bending tests can be ruled out. The nanotube bundles were dispersed isotropically in the epoxy/SWNT

composite and in the PVA film. Low-frequency Raman spectra were collected at the same location, at 0% strain, with different orientation of the sample, with respect to the incident laser polarization (Figure 6.77). The RBM positions and relative intensities are identical in all directions. All the spectra were collected around the center of the sample, where the sample surface was perpendicular to the laser beam to within $\pm 5^\circ$.

Low-frequency Raman spectra were also collected at five different areas on a sample without strain (Figure 6.78), with strain when the incident laser polarization is parallel to the direction along which the strain was applied (Figure 6.79), or perpendicular (Figure 6.80).

Polarized Raman spectroscopic studies on aligned nanotubes [77,92-95] or on individual nanotubes [96,97] have showed that the intensity of the Raman modes depends on the angle between the incident laser beam polarization and the nanotube axis. The intensity of some vibrational modes, such as the RBMs, reaches its maximum when the incident laser polarization is parallel to the nanotube axis.

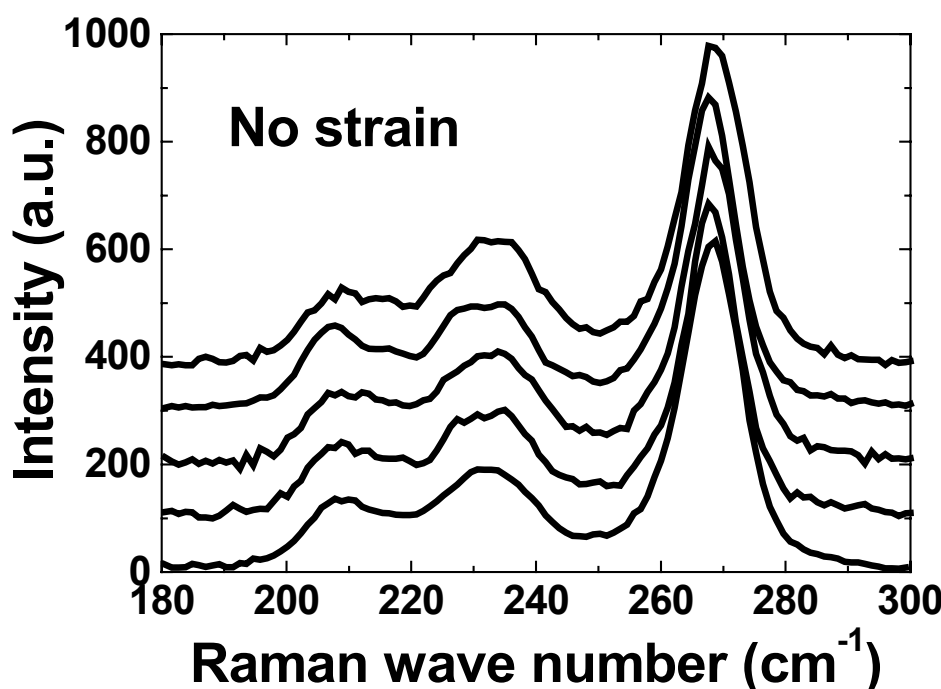


Figure 6.78: Low-frequency Raman spectra collected at 5 different areas on an epoxy/HiPco SWNT composite sample using a laser of wavelength 780 nm. The spectra are offset vertically for clarity.

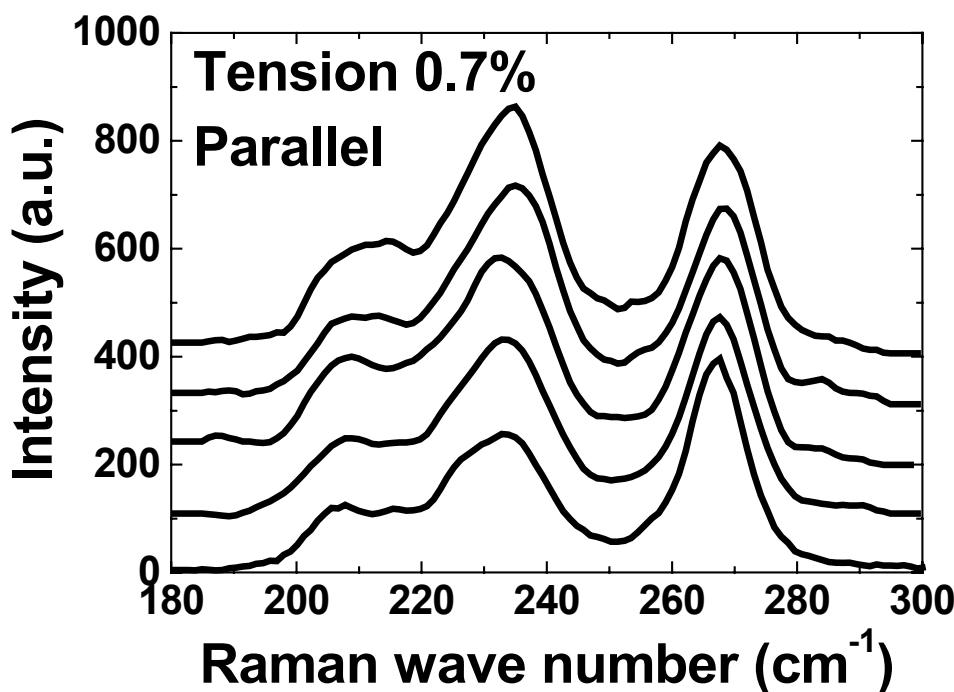


Figure 6.79: Low-frequency Raman spectra collected at 5 different areas on an epoxy/Hipco SWNT composite sample in tension (0.7%). The incident laser of wavelength 780 nm was polarized along the strain axis. The spectra are offset vertically for clarity.

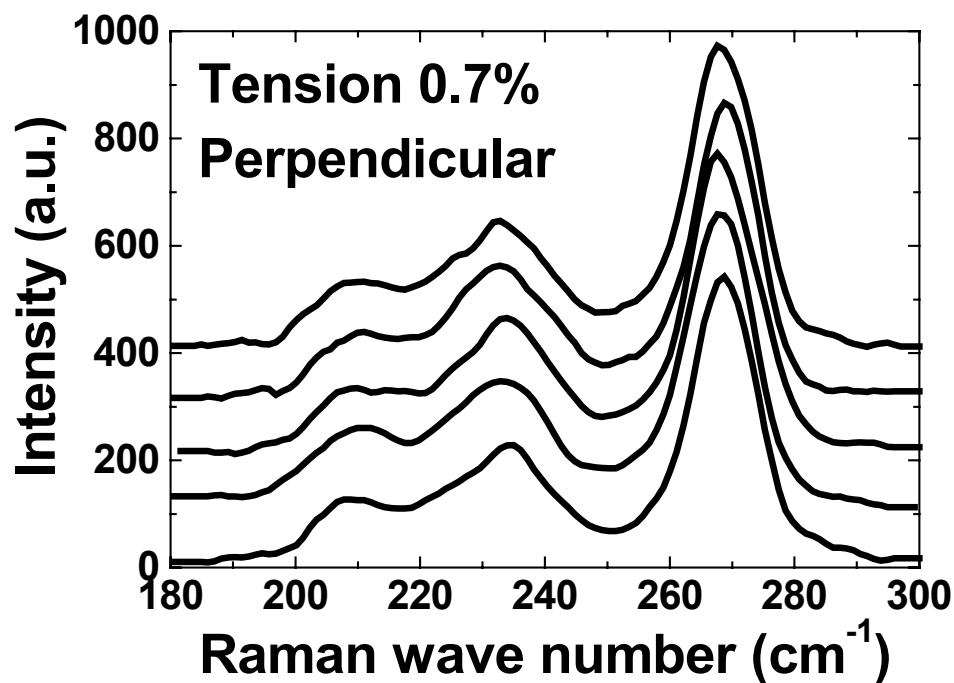


Figure 6.80: Low-frequency Raman spectra collected at 5 different areas on an epoxy/Hipco SWNT composite sample in tension (0.7%). The incident laser of wavelength 780 nm was polarized perpendicular to the strain axis. The spectra are offset vertically for clarity.

In this study, the laser polarization was always parallel to the strain axis, so the Raman signal came mainly from the nanotubes or the portions of nanotube that are parallel to the strain axis. In this case, intensity variations were observed in tension (Figures 6.78 and 6.79). When the laser polarization was perpendicular to the direction along which the strain was applied, the RBM profile under tensile strain are significantly different (see Figures 6.79 and 6.80). This was thought to be due to the nanotubes or the portions of nanotube perpendicular to the strain axis not being stretched axially. The nanotubes perpendicular to the strain axis are subject to Poisson contractions. Considering a Poisson's ratio of about 0.3 [204], the contraction is estimated to be about 0.2% in this direction. The spectra in Figure 6.80 are consistent with those in Figure 6.33, when the epoxy/Hipco SWNT sample was in -0.3% compression. It shows that the intensity variations are due to strain, and not to any artifact stemming from the experimental conditions.

6.5 Effect of Deformation on the RBM Intensity and Structure Determination

6.5.1 Resonance Theory

The origin of these observed intensity variations is attributed to the effect of deformation upon resonance. Deformation and strain cause the modification of the electronic band structure of SWNTs. The E_{ii} values shift closer to or further away from E_{laser} , affecting the resonance condition. The RBM intensity increases when the difference $|E_{ii} - E_{laser}|$ decreases and decreases in the other case.

Liu *et al.* compared the relative RBM intensities in a Hipco SWNT dispersion and in electrospun poly(methyl methacrylate)/SWNT and polyacrylonitrile/SWNT composite nanofibers. Relative RBM intensity variations were observed using a near-infrared laser of wavelength 785 nm and were accompanied by an upshift of the G and G' bands in the electrospun fibers. When the fibers were heated to 150°C to relax any residual strains, the relative RBM intensities became similar to those in the original Hipco SWNT dispersion.

These results were attributed to higher compressive strains in the composite fibers, resulting in the modification of the resonance conditions [205].

Table 6.1: List of RBMs observed in epoxy/SWNT composite or PVA/SWNT film with three different lasers and their intensity variation behavior in four-point bending tests.

Sample	Laser energy	Exp. RBM position	Type	Intensity variations	
				Compression	Tension
HiPco	1.49 eV	207	Semiconducting	Down	Up
		217	Semiconducting	Up	Down
		227	Semiconducting	Up	Down
		237	Semiconducting	Up	Down
		266	Semiconducting	Up	Down
	1.59 eV	210	Semiconducting	Down	Up
		232	Semiconducting	Down	Up
		238	Semiconducting	Down	Up
		268	Semiconducting	Up	Down
		272	Semiconducting	Up	Down
Elicarb	1.96 eV	200	Metallic	Down	Up
		221	Metallic	Up	Down
		257	Semiconducting	Down	Up
		284	Semiconducting	Down	Up
		299	Semiconducting	Down	Up
	1.49 eV	165	Metallic	Up	Down
		192	Semiconducting	Up	Down
		208	Semiconducting	Down	Up
		217	Semiconducting	Up	Down
		228	Semiconducting	Up	Down
Elicarb	1.59 eV	237	Semiconducting	Up	Down
		266	Semiconducting	Up	Down
		207	Semiconducting	Down	Up
		218	Semiconducting	Up	Down
		227	Semiconducting	Down	Up
	1.96 eV	235	Semiconducting	Down	Up
		266	Semiconducting	Up	Down
		201	Metallic	Down	Up
		221	Metallic	Up	Down
		254	Semiconducting	Down	Up
		284	Semiconducting	Down	Up

In the following section, tight-binding calculations are presented and showed to predict the trend of the RBM intensity variations. The E_{ii} values obtained by the two tight-binding models will not be corrected to take into

account the effect of the nanotube environment, since the structure-dependence of the possible shift induced by the environment is unknown. These RBM intensity variations under strain are used as an additional criterion for the assignment of SWNT structure. Only the nanotubes with their axis parallel to the strain axis and the laser polarization are considered. The nanotubes in interaction are supposed to remain straight and under uniaxial strain along their axis. Any strain along the circumferential direction was neglected, since the Poisson's ratio is predicted to be small, around 0.3 [204]. Thus the diameter of the nanotubes in this model remains constant: only the component of the bond vectors along the nanotube axis is modified with strain.

Here the study is focused on the strain-induced RBM intensity variations and not on the absolute intensity values, since the latter depend on the SWNT diameter distribution in the raw SWNT material. Table 6.1 is a list of RBMs observed in epoxy/SWNT composites or PVA/SWNT films with three different lasers and their intensity variation behavior in four-point bending tests.

6.5.2 Efficiency of the Load Transfer

This study was limited to low strains (less than 0.7%) in tension and compression, where the G or G' bands still shift linearly with strain. Phenomena such as debonding in tension and buckling in compression are neglected. Considering that the strain values were lower than 1%, it would be reasonable to assume that the axial strain applied on the composite sample (given by the strain gauge) is the same as the axial strain applied on the nanotubes in the composite, as is found for macroscopic fiber-reinforced composites [206,207].

One way to evaluate the efficiency of the load transfer is to compare the G' band shift rate in the low strain range. The G' band shift rate of $-11.8 \text{ cm}^{-1}/\%$ observed on the HiPco nanotubes in an epoxy matrix ($\lambda = 632 \text{ nm}$) is higher than the rate of $-6.0 \text{ cm}^{-1}/\%$ reported in Reference 128 from HiPco nanotubes using the same laser wavelength. However it is lower than the rates of $-15.5 \text{ cm}^{-1}/\%$ and $-18.0 \text{ cm}^{-1}/\%$ ($\lambda = 632 \text{ nm}$) reported for nanotubes embedded in a polyurethane [208] and a poly(urethane acrylate) matrix [209], respectively. An imperfect load transfer could be caused by the presence of nanotube

bundles and aggregates. In the following sections, the cases where the load transfer is perfect or not will be both considered.

6.5.3 Structure Assignments Based on the TB1 Model

The E_{ii} values were calculated for metallic nanotubes with theoretical RBM positions between 160 and 230 cm⁻¹, using the TB1 tight-binding model (Table 6.2). For each of the three strain values, two E^M_{11} values are provided because of the trigonal warping effect [168], except for armchair nanotubes. The E_{ii} values were computed with the adjustable hopping parameter set at 2.92 eV. Table 6.3 is a list of the semiconducting nanotubes with theoretical Raman RBM positions between 190 and 300 cm⁻¹. For a (n,m) nanotube, it gives the E^S_{22} values for three different strain values: -0.5%, 0.0% and 0.5%.

Table 6.2: List of the metallic (n,m) nanotubes with a calculated Raman RBM position between 160 and 230 cm⁻¹. The calculated Raman RBM position is given by Equation 6.3 (Calculation 1) or Equation 6.4 (Calculation 2).

n	m	RBM position (cm ⁻¹)		d (nm)	E^M_{11} (eV) at different strain values			
		Calc. 1	Calc. 2		-0.5%	0.0%	0.5%	
9	6	228	239	1.04	2.30	2.43	2.31	2.42
13	1	221	231	1.07	2.14	2.53	2.17	2.48
12	3	217	227	1.09	2.12	2.44	2.16	2.40
8	8	216	225	1.10	2.24	2.24	2.24	2.24
11	5	211	220	1.13	2.10	2.31	2.12	2.28
10	7	203	211	1.17	2.05	2.15	2.07	2.14
15	0	200	208	1.19	1.94	2.28	1.98	2.23
14	2	199	207	1.20	1.93	2.25	1.97	2.21
13	4	195	203	1.22	1.91	2.17	1.94	2.13
9	9	193	200	1.24	2.00	2.00	2.00	2.00
12	6	190	197	1.26	1.89	2.05	1.91	2.03
11	8	183	189	1.31	1.85	1.93	1.86	1.92
16	1	183	189	1.31	1.77	2.06	1.81	2.01
15	3	181	187	1.33	1.76	2.02	1.79	1.98
14	5	178	183	1.35	1.74	1.94	1.77	1.91
10	10	175	180	1.38	1.80	1.80	1.80	1.80
13	7	173	178	1.40	1.72	1.85	1.74	1.83
18	0	169	174	1.43	1.63	1.90	1.67	1.85
17	2	168	173	1.44	1.63	1.88	1.66	1.83
12	9	167	171	1.45	1.69	1.75	1.70	1.74
16	4	166	170	1.46	1.62	1.83	1.65	1.79
15	6	163	167	1.49	1.60	1.76	1.63	1.73
11	11	160	164	1.51	1.65	1.65	1.65	1.65
14	8	158	162	1.53	1.58	1.68	1.60	1.66
19	1	157	160	1.55	1.51	1.74	1.55	1.70
18	3	156	159	1.56	1.50	1.72	1.54	1.68

Table 6.3: List of the semiconducting (n,m) nanotubes whose calculated Raman RBM position is between 190 and 300 cm⁻¹. The calculated Raman RBM position is given by Equation 6.3 (Calculation 1) or Equation 6.4 (Calculation 2).

n	m	p	RBM position (cm ⁻¹)		d (nm)	E_{22}^S (eV) at different strain values		
			Calc. 1	Calc. 2		-0.5%	0.0%	0.5%
8	3	-1	299	318	0.78	2.00	2.03	2.06
10	0	1	294	313	0.79	2.28	2.23	2.18
9	2	1	290	308	0.80	2.21	2.17	2.13
7	5	-1	283	300	0.83	1.95	1.96	1.97
8	4	1	279	296	0.84	2.05	2.03	2.01
11	0	-1	269	284	0.87	1.77	1.81	1.85
10	2	-1	266	281	0.88	1.76	1.80	1.83
7	6	1	263	278	0.89	1.87	1.86	1.86
9	4	-1	257	271	0.91	1.73	1.76	1.78
11	1	1	257	271	0.91	1.97	1.92	1.87
10	3	1	252	265	0.93	1.89	1.85	1.81
8	6	-1	244	256	0.96	1.69	1.70	1.71
9	5	1	242	255	0.97	1.76	1.74	1.72
12	1	-1	238	250	0.99	1.56	1.60	1.64
11	3	-1	233	245	1.01	1.55	1.59	1.62
8	7	1	229	241	1.03	1.62	1.62	1.61
13	0	1	229	241	1.03	1.75	1.70	1.65
12	2	1	228	239	1.04	1.72	1.68	1.63
10	5	-1	226	237	1.05	1.52	1.55	1.57
11	4	1	222	233	1.07	1.65	1.61	1.58
9	7	-1	215	225	1.10	1.49	1.49	1.50
10	6	1	214	223	1.11	1.54	1.52	1.51
14	0	-1	214	223	1.11	1.40	1.44	1.48
13	2	-1	212	222	1.12	1.40	1.44	1.47
12	4	-1	208	217	1.14	1.38	1.42	1.45
14	1	1	207	215	1.15	1.56	1.51	1.47
9	8	1	204	212	1.17	1.43	1.43	1.42
13	3	1	204	212	1.17	1.52	1.48	1.44
11	6	-1	201	210	1.18	1.36	1.38	1.40
12	5	1	199	207	1.20	1.45	1.42	1.40
15	1	1	194	202	1.23	1.27	1.31	1.35
10	8	-1	193	200	1.24	1.33	1.33	1.34
11	7	1	192	199	1.25	1.37	1.36	1.34
14	3	-1	192	199	1.25	1.26	1.30	1.33
16	0	1	188	195	1.27	1.42	1.37	1.32
13	5	-1	187	194	1.28	1.25	1.28	1.30
15	2	1	187	194	1.28	1.40	1.36	1.32
14	4	1	184	191	1.30	1.37	1.33	1.29

From the data from Tables 6.2 and 6.3, only the RBMs located at 165 cm⁻¹ ($E_{laser} = 1.49$ eV), 200 cm⁻¹, 201 cm⁻¹ and 221 cm⁻¹ ($E_{laser} = 1.96$ eV) are expected to be metallic; the others are all semiconducting. A list of nanotubes that can be assigned to each RBM is made based only on the RBM position and the corresponding nanotube diameter (Table 6.4). For example, for the 208 cm⁻¹ RBM ($E_{laser} = 1.49$ eV) can be assigned to the (12,4), (14,1), (9,8),

(13,3), or (11,6) nanotube, if only the extreme theoretical RBM positions given by Equations 6.3 and 6.4 are considered.

Table 6.4: List of the possible candidates for each observed RBM according to the TB1 tight-binding model.

E_{laser} (eV)	Exp. RBM position	Diameter only	RBM intensity variation trend	Perfect transfer
1.49	165	(15,6)	(15,6)	(15,6)
	192	(14,3) (11,7) (16,0) (13,5) (15,2)	(11,7) (16,0) (15,2)	(11,7) (16,0) (15,2)
	207	(14,1) (9,8) (13,3) (11,6) (12,5)	(14,1) (11,6)	(11,6)
	208	(12,4) (14,1) (9,8) (13,3) (11,6)	(12,4) (14,1) (11,6)	(12,4) (11,6)
	217	(9,7) (14,0) (10,6) (13,2) (12,4)	(9,7)	(9,7)
	227	(10,5) (11,4)	(10,5)	(10,5)
	228	(12,2) (10,5) (11,4)	(10,5)	(10,5)
	237	(11,3) (8,7) (13,0) (12,2) (10,5)	(11,3) (10,5)	(11,3) (10,5)
	266	(10,2) (7,6) (9,4) (11,1)	(10,2) (9,4)	(10,2) (9,4)
1.59	207	(14,1) (9,8) (13,3) (11,6) (12,5)	(11,6)	(11,6)
	210	(12,4) (14,1) (9,8) (13,3) (11,6)	(12,4) (11,6)	(12,4) (11,6)
	218	(9,7) (14,0) (10,6) (13,2)	(10,6)	-
	227	(10,5) (11,4)	(10,5) (11,4)	(10,5) (11,4)
	232	(8,7) (13,0) (12,2) (10,5) (11,4)	(8,7) (13,0) (12,2) (10,5) (11,4)	(8,7) (13,0) (12,2) (10,5)
	235	(11,3) (8,7) (13,0) (12,2) (10,5)	(8,7) (13,0) (12,2) (10,5)	(8,7) (13,0) (12,2) (10,5)
	238	(12,1) (11,3) (8,7) (13,0) (12,2)	(8,7) (13,0) (12,2)	(8,7) (13,0) (12,2)
	266	(10,2) (7,6) (9,4) (11,1)	(10,2) (9,4)	(10,2) (9,4)
	268	(10,2) (7,6) (9,4) (11,1)	(10,2) (9,4)	(10,2) (9,4)
	272	(11,0) (10,2) (7,6)	(11,0) (10,2)	(11,0) (10,2)
1.96	200	(15,0) (14,2) (13,4) (9,9)	(13,4)	-
	201	(15,0) (14,2) (13,4)	(13,4)	-
	221	(13,1) (12,3) (8,8)	(13,1) (12,3)	(13,1) (12,3)
	254	(10,3) (8,6) (9,5)	(8,6)	(8,6)
	257	(9,4) (11,1) (10,3)	(9,4)	(9,4)
	284	(7,5) (8,4) (11,0)	(8,4) (11,0)	(8,4) (11,0)
	299	(8,3) (10,0) (9,2) (7,5)	(10,0) (9,2)	(10,0) (9,2)

The number of viable candidates is then reduced, to take into account the RBM intensity variations and resonance theory. To continue with the example of the 208 cm^{-1} RBM ($E_{\text{laser}} = 1.49 \text{ eV}$), the intensity of this RBM increases in tension and decreases in compression. According to resonance theory, this means that the E_{22}^S value of this semiconducting nanotube becomes closer to E_{laser} in tension and further away from E_{laser} in compression. Among the five nanotubes cited above, only the (12,4), (14,1), and (11,6) nanotubes satisfy this condition.

In some cases, the number of viable candidates is further reduced, if a perfect load transfer is assumed from the polymer matrix to the nanotubes. Among the three viable candidates cited for the 208 cm^{-1} RBM ($E_{laser} = 1.49\text{ eV}$), the (14,1) nanotube has its E_{22}^S value shifting closer to E_{laser} in tension and even reaching it in the strain range between -0.6% and 0.6%, which would result in a maximum in the RBM intensity. There is no evidence of an intensity maximum in Figure 6.55, so this nanotube would be discarded if a perfect load transfer is assumed. The assumption of a perfect load transfer is only useful in rare cases, and eliminates all possible candidates for the $200, 201\text{ cm}^{-1}$ RBMs ($E_{laser} = 1.96\text{ eV}$), and the 218 cm^{-1} RBM ($E_{laser} = 1.59\text{ eV}$). Therefore for the following structure assignments, the load transfer is not considered perfect, and after considering the strain behavior of the E_{ii} values, the RBMs should be assigned to the nanotube with the E_{ii} value at zero strain, which is the closest to E_{laser} .

6.5.3.1 830 nm and 780 nm Laser ($E_{laser} = 1.49\text{ eV}$ and 1.59 eV)

The 165 cm^{-1} RBM corresponds to a nanotube with a diameter of around 1.5 nm. In this diameter range, only metallic nanotubes are expected to be in resonance with the 1.49 eV laser (830 nm).

In this diameter range, the metallic nanotubes are relatively far apart from each other in RBM position. There is only one nanotube in Table 6.2 in the correct RBM position range: the (15,6) nanotube. The first E_{11}^M value that is closer to $E_{laser} = 1.49\text{ eV}$ shifts to higher energies in tension and so further away from E_{laser} . The (15,6) nanotube therefore moves out of the resonance conditions in tension and its RBM intensity is expected to decrease in tension and increase in compression, matching the experimental results displayed in Figure 6.53.

The 192 cm^{-1} RBM corresponds to a nanotube with a diameter of around 1.3 nm. In the diameter range between 0.8 and 1.3 nm, semiconducting nanotubes are expected to be in resonance with the 1.49 eV (830 nm) and 1.59 eV (780 nm) lasers. Five nanotubes are in the RBM range of the observed nanotube: the (15,2), (13,5), (16,0), (14,3) and (11,7) nanotubes. The RBM

intensity decreases in tension (Figure 6.54), so the corresponding nanotube shifts further away from resonance. The (14,3) and (13,5) nanotubes can be discarded, since their E_{22}^S values shift closer to $E_{laser} = 1.49$ eV in tension. Among the four remaining candidates, the (16,0) nanotube has the E_{22}^S values which are the closest to E_{laser} and therefore can be assigned to the 192 cm^{-1} RBM.

Then there are four RBMs separated only by 3 cm^{-1} : $207, 208\text{ cm}^{-1}$ ($E_{laser} = 1.49$ eV), 207 and 210 cm^{-1} ($E_{laser} = 1.59$ eV). Considering the diameter range and their positions, these 4 RBMs can possibly correspond to six nanotubes: (12,5), (11,6), (13,3), (9,8), (14,1) and (12,4) with predicted RBM positions between 199 and 217 cm^{-1} .

Although the (13,3) and (14,1) nanotubes have E_{22}^S values at zero strain which are closer to $E_{laser} = 1.59$ eV, the E_{22}^S behavior under strain has to be considered. The intensity of the 207 and 210 cm^{-1} RBMs ($E_{laser} = 1.59$ eV) increases in tension, as showed in Figures 6.35 and 6.64, which means that in tension the E_{22}^S value of the corresponding nanotubes shifts closer to E_{laser} . Among the six possible nanotubes cited above, only two satisfy this condition and they are the (12,4) and (11,6) nanotubes. Therefore the (12,4) nanotube with a higher predicted RBM position is assigned to the 210 cm^{-1} RBM and the (11,6) nanotube to the 207 cm^{-1} RBM.

There are five suitable candidates for the RBM located at 207 cm^{-1} ($E_{laser} = 1.49$ eV): the (14,1), (9,8), (13,3), (11,6) and (12,5) nanotubes. The E_{22}^S values are very close for these five nanotubes at zero strain. Resonance theory would favor the (13,3) nanotube because its E_{22}^S value of 1.48 eV is the closest to $E_{laser} = 1.49$ eV. With the additional information about the behavior under strain, the chirality assignment can be refined. The intensity of the RBM located at 207 cm^{-1} increases in tension and decreases in compression, as indicated in Figure 6.26, which means that the corresponding nanotube moves closer to resonance conditions in tension and further away in compression. There are two candidates satisfying this condition: the (14,1) and the (11,6) nanotube have E_{22}^S values shifting closer to E_{laser} in tension and further away in compression. The (11,6) nanotube was previously assigned to the 207 cm^{-1}

RBM ($E_{laser} = 1.59$ eV). Since they are at the same position, the (11,6) nanotube is also assigned to 207 cm^{-1} RBM ($E_{laser} = 1.49$ eV).

The 208 cm^{-1} RBM intensity increases in tension (Figure 6.55), so the E_{22}^S value of its corresponding nanotube shifts closer to $E_{laser} = 1.49$ eV in tension. The (12,4) nanotube, which was previously assigned to the 210 cm^{-1} RBM ($E_{laser} = 1.59$ eV), and the (11,6) nanotube, previously assigned to the 207 cm^{-1} RBM ($E_{laser} = 1.49$ eV and 1.59 eV), are suitable. Considering the closeness of its position with the 207 cm^{-1} RBM, the 208 cm^{-1} RBM is also assigned to the (11,6) nanotube.

Since the (12,4) nanotube is assigned to the 210 cm^{-1} RBM ($E_{laser} = 1.59$ eV), the RBMs located at 217 ($E_{laser} = 1.49$ eV), and 218 cm^{-1} ($E_{laser} = 1.59$ eV) RBMs can correspond to one or two of four nanotubes: the (13,2), (14,0), (10,6) and (9,7) nanotubes, which are only separated by 0.04 nm in diameter and 0.1 eV in their E_{22}^S value at zero strain. Both RBMs decrease in intensity in tension (Figures 6.27, 6.56 and 6.65) which means that their corresponding nanotubes have E_{22}^S values that shift further away from their respective E_{laser} value. Among the five candidates, only one satisfies this condition for each RBM: the (9,7) nanotube for the 217 cm^{-1} RBM and the (10,6) nanotube for the 218 cm^{-1} RBM.

The RBMs located at 227 cm^{-1} , 228 cm^{-1} , 237 cm^{-1} ($E_{laser} = 1.49$ eV), 227 cm^{-1} , 232 cm^{-1} , 235 cm^{-1} , and 238 cm^{-1} ($E_{laser} = 1.59$ eV) have to be analyzed together since their E_{22}^S values are very close to the two E_{laser} values. Among the three candidates possible for the 227 and 228 cm^{-1} RBMs ($E_{laser} = 1.49$ eV), the (11,4), (10,5) and (12,2) nanotubes, only the (10,5) nanotube has its E_{22}^S value shift further away from E_{laser} in tension, which would coincide with the decreasing intensity in Figures 6.28 and 6.57. The same nanotubes are possible for the 227 cm^{-1} RBM ($E_{laser} = 1.59$ eV) which increases in intensity in tension (Figure 6.66). Due to its proximity to the 228 cm^{-1} RBM and the closeness of the E_{22}^S values to E_{laser} , the 227 cm^{-1} RBM ($E_{laser} = 1.59$ eV) can also be assigned to the (10,5) nanotube. The E_{22}^S value of the (10,5) nanotube shifts to higher energies in tension and lower energies in compression, but stays between the two E_{laser} values (1.49 eV and 1.59 eV). In tension, the

nanotube moves out of resonance with the 1.49 eV laser and enters in resonance with the 1.59 eV laser, explaining the opposite behavior of the RBM intensity with the two lasers (Figure 6.81). The slight difference in the RBM position is within the accuracy of measurement but it could be attributed to the way the nanotubes are assembled in bundles [174].

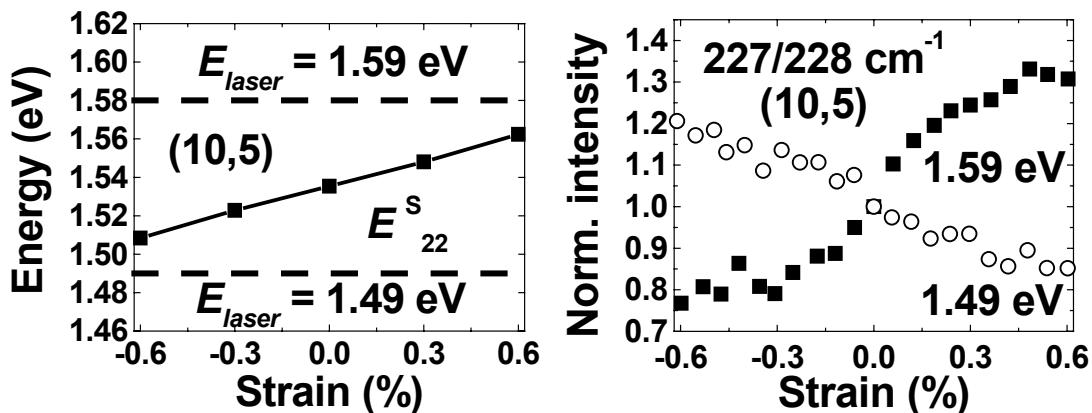


Figure 6.81: (left) E_{22}^S shift in energy as a function of axial strain for the (10,5) nanotube (The incident laser energies are indicated by dashed lines.). (right) Normalized intensity for the RBMs centered at 227 cm^{-1} (solid squares, $E_{laser} = 1.59 \text{ eV}$) and 228 cm^{-1} RBM (open circles, $E_{laser} = 1.49 \text{ eV}$).

Since the (10,5) nanotube is already assigned to the RBMs centered at $227/228 \text{ cm}^{-1}$, the 237 cm^{-1} RBM ($E_{laser} = 1.49 \text{ eV}$) can correspond to one of four nanotubes: the (11,3), (8,7), (13,0) and (12,2) nanotubes. Again the behavior under strain reduces the number of possibilities to one. Only the (11,3) nanotube has its E_{22}^S value shifting further away from E_{laser} in tension, consistent with the decrease of the RBM intensity in tension (Figures 6.29 and 6.58).

Considering the previous assignments, this leaves only three candidates (the (12,2), (13,0) and (8,7) nanotubes) for the 232, 235 and 238 cm^{-1} RBMs, all three observed with the 1.59 eV laser. They all have their intensity increase in tension and decrease in compression (Figures 6.36, 6.37 and 6.67), so the E_{22}^S values of their corresponding nanotubes shift closer in tension to E_{laser} . The 232, 235 and 238 cm^{-1} RBMs are assigned to the (12,2), (13,0) and (8,7) nanotubes respectively, based on their diameter. The 237 cm^{-1} RBM ($E_{laser} = 1.49 \text{ eV}$) is very close to the 238 cm^{-1} RBM ($E_{laser} = 1.59 \text{ eV}$) but they are assigned to different nanotubes because of their distinct behavior under strain.

Figures 6.38 and 6.39 showed that the 268 and 272 cm^{-1} RBMs ($E_{\text{laser}} = 1.59 \text{ eV}$) decrease in intensity in tension. In this diameter range, only a few nanotubes have E_{22}^S values shifting further away in tension from $E_{\text{laser}} = 1.59 \text{ eV}$. The (9,4) nanotube is a possible assignment but there is no other nanotube with a Raman RBM position close to it showing the same behavior under strain. The two best possibilities are therefore the (10,2) and (11,0) nanotubes, predicted to be at 266 and 269 cm^{-1} according to Equation 6.3.

The 266 cm^{-1} RBM observed with both near-infrared lasers can correspond to one of four nanotubes: the (11,1), (9,4), (7,6) and (10,2) nanotubes. The (10,2) and (9,4) nanotubes have E_{22}^S values that shift further away from the two E_{laser} values in tension, which matches the results from Figures 6.30, 6.59 and 6.68. The (10,2) nanotube was previously assigned to the 268 cm^{-1} RBM observed on HiPco nanotubes. Considering the proximity of these two experimental RBM positions and the gap of about 10 cm^{-1} between the theoretical values of the (10,2) and (9,4) nanotubes, it is reasonable to assign the 266 cm^{-1} RBM to the (10,2) nanotube.

6.5.3.2. 632 nm Laser ($E_{\text{laser}} = 1.96 \text{ eV}$)

The 200 and 201 cm^{-1} nanotubes are expected to be metallic nanotubes. There are four suitable nanotubes in this diameter range: the (15,0), (14,2), (13,4) and (9,9) nanotubes. The intensity of both RBMs increases in tension and decreases in compression (Figures 6.44 and 6.73). The E_{11}^M value of the armchair (9,9) nanotube is predicted to remain constant at 2 eV, so it can be discarded. The (15,0) and (14,2) nanotubes have E_{11}^M values that shift further away from $E_{\text{laser}} = 1.96 \text{ eV}$ in tension, so they are also discarded. That leaves the (13,4) nanotube which has its E_{11}^M value shift to higher energies over the considered strain range between -0.6% and 0.6%.

The (13,1), (12,3) and (8,8) nanotubes could be assigned to the metallic 221 cm^{-1} RBM (Figures 6.45 and 6.74). The armchair (8,8) nanotube is discarded due to its constant E_{11}^M value with uniaxial strain. Both the (12,3) and (13,1) nanotubes move further away from resonance in tension, but the (12,3)

nanotube is preferred over the (13,1) nanotube, since its E_{11}^M values are closer to E_{laser} .

Among the three possible candidates for the 254 cm^{-1} RBM (the (10,3), (8,6), (9,5) semiconducting nanotubes), only the (8,6) nanotube moves closer to resonance in tension, consistent with the increasing intensity in tension (Figure 6.75). A unique chirality can also be assigned to the 257 cm^{-1} RBM (Figure 6.46): among the three suitable candidates (the (9,4), (11,1), (10,3) semiconducting nanotubes), only the (9,4) nanotube has its E_{22}^S value shifting closer to E_{laser} .

The 284 cm^{-1} RBM (Figures 6.47 and 6.76) can be assigned to one of three nanotubes: the (7,5), (8,4) and (11,0) nanotubes. The (7,5) nanotube is expected to move further away from resonance in tension, in contradiction with the experimental data. The (11,0) nanotube was already assigned to the 272 cm^{-1} RBM observed on the HiPco nanotube composite using the 1.59 eV laser, so the 284 cm^{-1} RBM is assigned to the (8,4) nanotube.

Finally, the 299 cm^{-1} RBM (Figures 6.48) can correspond to one of four nanotubes: the (8,3), (10,0), (9,2) and (7,5) nanotubes. The (7,5) nanotube is discarded because it moves further away from resonance in tension. Among the three remaining candidates, only the (10,0) and (9,2) nanotubes move closer to resonance in tension. The (9,2) nanotube is preferred because of its E_{22}^S values closer to E_{laser} .

6.5.4 Structure Assignments Based on the TB3 Model

The E_{ii} values obtained from the TB3 tight-binding model, using the parameter values reported in Reference 192 (see Appendix I), are lower than those from the TB1 model. To explain the RBM intensity variations with the results from the TB3 model, the E_{ii} values are all rescaled to higher energies by a constant factor of 1.18, in the larger-diameter range between 1.0 and 1.6 nm, where the chirality-dependence of the E_{ii} values are small. This value was chosen so that the discrepancies between the two models are minimum.

Table 6.5 is a list of the metallic nanotubes with theoretical RBM positions between 160 and 230 cm^{-1} . For each of the three strain values, two

E_{11}^M values are provided because of the trigonal warping effect [168], except for armchair metallic nanotubes. Table 6.6 is a list of the semiconducting nanotubes with a theoretical Raman RBM position between 190 and 300 cm⁻¹. For a (n,m) nanotube, it gives the E_{22}^S values for three different strain values.

The difference between the rescaled E_{ii} values from the TB3 model and those from the TB1 model can reach 21 meV for the semiconducting and metallic nanotubes in the diameter ranges considered in Tables 6.5 and 6.6. Since the E_{ii} values are so close to E_{laser} in resonant conditions, the slightest change in the E_{ii} values can modify the structure assignments made from Raman spectroscopy, based on the strain-induced shifts of the E_{ii} values. Based on the data from Tables 6.5 and 6.6, a list of possible candidates is made for each RBM observed using a specific laser wavelength (Table 6.7).

Table 6.5: List of the metallic (n,m) nanotubes with a calculated Raman RBM position between 160 and 230 cm⁻¹. The calculated Raman RBM position is given by Equation 6.3 (Calc. 1) or Equation 6.4 (Calc. 2).

n	m	RBM position (cm ⁻¹)		d (nm)	E_{11}^M (eV) at different strain values					
		Calc. 1	Calc. 2		-0.5%	0.0%	0.5%			
9	6	228	239	1.04	2.25	2.44	2.27	2.42	2.29	2.41
13	1	221	231	1.07	2.06	2.74	2.11	2.67	2.17	2.60
12	3	217	227	1.09	2.06	2.57	2.10	2.51	2.15	2.46
8	8	216	225	1.10	2.22		2.22		2.23	
11	5	211	220	1.13	2.05	2.37	2.08	2.33	2.12	2.30
10	7	203	211	1.17	2.03	2.18	2.05	2.16	2.07	2.15
15	0	200	208	1.19	1.88	2.49	1.93	2.41	1.99	2.34
14	2	199	207	1.20	1.88	2.42	1.93	2.35	1.98	2.28
13	4	195	203	1.22	1.87	2.27	1.92	2.22	1.96	2.17
9	9	193	200	1.24	2.00		2.00		2.01	
12	6	190	197	1.26	1.86	2.11	1.89	2.08	1.93	2.05
11	8	183	189	1.31	1.84	1.96	1.86	1.95	1.88	1.93
16	1	183	189	1.31	1.73	2.24	1.78	2.16	1.83	2.09
15	3	181	187	1.33	1.72	2.16	1.77	2.09	1.82	2.03
14	5	178	183	1.35	1.72	2.04	1.76	1.99	1.80	1.95
10	10	175	180	1.38	1.82		1.82		1.82	
13	7	173	178	1.40	1.70	1.91	1.73	1.88	1.76	1.85
18	0	169	174	1.43	1.59	2.06	1.65	1.98	1.71	1.91
17	2	168	173	1.44	1.59	2.02	1.65	1.96	1.70	1.89
12	9	167	171	1.45	1.69	1.78	1.70	1.77	1.72	1.76
16	4	166	170	1.46	1.59	1.94	1.64	1.89	1.68	1.83
15	6	163	167	1.49	1.58	1.85	1.62	1.80	1.66	1.76
11	11	160	164	1.51	1.66		1.67		1.67	
14	8	158	162	1.53	1.57	1.74	1.60	1.71	1.63	1.69
19	1	157	160	1.55	1.48	1.89	1.54	1.81	1.59	1.74
18	3	156	159	1.56	1.48	1.84	1.53	1.78	1.58	1.72

Table 6.6: List of the semiconducting (n,m) nanotubes whose calculated Raman RBM position is between 190 and 300 cm⁻¹. The calculated Raman RBM position is given by Equation 6.3 (Calc. 1) or Equation 6.4 (Calc. 2).

n	m	p	RBM position (cm ⁻¹)		d (nm)	E_{22}^S (eV) at different strain values		
			Calc. 1	Calc. 2		-0.5%	0.0%	0.5%
8	3	-1	299	318	0.78	1.96	2.00	2.04
10	0	1	294	313	0.79	2.49	2.41	2.34
9	2	1	290	308	0.81	2.35	2.29	2.23
7	5	-1	283	300	0.83	1.93	1.95	1.97
8	4	1	279	296	0.84	2.11	2.08	2.05
11	0	-1	269	284	0.87	1.73	1.78	1.84
10	2	-1	266	281	0.88	1.72	1.77	1.82
7	6	1	263	278	0.89	1.89	1.88	1.88
9	4	-1	257	271	0.92	1.71	1.75	1.78
11	1	1	257	271	0.92	2.13	2.06	1.99
10	3	1	252	265	0.94	1.99	1.94	1.89
8	6	-1	244	256	0.97	1.69	1.70	1.72
9	5	1	242	255	0.98	1.82	1.79	1.77
12	1	-1	238	250	0.99	1.53	1.59	1.64
11	3	-1	233	245	1.01	1.53	1.58	1.62
8	7	1	229	241	1.03	1.65	1.65	1.64
13	0	1	229	241	1.03	1.89	1.82	1.75
12	2	1	228	239	1.04	1.84	1.78	1.72
10	5	-1	226	237	1.05	1.52	1.55	1.58
11	4	1	222	233	1.07	1.73	1.68	1.64
9	7	-1	215	225	1.10	1.50	1.51	1.53
14	0	-1	214	223	1.11	1.38	1.44	1.49
10	6	1	214	223	1.11	1.60	1.57	1.55
13	2	-1	212	222	1.12	1.38	1.43	1.48
12	4	-1	208	217	1.14	1.37	1.42	1.46
14	1	1	207	215	1.15	1.68	1.61	1.54
9	8	1	204	212	1.17	1.46	1.46	1.46
13	3	1	204	212	1.17	1.62	1.56	1.51
11	6	-1	201	210	1.19	1.36	1.39	1.42
12	5	1	199	207	1.20	1.53	1.49	1.45
15	1	-1	194	202	1.23	1.25	1.31	1.36
10	8	-1	193	200	1.24	1.34	1.36	1.37
14	3	-1	192	199	1.25	1.25	1.30	1.35
11	7	1	192	199	1.25	1.42	1.40	1.38
16	0	1	188	195	1.27	1.53	1.46	1.39
13	5	-1	187	194	1.28	1.24	1.28	1.32
15	2	1	187	194	1.28	1.51	1.44	1.38
14	4	1	184	191	1.30	1.45	1.39	1.34

Only the RBMs centered at 165 cm⁻¹ ($E_{laser} = 1.49$ eV), 200 cm⁻¹, 201 cm⁻¹ and 221 cm⁻¹ ($E_{laser} = 1.96$ eV) are expected to be metallic; the others are all semiconducting. For each experimental RBM, a first list of potential candidates among the semiconducting or metallic nanotubes is made based only on the nanotube diameter. The experimental RBM position has to be

between the two extreme theoretical values calculated using Equations 6.3 and 6.4. One to five nanotubes are considered viable at this stage of the analysis.

Table 6.7: List of the possible candidates for each observed RBM according to the TB3 tight-binding model.

E_{laser} (eV)	Exp. RBM position	Diameter only	RBM intensity variation trend	Perfect transfer
1.49	165	(15,6)	(15,6)	(15,6)
	192	(14,3) (11,7) (16,0) (13,5) (15,2)	(11,7) (16,0) (15,2)	(11,7)
	207	(14,1) (9,8) (13,3) (11,6) (12,5)	(14,1) (13,3) (11,6)	(14,1) (13,3) (11,6)
	208	(12,4) (14,1) (9,8) (13,3) (11,6)	(12,4) (14,1) (13,3) (11,6)	(12,4) (14,1) (13,3) (11,6)
	217	(9,7) (14,0) (10,6) (13,2) (12,4)	(9,7)	(9,7)
	227	(10,5) (11,4)	(10,5)	(10,5)
	228	(12,2) (10,5) (11,4)	(10,5)	(10,5)
	237	(11,3) (8,7) (13,0) (12,2) (10,5)	(11,3) (10,5)	(11,3) (10,5)
	266	(10,2) (7,6) (9,4) (11,1)	(10,2) (9,4)	(10,2) (9,4)
1.59	207	(14,1) (9,8) (13,3) (11,6) (12,5)	(14,1) (11,6)	(11,6)
	210	(12,4) (14,1) (9,8) (13,3) (11,6)	(12,4) (14,1) (11,6)	(12,4) (11,6)
	218	(9,7) (14,0) (10,6) (13,2)	(10,6)	-
	227	(10,5) (11,4)	(10,5) (11,4)	(10,5) (11,4)
	232	(8,7) (13,0) (12,2) (10,5) (11,4)	(8,7) (13,0) (12,2) (10,5) (11,4)	(8,7) (13,0) (12,2) (10,5) (11,4)
	235	(11,3) (8,7) (13,0) (12,2) (10,5)	(11,3) (8,7) (13,0) (12,2) (10,5)	(8,7) (13,0) (12,2) (10,5)
	238	(12,1) (11,3) (8,7) (13,0) (12,2)	(11,3) (8,7) (13,0) (12,2)	(8,7) (13,0) (12,2)
	266	(10,2) (7,6) (9,4) (11,1)	(10,2) (9,4)	(10,2) (9,4)
	268	(10,2) (7,6) (9,4) (11,1)	(10,2) (9,4)	(10,2) (9,4)
1.96	272	(11,0) (10,2) (7,6)	(11,0) (10,2)	(11,0) (10,2)
	200	(15,0) (14,2) (13,4) (9,9)	(15,0) (14,2) (13,4)	(13,4)
	201	(15,0) (14,2) (13,4)	(15,0) (14,2) (13,4)	(13,4)
	221	(13,1) (12,3) (8,8)	(13,1) (12,3) (8,8)	(13,1) (12,3) (8,8)
	254	(10,3) (8,6) (9,5)	(8,6)	(8,6)
	257	(9,4) (11,1) (10,3)	(9,4) (11,1)	(9,4) (11,1)
	284	(7,5) (8,4) (11,0)	(7,5) (8,4) (11,0)	(8,4) (11,0)
	299	(8,3) (10,0) (9,2) (7,5)	(10,0) (9,2) (7,5)	(10,0) (9,2)

Using the information on the strain-induced E_{ii} shift extracted from the data on the RBM intensity variations, several candidates can be eliminated. For some RBMs, this second analysis only leaves a unique possible candidate. This is the case for the RBMs centered at:

- 165 cm^{-1} ($E_{\text{laser}} = 1.49 \text{ eV}$), which can be assigned to the (15,6) nanotube;
- 217 cm^{-1} ($E_{\text{laser}} = 1.49 \text{ eV}$), assigned to the (9,7) nanotube;
- 218 cm^{-1} ($E_{\text{laser}} = 1.59 \text{ eV}$), assigned to the (10,6) nanotube;

- 227 and 228 cm⁻¹ ($E_{laser} = 1.49$ eV), both assigned to the (10,5) nanotube;
- 254 cm⁻¹ ($E_{laser} = 1.96$ eV), assigned to the (8,6) nanotube.

In some rare situations, if the load transfer is assumed perfect, meaning the strain applied to the macroscopic composite sample is identical to the strain applied to the nanotube, the number of possible candidates can be further reduced. For example, for the RBMs centered at 200 and 201 cm⁻¹ ($E_{laser} = 1.96$ eV), there remains three viable nanotubes after considering the strain-induced E_{ii} shifts: the (15,0), (14,2), and (13,4) nanotubes. Among these three nanotubes, the (15,0) and (14,2) nanotubes have E_{ii}^M values that shift to higher energies and reach E_{laser} , which should result in the appearance of an intensity maximum in Figures 6.44 and 6.73. No intensity maximum was observed for any RBM in the strain range investigated. So assuming that the load transfer is perfect would lead to the elimination of the (15,0) and (14,2) nanotubes as possible assignments for the 200 and 201 cm⁻¹ RBMs. However it is noted that this assumption would leave no viable candidates for the 218 cm⁻¹ RBM ($E_{laser} = 1.59$ eV). Therefore for the following structure assignments, the load transfer is not considered perfect, and after considering the strain behavior of the E_{ii} values, the RBMs should be assigned to the nanotube with the E_{ii} value at zero strain, which is the closest to E_{laser} .

Using this method, the 192 cm⁻¹ RBM ($E_{laser} = 1.49$ eV) is assigned to the semiconducting (16,0) nanotube. The 200 and 201 cm⁻¹ RBMs ($E_{laser} = 1.96$ eV) have the same behavior under strain and can reasonably be assigned to the same nanotube since their positions are so close. Among the three possible candidates, the (15,0), (14,2) and (13,4) nanotubes, the (15,0) nanotube have the E_{ii}^M values that are the closest to E_{laser} over the entire strain range considered, and can thus be assigned to the 200 and 201 cm⁻¹ RBMs.

The 210 cm⁻¹ RBM ($E_{laser} = 1.59$ eV) is assigned to the (14,1) nanotube which has the E_{ii}^S values that are the closest to E_{laser} . The 207 cm⁻¹ RBM observed with the same laser is assigned to the other viable candidate, the (11,6) nanotube. The 207 and 208 cm⁻¹ RBMs ($E_{laser} = 1.49$ eV) are very close to the previously assigned RBM and the (11,6) nanotube is also a possible

candidate for both of them, so it is reasonable to assign them to the same nanotube.

The 221 cm^{-1} RBM ($E_{laser} = 1.96\text{ eV}$) can be assigned to the (13,1), (12,3), or (8,8) nanotubes. Among these three, the (12,3) nanotube have the E_{11}^M values which are the closest to E_{laser} over the entire strain range considered and is thus assigned to this RBM. The 227 cm^{-1} RBM ($E_{laser} = 1.59\text{ eV}$) is very close to the previously assigned 227 and 228 cm^{-1} RBMs ($E_{laser} = 1.49\text{ eV}$) and therefore should correspond to the same nanotube: the (10,5) nanotube.

Since the (10,5) nanotube is already assigned, that leaves the (11,3) nanotube as the only viable candidate for the 237 cm^{-1} RBM ($E_{laser} = 1.49\text{ eV}$). The 238 cm^{-1} RBM ($E_{laser} = 1.59\text{ eV}$) is also assigned to the (11,3) nanotube, since its position is very close. There remains three possible nanotubes, the (8,7), (13,0), (12,2) nanotubes for the two RBMs located at 232 and 235 cm^{-1} ($E_{laser} = 1.59\text{ eV}$). The 232 cm^{-1} RBM is assigned to the (12,2) nanotube with a smaller diameter. The (8,7) and (13,0) nanotubes have the same diameter, but the (8,7) nanotube is closer to E_{laser} , and is therefore assigned to the 235 cm^{-1} RBM.

The 257 cm^{-1} RBM ($E_{laser} = 1.96\text{ eV}$) is assigned to the (11,1) nanotube, which is expected to be closer to the resonance window than the (9,4) nanotube. The 268 and 272 cm^{-1} RBM ($E_{laser} = 1.59\text{ eV}$) are close to each other and are assigned to the (10,2) and (11,0) nanotubes respectively, which are only separated by 3 cm^{-1} in Table 6.6. The (9,4) nanotube is located nearly 10 cm^{-1} away from the (10,2) nanotube. The 266 cm^{-1} RBMs ($E_{laser} = 1.49\text{ eV}$ and 1.59 eV) are very close to the 268 cm^{-1} RBM, and should also be assigned to the (10,2) nanotube.

This leaves two possible candidates for the 284 cm^{-1} RBM ($E_{laser} = 1.96\text{ eV}$): the (7,5) and (8,4) nanotubes. The (7,5) nanotube is expected to be much closer to the resonance window and is assigned to this RBM. Finally, the 299 cm^{-1} RBM observed with the same laser is assigned to the (9,2) nanotube.

6.5.5 Structure Assignments Based on the Experimental E_{ii} Values

The structure assignment method described above can be repeated using the combination of the experimental values of E_{ii} and the theoretical shifts predicted by the two tight-binding models (Tables 6.8 and 6.9). The experimental values of E_{ii} were reported for isolated nanotubes suspended in water, by fluorescence spectroscopy for semiconducting nanotubes [179] and Raman excitation profiles for metallic nanotubes using a tunable incident laser [196].

The theoretical shifts showed in Tables 6.8 and 6.9 were determined by the following method. The E_{ii} values were calculated with the tight-binding models TB1 and TB3 for three strain values: -0.5%, 0% and 0.5%. These theoretical values were then normalized to the experimental data using Equation 5.84 and the fit parameters from Tables 5.2 and 5.3. The normalized difference between the theoretical E_{ii} values for the undeformed and deformed nanotube was then added to the experimental E_{ii} values from References 179 and 196.

Based on the data from Tables 6.8 and 6.9, a list of possible candidates is made for each RBM observed using a specific laser wavelength (Table 6.10). For each experimental RBM, a first list of potential candidates is made based only on the nanotube diameter. The strain-induced E_{ii} shifts and the perfection of the load transfer are then considered to reduce the number of viable candidates.

The consideration of the strain-induced E_{ii} shifts leaves only one possible candidate for the following RBMs:

- 165 cm^{-1} ($E_{\text{laser}} = 1.49 \text{ eV}$), assigned to the (15,6) nanotube;
- 192 cm^{-1} ($E_{\text{laser}} = 1.49 \text{ eV}$), assigned to the (11,7) nanotube;
- 217 cm^{-1} ($E_{\text{laser}} = 1.49 \text{ eV}$), assigned to the (9,7) nanotube;
- 227 and 228 cm^{-1} ($E_{\text{laser}} = 1.49 \text{ eV}$), both assigned to the (10,5) nanotube;
- 254 cm^{-1} ($E_{\text{laser}} = 1.96 \text{ eV}$), assigned to the (8,6) nanotube.

The assumption that the load transfer is perfect further reduce the number of possible candidates for some RBMs: the 208 cm^{-1} RBM

($E_{laser} = 1.49$ eV), the 207, 210, 227, 232, 235, 238 cm^{-1} RBMs ($E_{laser} = 1.59$ eV), the 200 cm^{-1} RBM ($E_{laser} = 1.96$ eV). But it also eliminates all viable candidates for the 192 cm^{-1} RBM ($E_{laser} = 1.96$ eV). Therefore for the following structure assignments, the load transfer is not considered perfect.

The 200 and 201 cm^{-1} RBMs ($E_{laser} = 1.96$ eV) have the same behavior under strain and can reasonably be assigned to the same nanotube since their positions are so close. Among the three common possible candidates, the (15,0), (14,2) and (13,4) nanotubes, the (13,4) nanotube have the E_{11}^M values that are the closest to E_{laser} over the entire strain range considered, and can thus be assigned to the 200 and 201 cm^{-1} RBMs.

Table 6.8: List of the metallic (n,m) nanotubes with a calculated Raman RBM position between 160 and 230 cm^{-1} . The calculated Raman RBM position is given by Equation 6.3 (Calc. 1) or Equation 6.4 (Calc. 2). The results for the (19,1) nanotube are extrapolated and are not based on experiments.

n	m	RBM position (cm^{-1})		d (nm)	E_{11}^M (eV) at different strain values					
		Calc. 1	Calc. 2		-0.5%		0.0%	0.5%		
					TB3	TB1		TB1	TB3	
9	6	228	239	1.04	2.14, 2.23	2.14, 2.23	2.16, 2.22	2.17, 2.21	2.18, 2.20	
13	1	221	231	1.07	1.96, 2.30	1.97, 2.29	2.01, 2.24	2.04, 2.20	2.06, 2.18	
12	3	217	227	1.09	1.96, 2.24	1.98, 2.23	2.01, 2.19	2.04, 2.15	2.05, 2.14	
8	8	216	225	1.10	2.11, 2.11	2.11, 2.11	2.11, 2.11	2.11, 2.11	2.11, 2.11	
11	5	211	220	1.13	1.96, 2.14	1.97, 2.13	1.99, 2.10	2.02, 2.08	2.03, 2.07	
10	7	203	211	1.17	1.95, 2.02	1.95, 2.02	1.97, 2.01	1.98, 2.00	1.98, 2.00	
15	0	200	208	1.19	1.81, 2.12	1.83, 2.10	1.86, 2.06	1.90, 2.01	1.91, 2.00	
14	2	199	207	1.20	1.81, 2.10	1.83, 2.08	1.86, 2.04	1.90, 2.00	1.91, 1.98	
13	4	195	203	1.22	1.81, 2.03	1.82, 2.02	1.85, 1.98	1.88, 1.95	1.89, 1.94	
9	9	193	200	1.24	1.91, 1.91	1.92, 1.92	1.92, 1.92	1.92, 1.92	1.92, 1.92	
12	6	190	197	1.26	1.80, 1.94	1.81, 1.93	1.83, 1.91	1.85, 1.89	1.86, 1.88	
11	8	183	189	1.31	1.78, 1.84	1.79, 1.84	1.80, 1.83	1.81, 1.82	1.82, 1.82	
16	1	183	189	1.31	1.68, 1.95	1.69, 1.94	1.73, 1.89	1.77, 1.85	1.79, 1.83	
15	3	181	187	1.33	1.68, 1.92	1.69, 1.90	1.73, 1.86	1.76, 1.82	1.78, 1.81	
14	5	178	183	1.35	1.67, 1.85	1.69, 1.84	1.71, 1.81	1.74, 1.78	1.75, 1.77	
10	10	175	180	1.38	1.75, 1.75	1.75, 1.75	1.75, 1.75	1.75, 1.75	1.76, 1.76	
13	7	173	178	1.40	1.66, 1.77	1.67, 1.77	1.69, 1.75	1.71, 1.72	1.72, 1.72	
18	0	169	174	1.43	1.56, 1.82	1.58, 1.80	1.62, 1.75	1.65, 1.71	1.67, 1.69	
17	2	168	173	1.44	1.56, 1.80	1.58, 1.79	1.62, 1.74	1.65, 1.70	1.67, 1.68	
12	9	167	171	1.45	1.64, 1.69	1.65, 1.69	1.66, 1.68	1.67, 1.67	1.67, 1.67	
16	4	166	170	1.46	1.56, 1.76	1.57, 1.75	1.61, 1.71	1.64, 1.67	1.65, 1.66	
15	6	163	167	1.49	1.55, 1.70	1.56, 1.69	1.59, 1.66	1.62, 1.63	1.63, 1.62	
11	11	160	164	1.51	1.61, 1.61	1.61, 1.61	1.61, 1.61	1.61, 1.61	1.62, 1.62	
14	8	158	162	1.53	1.54, 1.63	1.55, 1.62	1.57, 1.61	1.58, 1.58	1.59, 1.58	
19	1	157	160	1.55	1.45, 1.69	1.48, 1.67	1.52, 1.63	1.56, 1.58	1.56, 1.56	
18	3	156	159	1.56	1.46, 1.67	1.47, 1.65	1.51, 1.61	1.54, 1.57	1.56, 1.55	

Table 6.9: List of the semiconducting (n,m) nanotubes whose calculated Raman RBM position is between 190 and 300 cm^{-1} . The calculated Raman RBM position is given by Equation 6.3 (Calc. 1) or Equation 6.4 (Calc. 2).

n	m	p	RBM position (cm^{-1})		d (nm)	E_{22}^S (eV) at different strain values					
						-0.5%		0.0%	0.5%		
			Calc. 1	Calc. 2		TB3	TB1		TB1	TB3	
8	3	-1	299	318	0.78	1.83	1.84	1.86	1.89	1.90	
10	0	1	294	313	0.79	2.38	2.36	2.31	2.26	2.24	
9	2	1	290	308	0.81	2.31	2.29	2.25	2.21	2.20	
7	5	-1	283	300	0.83	1.90	1.91	1.92	1.93	1.94	
8	4	1	279	296	0.84	2.14	2.13	2.11	2.08	2.07	
11	0	-1	269	284	0.87	1.61	1.63	1.67	1.70	1.72	
10	2	-1	266	281	0.88	1.64	1.65	1.68	1.72	1.73	
7	6	1	263	278	0.89	1.92	1.92	1.91	1.91	1.91	
9	4	-1	257	271	0.92	1.68	1.69	1.72	1.74	1.75	
11	1	1	257	271	0.92	2.10	2.08	2.03	1.98	1.96	
10	3	1	252	265	0.94	2.02	2.00	1.96	1.93	1.91	
8	6	-1	244	256	0.97	1.71	1.72	1.73	1.74	1.74	
9	5	1	242	255	0.98	1.87	1.87	1.85	1.82	1.82	
12	1	-1	238	250	0.99	1.50	1.51	1.55	1.59	1.61	
11	3	-1	233	245	1.01	1.52	1.53	1.56	1.60	1.61	
8	7	1	229	241	1.03	1.71	1.71	1.70	1.70	1.70	
13	0	1	229	241	1.03	1.90	1.88	1.83	1.78	1.76	
12	2	1	228	239	1.04	1.87	1.85	1.81	1.76	1.74	
10	5	-1	226	237	1.05	1.54	1.55	1.57	1.60	1.61	
11	4	1	222	233	1.07	1.79	1.78	1.74	1.70	1.69	
9	7	-1	215	225	1.10	1.55	1.55	1.56	1.57	1.58	
14	0	-1	214	223	1.11	1.39	1.40	1.44	1.48	1.50	
10	6	1	214	223	1.11	1.67	1.66	1.64	1.62	1.62	
13	2	-1	212	222	1.12	1.39	1.41	1.45	1.48	1.50	
12	4	-1	208	217	1.14	1.40	1.42	1.45	1.48	1.50	
14	1	1	207	215	1.15	1.73	1.71	1.66	1.61	1.59	
9	8	1	204	212	1.17	1.54	1.54	1.53	1.53	1.53	
13	3	1	204	212	1.17	1.69	1.67	1.62	1.58	1.56	
11	6	-1	201	210	1.19	1.41	1.43	1.45	1.47	1.48	
12	5	1	199	207	1.20	1.61	1.60	1.56	1.53	1.52	
15	1	-1	194	202	1.23	1.29	1.30	1.35	1.39	1.41	
10	8	-1	193	200	1.24	1.41	1.42	1.43	1.44	1.44	
14	3	-1	192	199	1.25	1.29	1.31	1.35	1.39	1.40	
11	7	1	192	199	1.25	1.51	1.50	1.48	1.47	1.46	
16	0	1	188	195	1.27	1.60	1.57	1.52	1.47	1.45	
13	5	-1	187	194	1.28	1.30	1.31	1.34	1.38	1.39	
15	2	1	187	194	1.28	1.58	1.56	1.51	1.46	1.44	
14	4	1	184	191	1.30	1.53	1.52	1.47	1.43	1.42	

Among the possible candidates for the 207 and 210 cm^{-1} RBMs ($E_{\text{laser}} = 1.59$ eV), the (12,4) and (11,6) nanotubes have the E_{22}^S values that are the closest to E_{laser} . So the 207 and 210 cm^{-1} RBMs are respectively assigned to the (11,6) and (12,4) nanotubes. The 207 and 208 cm^{-1} RBMs ($E_{\text{laser}} = 1.49$ eV) are very close to the previously assigned RBM and the (11,6) nanotube is also

a possible candidate for both of them, so it is reasonable to assign them to the same nanotube.

Table 6.10: List of the possible candidates for each observed RBM according to the experimental E_{ii} values and the energy shifts from tight-binding calculations.

E_{laser} (eV)	Exp. RBM position	Diameter only	RBM intensity variation trend	Perfect transfer TB1	Perfect transfer TB3
1.49	165	(15,6)	(15,6)	(15,6)	(15,6)
	192	(14,3) (11,7) (16,0) (13,5) (15,2)	(11,7)	-	-
	207	(14,1) (9,8) (13,3) (11,6) (12,5)	(14,1) (9,8) (13,3) (11,6)	(14,1) (9,8) (13,3) (11,6)	(14,1) (9,8) (13,3) (11,6)
	208	(12,4) (14,1) (9,8) (13,3) (11,6)	(12,4) (14,1) (9,8) (13,3) (11,6)	(12,4) (14,1) (9,8) (13,3) (11,6)	(9,8) (14,1) (11,6)
	217	(9,7) (14,0) (10,6) (13,2) (12,4)	(9,7)	(9,7)	(9,7)
	227	(10,5) (11,4)	(10,5)	(10,5)	(10,5)
	228	(12,2) (10,5) (11,4)	(10,5)	(10,5)	(10,5)
	237	(11,3) (8,7) (13,0) (12,2) (10,5)	(11,3) (10,5)	(11,3) (10,5)	(11,3) (10,5)
	266	(10,2) (7,6) (9,4) (11,1)	(10,2) (9,4)	(10,2) (9,4)	(10,2) (9,4)
	207	(14,1) (9,8) (13,3) (11,6) (12,5)	(14,1) (13,3) (11,6)	(14,1) (11,6)	(14,1) (11,6)
1.59	210	(12,4) (14,1) (9,8) (13,3) (11,6)	(12,4) (14,1) (13,3) (11,6)	(12,4) (14,1) (11,6)	(12,4) (14,1) (11,6)
	218	(9,7) (14,0) (10,6) (13,2)	-	-	-
	227	(10,5) (11,4)	(10,5) (11,4)	(11,4)	(11,4)
	232	(8,7) (13,0) (12,2) (10,5) (11,4)	(8,7) (13,0) (12,2) (10,5) (11,4)	(8,7) (13,0) (12,2) (11,4)	(8,7) (13,0) (12,2) (11,4)
	235	(11,3) (8,7) (13,0) (12,2) (10,5)	(11,3) (8,7) (13,0) (12,2) (10,5)	(8,7) (13,0) (12,2)	(8,7) (13,0) (12,2)
	238	(12,1) (11,3) (8,7) (13,0) (12,2)	(12,1) (11,3) (8,7) (13,0) (12,2)	(12,1) (8,7) (13,0) (12,2)	(12,1) (8,7) (13,0) (12,2)
	266	(10,2) (7,6) (9,4) (11,1)	(10,2) (9,4)	(10,2) (9,4)	(10,2) (9,4)
	268	(10,2) (7,6) (9,4) (11,1)	(10,2) (9,4)	(10,2) (9,4)	(10,2) (9,4)
	272	(11,0) (10,2) (7,6)	(11,0) (10,2)	(11,0) (10,2)	(11,0) (10,2)
	200	(15,0) (14,2) (13,4) (9,9)	(15,0) (14,2) (13,4) (9,9)	(15,0) (14,2) (13,4)	(15,0) (14,2) (13,4) (9,9)
1.96	201	(15,0) (14,2) (13,4)	(15,0) (14,2) (13,4)	(15,0) (14,2) (13,4)	(15,0) (14,2) (13,4)
	221	(13,1) (12,3) (8,8)	(13,1) (12,3) (8,8)	(13,1) (12,3)	(13,1) (12,3) (8,8)
	254	(10,3) (8,6) (9,5)	(8,6)	(8,6)	(8,6)
	257	(9,4) (11,1) (10,3)	(9,4) (11,1)	(9,4) (11,1)	(9,4) (11,1)
	284	(7,5) (8,4) (11,0)	(7,5) (8,4) (11,0)	(7,5) (8,4) (11,0)	(7,5) (8,4) (11,0)
	299	(8,3) (10,0) (9,2) (7,5)	(8,3) (10,0) (9,2) (7,5)	(8,3) (10,0) (9,2) (7,5)	(8,3) (10,0) (9,2) (7,5)

According to Table 6.9, there are no suitable nanotubes for the 218 cm^{-1} RBM ($E_{laser} = 1.59\text{ eV}$). This RBM decreases in intensity in tension and no nanotube in this diameter range can explain the data. In this diameter range, the (9,7) and (10,6) nanotubes have E_{22}^S values very close to E_{laser} . The E_{22}^S value from photoluminescence spectroscopy for the unstrained (9,7) nanotube is just 30 meV below E_{laser} [179]. It is important to stress here that the E_{ii} values from photoluminescence spectroscopy depend heavily on the environment around the nanotubes [187]. The sets of E_{ii} values in References 179 and 196 differ by as much as 25 meV for some nanotubes. The E_{22}^S value for the unstrained (9,7) nanotube is 1.572 eV in Reference 196, compared to the value of 1.563 eV reported in Reference 179. A value above $E_{laser} = 1.59\text{ eV}$ would make the (9,7) nanotube a suitable candidate.

Another fact to emphasize is that the E_{22}^S values from Table 6.9 are from photoluminescence spectroscopic measurements on isolated nanotubes suspended in water with surfactants. Measurements of E_{22}^S by optical absorption spectroscopy revealed that their values in nanotube bundles are downshifted by 50 meV compared to the values in individual HiPco nanotubes [161]. A downshift of the E_{22}^S of the (10,6) nanotube of this magnitude could make the (10,6) nanotube a suitable candidate, if the E_{22}^S value falls below $E_{laser} = 1.59\text{ eV}$. The 218 cm^{-1} RBM was previously assigned to the (10,6) nanotube using the E_{22}^S values from the TB1 and TB3 models.

Among the three possible candidates for the 221 cm^{-1} RBM ($E_{laser} = 1.96\text{ eV}$), the (12,3) nanotube have the E_{11}^M values which are the closest to E_{laser} over the entire strain range considered and is thus assigned to this RBM. The 227 cm^{-1} RBM ($E_{laser} = 1.59\text{ eV}$) is very close to the previously assigned 227 and 228 cm^{-1} RBMs ($E_{laser} = 1.49\text{ eV}$) and therefore should correspond to the same nanotube: the (10,5) nanotube.

Since the (10,5) nanotube is already assigned, that leaves the (11,3) nanotube as the only viable candidate for the 237 cm^{-1} RBM ($E_{laser} = 1.49\text{ eV}$). Since the 238 cm^{-1} RBM ($E_{laser} = 1.59\text{ eV}$) is very close to it, it is assigned to the same nanotube. There remains three possible candidates, the (8,7), (13,0), (12,2) nanotubes for the two RBMs located at 232 and 235 cm^{-1} RBMs

($E_{laser} = 1.59$ eV). The 232 cm^{-1} RBM is assigned to the (12,2) nanotube with a smaller diameter. Since (8,7) and (13,0) nanotubes have the same diameter, the 235 cm^{-1} RBM is assigned to the (8,7) nanotube which has the E_{22}^S values that are the closest to E_{laser} .

Table 6.4: (n,m) assignments to the different experimental RBMs in epoxy composites and PVA films, using different sets of E_{ii} values.

Laser energy	Exp. RBM position	TB1 model	TB3 model	Exp. E_{ii} values
HiPco SWNTs				
1.49 eV	207	(11,6)	(11,6)	(11,6)
	217	(9,7)	(9,7)	(9,7)
	227	(10,5)	(10,5)	(10,5)
	237	(11,3)	(11,3)	(11,3)
	266	(10,2)	(10,2)	(10,2)
1.59 eV	210	(12,4)	(14,1)	(12,4)
	232	(12,2)	(12,2)	(12,2)
	238	(8,7)	(11,3)	(11,3)
	268	(10,2)	(10,2)	(10,2)
	272	(11,0)	(11,0)	(11,0)
1.96 eV	200	(13,4)	(15,0)	(13,4)
	221	(12,3)	(12,3)	(12,3)
	257	(9,4)	(11,1)	(11,1)
	284	(8,4)	(7,5)	(7,5)
	299	(9,2)	(9,2)	(8,3)
Elicarb SWNTs				
1.49 eV	165	(15,6)	(15,6)	(15,6)
	192	(16,0)	(16,0)	(11,7)
	208	(11,6)	(11,6)	(11,6)
	217	(9,7)	(9,7)	(9,7)
	228	(10,5)	(10,5)	(10,5)
	237	(11,3)	(11,3)	(11,3)
	266	(10,2)	(10,2)	(10,2)
1.59 eV	207	(11,6)	(11,6)	(11,6)
	218	(10,6)	(10,6)	-
	227	(10,5)	(10,5)	(10,5)
	235	(13,0)	(8,7)	(8,7)
	266	(10,2)	(10,2)	(10,2)
1.96 eV	201	(13,4)	(15,0)	(13,4)
	221	(12,3)	(12,3)	(12,3)
	254	(8,6)	(8,6)	(8,6)
	284	(8,4)	(7,5)	(7,5)

The 257 cm^{-1} RBM ($E_{laser} = 1.96\text{ eV}$) is assigned to the (11,1) nanotube, which is expected to be closer to the resonance window than the (9,4) nanotube. The 268 and 272 cm^{-1} RBMs ($E_{laser} = 1.59\text{ eV}$) are assigned to the (10,2) and (11,0) nanotubes respectively, because of their proximity. The 266 cm^{-1} RBMs ($E_{laser} = 1.49\text{ eV}$ and 1.59 eV) are very close to the 268 cm^{-1} RBM, and should also be assigned to the (10,2) nanotube.

This leaves two possible candidates for the 284 cm^{-1} RBM ($E_{laser} = 1.96\text{ eV}$): the (7,5) and (8,4) nanotubes. The (7,5) nanotube is expected to be much closer to the resonance window and is assigned to this RBM. Finally, among the three remaining nanotubes suitable for the 299 cm^{-1} RBM ($E_{laser} = 1.96\text{ eV}$), the (8,3) nanotube has the E_{11}^M values that are the closest to E_{laser} .

Table 6.10 is a list of the (n,m) assignments for the RBMs observed in epoxy/SWNT composites and PVA/SWNT film, using the different sets of E_{ii} values.

6.6 Conclusions

Resonant Raman spectroscopy has proven to be a powerful technique to characterize the nanotube structure. The typical Raman spectrum collected from SWNTs exhibits four main bands: the low-frequency RBMs, the D, G and G' bands. These bands have different positions and relative intensities depending on the incident laser wavelength used. Different RBMs with various relative intensities appear depending on the laser wavelength and the nanotube diameter distribution in the sample, as expected by resonance theory.

The position of these bands from nanotubes embedded in an epoxy or PVA matrix were found to be upshifted, compared to their position in the powder. This apparent upshift of the Raman band positions is attributed to heating effects: the black nanotube powder is heated under laser irradiation, and as a consequence the Raman band positions are downshifted. Nanotube heating is limited in the composite sample because of their low concentration in the polymer matrix.

The strain-induced intensity variations of the Raman RBMs of SWNTs in epoxy/SWNT composites and PVA/SWNT films were investigated using three different lasers of wavelengths 830, 780 and 632 nm. Variations of between 10% and 200% of the RBM intensities were observed over a range of strain between -0.6% and 0.7%. The trend (increase or decrease) as well as the magnitude of the intensity variations depends on the nanotube diameter and its chirality. RBMs separated by just $1\text{-}2\text{ cm}^{-1}$, which is close to the resolution of the spectrometer, can have opposite behaviors under strain, depending on the laser wavelength used. The RBM position and width remain constant, within the resolution of the spectrometer, in the entire strain range. These RBM intensity variations were accompanied by a shift of the G and G' bands, which have showed to be a good indicator of nanotube deformation.

These RBM intensity variations are explained entirely by resonance theory. Using tight-binding calculations, the electronic band structure of SWNTs is predicted to vary significantly with uniaxial strain. The nanotubes are thus moved closer or further away from resonance depending on their structure, causing the intensity variations.

Previous structure assignments by Raman spectroscopy of isolated nanotubes based only on the RBM position and the electronic DOS calculations were difficult [70]. Using the nanotube RBM position, their electronic DOS and also the effect of strain upon the RBM intensity, a new and more reliable method was developed to determine the nanotube structure.

Several nanotubes can correspond to a specific RBM, if only the diameter and electronic DOS are considered. The effect of strain upon the electronic DOS reduces the number of possible candidates, and in some cases can be used to assign a unique structure to a RBM. The information from deformation and the use of two lasers of close wavelengths can confirm if two RBMs separated by just $1\text{-}2\text{ cm}^{-1}$ correspond or not to the same nanotube. This method to assign structure to nanotubes can be applied to metallic and semiconducting nanotubes in a close diameter range. It was applied to macroscopic mixtures of nanotubes and not isolated nanotubes, so it is

applicable to any synthesis products, without having to fractionate the nanotubes and separate them from bundles.

The structure assignment depends on the E_{ii} values of the nanotubes and different assignments were made depending on the set of E_{ii} values used: those from the tight-binding models or those found in the literature from photoluminescence and Raman spectroscopy measurements on isolated nanotubes suspended in water.

Chapter 7

Effect of Residual Stresses Upon the RBMs of Nanotubes in Epoxy Composites

7.1 Introduction

Extensive research work has been done upon the reinforcement of polymer matrices by SWNTs [3]. With their aspect ratio and their exceptionally high tensile modulus [210], they can become the future reinforcement agents in composite materials. Apart from the properties of the reinforcement agent, other factors such as the processing conditions affect the mechanical properties of the composite. Curing temperature affects the tensile modulus and strength of epoxy resins [211]. High-temperature curing of composites also results in the presence of residual stresses, which arise from the thermal shrinkage and the thermal expansion mismatch between the polymer matrix and the reinforcement agent [211]. The shrinkage during the cure of the epoxy resin must be differentiated from the one during the cooling above and below the glass transition temperature T_g . Lange *et al.* reported that the shrinkage of an epoxy resin during the cure or during the cooling above T_g is negligible compared to the one during the cooling below T_g [212]. The magnitude of these residual stresses was found to increase with the increasing difference between T_g and room temperature [213]. Large residual stresses may lead to the formation of cracks and a reduction in strength [212]. On the other hand, they can also have a positive influence on the toughness of the composite [214] and improve the strength of the interface between the polymer matrix and the reinforcing agent [211].

Raman spectroscopy has proven to be a powerful tool to investigate the local strains in fiber- or nanotube-reinforced composites [128,211] (see Chapter 3). The G' band behavior under strain was found to be sensitive to the curing temperature of the epoxy composite and the difference between the cold-cured

and hot-cured samples was attributed to the presence of residual stresses induced by the shrinkage of the epoxy matrix [128]. The RBM intensity also varies with strain, since strain leads to the modification of the resonance conditions that enhance the Raman intensity (see Chapter 6). In the following section, the residual stresses in epoxy composites reinforced by SWNTs are investigated by Raman spectroscopy. Relative RBM intensity variations and the G' band position are reported as a function of the curing temperature between 20°C and 150°C. The G' band position shift in the hot-cured samples is compared to the one from four-point bending tests, the magnitude of the residual strains is estimated.

7.2 Experimental

The purified SWNTs were prepared by the HiPco process [7] and obtained from Carbon Nanotechnologies Inc. (USA). A mixture of nanotubes and 19 parts of Araldite iso-4-one hardener HY5052 was first sonicated for an hour and then magnetically stirred for 30 minutes. After the addition of 50 parts of Araldite epoxy resin LY5052, the mixture was manually stirred for five minutes, cast on a mould (dimensions 120 x 10 x 5 mm) made in poly(tetrafluoroethylene) and left in a vacuum oven for 30 minutes to degas. The cold-cured sample was prepared by leaving the composite to cure at room temperature (20°C) in air for seven days, while the hot-cured samples were prepared by leaving the mould in an oven overnight (about 12 hours) at a fixed temperature. The hot-cured samples were solid when taken out of the oven and left to cool down to room temperature in air. The nanotube weight fraction was 0.05% for all samples. When the composite beams (about 3 mm thick) were released from the mould, their surfaces were ground using SiC grinding papers (grade 600) and water as a lubricant.

For each sample, between 50 and 100 Raman spectra were collected in the backscattering geometry using a Renishaw 1000 Raman microprobe system. The peak positions and relative intensity values presented in the following section are the mean values from the different spectra. The laser beam was of near-infrared wavelength $\lambda = 780$ nm ($E_{laser} = 1.59$ eV). For

comparison, a cold-cured composite sample was deformed in compression using a four-point bending rig, and the G' band position was measured as a function of strain. The strain value was given by a strain gauge, of gauge factor 2.07, fixed on the top surface of the beam.

The glass transition temperature T_g was measured using a Perkin Elmer Pyris 1 Differential Scanning Calorimeter (DSC). The DSC measures the energy provided to the sample to maintain a zero temperature difference between the sample and a reference material, as the two specimens are heated at a controlled rate [215]. Samples of about 6 mg were inserted in aluminum pans and heated from 40 to 200°C at a scan rate of 10°C/min, in a nitrogen atmosphere flowing at a rate of 20 mL/minute. The reference material was an empty pan.

7.3 Results

Typical low-frequency Raman spectra from the samples cured at different temperatures are shown in Figure 7.1. All these spectra were collected from nanotube powder particles embedded in the epoxy composite to ensure that the Raman peak intensities are high, even at a low exposure time. All the Raman spectra are fitted with six Lorentzian components. In the sample cured at room temperature, they are centered at 207, 216, 227, 235, 268, and 273 cm^{-1} . These RBM positions are similar to those in the HiPco powder, and lower than the positions of the same RBMs in the well-dispersed areas of the composite. The RBM widths are approximately the same in all spectra.

The absolute RBM intensity values vary depending on the position of the laser spot. However, the relative RBM intensities were found to be similar from one area to another on the same sample. Therefore, the RBM intensities were all normalized to the intensity of the main RBM centered at 268 cm^{-1} . The RBM intensities relative to the 268 cm^{-1} RBM are displayed in Figures 7.2-7.6. The intensities of the RBMs centered at 207, 216, 227, 235 and 273 cm^{-1} decrease compared to the 268 cm^{-1} RBM intensity. The magnitude of the decrease depends on the RBM considered. The decrease of the RBM intensity ratio is between 40% to 70% for the RBMs centered at 207, 216, 227 and 235 cm^{-1} as

the curing temperature increases from 20°C to 150°C., while there is only a slight decrease for the 273 cm⁻¹ RBM.

The RBM positions are plotted against the curing temperature in Figures 7.7-7.12. They appear to shift to lower wave numbers by 1 to 2 cm⁻¹, which is slightly larger than the resolution of the spectrometer, as the curing temperature increases from 20°C to 150°C.

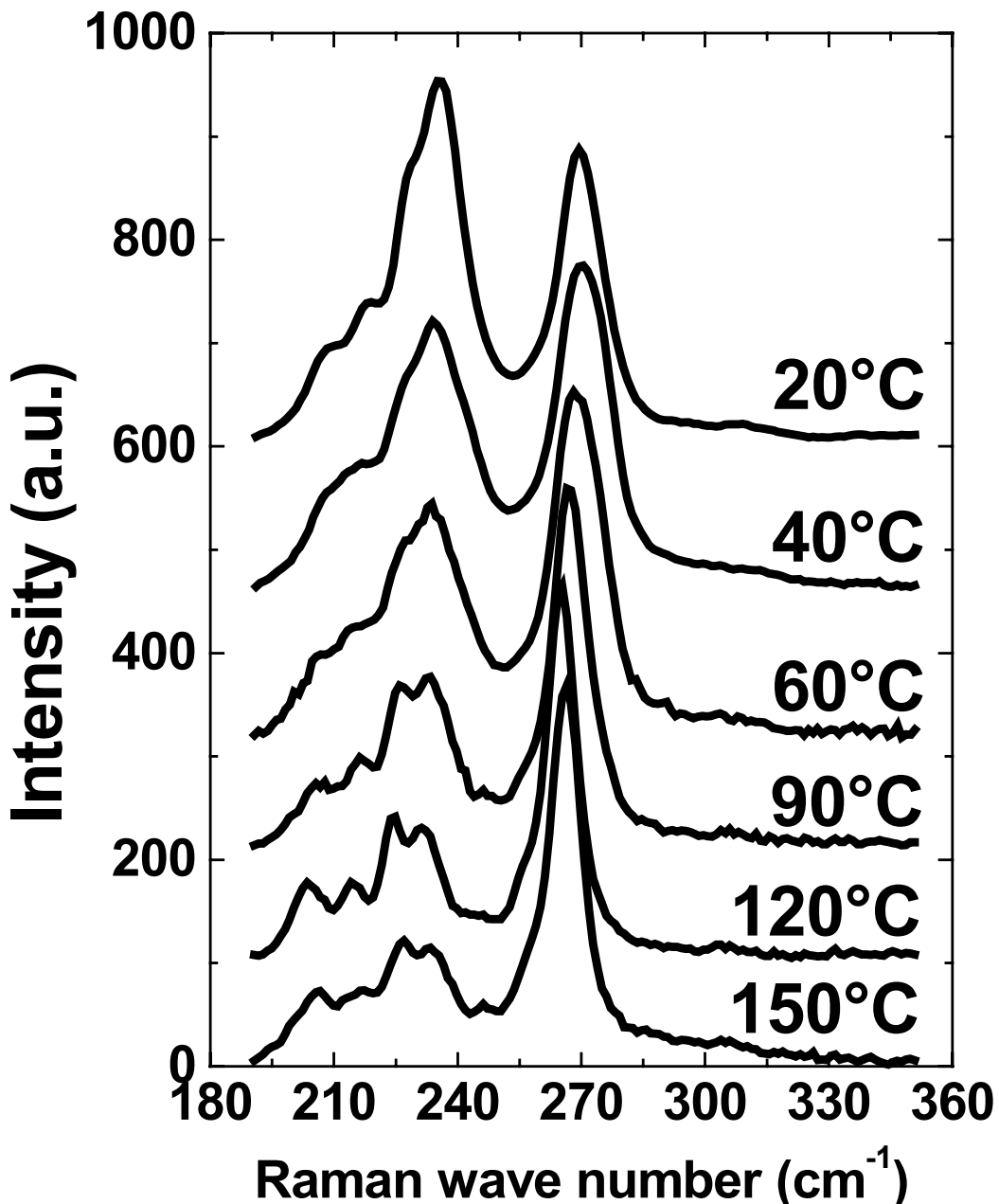


Figure 7.1: Typical low-frequency Raman spectra from HiPco nanotubes embedded in an epoxy composite cured at different temperatures. The spectra were arbitrarily offset vertically for clarity.

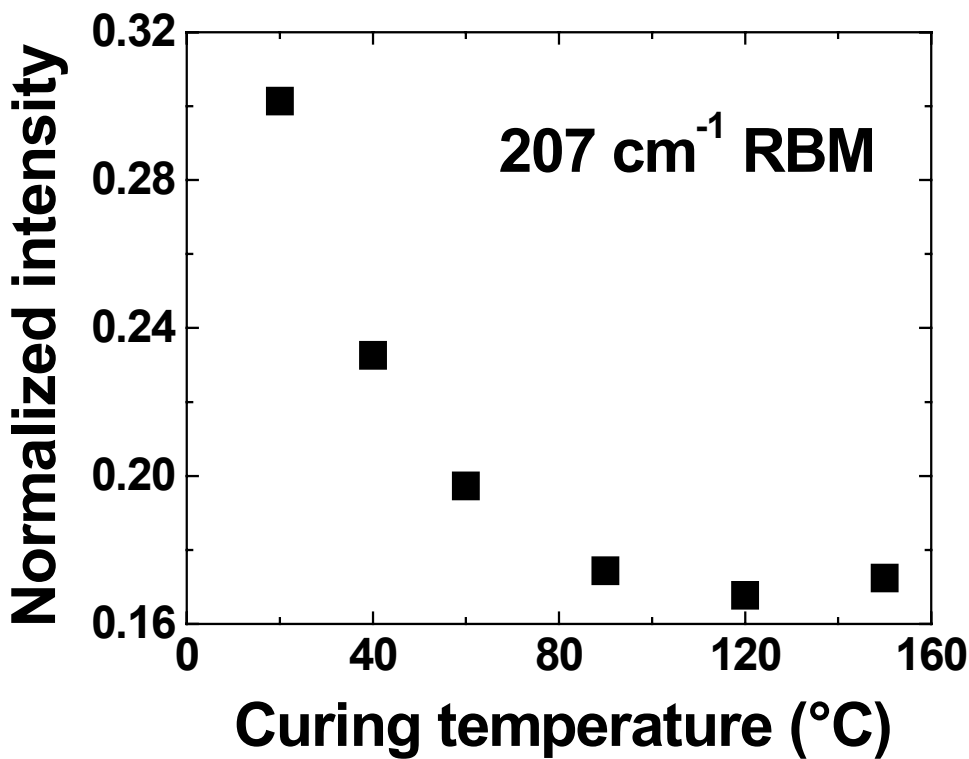


Figure 7.2: Normalized intensity of the RBM located at 207 cm^{-1} as a function of curing temperature. The intensity values were normalized to the intensity value of the main RBM, centered at 268 cm^{-1} .

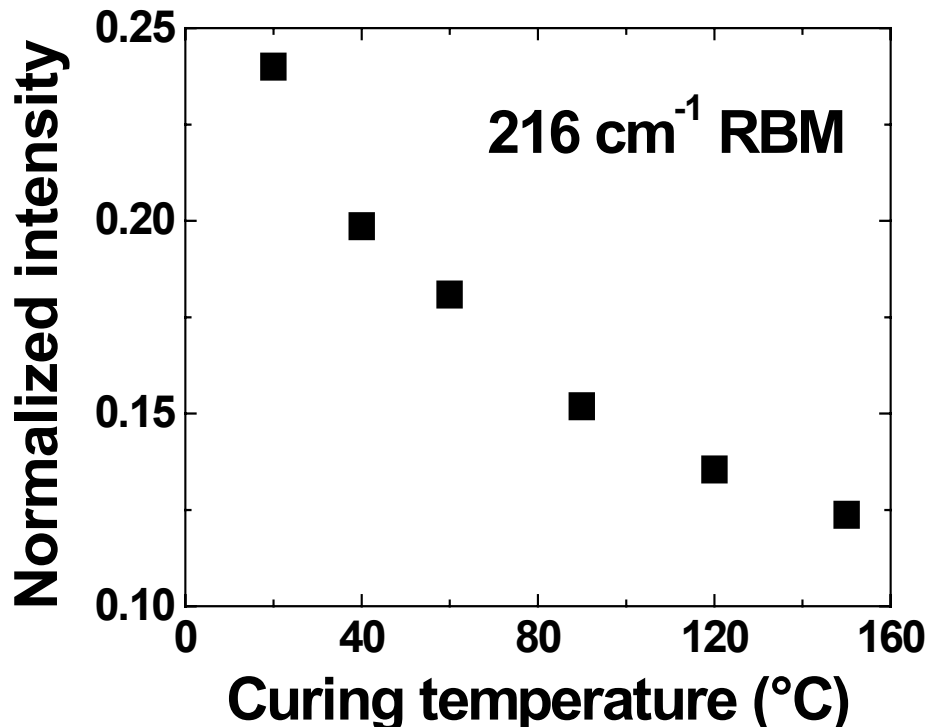


Figure 7.3: Normalized intensity of the RBM located at 216 cm^{-1} as a function of curing temperature. The intensity values were normalized to the intensity value of the main RBM, centered at 268 cm^{-1} .

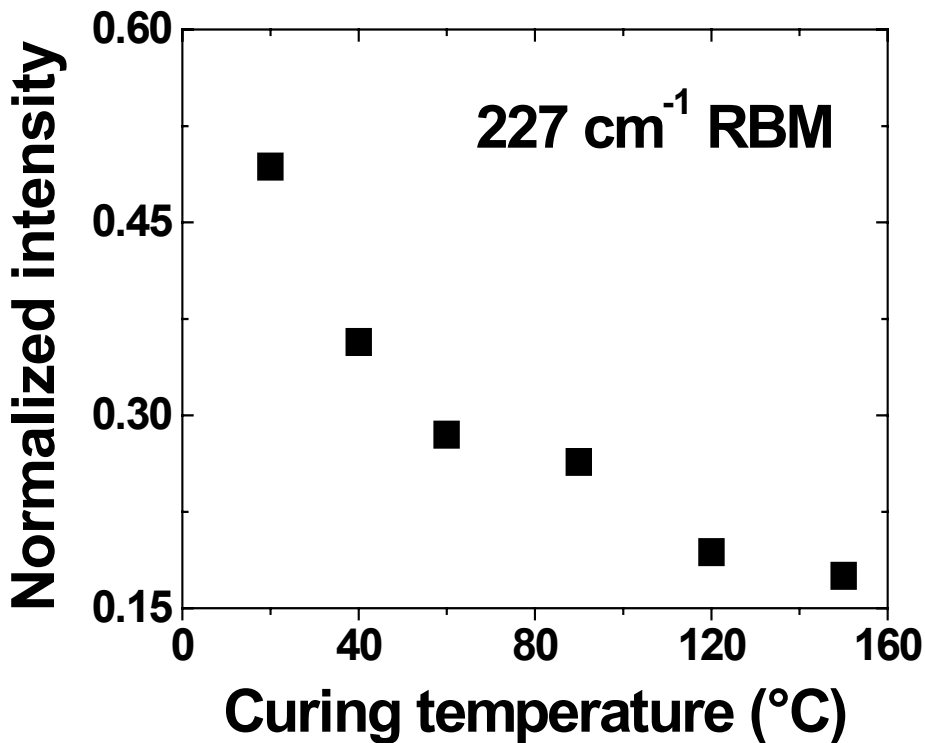


Figure 7.4: Normalized intensity of the RBM located at 227 cm^{-1} as a function of curing temperature. The intensity values were normalized to the intensity value of the main RBM, centered at 268 cm^{-1} .

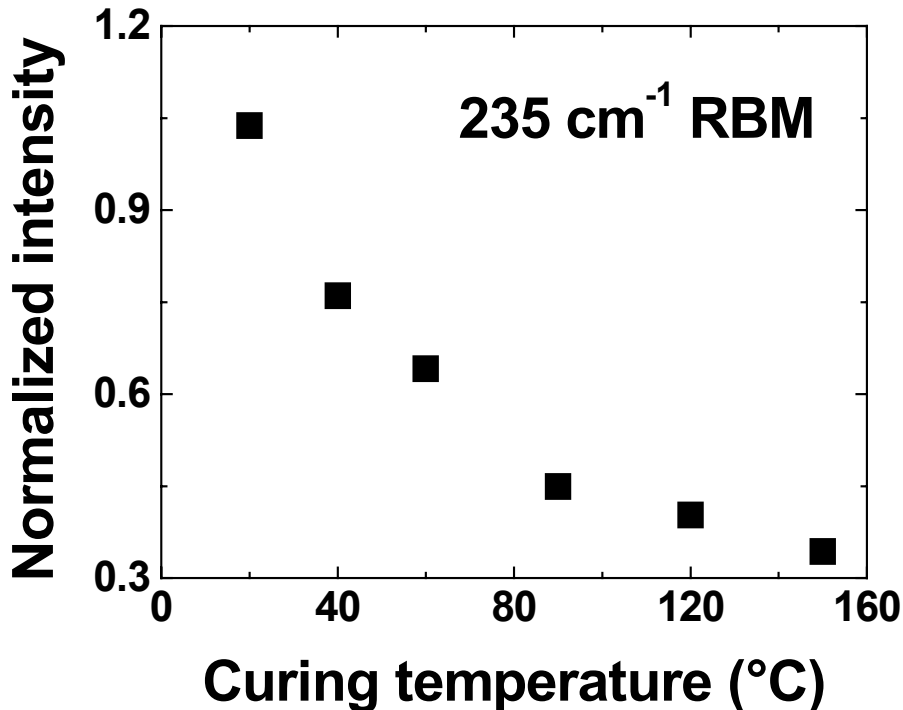


Figure 7.5: Normalized intensity of the RBM located at 235 cm^{-1} as a function of curing temperature. The intensity values were normalized to the intensity value of the main RBM, centered at 268 cm^{-1} .

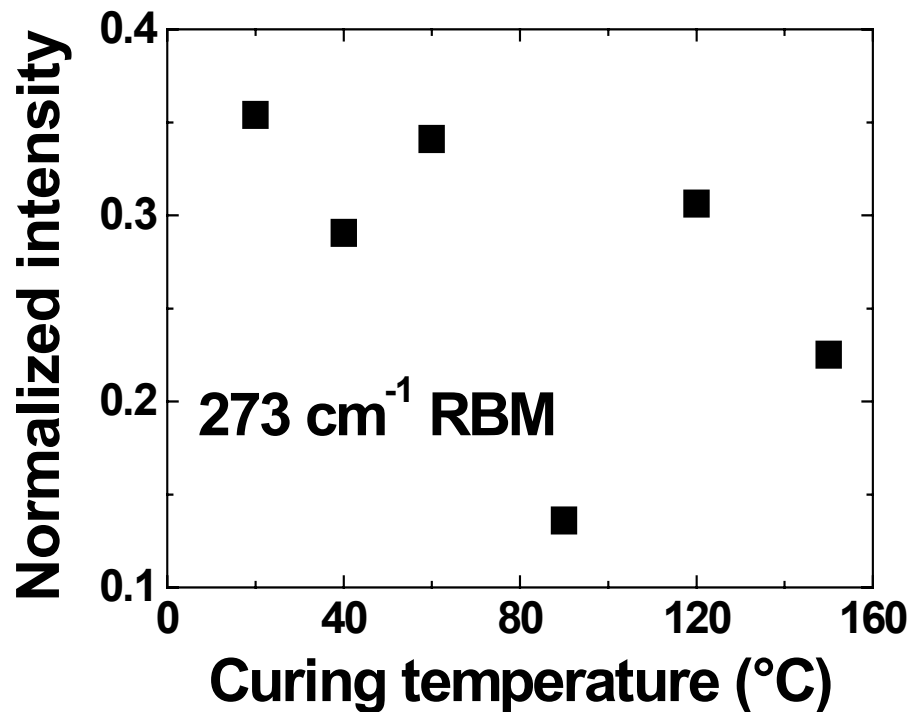


Figure 7.6: Normalized intensity of the RBM located at 273 cm^{-1} as a function of curing temperature. The intensity values were normalized to the intensity value of the main RBM, centered at 268 cm^{-1} .

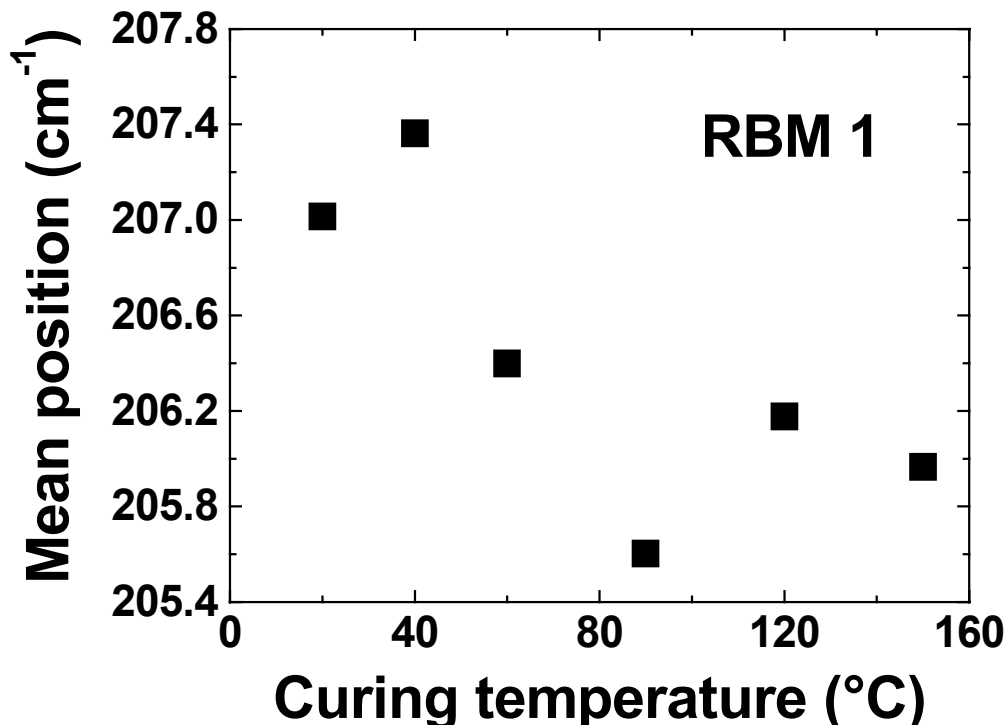


Figure 7.7: Mean position as a function of curing temperature of the RBM located at 207 cm^{-1} in the cold-cured sample.

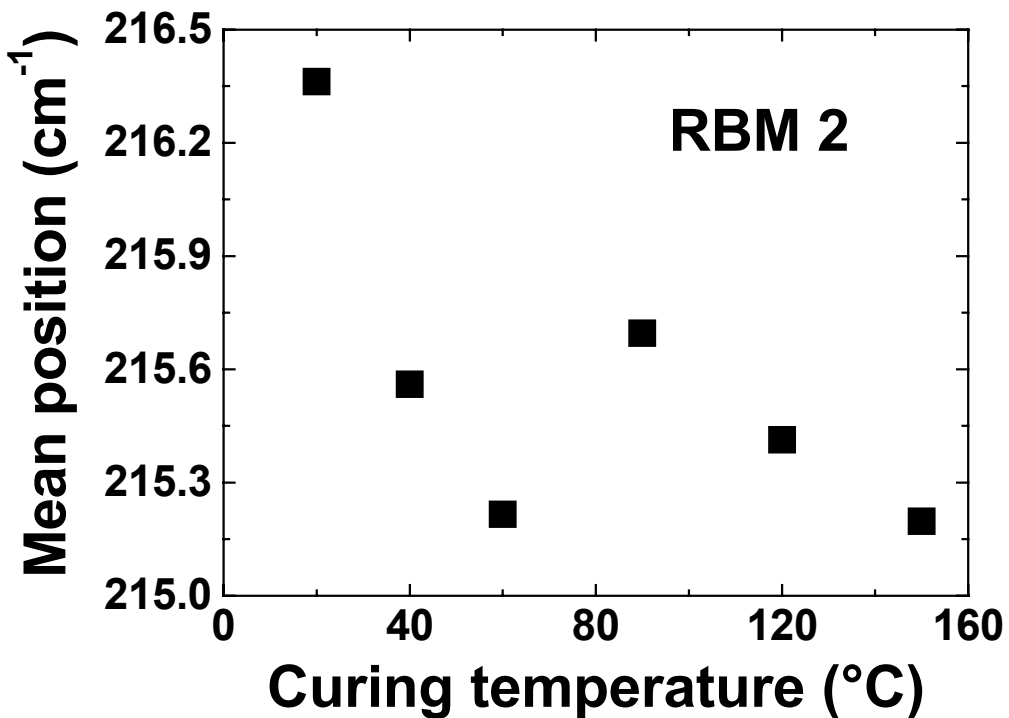


Figure 7.8: Mean position as a function of curing temperature of the RBM located at 216 cm^{-1} in the cold-cured sample.

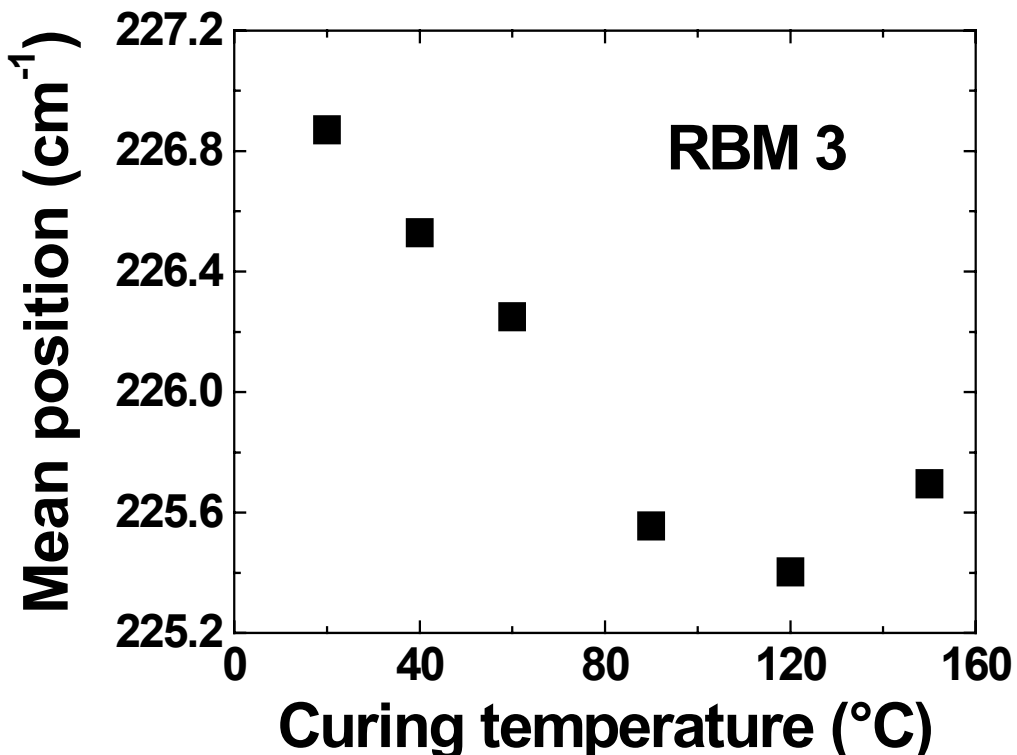


Figure 7.9: Mean position as a function of curing temperature of the RBM located at 227 cm^{-1} in the cold-cured sample.

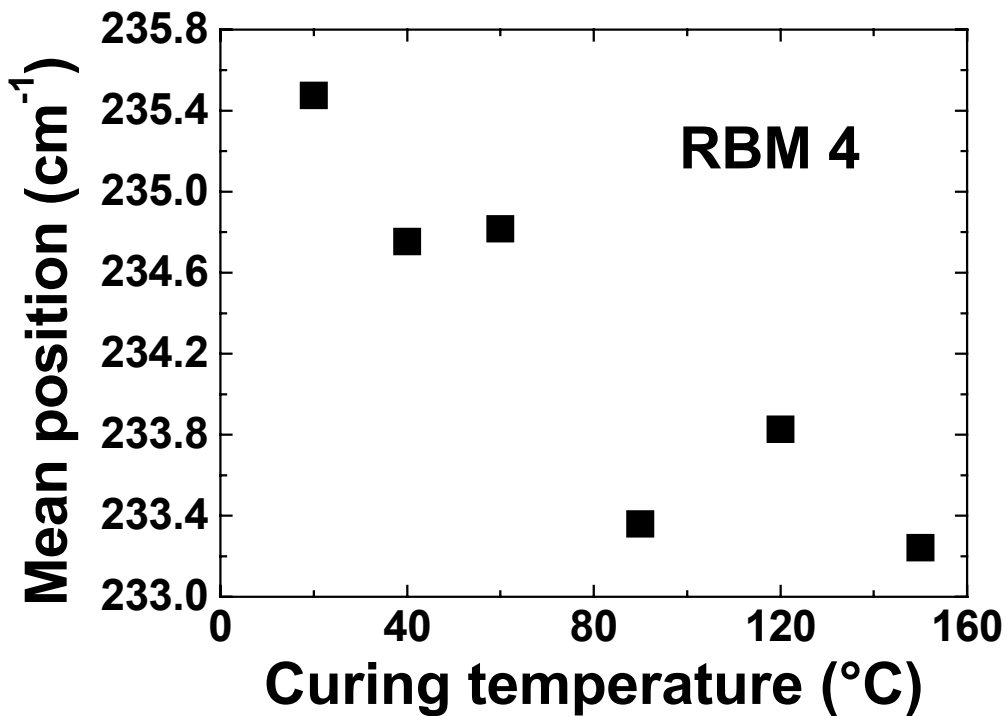


Figure 7.10: Mean position as a function of curing temperature of the RBM located at 235 cm^{-1} in the cold-cured sample.

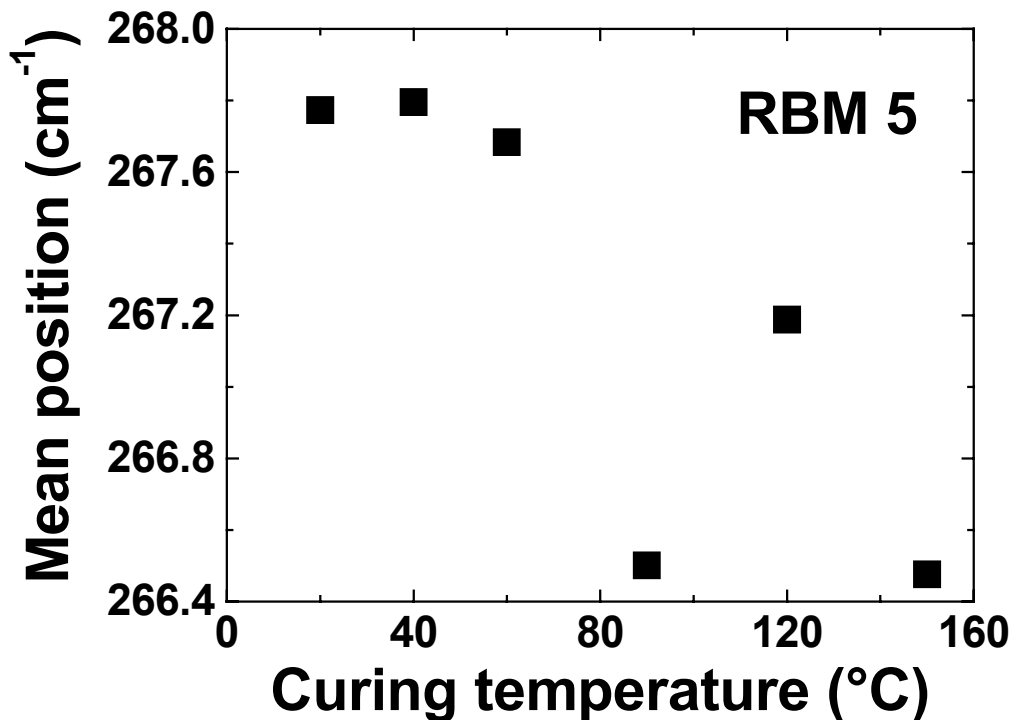


Figure 7.11: Mean position as a function of curing temperature of the RBM located at 268 cm^{-1} in the cold-cured sample.

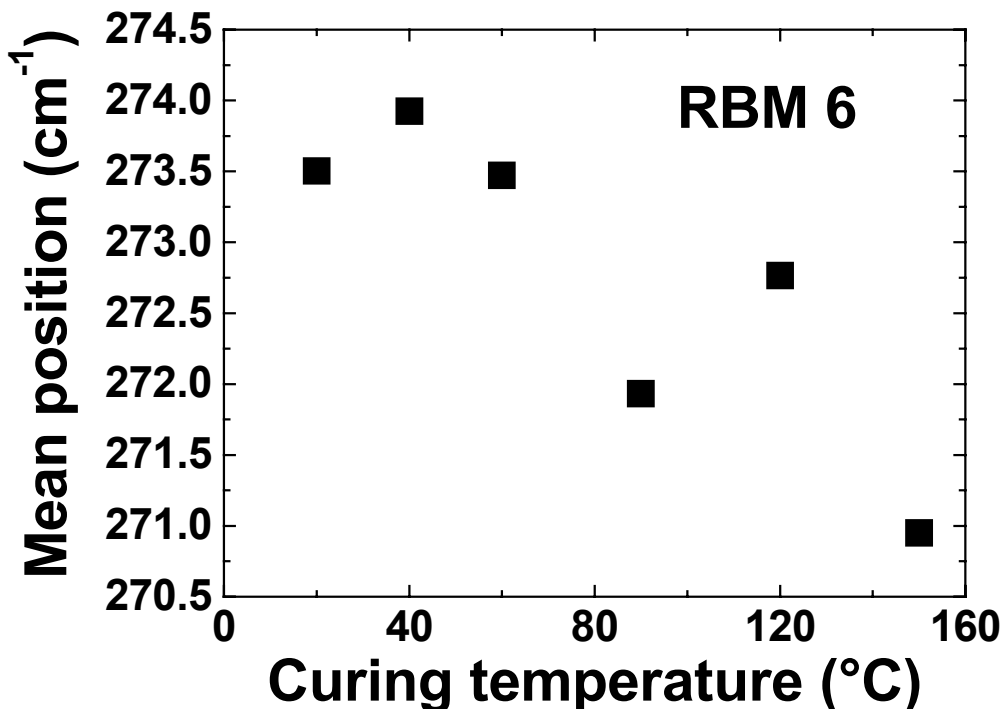


Figure 7.12: Mean position as a function of curing temperature of the RBM located at 273 cm^{-1} in the cold-cured sample.

The results on the relative intensity variations are comparable to the ones in compressive four-point bending tests and can be attributed to residual compressive strains inside the hot-cured samples. These intensity variations are explained by resonance theory. The RBM intensity reaches its maximum when the laser excitation energy E_{laser} matches the energy separation E_{ii} between the electronic bands below and above the Fermi level. The intensity variation is attributed to the shift in energy of the electronic transitions in the nanotubes under strain, moving the nanotubes closer or further away from the resonance conditions. Depending on the nanotube structure, the corresponding RBM can increase or decrease in intensity. In Chapter 6, the intensity of the RBMs at 268 and 272 cm^{-1} increased by about the same magnitude, between 15% and 20% at 0.3% compressive strain, explaining the small decrease in their intensity ratio in this study. The significant decrease of the intensity ratios with increasing curing temperature for the RBMs at 207 , 216 , 227 and 235 cm^{-1} could mean that they are moved further away from resonance in compression, while the 268 cm^{-1} RBM is moved closer to resonance.

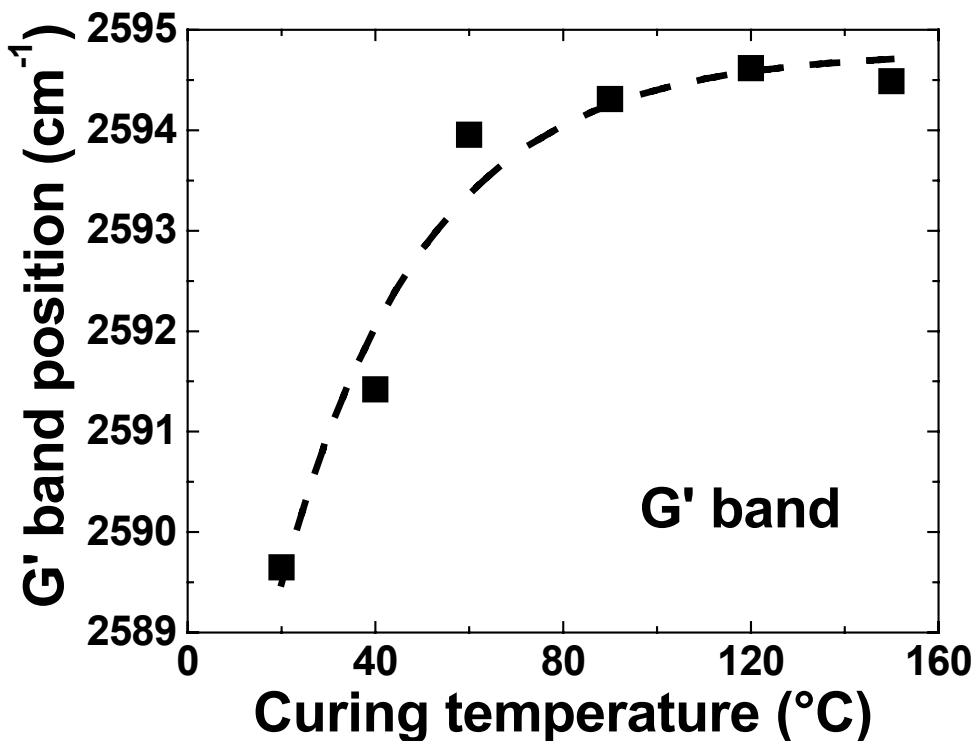


Figure 7.13: G' band position as a function of curing temperature. The dashed line is a guide for the eye.

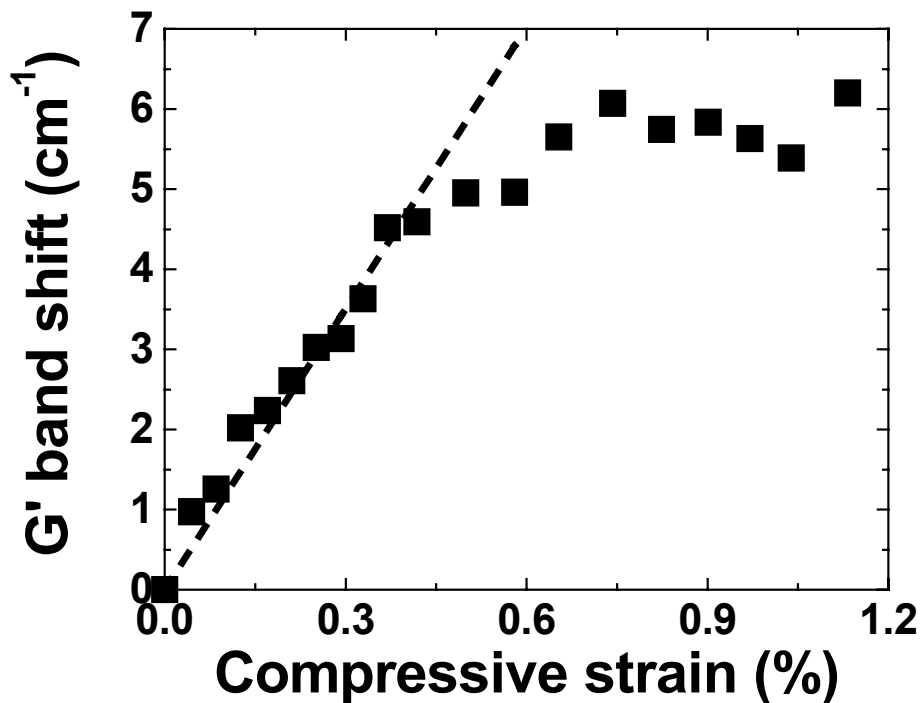


Figure 7.14: G' band position as a function of compressive strain in a four-point bending test (solid squares). A linear fit in the low strain range (dashed line) yields an initial band shift rate of $11.7 \text{ cm}^{-1}/\%$ strain.

These RBM intensity variations are accompanied by a shift of the G' band to higher wave numbers, as indicated in Figure 7.13. The G' band shifts from 2589 cm^{-1} in the cold-cured sample to nearly 2595 cm^{-1} in the sample cured at 150°C . The G' band position shifts linearly for the samples cured at 60°C and below, then deviates from linearity to reach a constant value above 90°C .

This behavior is also similar to the one observed in compressive four-point tests (Figure 7.14), where the G' band shifts linearly with compressive strain up to 0.5% and then deviates from linearity to reach a constant value. A linear fit of the data at low strains yields an initial shift rate of $11.7\text{ cm}^{-1}/\%$ strain. If we compare the data in Figures 7.13 and 7.14, the G' band shift of 4.7 cm^{-1} between the sample cured at 20°C and 90°C corresponds to a compressive residual strain of 0.5%.

7.4 Determination of the Thermal Expansion

Coefficient of the Epoxy Matrix

Using the curing temperature and the corresponding compressive residual strain value, the thermal expansion coefficient of the epoxy resin can be estimated. The expansion coefficients of the polymer matrix and the nanotubes are assumed to be constant in the temperature range between 20°C and 150°C . The residual strain ε along the carbon nanotubes can be estimated by the mismatch of the thermal expansion coefficients between the nanotubes and the epoxy matrix [211]:

$$\varepsilon = (\xi_m - \xi_n) \Delta T \quad (7.1)$$

where ΔT is the difference between room temperature and the curing temperature or T_g , whichever is the lowest, and ξ_m and ξ_n are respectively the axial expansion coefficient of the epoxy matrix and the nanotubes. The thermal expansion coefficient of the nanotube diameter and of the lattice constant in nanotube bundles have been measured by X-ray scattering as $-1.5 \times 10^{-6}\text{ }^\circ\text{C}^{-1}$ and $7.5 \times 10^{-6}\text{ }^\circ\text{C}^{-1}$ respectively [130]. These values are compared to the in-plane linear-expansion coefficient in graphite [133] of about $-13.0 \times 10^{-6}\text{ }^\circ\text{C}^{-1}$ and

the in-plane thermal expansion coefficient in multiwalled carbon nanotubes which was found to be negligible [216] (less than $1.0 \times 10^{-6} \text{ }^{\circ}\text{C}^{-1}$). The in-plane expansion coefficient in graphite of $-13.0 \times 10^{-6} \text{ }^{\circ}\text{C}^{-1}$ is taken as the expansion coefficient ξ_n along the nanotube axis.

The T_g values measured by DSC for the samples cured at 20°C, 40°C, 60°C and 90°C are 74°C, 82°C, 96°C and 115°C respectively and are higher than the curing temperature. Therefore, ΔT is the difference between room temperature and the curing temperature. Using the estimated value of 0.5% for the residual strain in the sample cured at 90°C, Equation 7.1 yields an expansion coefficient of $58 \times 10^{-6} \text{ }^{\circ}\text{C}^{-1}$ for the epoxy matrix. A similar analysis of the data for the samples cured at 40°C and 60°C gives expansion coefficients of $62 \times 10^{-6} \text{ }^{\circ}\text{C}^{-1}$ and $69 \times 10^{-6} \text{ }^{\circ}\text{C}^{-1}$ respectively. These values are close to the reported value of $63 \times 10^{-6} \text{ }^{\circ}\text{C}^{-1}$ for the same epoxy resin [211].

7.5 Conclusions

The relative intensities of the nanotube RBMs in epoxy composites are found to vary as a function of the curing temperature. The intensity variation magnitude depends on the RBM considered. These variations are similar to the variations in compressive four-point bending tests, and attributed to the compressive residual strains inside the hot-cured samples, which induce the shift in energy of the electronic transitions in the nanotubes under strain. The G' band position shifts to higher wave numbers with rising curing temperature. By comparing this shift to the one from compressive four-point bending tests, the residual strains are estimated to be less than 0.5%. The values of the expansion coefficient for the epoxy matrix estimated from the experimental data are consistent with the previously reported value of $63 \times 10^{-6} \text{ }^{\circ}\text{C}^{-1}$.

Chapter 8

Conclusions

8.1 Raman Spectroscopy on SWNTs

Resonant Raman spectroscopy has proven to be a powerful technique to characterize the nanotube structure. The typical Raman spectrum collected from SWNTs exhibits four main bands: the low-frequency RBMs, the D, G and G' bands. These bands have different positions and relative intensities depending on the incident laser wavelength used. Different RBMs with various relative intensities appear depending on the laser wavelength and the nanotube diameter distribution in the sample, as expected by resonance theory.

The position of these bands from nanotubes embedded in an epoxy or PVA matrix were found to be upshifted, compared to their position in the powder. This apparent upshift of the Raman band positions is attributed to heating effects: the black nanotube powder is heated under laser irradiation, and as a consequence the Raman band positions are downshifted. Nanotube heating is limited in the composite sample because of their low concentration in the polymer matrix.

8.2 Effect of Uniaxial Deformation on the Intensity of the Raman RBMs of Nanotubes

The strain-induced intensity variations of the Raman RBMs of SWNTs in epoxy/SWNT composites and PVA/SWNT films were investigated using three different lasers of wavelengths 830, 780 and 632 nm. Variations of between 10% and 200% of the RBM intensities were observed over a range of strain between -0.6% and 0.7%. The trend (increase or decrease) as well as the magnitude of the intensity variations depends on the nanotube diameter and its chirality. RBMs separated by just $1\text{-}2\text{ cm}^{-1}$, which is close to the resolution of the spectrometer, can have opposite behaviors under strain, depending on the laser

wavelength used. The RBM position and width remain constant, within the resolution of the spectrometer, in the entire strain range. These RBM intensity variations were accompanied by a shift of the G and G' bands, which have showed to be a good indicator of nanotube deformation.

These RBM intensity variations are explained entirely by resonance theory. Using tight-binding calculations, the electronic band structure of SWNTs is predicted to vary significantly with uniaxial strain. The nanotubes are thus moved closer or further away from resonance depending on their structure, causing the intensity variations.

8.3 Tight-Binding Calculations on the electronic DOS of Nanotubes

Two models based on the tight-binding approximation, previously developed by Yang *et al.* and Reich *et al.*, were presented to calculate the nanotube electronic band structure and DOS, and their modifications under uniaxial strain: one includes only the interactions with the nearest-neighboring carbon atoms in the hexagonal lattice (TB1 model), the other includes the interactions with up to the third-nearest neighboring carbon atoms (TB3 model). The electronic transition energies E_{ii} obtained by the TB3 model are systematically lower than those from the TB1 model. The E_{ii} values are found to vary with strain by the two models. The variation trends and magnitudes depend strongly on the nanotube structure. The variation trends predicted by the two models are identical, except for the armchair nanotubes which are sensitive to uniaxial strain according to the TB3 model. Also, the magnitude of the shift predicted by the TB3 model is systematically higher than those from the TB1 model.

The chirality assignments from Raman spectroscopy are heavily dependent on the theoretical E_{ii} values. A difference of several tens of meV for the E_{ii} values can lead to the assignment of a different structure to a RBM. In order to check the accuracy of the results from the tight-binding models, the E_{ii} values obtained by the tight-binding models were compared to experimental values from photoluminescence spectroscopy (semiconducting nanotubes) and

Raman excitation profiles (metallic nanotubes). For the semiconducting nanotubes, the theoretical E_{22}^S values are generally lower than the experimental ones. For the metallic nanotubes, the experimental E_{11}^M values are between the two sets of theoretical values. The ratio between the experimental and theoretical E_{ii} values for the semiconducting and metallic nanotubes was fitted successfully with functions of the nanotube diameter and chiral angle, with mean errors of several meV in the diameter range between 0.8 and 1.6 nm. These fit functions can now be used to predict the strain-induced shifts of the experimental values.

These calculations confirm that the nanotubes are moved closer or further away from resonance conditions depending on the nanotube structure and the laser wavelength used in the Raman spectroscopic measurements.

8.4 Structure Assignments by Raman Spectroscopy

Previous structure assignments by Raman spectroscopy of isolated nanotubes based only on the RBM position and the electronic DOS calculations were difficult. Using the nanotube RBM position, their electronic DOS and also the effect of strain upon the RBM intensity, a new and more reliable method was developed to determine the nanotube structure.

Several nanotubes can correspond to a specific RBM, if only the diameter and electronic DOS are considered. The effect of strain upon the electronic DOS reduces the number of possible candidates, and in some cases can be used to assign a unique structure to a RBM. The information from deformation and the use of two lasers of close wavelengths can confirm if two RBMs separated by just $1\text{-}2 \text{ cm}^{-1}$ correspond or not to the same nanotube. This method to assign structure to nanotubes can be applied to metallic and semiconducting nanotubes in a close diameter range. It was applied to macroscopic mixtures of nanotubes and not isolated nanotubes, so it is applicable to any synthesis product, without having to fractionate the nanotubes and separate them from bundles.

The structure assignment depends on the E_{ii} values of the nanotubes and different assignments were made depending on the set of E_{ii} values used: those from the tight-binding models or those found in the literature from photoluminescence and Raman spectroscopy measurements on isolated nanotubes suspended in water.

8.5 Effect of Residual Stresses Upon the RBMs of Nanotubes in Epoxy Composites

The relative intensities of the nanotube RBMs in epoxy composites are found to vary as a function of the curing temperature. The intensity variation magnitude depends on the RBM considered. These variations are similar to the variations in compressive four-point bending tests, and attributed to the compressive residual strains inside the hot-cured samples, which induce the shift in energy of the electronic transitions in the nanotubes under strain. The G' band position shifts to higher wave number with rising curing temperature. By comparing this shift to the one from compressive four-point bending tests, the residual strains are estimated to be less than 0.5%. The values of the expansion coefficient for the epoxy matrix estimated from the experimental data are consistent with the previously reported value of $63 \times 10^{-6} \text{ }^{\circ}\text{C}^{-1}$.

Chapter 9

Suggestions for Future Work

9.1 Different Laser Wavelengths and Polymer Matrices

The four-point bending test results were obtained using three different wavelengths. In order to study different nanotubes, especially nanotubes with larger diameters and metallic nanotubes, other laser wavelengths are needed to bring them in resonance. Preliminary experiments were performed with an Ar⁺ ion laser (514 nm, $E_{laser} = 2.41$ eV) on epoxy/SWNT composite, but the fluorescence of the epoxy matrix makes the collection of Raman spectra difficult. Tests on non-fluorescent PMMA/SWNT composites revealed that there was a very poor load transfer from the PMMA matrix to the SWNTs, judging from the near-constant G' band position during the four-point bending tests.

Other polymer matrices might also yield a higher load transfer to the nanotubes. The G and G' band were used to monitor the load transfer, and so far, they indicate a failure of the polymer-nanotube interface around 0.5% in tension and -0.4% in compression. A higher strain applied to the nanotube can induce a shift of the E_{ii} values through the entire resonance window, which could result in the observation of a maximum of the RBM intensity in some cases.

9.2 Different Nanotube Sources

These experiments also have to be repeated on nanotubes from other sources. Depending on the synthesis method and the synthesis parameters, different nanotubes and diameter distributions can be obtained. At larger diameters (larger than 2 nm), many nanotubes are expected to have very close E_{ii} values and this is where this new method to determine the nanotube structure would be the most useful.

Measurements on double-walled carbon nanotubes are another important aspect. It is possible to obtain two different RBMs from double-walled carbon nanotubes corresponding to the two concentric nanotubes [217]. These two concentric nanotubes could have different chiralities and thus different behavior under strain. Also the load transfer to the outer nanotube is expected to differ from the one to the inner nanotube.

9.3 Pressure

This study was restricted to low strain values (less than 1%), mainly because of the poor load transfer at higher strain values between the nanotubes and the polymer matrix. In order to increase the maximum strain applied on the nanotubes, experiments in a pressure cell where the pressure can be higher than 10 GPa are possible. A wider strain range would enable the observation of a maximum in the Raman RBM intensity which is the signature of resonance effects. Also, according to theory, the DOS variations depend on the type of strain applied on the nanotube [12]. For example, the semiconducting nanotubes are expected to be sensitive to strain along their axis, but not along their circumferential direction. It would be interesting to see if pressure will have the same effect on the RBM intensities as uniaxial strain.

Optical absorption spectroscopy on films of nanotube bundles [111] and suspensions of debundled nanotubes [112] under pressure indicate that all electronic transition energies E_{ii} shift to lower energies with increasing pressure. This result is in contradiction with tight-binding and local-density approximation calculations that predict that the band gap variation trend with strain depends on the nanotube (n,m) indexes [113].

9.4 Isolated Carbon Nanotubes

Finally, it would be interesting to repeat these experiments at the individual nanotube level. The orientation of the isolated nanotubes can lead to different behaviors under strain depending on the angle between the nanotube and the strain axis and also on the angle between the nanotube axis and the polarization of the laser. The RBMs from individual nanotubes are generally

sharper and more definite, thus giving a more precise value of the RBM intensity and position.

Cronin *et al.* reported a Raman spectroscopic study of an isolated nanotube stretched uniaxially with an atomic force microscope tip. In one case, when stretched by 0.53%, the D, G and G' bands of the nanotube shift to lower wave numbers by 16.1, 14.8 and 27.7 cm⁻¹ respectively. No modification of the RBM in position or in intensity was detected within the resolution of the spectrometer and the anti-Stokes/Stokes RBM intensity ratio remained constant. The absence of a change under strain was explained by the fact that the E_{ii} value variation was small compared to the resonance window or that the unstressed nanotube was off resonance, so that the E_{ii} value variation does not induce an intensity variation exceeding the experimental resolution [218]. It is noted that in this study the RBM located at 186 cm⁻¹ is weak in intensity and that the holographic notch filter of the spectrometer attenuates the intensity of the Raman signal for wave numbers under 190-200 cm⁻¹, making the measurement of the RBM intensity difficult.

Appendix I

Electronic Band Structure Calculations

I.1 The TB1 Model

I.1.1 Procedure

The electronic band structure and DOS calculations of the carbon nanotubes were performed using a tight-binding approximation, based on the zone-folding scheme, following the method described in Chapter 5, which was developed by Yang *et al.* [12,13].

The value of the hopping parameter and the carbon-carbon bond length for an unstrained nanotube used in these calculations are 2.9 eV and 0.144 nm respectively. The electronic DOS was determined using:

$$DOS(E) = \frac{2}{N_{hex}} \sum_{j=1}^{N_{hex}} \int \frac{1}{\left| \frac{dE_j(k_t)}{dk_t} \right|} \delta(E_j(k_t) - E) dE \quad (I.1)$$

The derivation in the denominator was determined by calculating the difference between the $E_j(k_t)$ values at two different k_t values, divided by the difference of the k_t values. The gap between the two k_t values was determined by the width of the first Brillouin zone divided by the number of steps used in the integration.

The calculations were performed using a C/C++ program compiled using the Microsoft Visual C++ 6.0 package and executed on a laptop PC computer equipped with an Intel Pentium IV processor operating at 2.40 GHz. Two important parameters determine the accuracy and the computation time: the number of integration steps needed for the computation of the DOS and the number of points where the DOS is evaluated.

I.1.2 C/C++ Code

Following is the C/C++ code of the program that calculates the electronic DOS of the conduction band of any (n,m) nanotube as a function of energy and

as a function of strain. The valence band is exactly symmetrical to the conduction band in this model.

```
#include <stdio.h>
#include <math.h>
#include <malloc.h>

int n, m; /* Nanotube parameters */
int dr;
int Nhex; /* Number of hexagons in the 1D unit cell */
double PI=3.141592653;
double circum; /* Circumference of the nanotube in unit of a0 */
double period; /* Period of the nanotube along its axis */
double Emax=9.0; /* Energy range to take into account */
double E0=2.9; /* Hopping parameter without strain */
double a0=2.49; /* Length of the lattice vector without strain */
double E1, E2, E3; /* New hopping parameters with strain */
double r1, r2, r3; /* Strained bond lengths */
float straint; /* Strain along the nanotube axis */
float strainc; /* Strain along the nanotube circumference */
int gcdn(int n, int m); /* Program to calculate the gcdn of n and m */
void density(); /* Subprogram to calculate the electronic DOS */

void main(){

printf("Enter index n: ");
scanf("%d", &n);
printf("Enter index m: ");
scanf("%d", &m);
printf("Enter strain along axis in percent: ");
scanf("%f", &straint);
printf("Enter strain along circumference in percent: ");
scanf("%f", &strainc);
printf("\n");

circum=sqrt(n*n+m*m+n*m);
dr=gcdn(2*n+m,2*m+n);
Nhex=2*(n*n+m*m+n*m)/dr;
period=(1+straint/100)*sqrt(3)*circum*a0/dr;
r1=sqrt((n+m)*(n+m)*a0*a0*(1+strainc/100)*(1+strainc/100)/4/circum/circum+(n-m)*(n-m)*a0*a0*(1+straint/100)*(1+straint/100)/12/circum/circum);
r2=sqrt(m*m*a0*a0*(1+strainc/100)*(1+strainc/100)/4/circum/circum+(2*n+m)*(2*n+m)*a0*a0*(1+straint/100)*(1+straint/100)/12/circum/circum);
r3=sqrt(n*n*a0*a0*(1+strainc/100)*(1+strainc/100)/4/circum/circum+(n+2*m)*(n+2*m)*a0*a0*(1+straint/100)*(1+straint/100)/12/circum/circum);
E1=E0*a0*a0/3/r1/r1;
E2=E0*a0*a0/3/r2/r2;
E3=E0*a0*a0/3/r3/r3;
density();
}

void density(){

    int i, j, p, iter, channel;
    double interp, kt, energy0, energyl, result, slope;
    double med1, med2, med3, med4;
```

```

double *data;
FILE *fp2;
fp2=fopen("density.txt", "w");

printf("Enter number of points in the graph N: ");
scanf("%d", &iter);
printf("Enter number of points analyzed p: ");
scanf("%d", &p);

data=(double *) (malloc(sizeof(double)*iter));
interp=PI/period/(double)p;
med1=PI/circum/circum;
med2=sqrt(3)/2/circum*a0;

for(i=0; i<iter; i++){
    data[i]=0;
}

for(i=1; i<Nhex+1; i++) {
energy0=sqrt(fabs(E1*E1+E2*E2+E3*E3+2*E1*E2*cos(med1*i*(n+2*m)-
n*med2*(1+straint/100)*(1-p)*interp)+2*E1*E3*cos(med1*i*(2*n+m)+m*med2
*(1+straint/100)*(1-p)*interp)+2*E2*E3*cos(med1*i*(n-m)+(n+m)*med2*(1+
straint/100)*(1-p)*interp)));

    for(j=1-p; j<p; j++) {

        kt=(j+1)*interp;
        med3=n*kt*med2*(1+straint/100);
        med4=m*kt*med2*(1+straint/100);

energy1=sqrt(fabs(E1*E1+E2*E2+E3*E3+2*E1*E2*cos(med1*i*(n+2*m)-med3)+2
*E1*E3*cos(med1*i*(2*n+m)+med4)+2*E2*E3*cos(med1*i*(n-m)+med3+med4))));

        if((energy0>=0) && (energy0<Emax)){
            channel=(int)(energy0/Emax*iter);
            slope=fabs(energy1-energy0)/interp;

            if(slope==0){
                result=100;
            }
            else{
                result=1/slope;
            }
            data[channel]+=result;
        }
        energy0=energy1;
    }
}

fprintf(fp2, "Energy\t DOS\t 2*Energy\n");

for(i=0; i<iter; i++){

fprintf(fp2, "%f\t %f\t %f\n", i*Emax/iter, data[i]*2/Nhex/(2*p-1),
2*i*Emax/iter);
}

free(data);
fclose(fp2);

```

```

        printf("\n");
        main();
    }

int gcdn(int n, int m) {
    int result, i;
    if(m==0) {
        result=n;
    }
    if(m>0) {
        for(i=1; i<m+1; i++) {
            if( ((float)n/(float)i)==(int)((float)n/(float)i)) &&
((float)m/(float)i)==(int)((float)m/(float)i) ) {
                result=i;
            }
        }
    }
    return(result);
}

```

I.1.3 Convergence

In order to have a correct value of the energy separation E_{ii} between the vHs, the minimum number of integration steps needed in the DOS calculation to converge to the right energy position of the van Hove singularities has to be determined. The following plots are the results of calculations performed on a (8,0) nanotube with different numbers of integration steps. The DOS was evaluated at different energies separated by constant interval of 9 meV.

From Figure I.1, the vHs position has already reached its stable value after only 100 steps of integration. The DOS far away of the vHs is noisy for a number of integration steps lower than 10,000 (it is especially true for the case of only 100 integration steps), and converges towards its stable profile after 10,000 integration steps. The resolution chosen in these calculations is relatively low (9 meV), but is already high enough to explain the Raman results.

Another important remark about Figure I.1 is the non-converging intensity of these vHs. The intensity was found to increase on some vHs and decrease on others. This non-convergence of the vHs intensities makes the integration of the DOS over the entire energy spectrum and its normalization impossible. The integration of the DOS would normally give four, since there are two carbon atoms in the graphite unit cell and only the π and π^* bands were considered. The non-convergence makes a quantitative study of the resonance theory impossible. Therefore the study was limited to the value of the energy

separation between vHs, and to calculate it 100,000 integration steps were typically used.

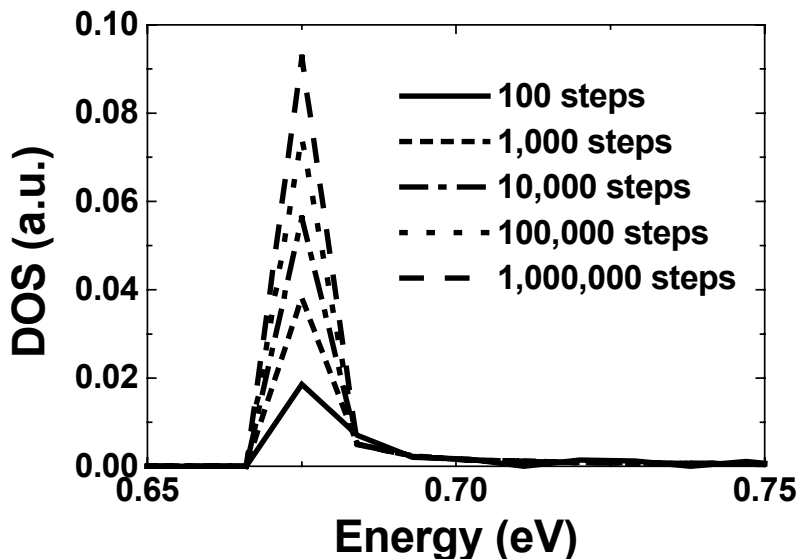


Figure I.1: Electronic DOS of a (8,0) nanotube around the first vHs in the conduction band as a function of the number of steps used in the integration process. The number of evaluation points is 10,000.

I.1.4 Resolution in Energy

The resolution in energy of the DOS plots depends on the number of points where the DOS is evaluated for energies between 0 and 9 eV in the conduction band. It is thus given by the ratio of this interval width (9 eV) by the number of evaluation points used in the calculations.

In Figure I.2, the position in energy of the first vHs in the conduction band of the (8,0) nanotube is plotted as a function of the number of evaluation points. Its value converges fast towards its stable value: it is already within 10 meV for a number of evaluation points higher than 1,000 and becomes stable for numbers higher than 10,000. All these results were obtained using 100,000 integration steps in the calculations.

In Figure I.3, the intensity of the first vHs in the conduction band of the (8,0) nanotube is plotted as a function of the number of evaluation points. It oscillates around a linear trend line towards lower values. This is another indication that the DOS cannot be studied quantitatively and is simply explained by the constant number of integration steps. All the E_{ii} values calculated with the

TB1 model were calculated using 100,000 integration steps and 10,000 evaluation points.

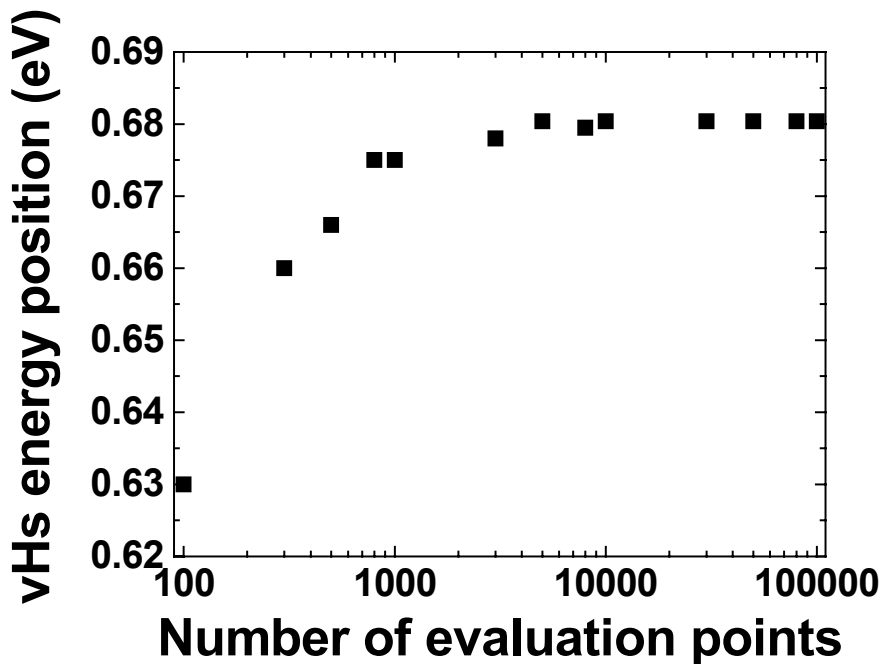


Figure I.2: Position in energy of the first vHs in the conduction band of the (8,0) nanotube as a function of the number of points where the electronic DOS was evaluated. The number of integration steps is 100,000.

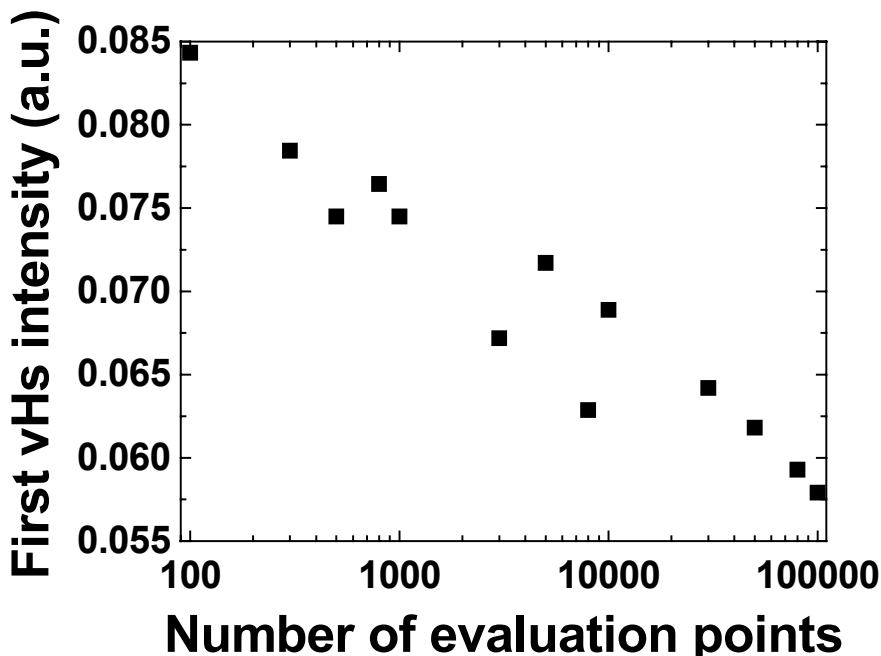


Figure I.3: Intensity of the first vHs in the conduction band of the (8,0) nanotube as a function of the number of points where the electronic DOS was evaluated. The number of integration steps is 100,000.

I.1.5 Computation Time

One important aspect that must be taken into account is the computation time. A compromise has to be reached between the accuracy of the calculations and the time it takes to perform them. The carbon nanotube is periodic along its axis and the period of its 1D unit cell depends on its chirality. Since the number of electronic bands increases with the number of hexagons in this 1D unit cell, the computation time also increases with the number of hexagons and thus the period of the nanotube along its axis.

Table I.1: Number of hexagons in the 1D unit cell for an (n,m) nanotube.

n	m	Number of hexagons in the unit cell	n	m	Number of hexagons in the unit cell
5	5	10	7	6	254
15	0	30	25	5	310
30	0	60	11	4	362
12	6	84	33	15	402
21	3	114	14	1	422
12	8	152	21	9	474
13	7	206	28	21	518

In Figure I.4a, the computation time needed to determine the DOS of the nanotube is plotted as a function of the number of hexagons in the 1D unit cell of the nanotube. The nanotubes used in this study are indicated in Table I.1 and the number of integration steps is 100,000. It was found that the computation time increases linearly with the number of hexagons.

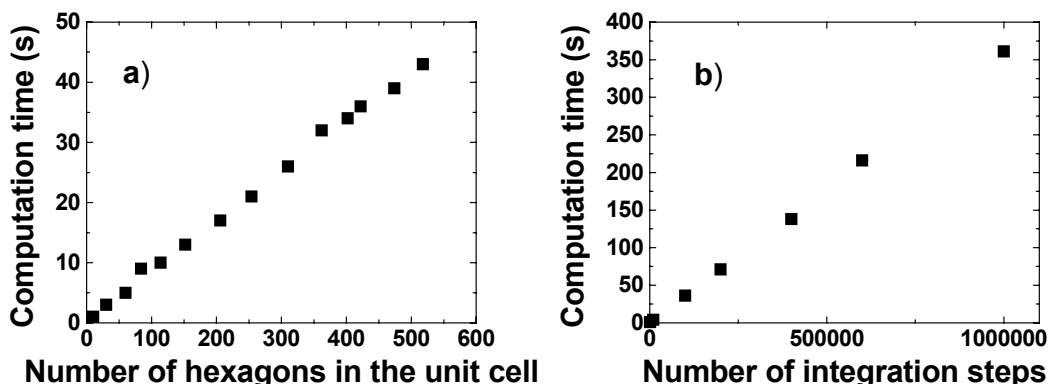


Figure I.4: Computation time as a function of a) the number of hexagons in the 1D unit cell of the nanotube (The number of integration steps is 100,000.); and b) the number of integration steps for the (14,1) nanotube. The number of evaluation points is 10,000.

In Figure I.4b, the computation time was measured as a function of the number of integration steps used in the calculations for the (14,1) nanotube. The number of evaluation points is 10,000. It was found to vary linearly with the number of integration steps.

I.2 The TB3 Model

I.2.1 Procedure

The strain-sensitive TB3 tight-binding model was presented in Chapter 5. It was introduced by Reich *et al.* [192] and extended to take into account uniaxial strain, following a similar procedure as Yang *et al.* [12,13].

The 7 parameters of the model have the following values: $\varepsilon_{2p} = -2.03 \text{ eV}$, $\gamma_0 = -2.79 \text{ eV}$, $\gamma_1 = -0.68 \text{ eV}$, $\gamma_2 = -0.30 \text{ eV}$, $s_0 = 0.30 \text{ eV}$, $s_1 = 0.046 \text{ eV}$, and $s_2 = 0.039 \text{ eV}$. These values were selected by Reich *et al.* to reproduce the optical transition energies from *ab initio* calculations [192], which underestimate the experimental values (see Chapter 5). The method to compute the electronic DOS is similar to the one described in Section I.1.1.

The calculations were performed using a C/C++ program compiled using the Microsoft Visual C++ 6.0 package and executed on a PC computer equipped with an Intel Pentium III processor operating at 500 MHz.

I.2.2 C/C++ Code

Following is the C/C++ code of the program used to calculate the electronic DOS (valence and conduction bands) of any (n,m) nanotube as a function of energy and uniaxial strain, using the TB3 tight-binding model described in Chapter 5.

```
#include <stdio.h>
#include <math.h>
#include <malloc.h>

int n, m; /* Nanotube parameters */
int dr;
int Nhex; /* Number of hexagons in the 1D unit cell */
double PI=3.141592653;
double circum; /* Circumference of the nanotube in unit of a0 */
```

```

double period; /* Period of the nanotube along its axis */
double a0=2.46;
double Emax=9.0; /* Energy range to take into account */

/* Definition of the tight-binding model parameters */
double E2p=-2.03;
double E0=-2.79;
double E1=-0.68;
double E2=-0.30;
double s0=0.30;
double s1=0.046;
double s2=0.039;

/* Definition of the parameter values when nanotube is deformed*/
double E01, E02, E03;
double E11, E12, E13;
double E21, E22, E23;
double s01, s02, s03;
double s11, s12, s13;
double s21, s22, s23;

double r1c, r1t, r2c, r2t; /* Components of r1 and r2 along c and t */
float straint; /* Strain along the nanotube axis */
float strainc; /* Strain along the nanotube circumference */

/* Subprogram to calculate the greatest common divisor */
int gcdn(int n, int m);
/* Subprogram to calculate the nanotube density of states */
void density();

void main(){

    printf("Enter index n: ");
    scanf("%d", &n);
    printf("Enter index m: ");
    scanf("%d", &m);
    printf("Enter strain along axis in percent: ");
    scanf("%f", &straint);
    printf("Enter strain along circumference in percent: ");
    scanf("%f", &strainc);
    printf("\n");

    circum=sqrt(n*n+m*m+n*m);
    dr=gcdn(2*n+m,2*m+n);
    Nhex=2*(n*n+m*m+n*m)/dr;
    period=sqrt(3)*circum*a0/dr;
    r1c=(n+m)*a0*(1+strainc/100)/2/circum;
    r1t=(m-n)*a0*(1+straint/100)/2/sqrt(3)/circum;
    r2c=-m*a0*(1+strainc/100)/2/circum;
    r2t=(2*n+m)*a0*(1+straint/100)/2/sqrt(3)/circum;
    E01=E0*a0*a0/3/(r1c*r1c+r1t*r1t);
    E02=E0*a0*a0/3/(r2c*r2c+r2t*r2t);
    E03=E0*a0*a0/3/((r1c+r2c)*(r1c+r2c)+(r1t+r2t)*(r1t+r2t));
    s01=s0*a0*a0/3/(r1c*r1c+r1t*r1t);
    s02=s0*a0*a0/3/(r2c*r2c+r2t*r2t);
    s03=s0*a0*a0/3/((r1c+r2c)*(r1c+r2c)+(r1t+r2t)*(r1t+r2t));
    E11=E1*a0*a0/((r1c-r2c)*(r1c-r2c)+(r1t-r2t)*(r1t-r2t));
    E12=E1*a0*a0/((2*r1c+r2c)*(2*r1c+r2c)+(2*r1t+r2t)*(2*r1t+r2t));
    E13=E1*a0*a0/((r1c+2*r2c)*(r1c+2*r2c)+(r1t+2*r2t)*(r1t+2*r2t));
}

```

```

s11=s1*a0*a0/((r1c-r2c)*(r1c-r2c)+(r1t-r2t)*(r1t-r2t));
s12=s1*a0*a0/((2*r1c+r2c)*(2*r1c+r2c)+(2*r1t+r2t)*(2*r1t+r2t));
s13=s1*a0*a0/((r1c+2*r2c)*(r1c+2*r2c)+(r1t+2*r2t)*(r1t+2*r2t));
E21=E2*a0*a0/3/((r1c+r2c)*(r1c+r2c)+(r1t+r2t)*(r1t+r2t));
E22=E2*a0*a0/3/(r1c*r1c+r1t*r1t);
E23=E2*a0*a0/3/(r2c*r2c+r2t*r2t);
s21=s2*a0*a0/3/((r1c+r2c)*(r1c+r2c)+(r1t+r2t)*(r1t+r2t));
s22=s2*a0*a0/3/(r1c*r1c+r1t*r1t);
s23=s2*a0*a0/3/(r2c*r2c+r2t*r2t);

density();
}

void density(){

    int i, j, p, iter, channel;
    double interp, kt, k_r1, k_r2, med1, med2, slope1, slope2;
    double result1_a, result1_b, result2_a, result2_b;
    double energy0, energyl, energy2, energy3;
    double *data;
    FILE *fp2;
    fp2=fopen("density.txt","w");
    printf("Enter number of points in the graph N: ");
    scanf("%d", &iter);
    printf("Enter number of points analyzed p: ");
    scanf("%d", &p);
    data=(double *) (malloc(sizeof(double)*iter));
    interp=PI/period/(double)p;

    for(i=0; i<2*iter; i++){
        data[i]=0;
    }

    /* Iteration on q value */

    for(i=1; i<Nhex+1; i++){

        kt=(1-p)*interp;

        k_r1=PI*i*(n+m)/circum/circum+kt*a0*(m-n)*(1+straint/100)/sqrt(3)/2/circum;
        k_r2=-PI*i*m/circum/circum+kt*a0*(2*n+m)*(1+straint/100)/sqrt(3)/2/circum;
        med1=E2p+2*E11*cos(k_r1-k_r2)+2*E12*cos(2*k_r1+k_r2)+2*E13*cos(k_r1+2*k_r2); /* Definition of Haa */
        med2=1+2*s11*cos(k_r1-k_r2)+2*s12*cos(2*k_r1+k_r2)+2*s13*cos(k_r1+2*k_r2); /* Definition of Saa */

        energy0=med1*med2;

        energyl=2*(s01*E01+s02*E02+s03*E03+s21*E21+s22*E22+s23*E23)+2*cos(k_r1-k_r2)*(s01*E02+s02*E01+s03*E22+s03*E23+s22*E03+s23*E03)+2*cos(2*k_r1+k_r2)*(s01*E03+s02*E22+s03*E01+s22*E02+s02*E21+s21*E02)+2*cos(k_r1+2*k_r2)*(s01*E21+s01*E23+s02*E03+s03*E02+s21*E01+s23*E01)+2*cos(3*k_r1)*(s01*E22+s22*E01)+2*cos(3*k_r2)*(s02*E23+s23*E02)+2*cos(3*k_r1+3*k_r2)*(s03*E21+s21*E03)+2*cos(4*k_r1+2*k_r2)*(s21*E22+s22*E21)+2*cos(4*k_r2+2*k_r1)*(s21*E23+s23*E21)+2*cos(2*k_r1-2*k_r2)*(s22*E23+s23*E22);
    }
}

```

```

energy2=med1*med1-(E01*E01+E02*E02+E03*E03+E21*E21+E22*E22+E23*E23+2*c
os(k_r1-k_r2)*(E01*E02+E03*E22+E03*E23)+2*cos(2*k_r1+k_r2)*(E01*E03+E0
2*E21+E02*E22)+2*cos(k_r1+2*k_r2)*(E01*E21+E01*E23+E02*E03)+2*cos(3*k_
r1)*E01*E22+2*cos(3*k_r2)*E02*E23+2*cos(3*k_r1+3*k_r2)*E03*E21+2*cos(4
*k_r1+2*k_r2)*E21*E22+2*cos(4*k_r2+2*k_r1)*E21*E23+2*cos(2*k_r1-
2*k_r2)*E22*E23);

energy3=med2*med2-(s01*s01+s02*s02+s03*s03+s21*s21+s22*s22+s23*s23+2*c
os(k_r1-k_r2)*(s01*s02+s03*s22+s03*s23)+2*cos(2*k_r1+k_r2)*(s01*s03+s0
2*s21+s02*s22)+2*cos(k_r1+2*k_r2)*(s01*s21+s01*s23+s02*s03)+2*cos(3*k_
r1)*s01*s22+2*cos(3*k_r2)*s02*s23+2*cos(3*k_r1+3*k_r2)*s03*s21+2*cos(4
*k_r1+2*k_r2)*s21*s22+2*cos(4*k_r2+2*k_r1)*s21*s23+2*cos(2*k_r1-
2*k_r2)*s22*s23);

result1_a=(2*energy0-energy1+sqrt(fabs((energy1-2*energy0)*(energy1-
2*energy0)-4*energy2*energy3)))/2/energy3;
result2_a=(2*energy0-energy1-sqrt(fabs((energy1-2*energy0)*(energy1-
2*energy0)-4*energy2*energy3)))/2/energy3;

/* Iteration on kt value */

for(j=1-p; j<p; j++) {

kt=(j+1)*interp;
k_r1=PI*i*(n+m)/circum/circum+kt*a0*(m-n)*(1+straint/100)/sqrt(3)/2/ci
rcum;
k_r2=-PI*i*m/circum/circum+kt*a0*(2*n+m)*(1+straint/100)/sqrt(3)/2/cir
cum;
med1=E2p+2*E11*cos(k_r1-k_r2)+2*E12*cos(2*k_r1+k_r2)+2*E13*cos(k_r1+2*
k_r2); /* Definition of Haa */
med2=1+2*s11*cos(k_r1-k_r2)+2*s12*cos(2*k_r1+k_r2)+2*s13*cos(k_r1+2*k_
r2); /* Definition of Saa */

energy0=med1*med2;

energy1=2*(s01*E01+s02*E02+s03*E03+s21*E21+s22*E22+s23*E23)+2*cos(k_r1
-k_r2)*(s01*E02+s02*E01+s03*E22+s03*E23+s22*E03+s23*E03)+2*cos(2*k_r1+
k_r2)*(s01*E03+s02*E22+s03*E01+s22*E02+s02*E21+s21*E02)+2*cos(k_r1+2*k_
r2)*(s01*E21+s01*E23+s02*E03+s03*E02+s21*E01+s23*E01)+2*cos(3*k_r1)*(s01*E22+s22*E01)+2*cos(3*k_r2)*(s02*E23+s23*E02)+2*cos(3*k_r1+3*k_r2)*(s03*E21+s21*E03)+2*cos(4*k_r1+2*k_r2)*(s21*E22+s22*E21)+2*cos(4*k_r2+2*k_r1)*(s21*E23+s23*E21)+2*cos(2*k_r1-2*k_r2)*(s22*E23+s23*E22);

energy2=med1*med1-(E01*E01+E02*E02+E03*E03+E21*E21+E22*E22+E23*E23+2*c
os(k_r1-k_r2)*(E01*E02+E03*E22+E03*E23)+2*cos(2*k_r1+k_r2)*(E01*E03+E0
2*E21+E02*E22)+2*cos(k_r1+2*k_r2)*(E01*E21+E01*E23+E02*E03)+2*cos(3*k_
r1)*E01*E22+2*cos(3*k_r2)*E02*E23+2*cos(3*k_r1+3*k_r2)*E03*E21+2*cos(4
*k_r1+2*k_r2)*E21*E22+2*cos(4*k_r2+2*k_r1)*E21*E23+2*cos(2*k_r1-
2*k_r2)*E22*E23);

energy3=med2*med2-(s01*s01+s02*s02+s03*s03+s21*s21+s22*s22+s23*s23+2*c
os(k_r1-k_r2)*(s01*s02+s03*s22+s03*s23)+2*cos(2*k_r1+k_r2)*(s01*s03+s0
2*s21+s02*s22)+2*cos(k_r1+2*k_r2)*(s01*s21+s01*s23+s02*s03)+2*cos(3*k_
r1)*s01*s22+2*cos(3*k_r2)*s02*s23+2*cos(3*k_r1+3*k_r2)*s03*s21+2*cos(4
*k_r1+2*k_r2)*s21*s22+2*cos(4*k_r2+2*k_r1)*s21*s23+2*cos(2*k_r1-
2*k_r2)*s22*s23);

result1_b=(2*energy0-energy1+sqrt(fabs((energy1-2*energy0)*(energy1-
2*energy0)-4*energy2*energy3)))/2/energy3;

```

```

result2_b=(2*energy0-energy1-sqrt(fabs((energy1-2*energy0)*(energy1-
2*energy0)-4*energy2*energy3)))/2/energy3;

        if(fabs(result1_a)<Emax) {
            if(result1_a>=0)
                channel=(int)(result1_a/Emax*iter);
            }
            else{
                channel=-1-(int)(fabs(result1_a)/Emax*iter);
            }
            slope1=fabs(result1_b-result1_a)/interp;
            if(slope1==0){
                data[channel+iter]+=100;
            }
            else{
                data[channel+iter]+=(1/slope1);
            }
        }

        if(fabs(result2_a)<Emax) {
            if(result2_a>=0){
                channel=(int)(result2_a/Emax*iter);
            }
            else{
                channel=-1-(int)(fabs(result2_a)/Emax*iter);
            }
            slope2=fabs(result2_b-result2_a)/interp;
            if(slope2==0){
                data[channel+iter]+=100;
            }
            else{
                data[channel+iter]+=(1/slope2);
            }
        }
        result1_a=result1_b;
        result2_a=result2_b;
    }
}

fprintf(fp2, "Energy\t DOS\t 2*Energy\n");

for(i=0; i<2*iter; i++){
fprintf(fp2, "%f\t %f\t %f\n", (i-iter)*Emax/iter,
data[i]*2/Nhex/(2*p-1), 2*(i-iter)*Emax/iter);
}
fclose(fp2);
printf("\n");
}

int gcdn(int n, int m){

    int result, i;
    if(m==0){
        result=n;
    }
    if(m>0){
        for(i=1; i<m+1; i++) {

```

```

        if( ((float)n/(float)i==(int)((float)n/(float)i)) &&
((float)m/(float)i==(int)((float)m/(float)i)) ){
            result=i;
        }
    }
    return(result);
}

```

I.2.3 Convergence

The electronic DOS is plotted for four different numbers of integration steps used in the program (Figure I.5). The position of the first vHs in the conduction band of a (8,0) nanotube is nearly stable for a number of integration steps higher than 1,000. After only 100 integration steps, the vHs position is within 1 meV of the converged value.

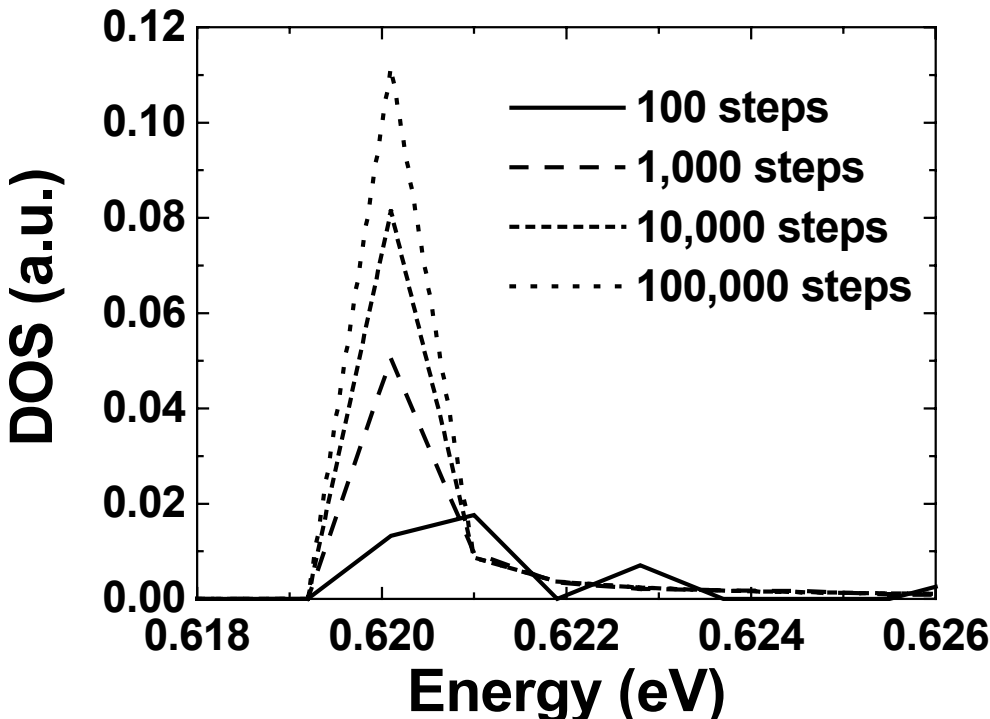


Figure I.5: Electronic DOS of a (8,0) nanotube around the first vHs in the conduction band as a function of the number of steps used in the integration process. The number of evaluation points is 10,000.

The intensity of vHs depends heavily on the number on integration steps considered in the calculations and does not converge when the number of integration steps increases. Therefore it is impossible to normalize the DOS to the number of electrons in the unit cell. A quantitative study of the DOS variation with strain and the resulting Raman intensity variation is not possible.

I.2.4 Resolution in Energy

In Figure I.6, the position of the first vHs in the conduction band is plotted against the number of evaluation points between 100 and 10,000 (for an energy range of 9 eV). The energy value converges quickly, and with only 500 evaluation points (intervals of 18 meV between 2 points), it becomes within 10 meV of the converged value. In all these calculations, the number of integration steps is 20,000. To compute the electronic transition energies E_{ii} used in Chapter 6, the number of evaluation points was 10,000 for an energy range of 2 eV, so the interval between two points was about 0.2 meV.

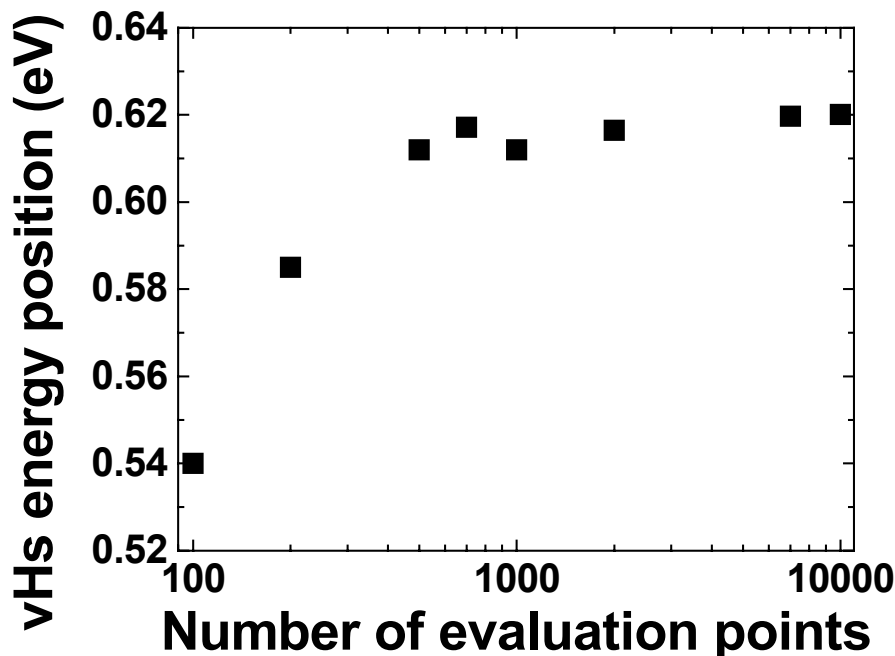


Figure I.6: Position in energy of the first vHs in the conduction band of the (8,0) nanotube as a function of the number of points where the electronic DOS was evaluated. The number of integration steps is 20,000.

I.2.5 Computation Time

The computation time was evaluated for 8 nanotubes: the (5,5), (15,0), (30,0) (12,6), (21,3), (12,8), (13,7), and (7,6) nanotubes (Figure I.7a). These nanotubes have respectively 10, 30, 60, 84, 114, 152, 206 and 254 hexagons in their unit cell (Table I.1).

For a number of integration steps of 20,000 and a number of evaluation points of 10,000, the computation time increases linearly with the number of hexagons in the unit cell considered. Compared to the values reported in Figure I.5, the computation time increased by a factor 10. This is mainly due to the poorer performance of the PC computers used. The additional factors and parameters that are taken into account in the TB3 tight-binding model further increase the computation time. The computation time also increases linearly with the number of integration steps used in the calculation of the electronic DOS of a (14,1) nanotube (Figure I.7b) (The number of evaluation points was set at 10,000).

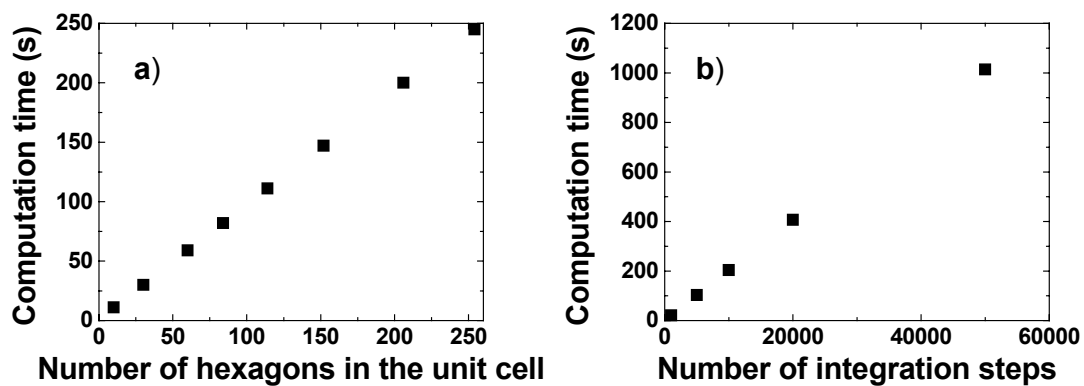


Figure I.7: Computation time as a function of a) the number of hexagons in the 1D unit cell of the nanotube (The number of integration steps is 20,000.); and b) the number of integration steps for the (14,1) nanotube. The number of evaluation points is 10,000.

Due to the long computation time required for the larger diameter chiral nanotubes, the electronic transition energies E_{ii} used in Chapter 6 were calculated with 10,000 evaluation points in an energy range of 2 eV below and above the Fermi level, using 20,000 integration steps.

Appendix II

Heating Effects on the Band Position

II.1 Laser Power Effect on the Band Position

II.1.1 D, G and G' Bands

The position of the Raman D, G and G' bands was measured on HiPco and Elicarb SWNT powder as a function of the laser power density (Figure II.1). The maximum laser power on the sample is 2.5 mW, 3.0 mW and 30 mW for the lasers of wavelength 632 nm, 780 nm and 830 nm, respectively. These values are about 10% of the power of the incident laser source. Additional filters give access to five different power values: 1, 10, 25, 50 and 100% of the maximum power. The laser spot was focused with a x50 microscope lens and its diameter was about 2 μm . However, the Raman spectra obtained at 1% of the maximum power with the 780 nm laser were too noisy to fit with Lorentzian lines and therefore were not analyzed. Also, the Elicarb SWNT samples were irreversibly damaged by the high power of the 830 nm laser, which resulted in the overall low intensity of the Raman spectra. The G' band, which is usually barely observable with this laser, was not detected at maximum power on the Elicarb SWNTs.

The D, G and G' bands were found to shift to lower wave numbers with increasing laser power density, following a trend similar to the one reported in the literature [83-85], due to the thermal expansion of the C-C bonds with the laser power density. The same trend was observed using three different lasers: one of wavelength 830 nm, another of 780 nm, and another of 632 nm, on HiPco and Elicarb SWNTs. In most cases, the most significant shift was obtained from the G' band. The upshift of the G' band at high power density for the Elicarb SWNT powder is attributed to the destruction of the nanotubes with smaller diameters.

These experiments were repeated on HiPco and Elicarb SWNTs embedded in an epoxy or PVA matrix, using the three lasers.

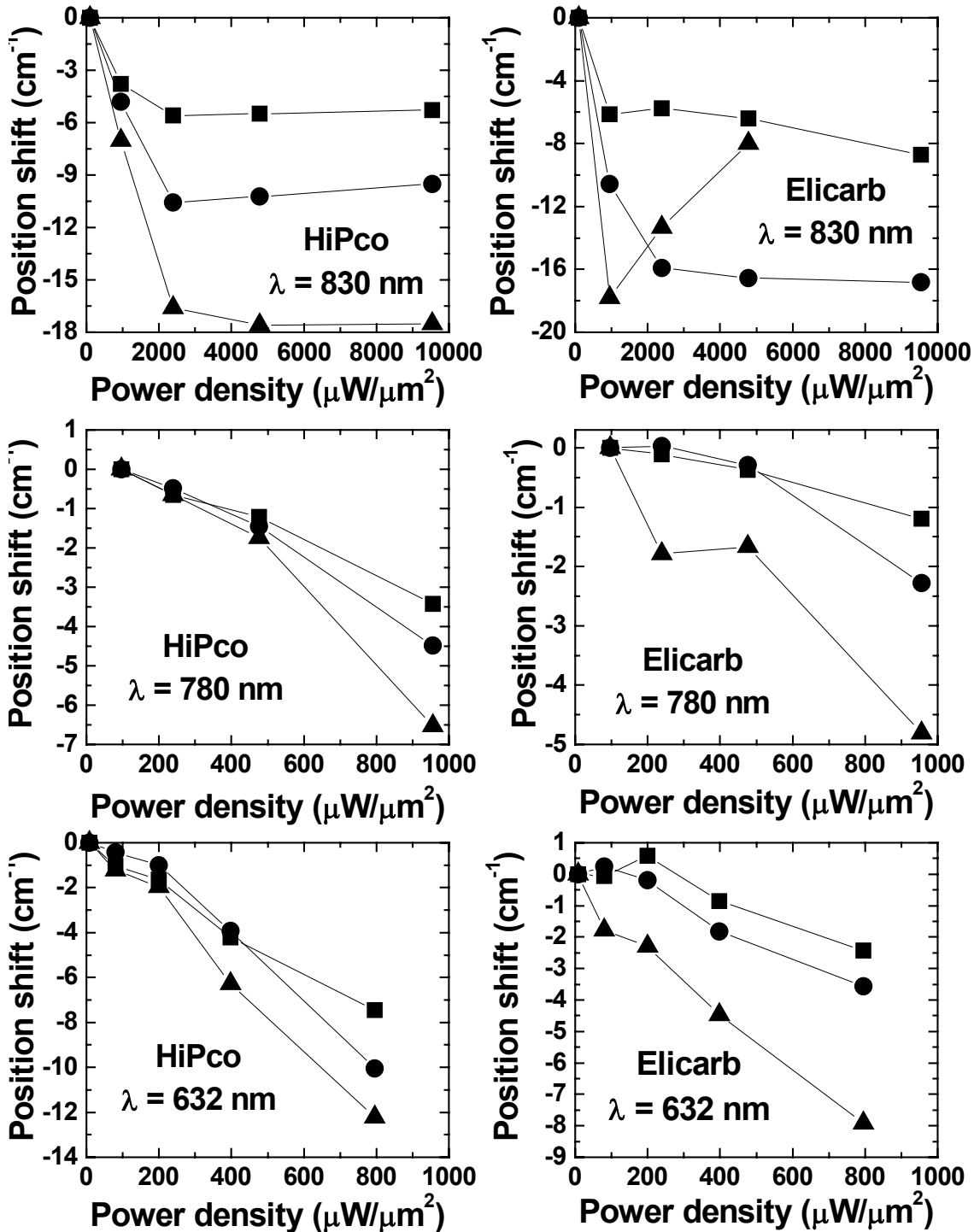


Figure II.1: Peak position shift of the D (squares), G (circles) and G' (triangles) bands as a function of the laser power density for purified HiPco and Elicarb nanotube powder.

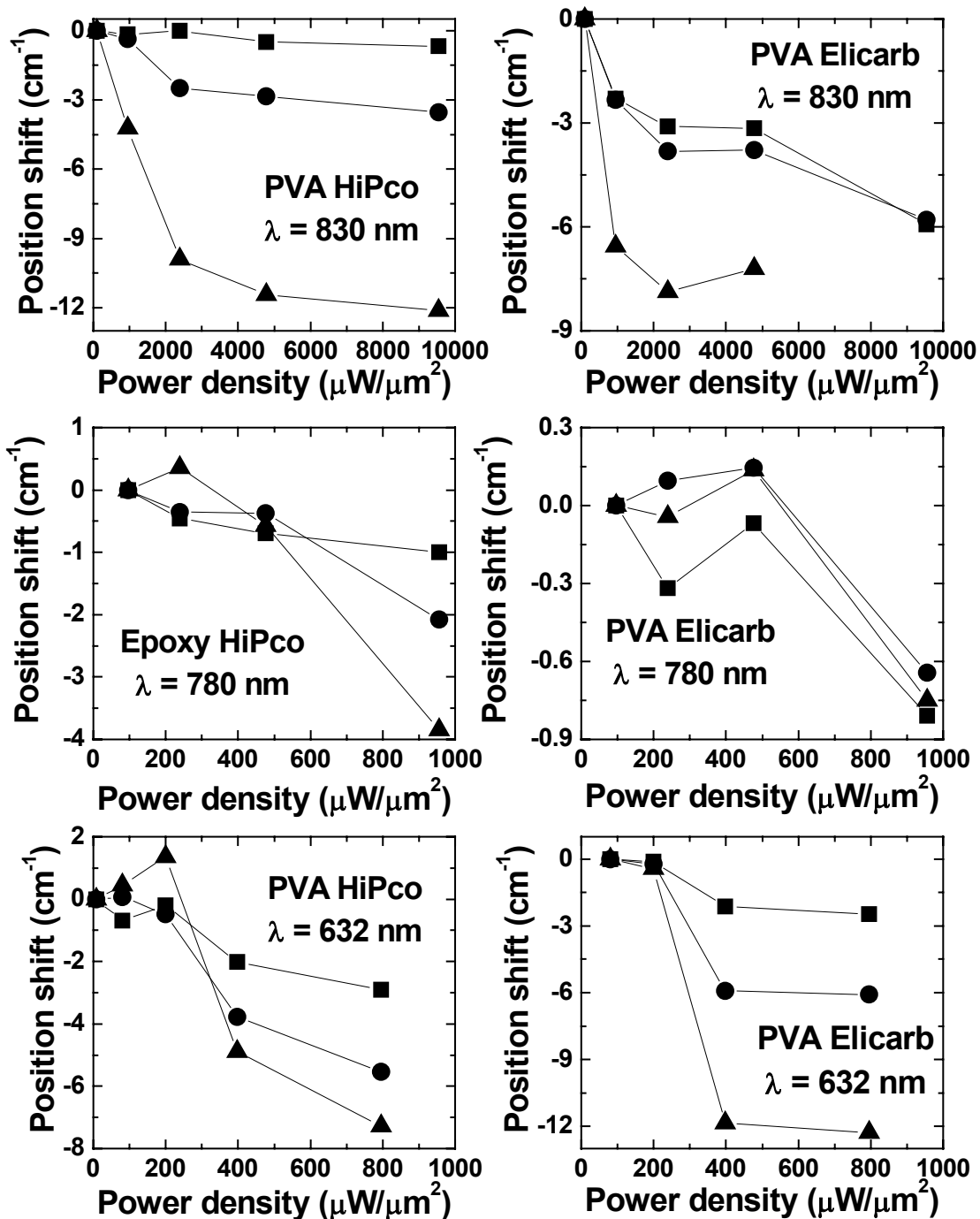


Figure II.2: Peak position shift of the D (squares), G (circles) and G' (triangles) bands as a function of the laser power density for purified HiPco and Elicarb nanotube powder in composites.

In the composite samples, a downshift of the D, G and G' bands is also observed (Figure II.2). In all cases, the magnitude of the downshift is reduced in the composite, compared to the downshift in the powder.

II.1.2 RBMs

The RBMs also shift to lower wave numbers with the laser power, with different magnitudes depending on the RBM considered and the sample (Figures II.3 to II.14). The downshift range is between less than -0.5 cm^{-1} (Figure II.6) and -6 cm^{-1} (Figure II.3). The largest downshift was recorded on the 227 cm^{-1} RBM (Figure II.3) from HiPco SWNTs using the 830 nm laser.

There is no clear relationship between the nanotube diameter and the magnitude of the downshift. In Figure II.8, the 219 and 282 cm^{-1} RBM shifts at maximum power are approximately the same.

Similar measurements were made on HiPco SWNT bundles embedded in an epoxy matrix (Figure II.10), in PVA films (Figures II.9 and II.11), and also on Elicarb SWNT bundles in PVA films (Figures II.12 and II.14). The magnitude of the RBM position shifts is lower in the composite compared to the powder. The downshifts range is between -1 and -6 cm^{-1} for RBMs from HiPco SWNT powder (Figure II.5), and between -0.2 and -2.5 cm^{-1} for RBMs from HiPco SWNTs in PVA films (Figure II.11).

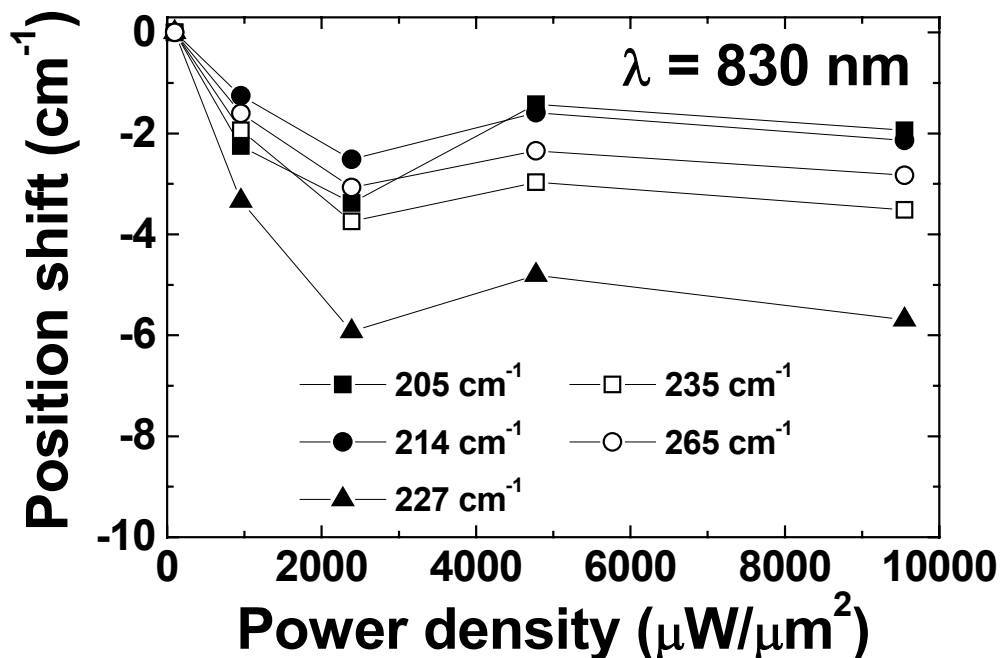


Figure II.3: Peak position shift of 5 RBMs as a function of the laser power density for purified HiPco nanotube powder. The laser used was of wavelength 830 nm.

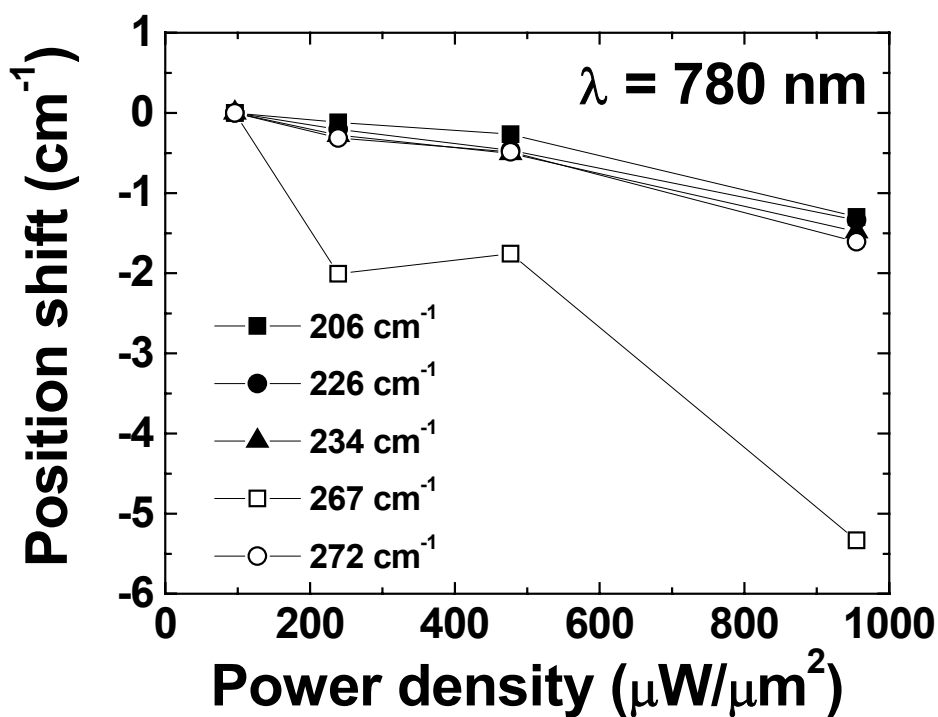


Figure II.4: Peak position shift of 5 RBMs as a function of the laser power density for purified HiPco nanotube powder. The laser used was of wavelength 780 nm.

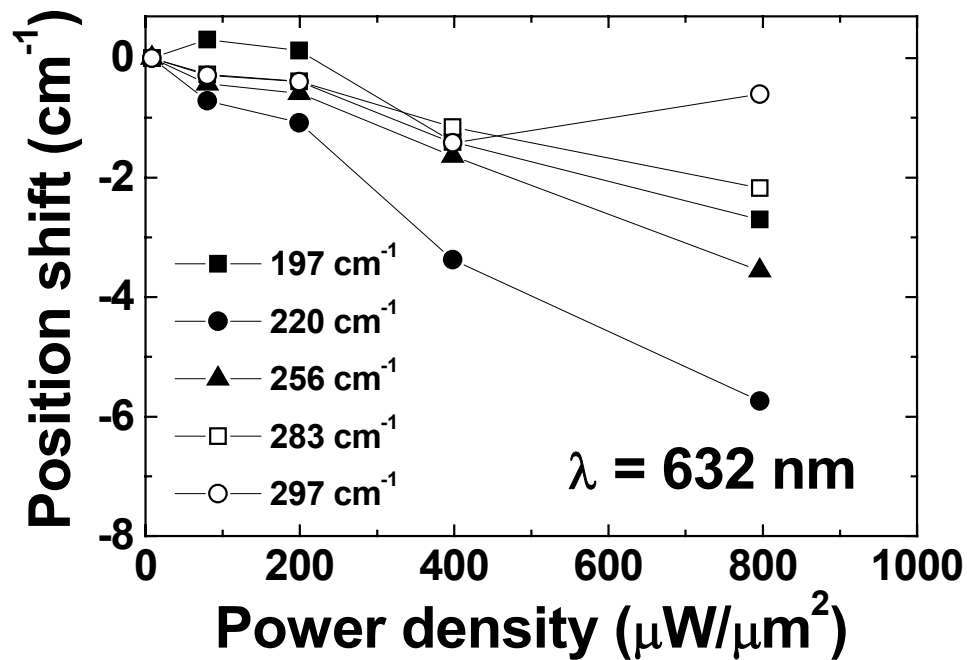


Figure II.5: Peak position shift of 5 RBMs as a function of the laser power density for purified HiPco nanotube powder. The laser used was of wavelength 632 nm.

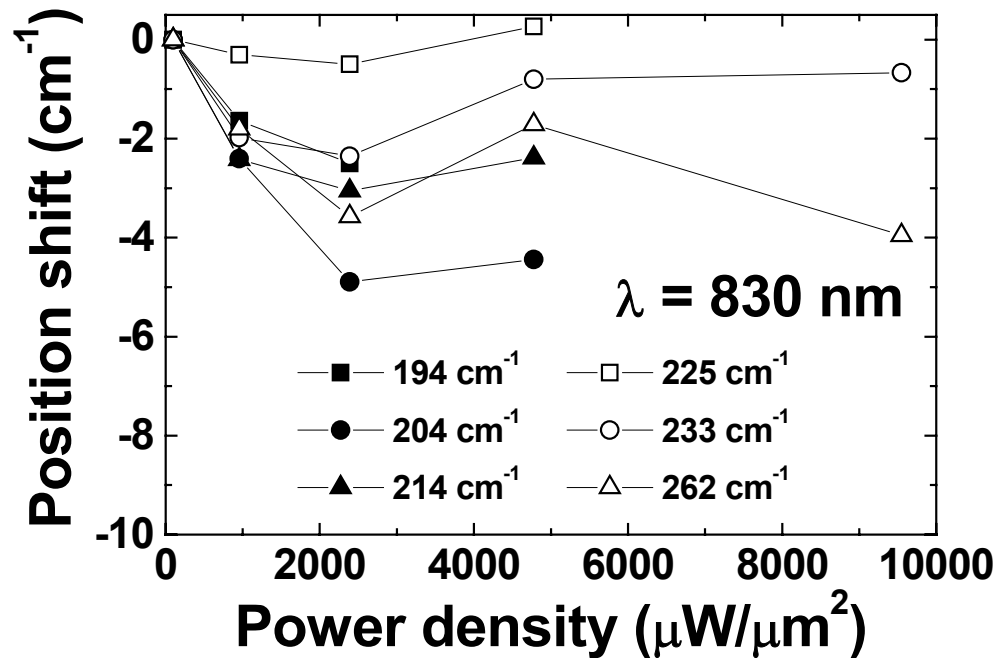


Figure II.6: Peak position shift of 6 RBMs as a function of the laser power density for purified Elicarb nanotube powder. The laser used was of wavelength 830 nm.

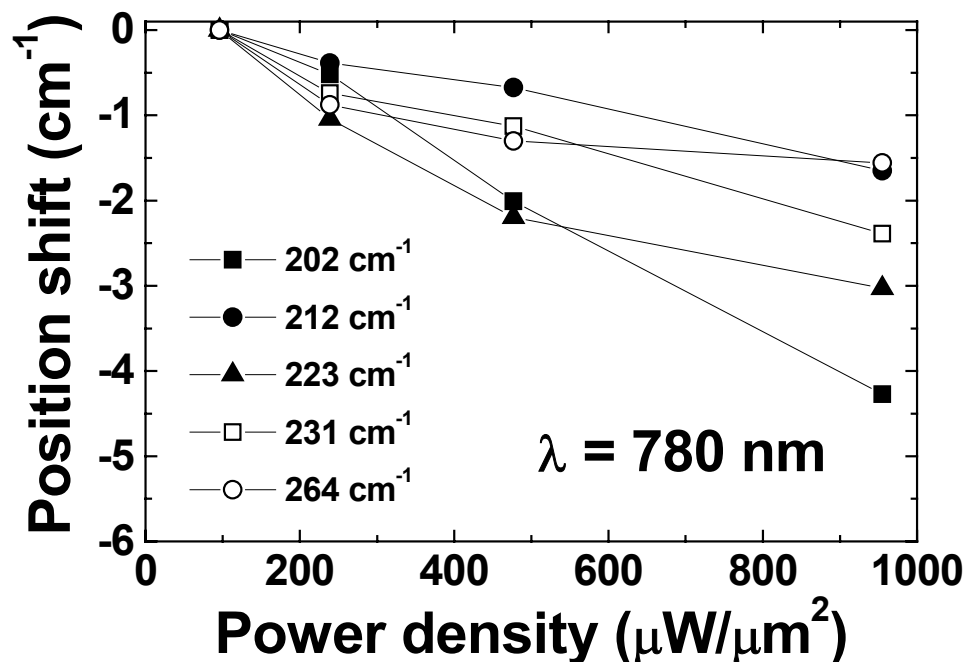


Figure II.7: Peak position shift of the 5 RBMs as a function of the laser power density for purified Elicarb nanotube powder. The laser used was of wavelength 780 nm.

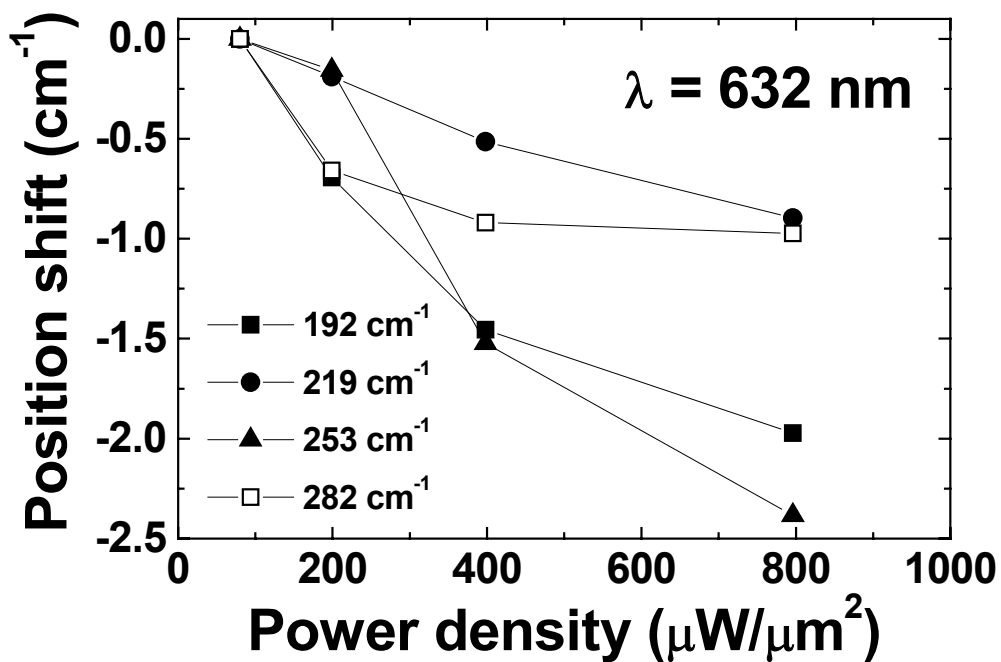


Figure II.8: Peak position shift of the 4 RBMs as a function of the laser power density for purified Elicarb nanotube powder. The laser used was of wavelength 632 nm.

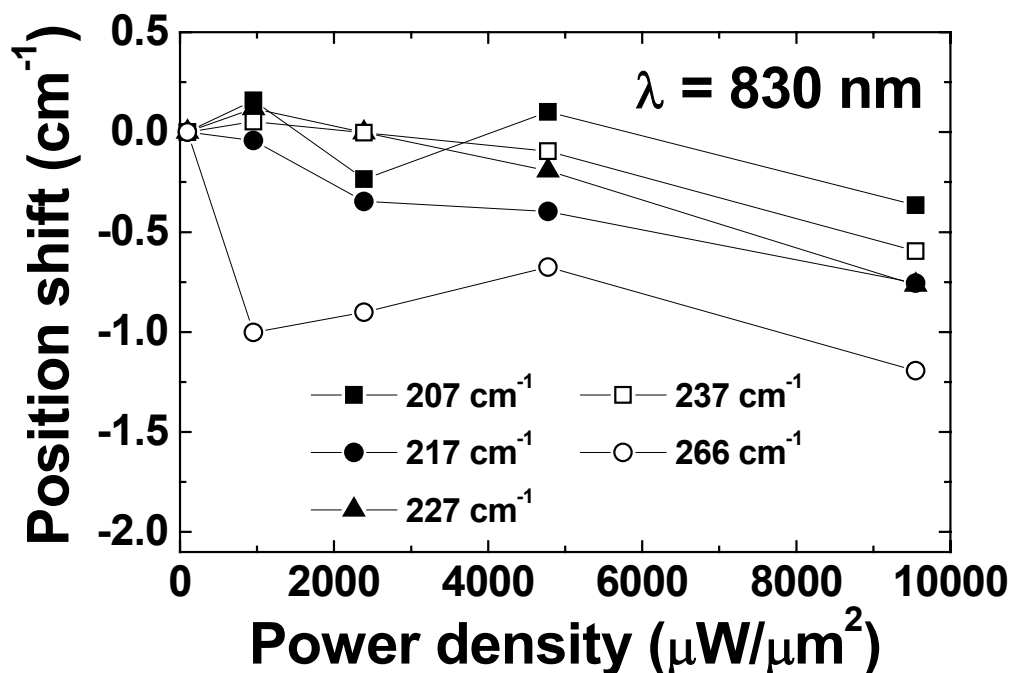


Figure II.9: Peak position shift of 5 RBMs as a function of the laser power density for purified HiPco nanotubes in PVA films. The laser used was of wavelength 830 nm.

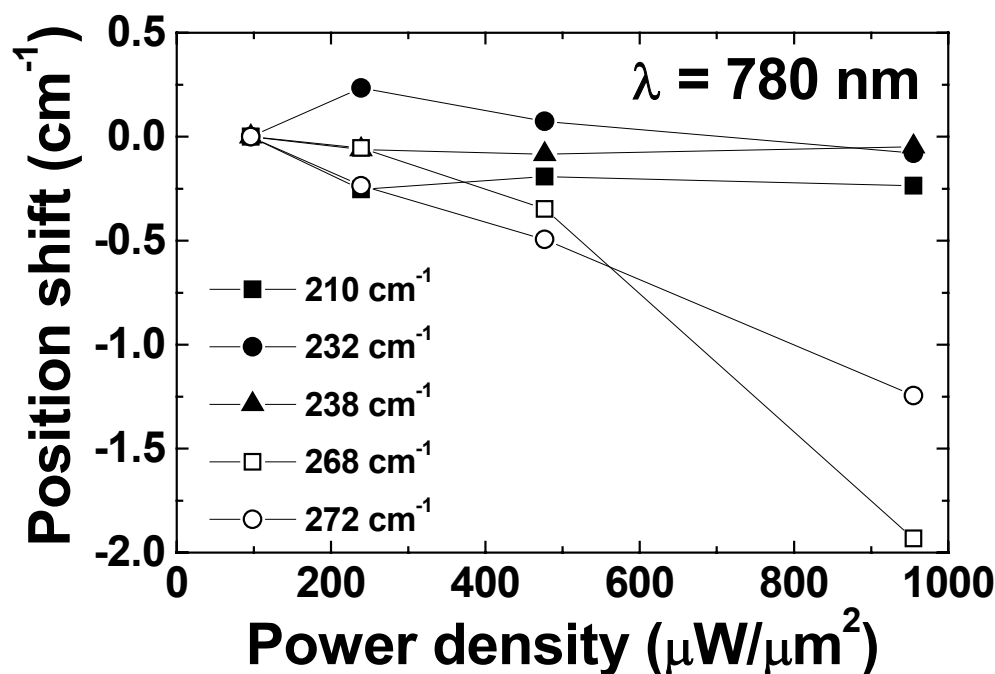


Figure II.10: Peak position shift of 5 RBMs as a function of the laser power density for purified HiPco nanotubes in epoxy composite. The laser used was of wavelength 780 nm.

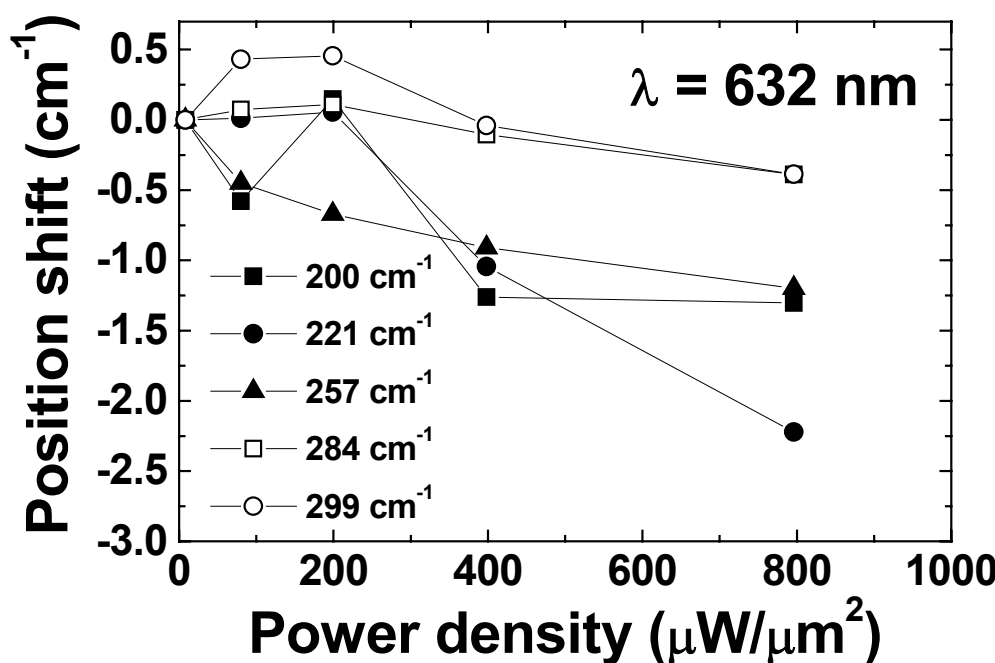


Figure II.11: Peak position shift of 5 RBMs as a function of the laser power density for purified HiPco nanotubes in PVA films. The laser used was of wavelength 632 nm.

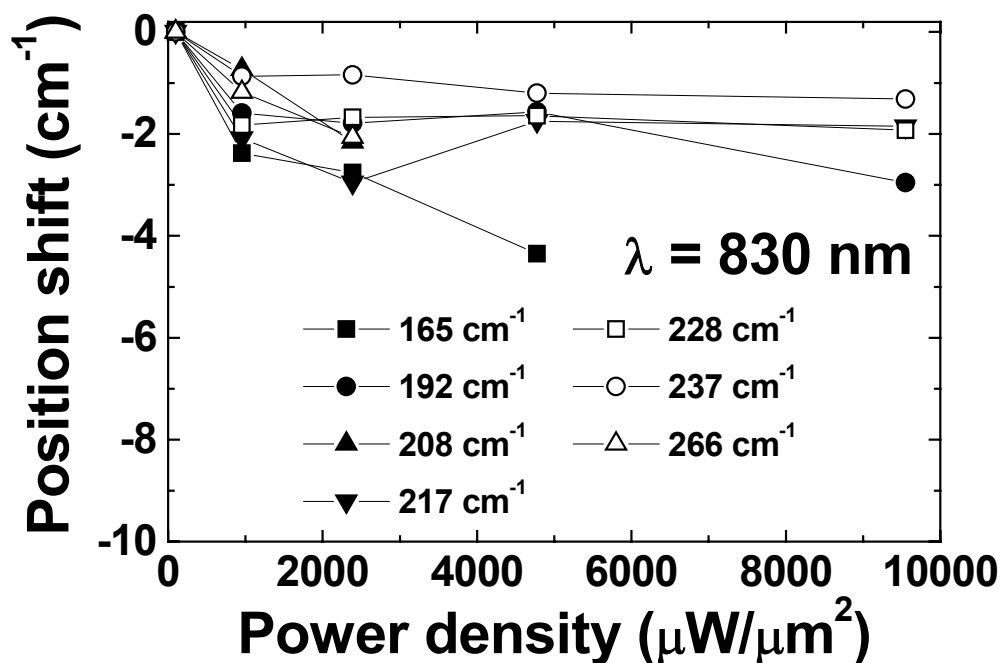


Figure II.12: Peak position shift of 7 RBMs as a function of the laser power density for purified Elicarb nanotubes in PVA films. The laser used was of wavelength 830 nm.

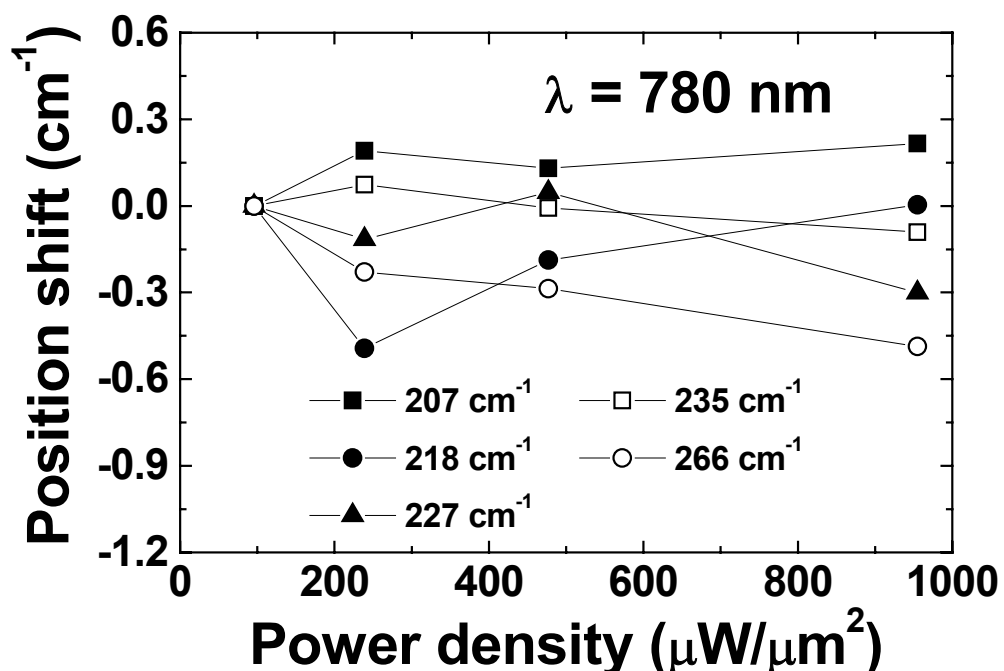


Figure II.13: Peak position shift of 5 RBMs as a function of the laser power density for purified Elicarb nanotubes in PVA films. The laser used was of wavelength 780 nm.

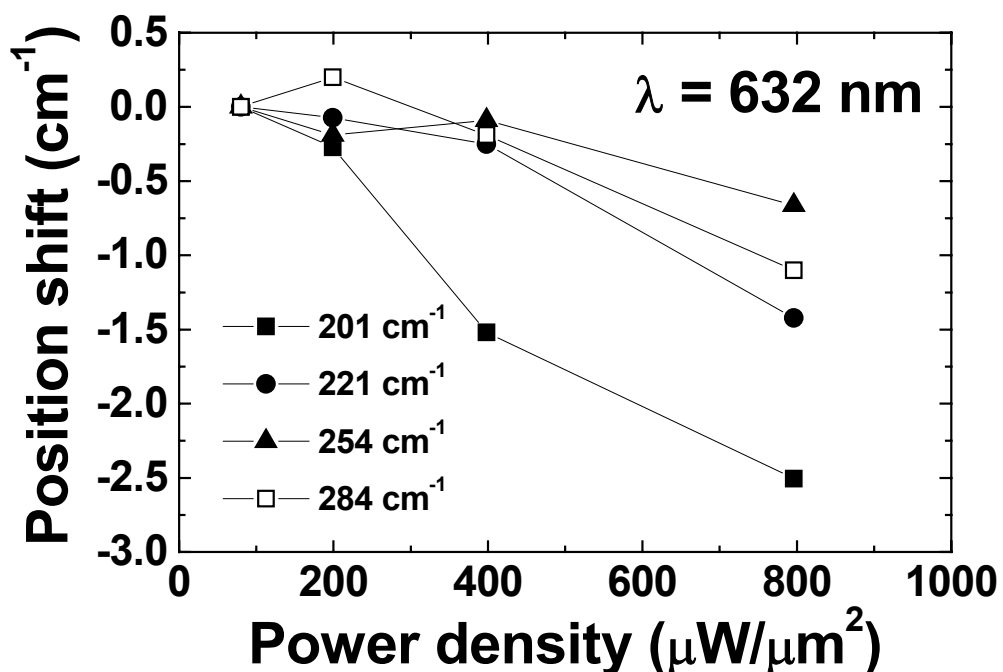


Figure II.14: Peak position shift of 4 RBMs as a function of the laser power density for purified Elicarb nanotubes in PVA films. The laser used was of wavelength 632 nm.

II.2 Focus Effect on the Band Position

Usually the laser spot can be seen in the Raman experiments and its size varies with the distance between the sample and the microscope lens. When its size is minimum, the laser beam is considered focused on the sample surface. The video camera coupled with the Raman spectroscope is particularly sensitive to the laser of wavelength 632 nm.

However, the epoxy composite samples reinforced with 0.025 wt.% HiPco nanotubes are generally very dark and thus it is usually difficult to focus the laser beam of wavelength 780 nm by looking at the spot size. Due to the low sensitivity of the video camera at this wavelength, the laser spot, which is already weak normally, is undetectable with the naked eye. The situation is similar during the experiments using the 830 nm laser. Therefore in these cases, the laser beam was considered focused when the image of the sample surface was focused. In order to study the effect of focus on the Raman bands, several series of Raman spectra were collected at different distances between the sample and the objective lens used to focus the laser. The laser power was

1%, 100% and 10% of the maximum power for the lasers of wavelength 830 nm, 780 nm and 632 nm, respectively.

The exact distance between the sample and the lens could not be measured accurately. Only the distance variations were measured with a $\pm 5 \mu\text{m}$ accuracy. The distance at which the image of the surface sample was focused was taken as a reference (distance zero on the figures).

II.2.1 G and G' bands

The effect of focus was first measured, on HiPco and Elicarb SWNT powders, on the position and the intensity of the G band ($\lambda=830 \text{ nm}$) and G' band ($\lambda=632 \text{ nm}$ and 780 nm) (Figure II.15). A large variation of about 12 cm^{-1} on the G' band position was observed on HiPco SWNT powder using the 780 nm laser. Its position reached the lowest wavenumber when the image was focused. At the same time, the G' band intensity varied significantly and reached its maximum when the image was nearly focused. However, the distance at which the G' band position reached its minimum did not always match the distance at which the G' band intensity reached its maximum.

The effect of focus was also investigated on HiPco and Elicarb SWNT composite samples (Figure II.16). In HiPco SWNT composite samples, variations of smaller amplitudes were measured on the position and the intensity of the G and G' bands. For the epoxy composite sample (HiPco SWNT, 780 nm), the G' band could be observed for a range of distance between -180 and $50 \mu\text{m}$. For the PVA composite films, the G or G' band could not be observed over a similar range, so the distance range studied is between -60 and $60 \mu\text{m}$. For the epoxy composite sample, as the microscope lens became closer to the sample surface, their values reached several minima or maxima. In the other samples, only one maximum was observed. This is explained by the inhomogeneous nanotube density deep in the epoxy composite sample. It is noted that the intensity values cannot be used to quantify the local density of nanotubes, since the Raman spectrometer was not set up to be confocal.

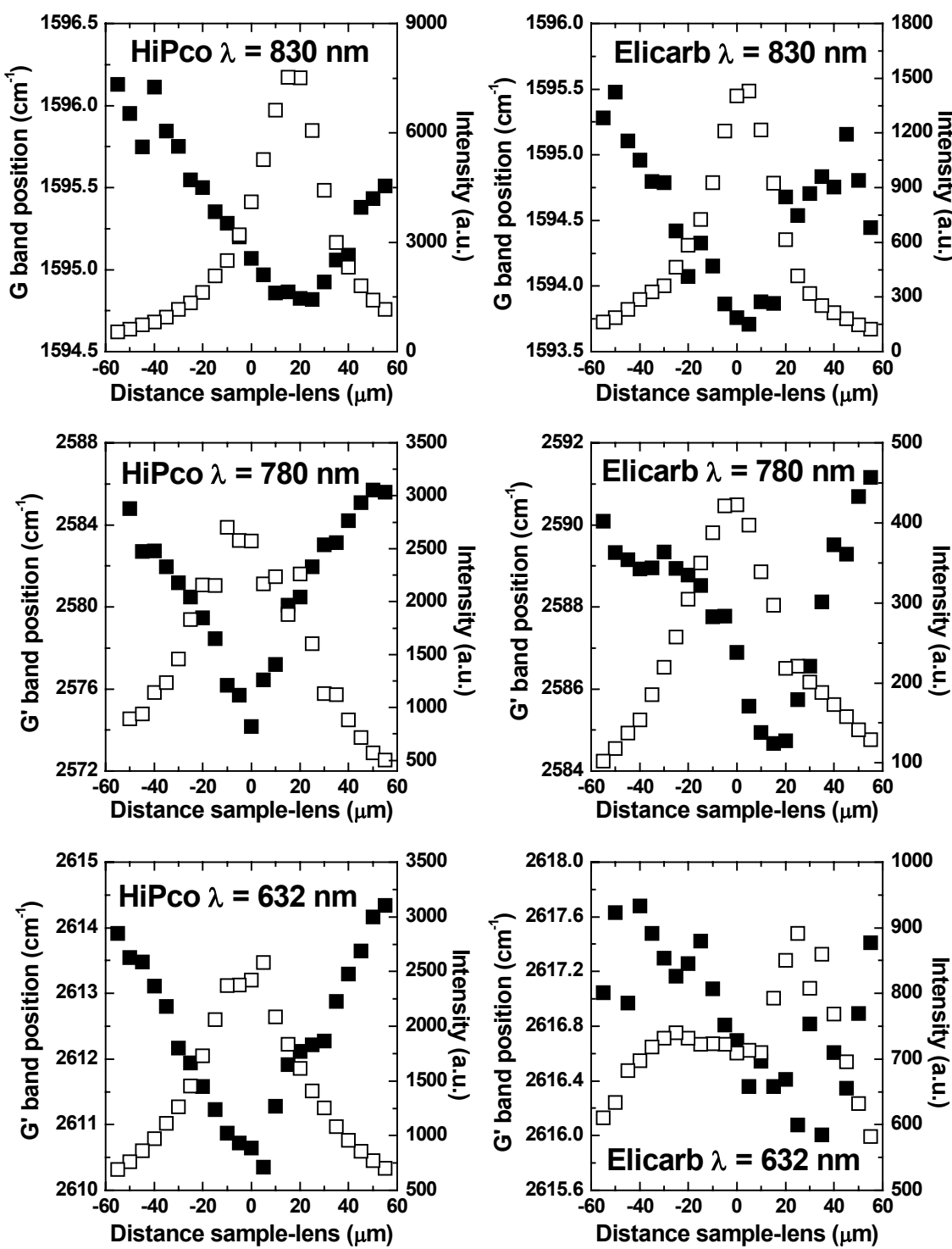


Figure II.15: G band ($\lambda = 830 \text{ nm}$) and G' band ($\lambda = 780 \text{ nm}$ and 632 nm) position (solid squares) and intensity (open squares) as a function of the distance between the microscope lens and the purified HiPco and Elicarb nanotube powder. The image of the sample surface is focused when the distance sample-lens is zero.

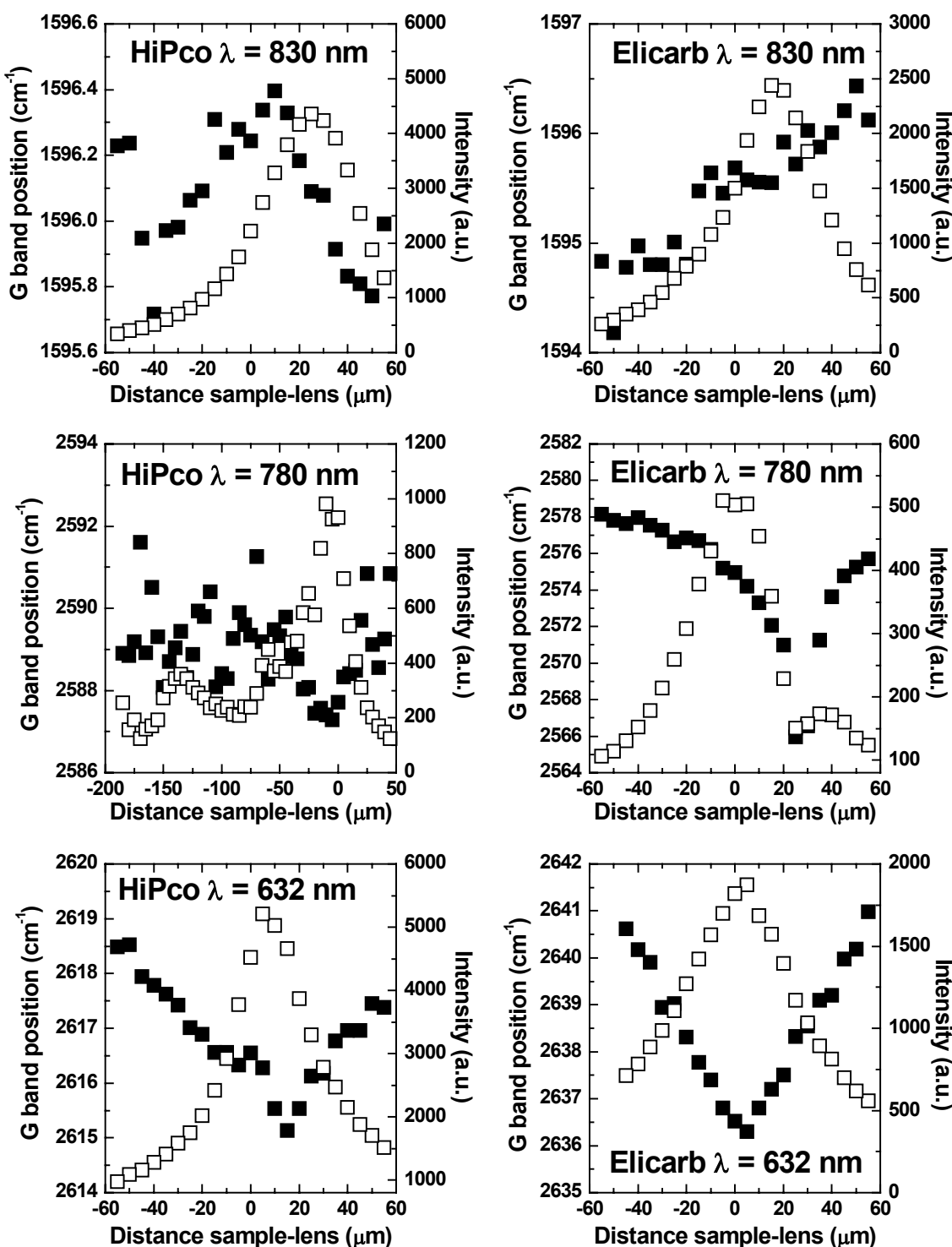


Figure II.16: G band ($\lambda = 830 \text{ nm}$) and G' band ($\lambda = 780 \text{ nm}$ and 632 nm) position (solid squares) and intensity (open squares) as a function of the distance between the microscope lens and the purified HiPco and Elicarb nanotubes in composites. The image of the sample surface is focused when the distance sample-lens is zero.

II.2.2 RBMs

The effect of focus was also studied on the RBMs. Their position and their intensity in HiPco nanotube powder (Figures II.17 to II.22) and Elicarb nanotube powder (Figures II.23 to II.28) were measured as a function of the distance between the sample and the microscope lens. The distance at which the RBM positions reached their minimum was close to zero, but in some cases the maximum was reached when the image was underfocused.

Their intensity values were all normalized by dividing the absolute intensity value at a given distance by the maximum intensity value recorded the series of Raman spectra. The distance at which the maximum intensity was recorded did not always match the distance at which the position reached its minimum.

The 215 cm^{-1} RBM (Elicarb SWNT, 830 nm) was only visible when the sample image was focused. Typical low-frequency Raman spectra collected from purified HiPco nanotube powder, using the 780 nm laser are showed in Figure II.29.

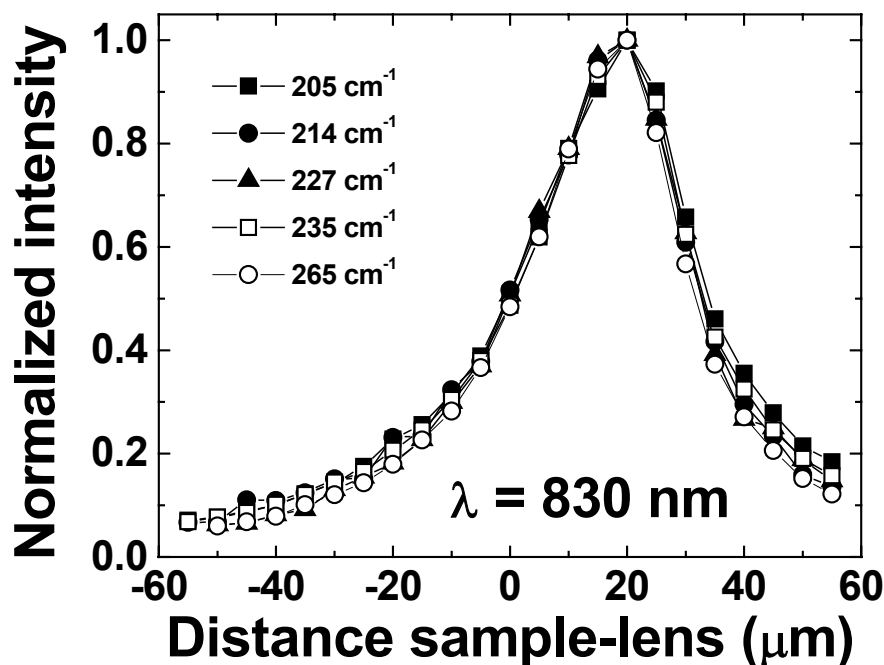


Figure II.17: RBM normalized intensities as a function of the distance between the microscope lens and the sample for purified HiPco nanotube powder. The laser used was of wavelength 830 nm. The image of the sample surface is focused when the distance sample-lens is zero.

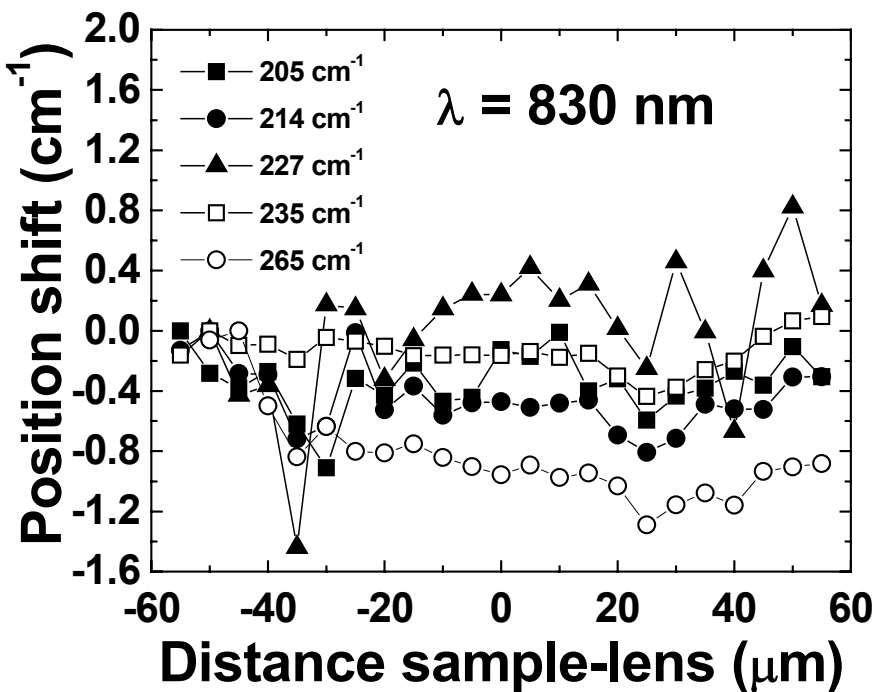


Figure II.18: RBM position shifts as a function of the distance between the microscope lens and the sample for purified HiPco nanotube powder. The laser used was of wavelength 830 nm. The image of the sample surface is focused when the distance sample-lens is zero.

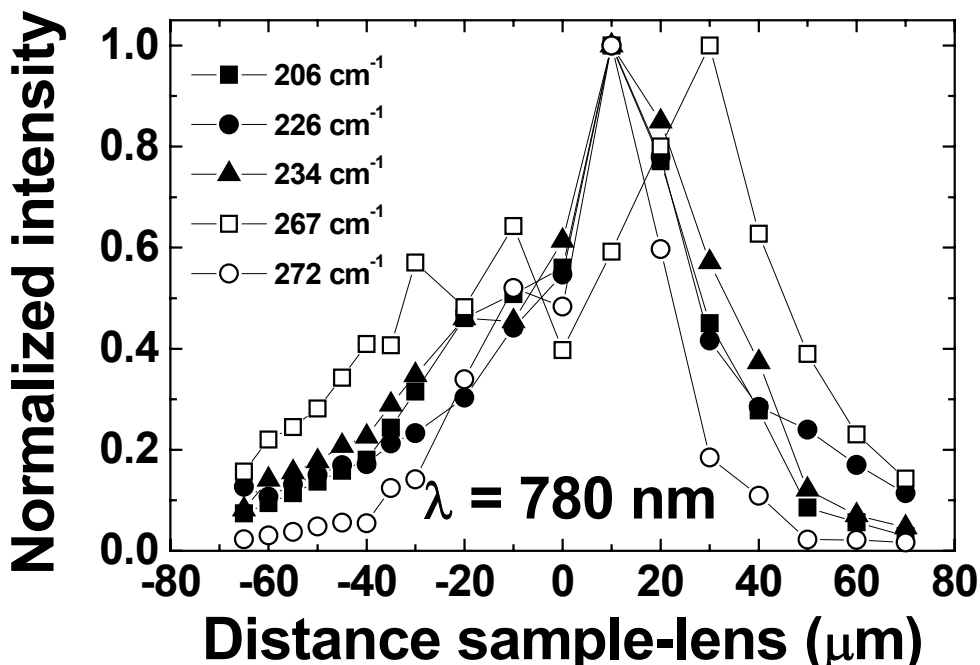


Figure II.19: RBM normalized intensities as a function of the distance between the microscope lens and the sample for purified HiPco nanotube powder. The laser used was of wavelength 780 nm. The image of the sample surface is focused when the distance sample-lens is zero.

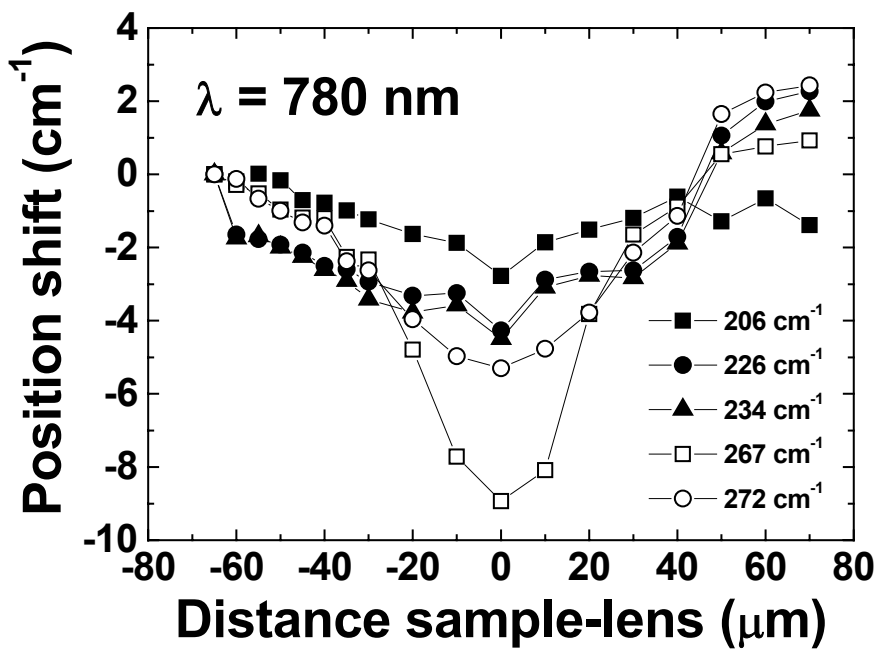


Figure II.20: RBM position shifts as a function of the distance between the microscope lens and the sample for purified HiPco nanotube powder. The laser used was of wavelength 780 nm. The image of the sample surface is focused when the distance sample-lens is zero.

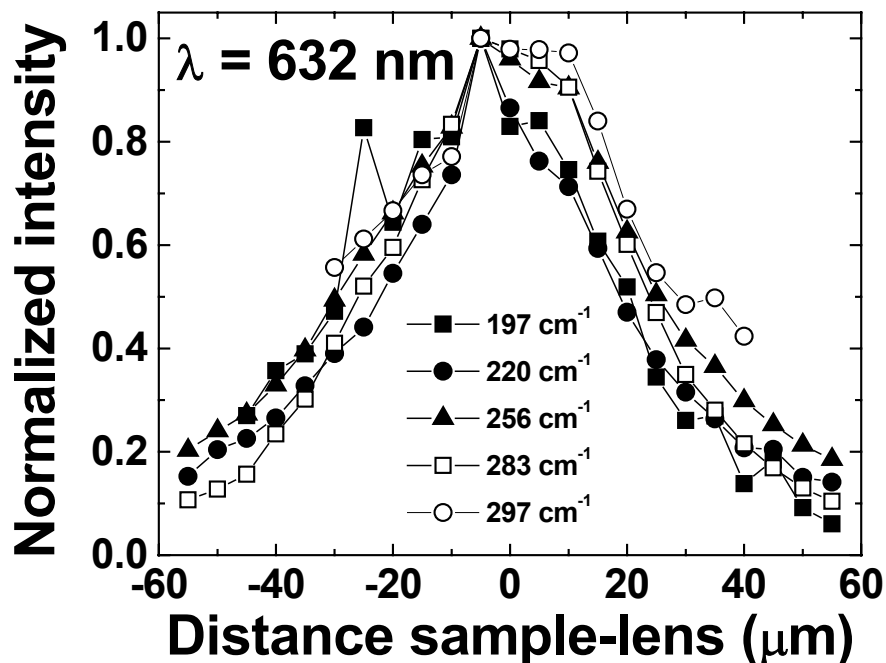


Figure II.21: RBM normalized intensities as a function of the distance between the microscope lens and the sample for purified HiPco nanotube powder. The laser used was of wavelength 632 nm. The image of the sample surface is focused when the distance sample-lens is zero.

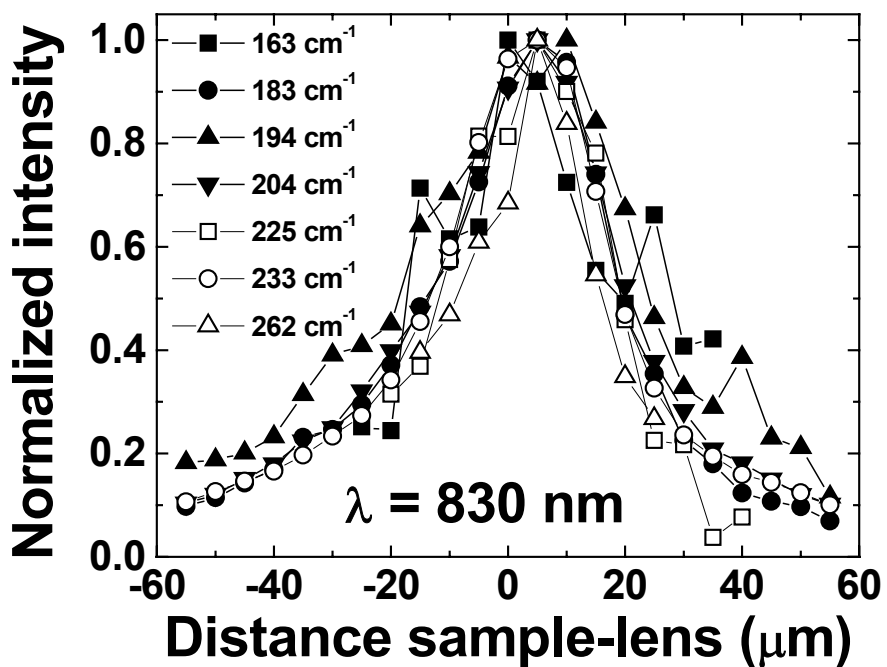
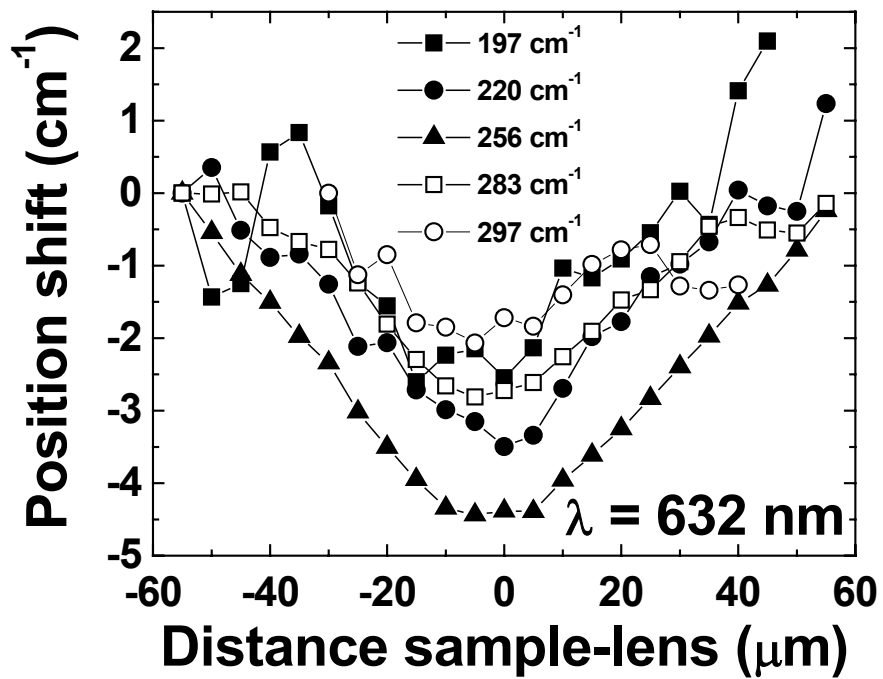


Figure II.23: RBM normalized intensities as a function of the distance between the microscope lens and the sample for purified Elicarb nanotube powder. The laser used was of wavelength 830 nm. The image of the sample surface is focused when the distance sample-lens is zero.

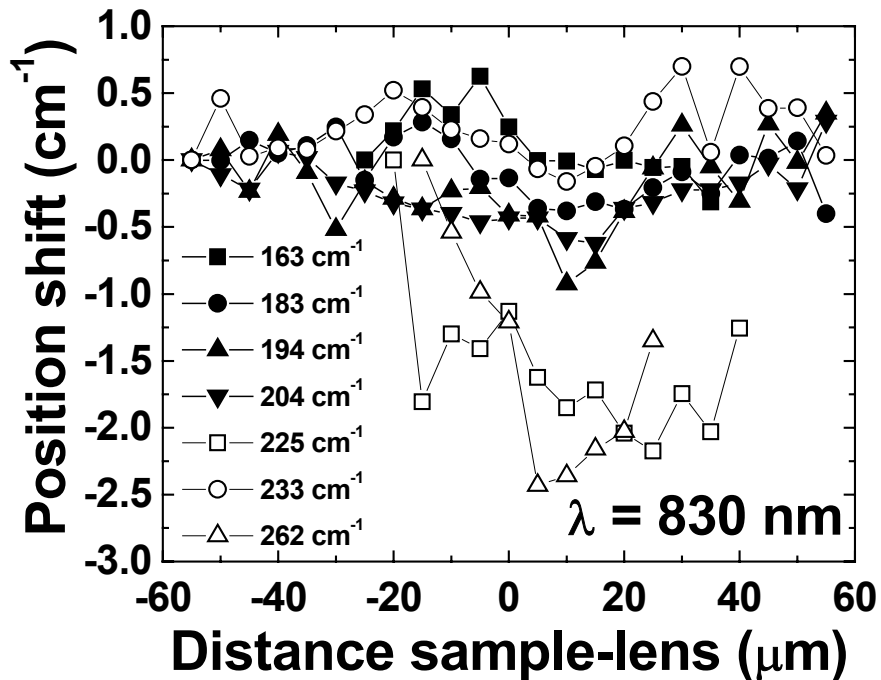


Figure II.24: RBM position shifts as a function of the distance between the microscope lens and the sample for purified Elicarb nanotube powder. The laser used was of wavelength 830 nm. The image of the sample surface is focused when the distance sample-lens is zero.

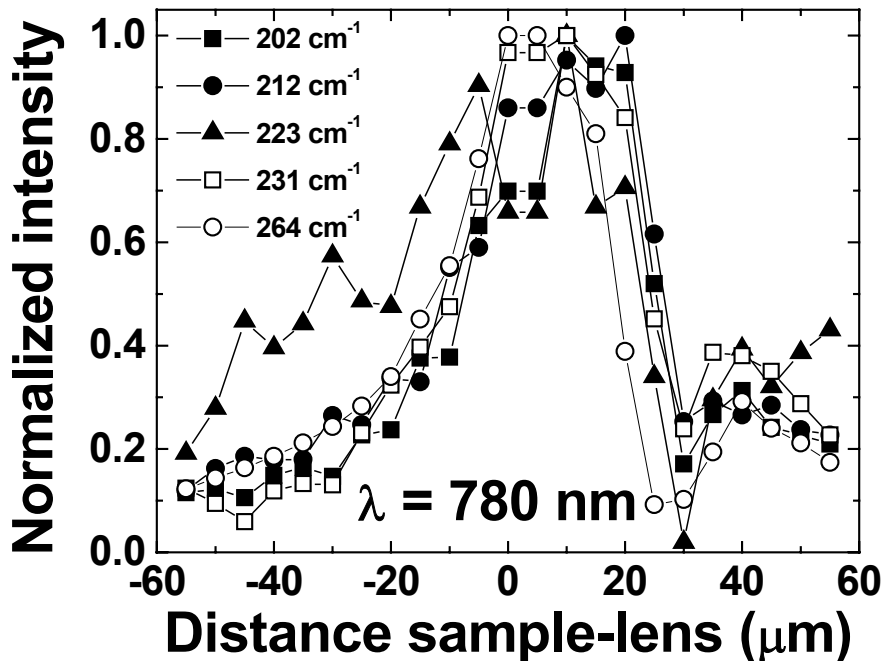


Figure II.25: RBM normalized intensities as a function of the distance between the microscope lens and the sample for purified Elicarb nanotube powder. The laser used was of wavelength 780 nm. The image of the sample surface is focused when the distance sample-lens is zero.

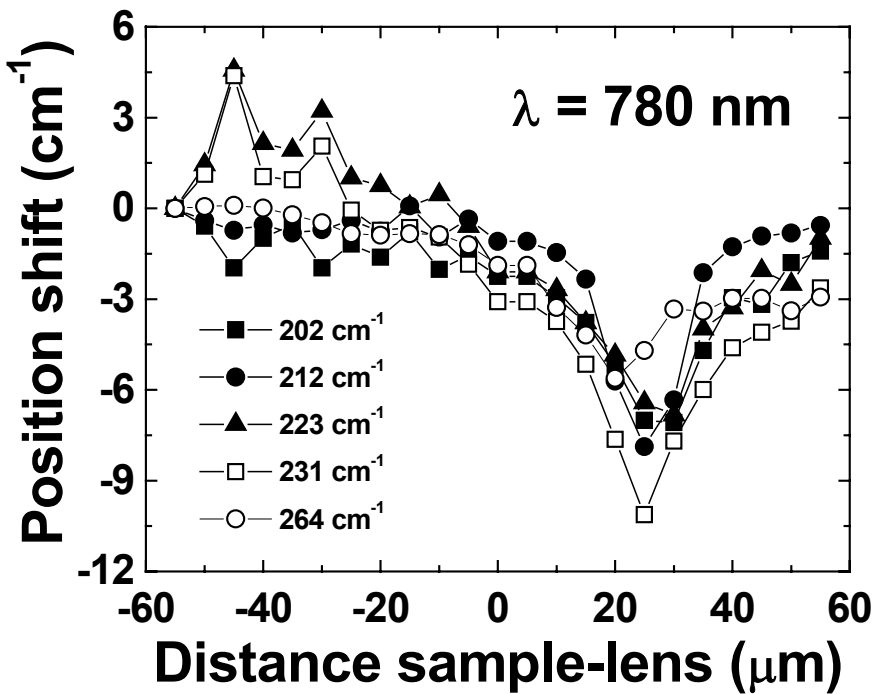


Figure II.26: RBM position shifts as a function of the distance between the microscope lens and the sample for purified Elicarb nanotube powder. The laser used was of wavelength 780 nm. The image of the sample surface is focused when the distance sample-lens is zero.

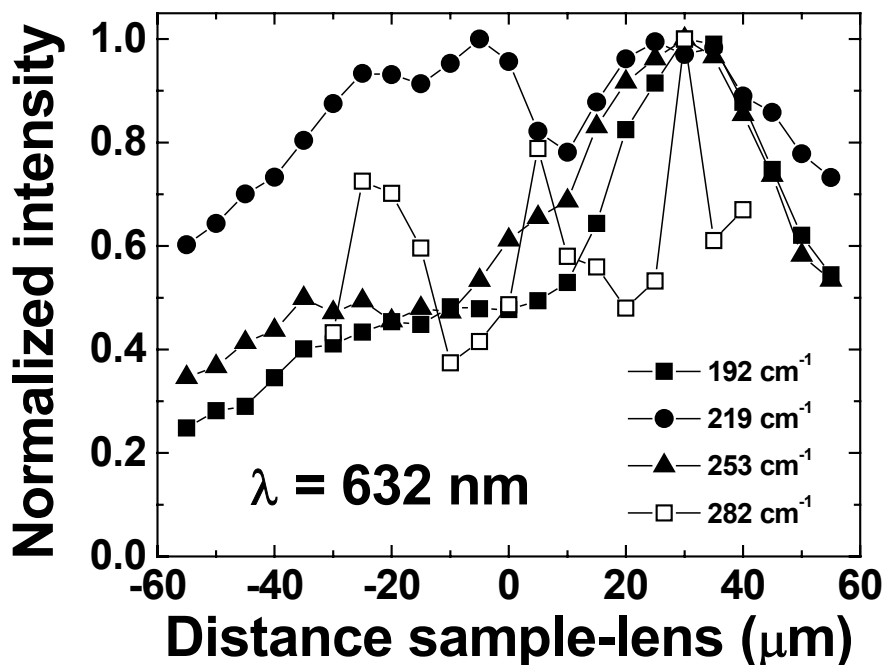


Figure II.27: RBM normalized intensities as a function of the distance between the microscope lens and the sample for purified Elicarb nanotube powder. The laser used was of wavelength 632 nm. The image of the sample surface is focused when the distance sample-lens is zero.

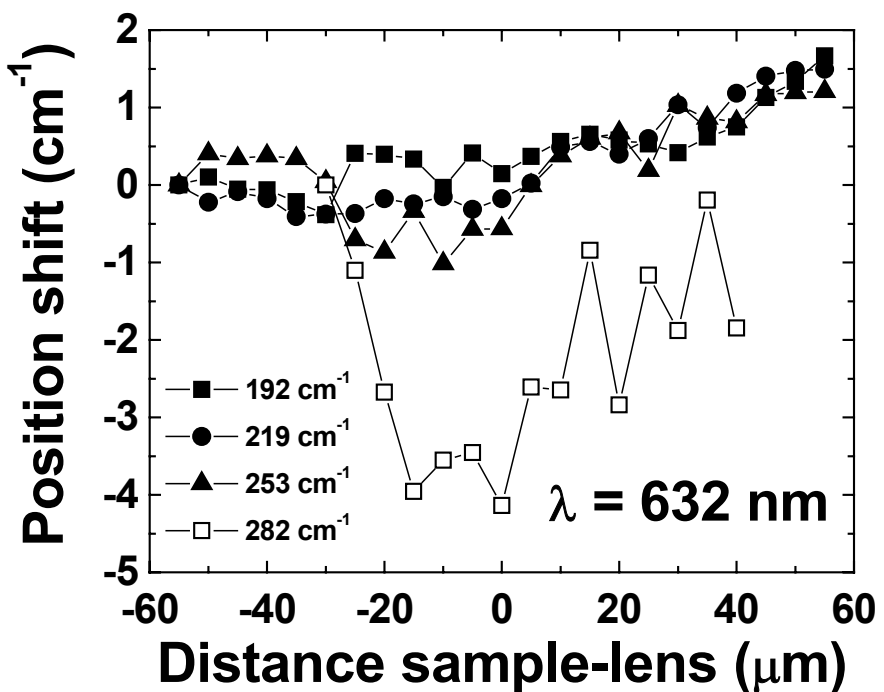


Figure II.28: RBM position shifts as a function of the distance between the microscope lens and the sample for purified Elicarb nanotube powder. The laser used was of wavelength 632 nm. The image of the sample surface is focused when the distance sample-lens is zero.

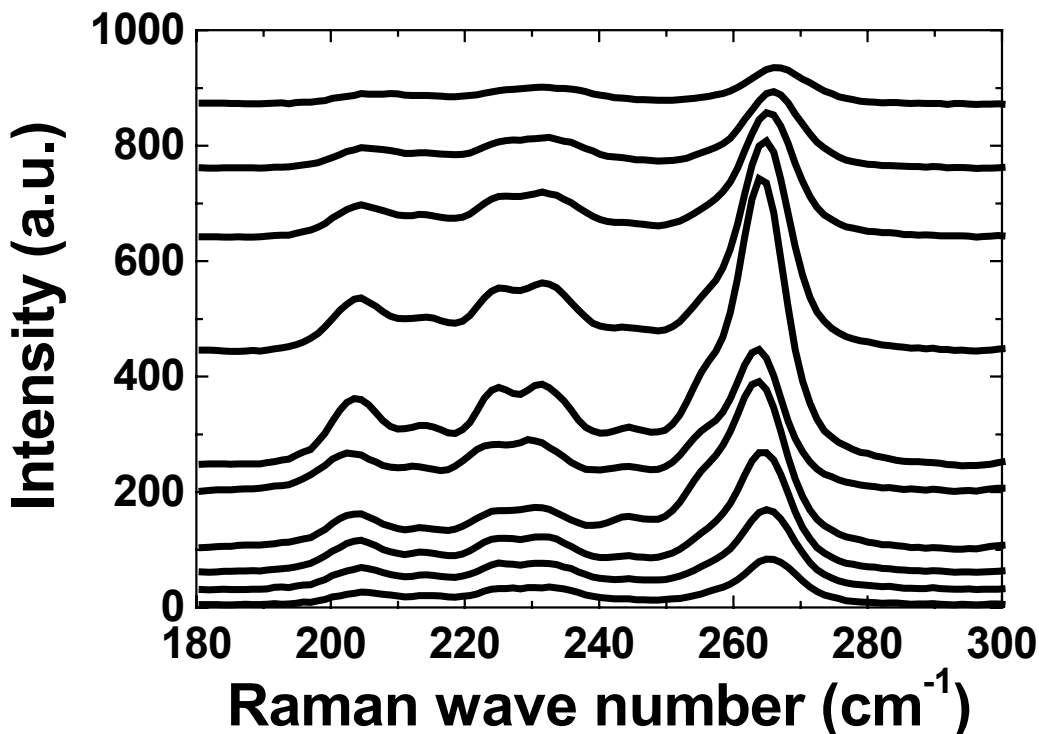


Figure II.29: Low-frequency Raman spectra collected from purified HiPco nanotube powder. The laser used was of wavelength 780 nm. From bottom to top, the spectra were measured consecutively from the same spot, while increasing the distance between the lens and the sample by 10 μm steps.

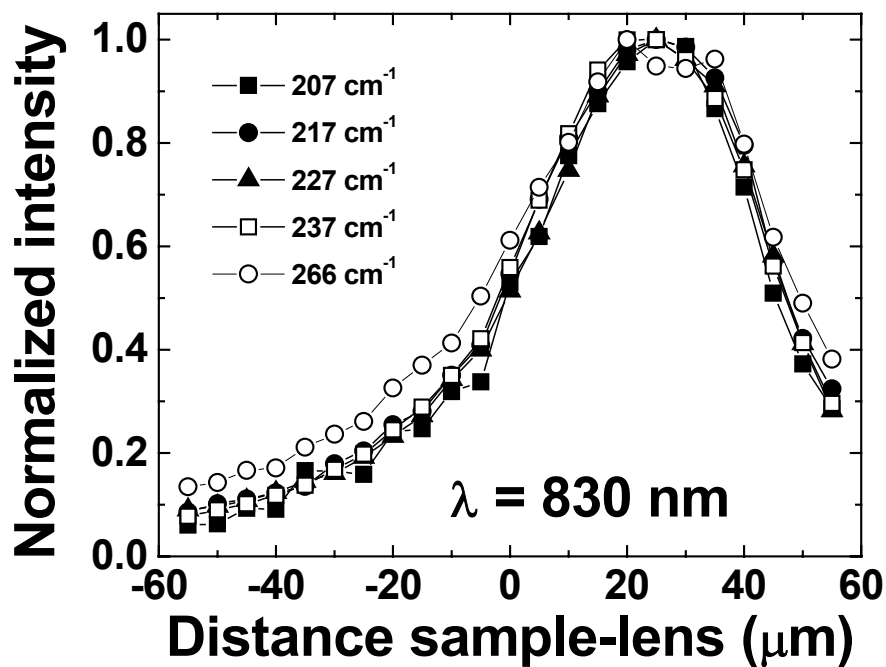


Figure II.30: Intensity of the RBMs as a function of the distance between the microscope lens and the sample for purified HiPco nanotubes in a PVA film. The laser used was of wavelength 830 nm. The image of the sample surface is focused when the distance sample-lens is zero.

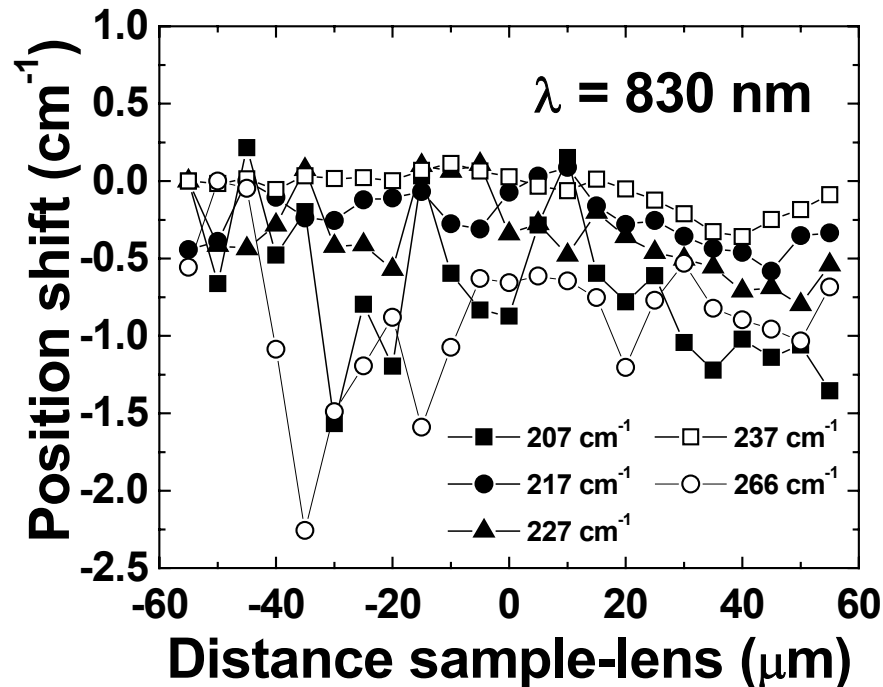


Figure II.31: RBM position shifts as a function of the distance between the microscope lens and the sample for purified HiPco nanotubes in a PVA film. The laser used was of wavelength 830 nm. The image of the sample surface is focused when the distance sample-lens is zero.

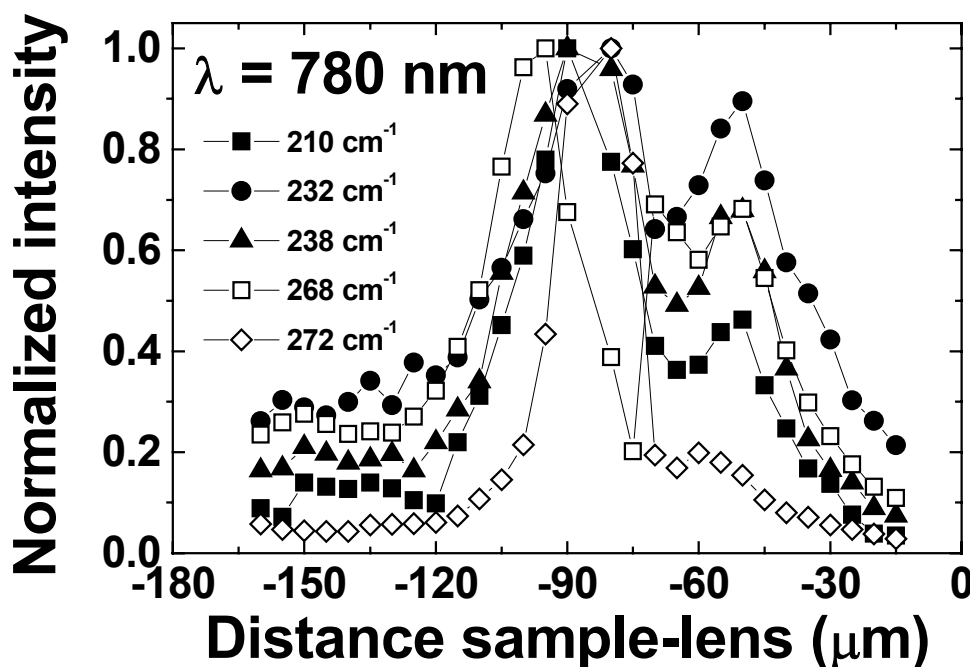


Figure II.32: Intensity of the RBMs as a function of the distance between the microscope lens and the sample for purified HiPco nanotubes in epoxy composite. The laser used was of wavelength 780 nm. The image of the sample surface is focused when the distance sample-lens is zero.

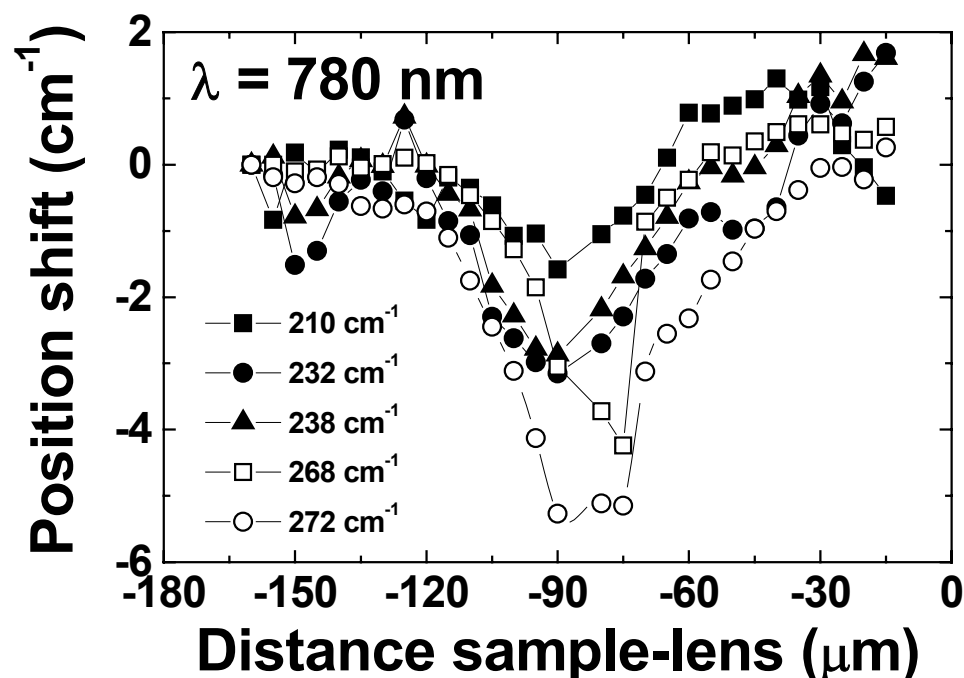


Figure II.33: RBM position shifts as a function of the distance between the microscope lens and the sample for purified HiPco nanotubes in epoxy composite. The laser used was of wavelength 780 nm. The image of the sample surface is focused when the distance sample-lens is zero.

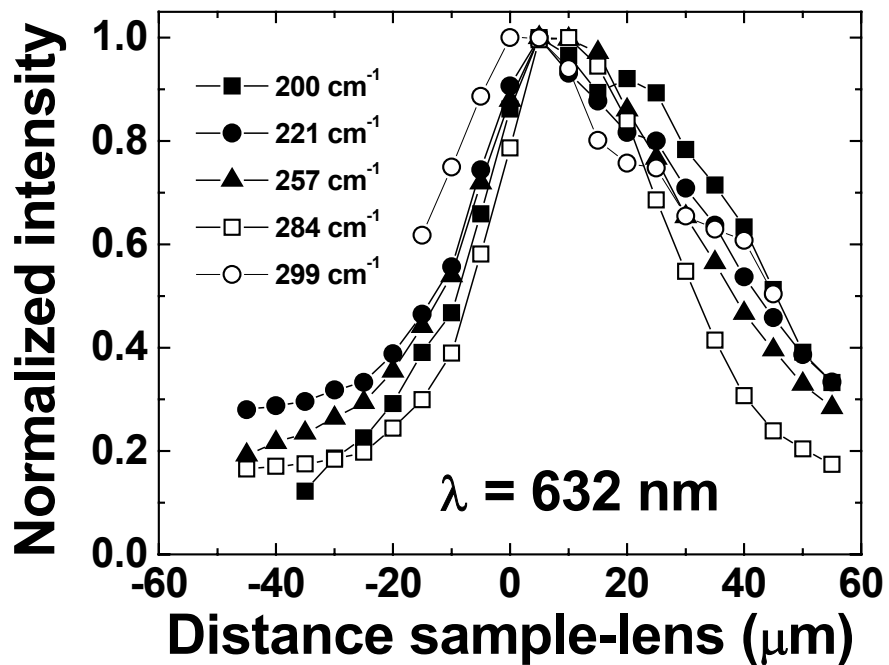


Figure II.34: Intensity of the RBMs as a function of the distance between the microscope lens and the sample for purified HiPco nanotubes in a PVA film. The laser used was of wavelength 632 nm. The image of the sample surface is focused when the distance sample-lens is zero.

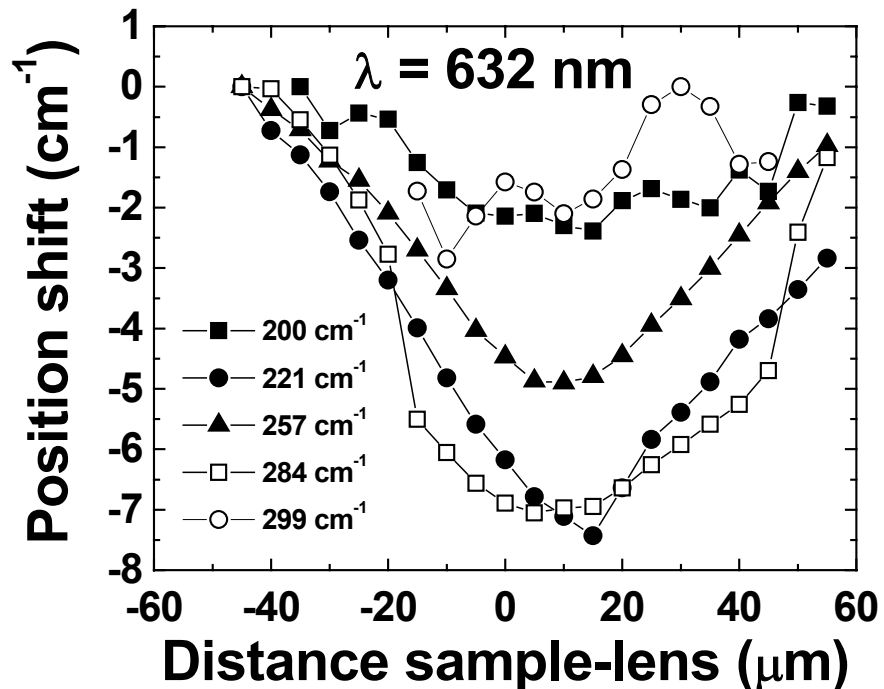


Figure II.35: RBM position shifts as a function of the distance between the microscope lens and the sample for purified HiPco nanotubes in a PVA film. The laser used was of wavelength 632 nm. The image of the sample surface is focused when the distance sample-lens is zero.

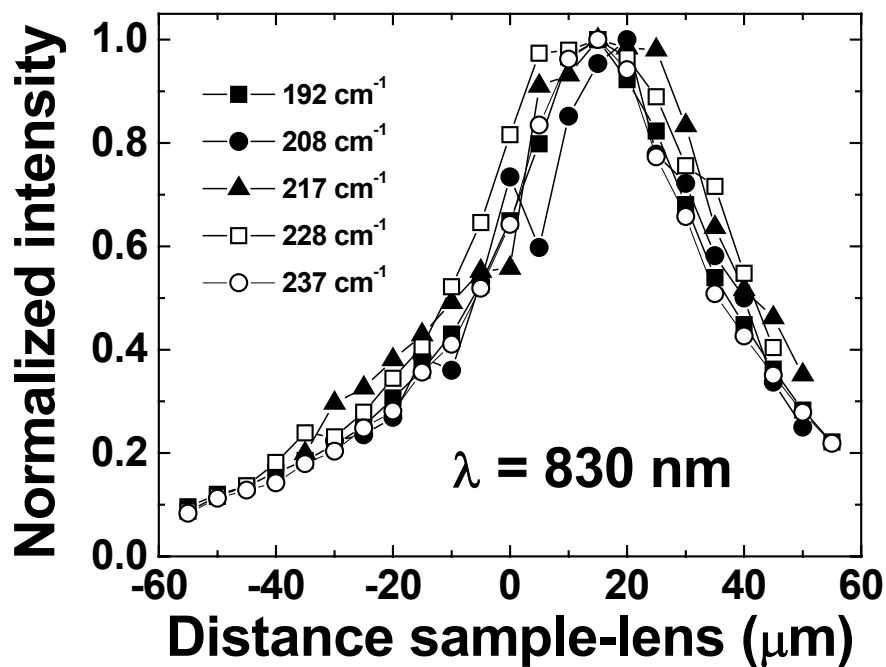


Figure II.36: Intensity of the RBMs as a function of the distance between the microscope lens and the sample for purified Elicarb nanotubes in a PVA film. The laser used was of wavelength 830 nm. The image of the sample surface is focused when the distance sample-lens is zero.

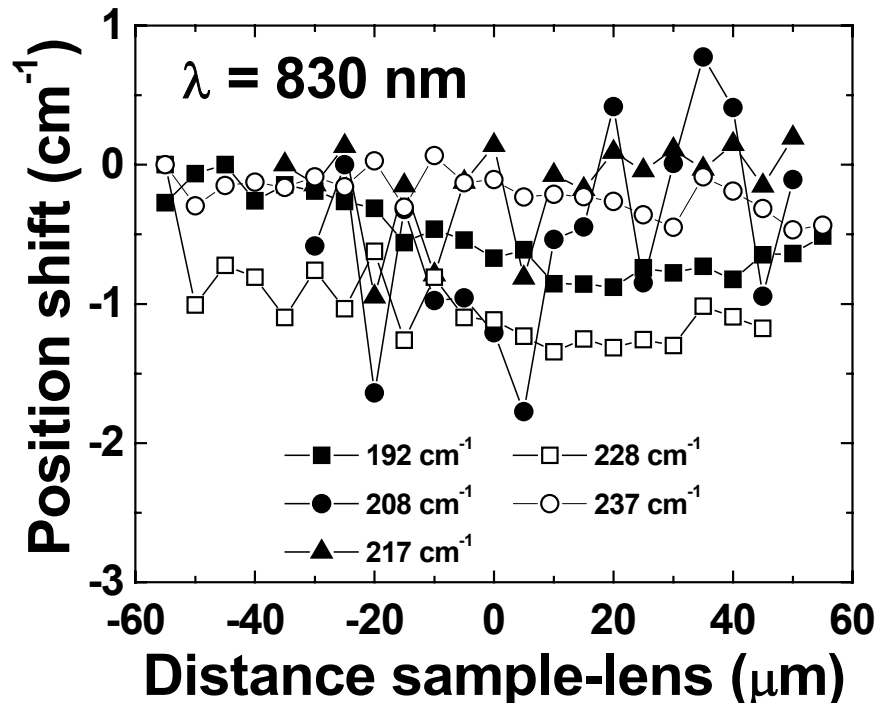


Figure II.37: RBM position shifts as a function of the distance between the microscope lens and the sample for purified Elicarb nanotubes in a PVA film. The laser used was of wavelength 830 nm. The image of the sample surface is focused when the distance sample-lens is zero.

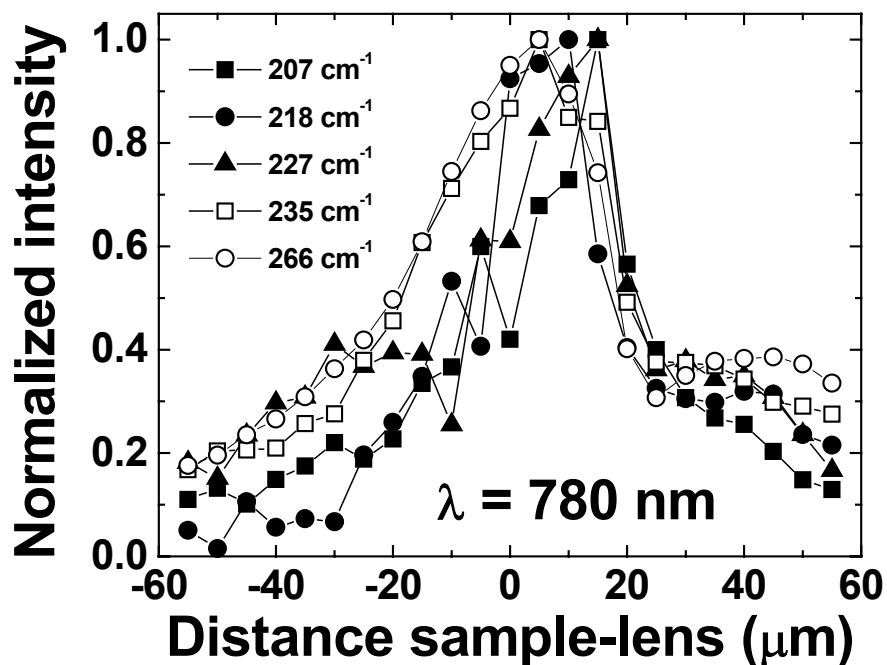


Figure II.38: Intensity of the RBMs as a function of the distance between the microscope lens and the sample for purified Elicarb nanotubes in a PVA film. The laser used was of wavelength 780 nm. The image of the sample surface is focused when the distance sample-lens is zero.

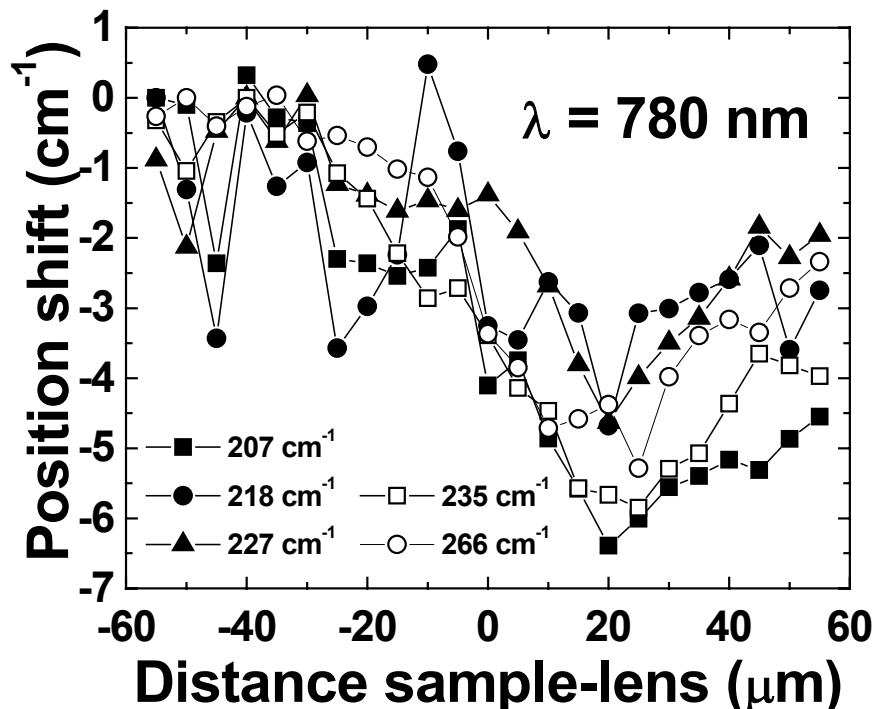


Figure II.39: RBM position shifts as a function of the distance between the microscope lens and the sample for purified Elicarb nanotubes in a PVA film. The laser used was of wavelength 780 nm. The image of the sample surface is focused when the distance sample-lens is zero.

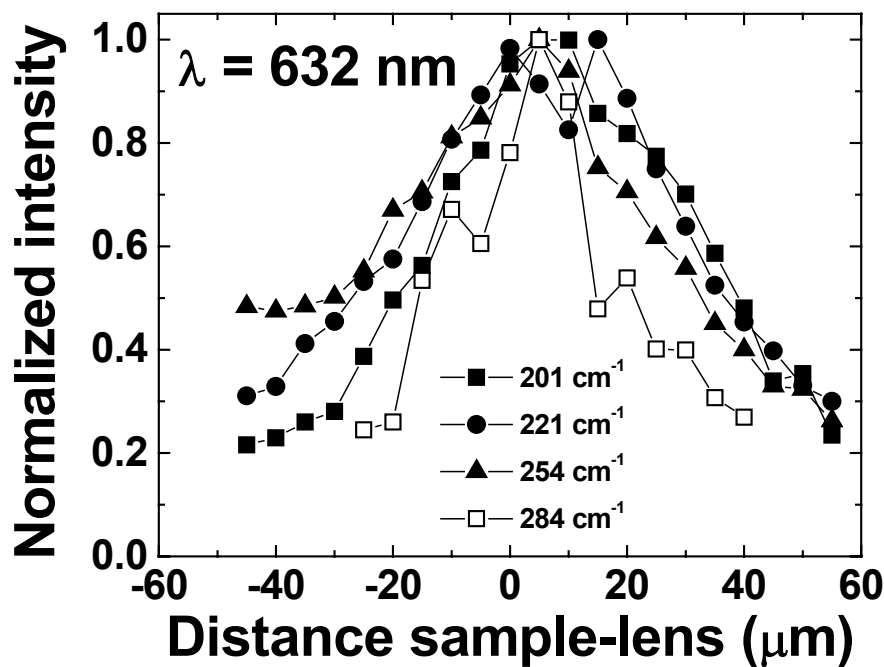


Figure II.40: Intensity of the RBMs as a function of the distance between the microscope lens and the sample for purified Elicarb nanotubes in a PVA film. The laser used was of wavelength 632 nm. The image of the sample surface is focused when the distance sample-lens is zero.

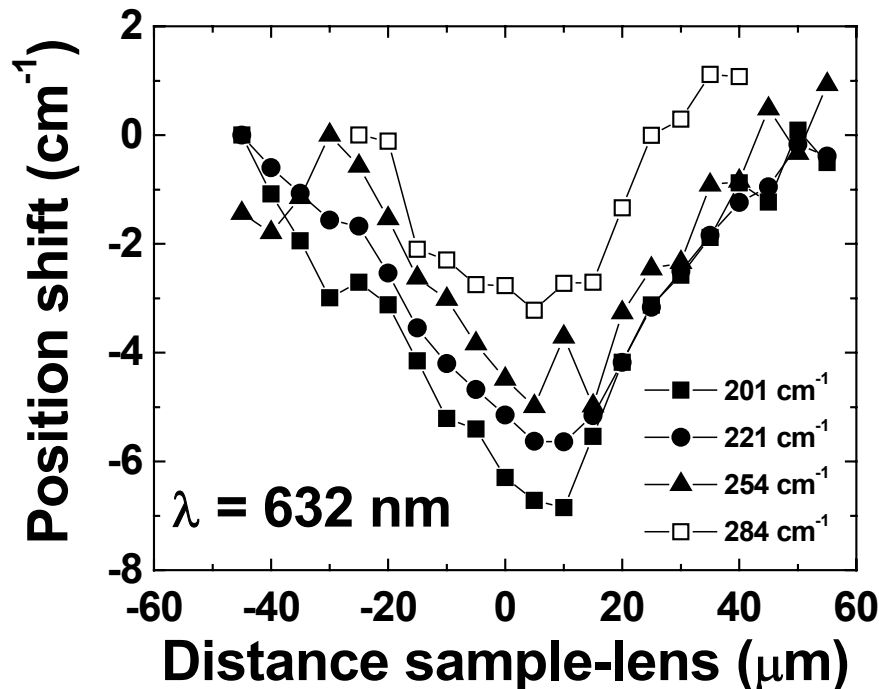


Figure II.41: RBM position shifts as a function of the distance between the microscope lens and the sample for purified Elicarb nanotubes in a PVA film. The laser used was of wavelength 632 nm. The image of the sample surface is focused when the distance sample-lens is zero.

The effect of focus was also studied on the RBMs in composites. Their position and their intensity in epoxy and PVA/HiPco SWNT composites (Figures II.30 to II.35) and PVA/Elicarb SWNT composites (Figures II.36 to II.41) were measured as a function of the distance between the sample and the microscope lens.

Several RBMs from Elicarb SWNTs were only observed when the overall intensity of the Raman spectrum was maximum, so a study on the focus effect was impossible for the following RBMs: 165 cm^{-1} and 266 cm^{-1} ($\lambda=830\text{ nm}$).

In the epoxy/HiPco SWNT composites, an intensity maximum roughly matched a RBM position minimum. The intensity maximum was found "deep into the sample," about 90 microns below the distance at which the image of the sample surface is focused. In Figure II.32, there is another local maximum in intensity at around -50 microns, which is not matched by any local minimum in position (Figure II.33).

On the PVA composite samples, at distance zero, all RBM intensities vary following the same trend, so focus effects cannot explain the intensity variations observed during the deformation tests.

These focus effects are very similar to the heating effects and can be explained by the variations of the laser power density. When the laser spot is focused on the sample, the power density is maximum and therefore the temperature is expected to reach its maximum, inducing the shift of the Raman bands of the nanotubes.

II.3 Hot Stage Experiments

A programmable hot-stage (Model TMS91 from Linkam Scientific Instruments Ltd., UK) was used for *in situ* heating of purified HiPco SWNTs. The HiPco SWNT powder was manually crushed to smaller particles. The particles were placed between two glass slides on a silver block, which contains a platinum resistor and a heater. The sample was then heated in air from 20°C to 360°C . The laser used was of wavelength 780 nm.

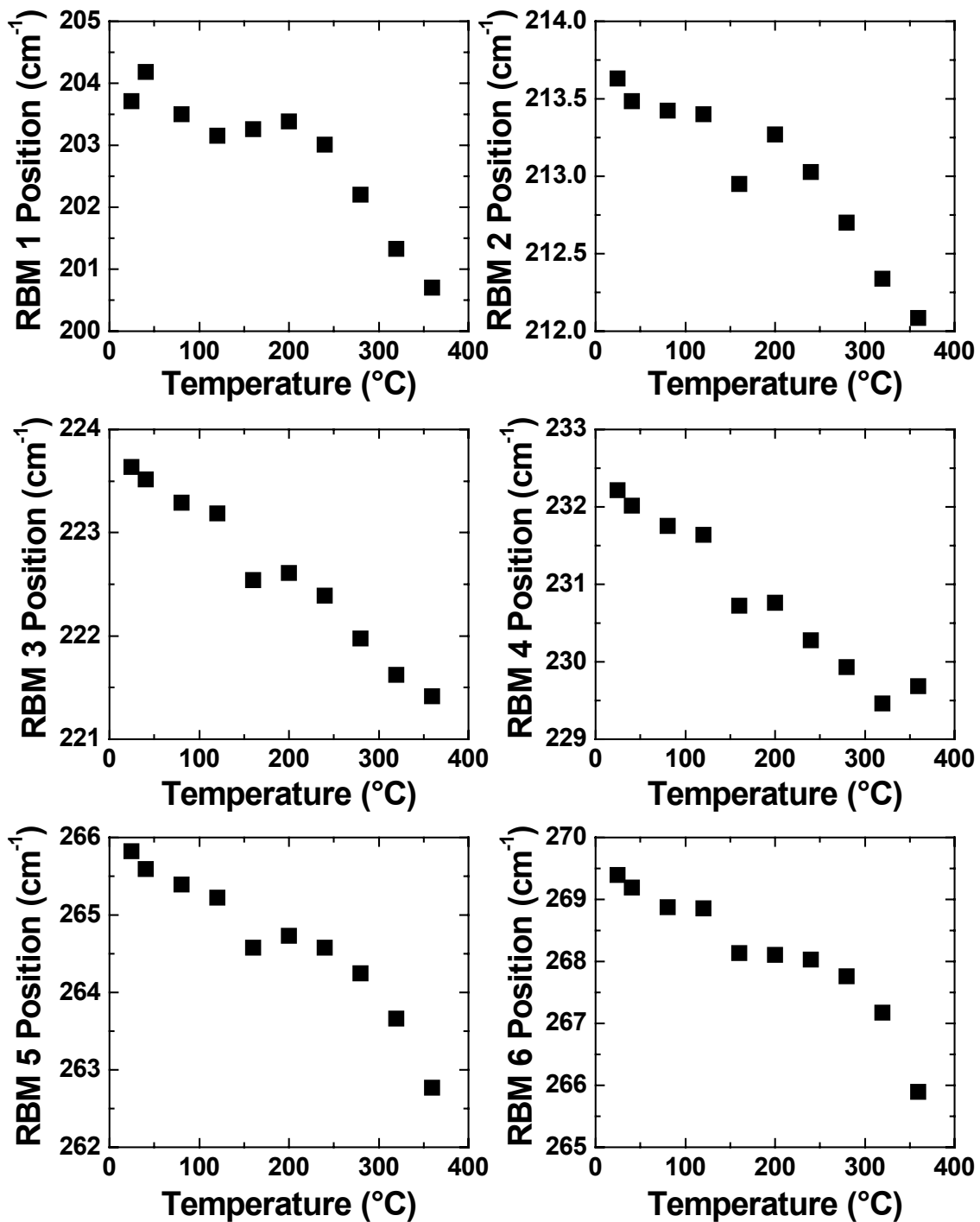


Figure II.42: Raman peak position of the 6 RBMs located at 204, 214, 224, 232, 266 and 269 cm^{-1} at room temperature in purified HiPco powder as a function of temperature.

The positions of the 6 RBMs and the G' band are showed in Figures II.42 and II.43. The 6 RBMs are located at 204, 214, 224, 232, 266, and 269 cm^{-1} at

room temperature. The 7 peaks shift to lower wave numbers with rising temperature between 20 and 360°C, consistent with the results reported in the literature [83-85]. The G' band downshift rate of $-0.046 \text{ cm}^{-1} \cdot \text{K}^{-1}$ is slightly higher than the $-0.034 \text{ cm}^{-1} \cdot \text{K}^{-1}$ value reported in Reference 84. The magnitude of the RBM downshift depends on the nanotube diameter.

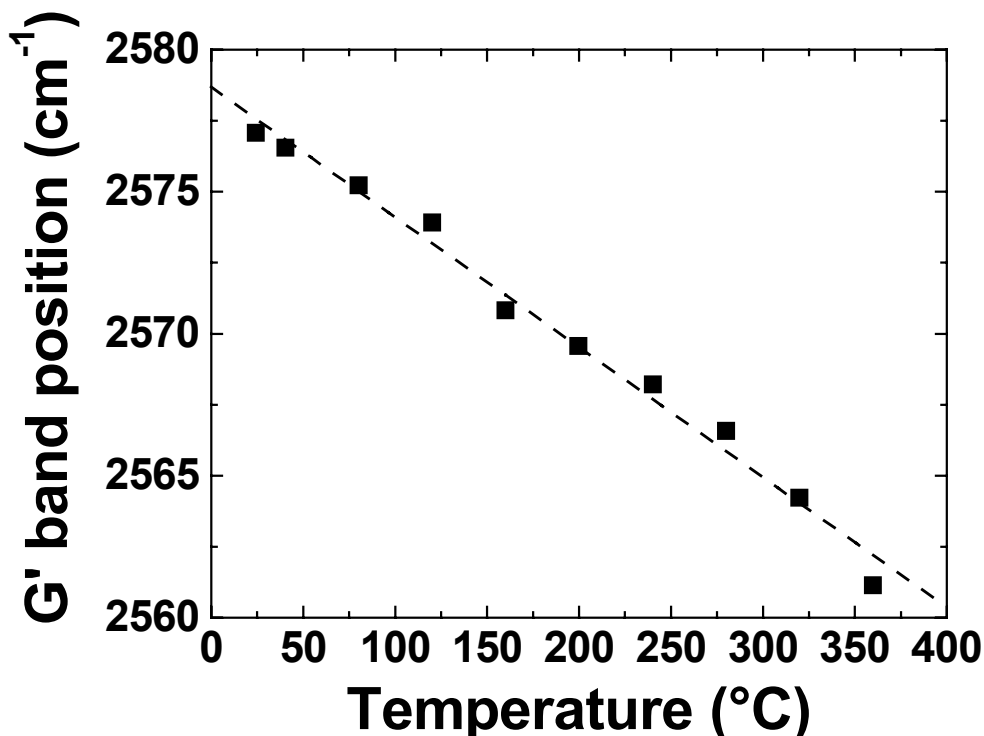


Figure II.43: G' band position as a function of the temperature in the hot stage.

For each temperature value, ten Raman spectra were collected on different nanotube grains. The absolute RBM intensity values vary significantly from one location to another, so in order to compare the results, the RBM intensities were normalized relative to the strongest RBM located at 266 cm^{-1} at room temperature. The RBM relative intensities are plotted against temperature in Figure II.44. The intensity of the RBM located at 269 cm^{-1} at room temperature remains constant relative to the main RBM over the whole temperature range. The RBM located at 204 cm^{-1} at room temperature increases slightly with rising temperature, while the others decrease in relative intensity for temperature below 240°C.

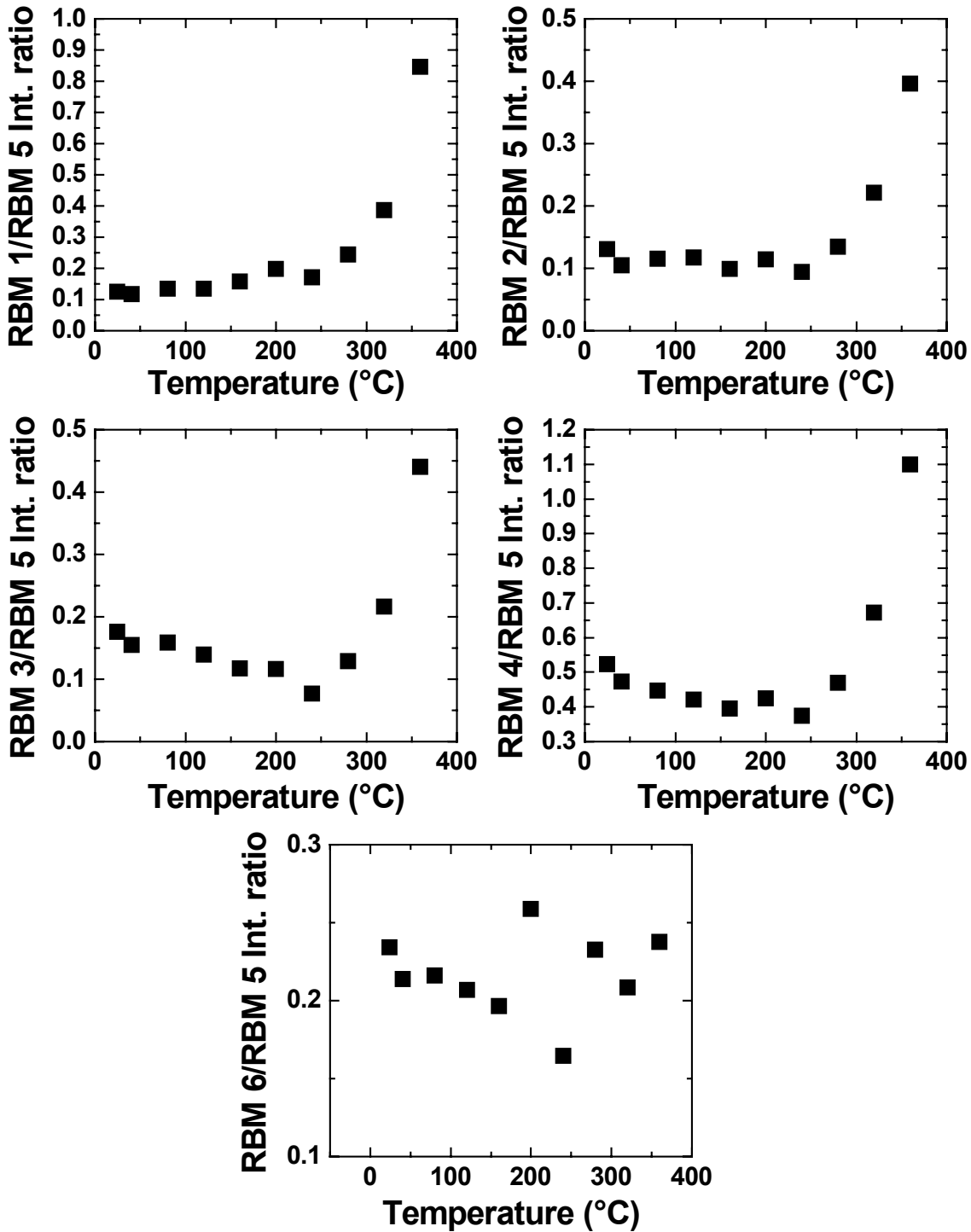


Figure II.44: Relative intensity of the 5 RBMs located at 204, 214, 224, 232 and 269 cm^{-1} at room temperature (normalized to the intensity of the 266 cm^{-1} RBM) in purified HiPco powder as a function of the temperature.

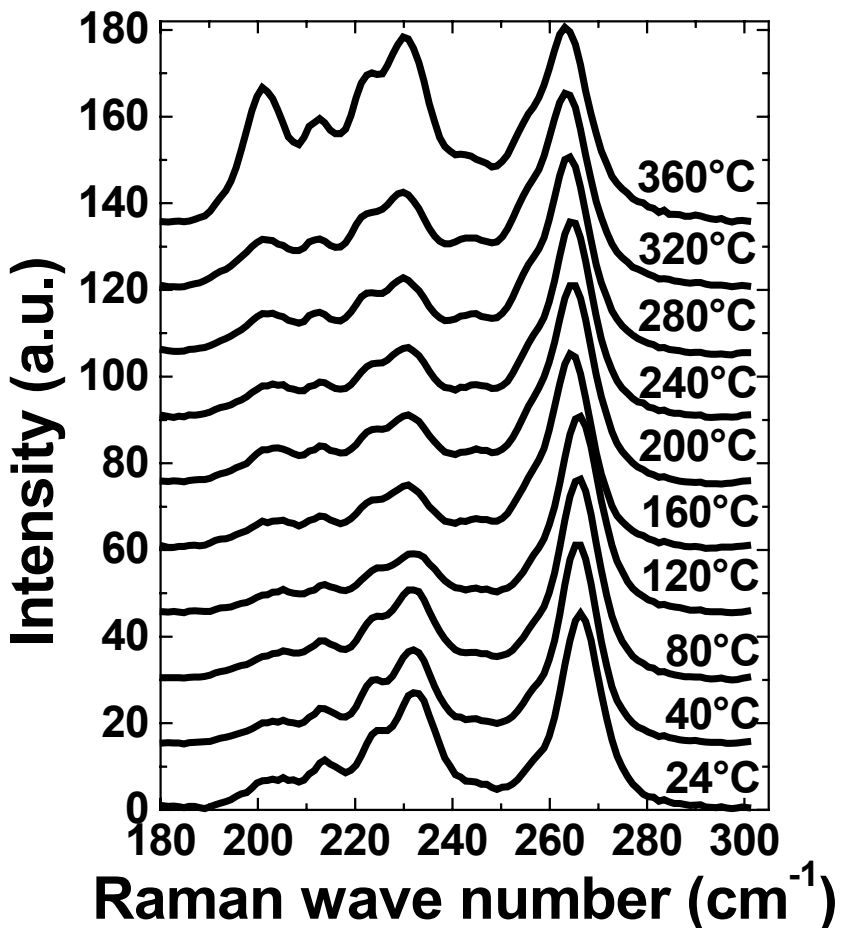


Figure II.45: Typical low-frequency Raman spectra at various temperatures. The spectra were normalized to the intensity of the 266 cm^{-1} RBM and offset vertically for clarity.

Above 240°C , all RBMs, except the one located at 269 cm^{-1} at room temperature, increase dramatically in intensity compared to the main RBM. This significant increase above 240°C is probably due to the destruction of the nanotubes with smaller diameters [89], as showed in Figure II.45.

The heat treatment leads to irreversible results, such as the downshift of the G' band and the modification of the relative RBM intensities (Table II.1). The temperature value is consistent with the thermogravimetric results on purified HiPco nanotubes reported in Reference 197. The purified material starts to lose weight significantly from 300°C and the maximum weight loss rate occurs around 500°C .

Table II.1: Position of the G' band and the 6 RBMs and the relative intensities of the RBMs at room temperature before and after the heat treatment. The laser wavelength was 780 nm.

Average values	Original		After heat treatment	
	Position	Norm. intensity	Position	Norm. intensity
G' band	2577	-	2572	-
RBM 1	204	0.19	203	0.61
RBM 2	214	0.13	213	0.22
RBM 3	224	0.16	223	0.34
RBM 4	232	0.58	231	1.07
RBM 5	266	1.00	265	1.00
RBM 6	269	0.26	270	0.20

Epoxy/HiPco nanotubes and PVA/HiPco nanotubes composites were studied in the 20-150°C (Figures II.46 and II.48) and 20-360°C (Figures II.47 and II.49) temperature range, respectively. The epoxy matrix was not stable enough above 150°C to extend the temperature range studied. The position and depth of the nanotube particles in the composite vary at high temperature, making the study on the RBM intensities difficult. The Raman spectra from epoxy composites were fitted with five Lorentzian lines and those from PVA composites with four. The G' band shifts to lower wave numbers with rising temperature, at a rate of $-0.037 \text{ cm}^{-1} \cdot \text{°C}^{-1}$ (Figure II.46) and $-0.053 \text{ cm}^{-1} \cdot \text{°C}^{-1}$ (Figure II.48) for the epoxy and PVA composites respectively.

All RBMs also shift to lower wave numbers with rising temperature, with different rates depending on the nanotube structure. The magnitude of the downshifts in the composites (Figures II.46 and II.47) are comparable to those of the SWNT powder (Figures II.42), indicating an effective heat transfer. The RBM relative intensities (Figures II.48 and II.49) exhibit similar trends as the RBMs in the nanotube powder (Figure II.44). The relative RBM intensity variations are consistent with the structure-dependent shift of the E_{ii} values observed by Fantini *et al.* [140]. The smaller diameter nanotubes are progressively destroyed above 280°C in the PVA composites. The upshift of the RBMs above 300°C coincides with the degradation of the PVA matrix, which occurs at temperatures between 200°C and 300°C [219,220].

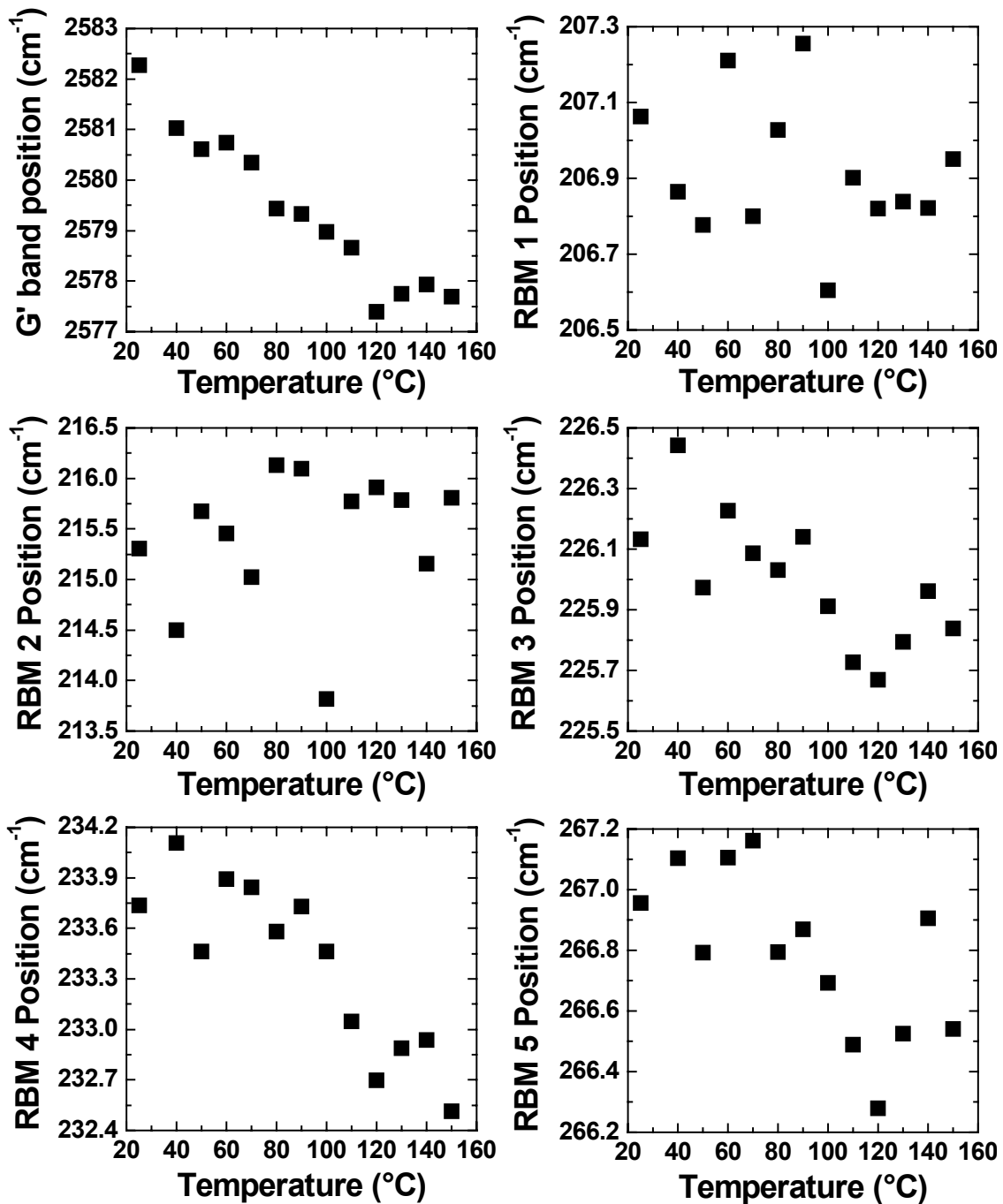


Figure II.46: Position of the G' band and the 5 RBMs located at 207, 216, 226, 234, and 267 cm^{-1} at room temperature in epoxy/HIPco composites as a function of the temperature in the hot stage.

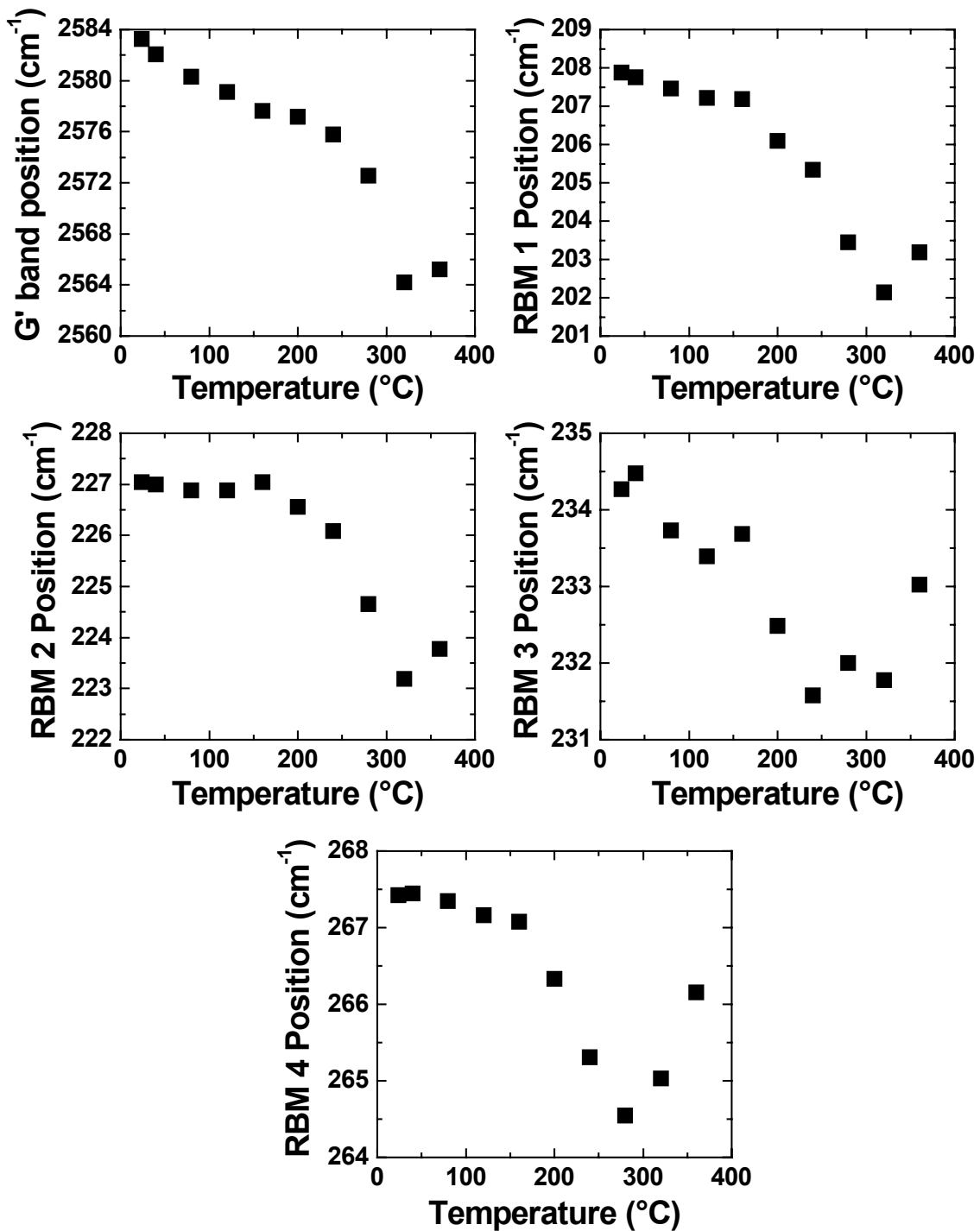


Figure II.47: Position of the G' band and the 4 RBMs located at 208, 227, 234, and 268 cm⁻¹ at room temperature in a PVA/HiPco film as a function of the temperature in the hot stage.

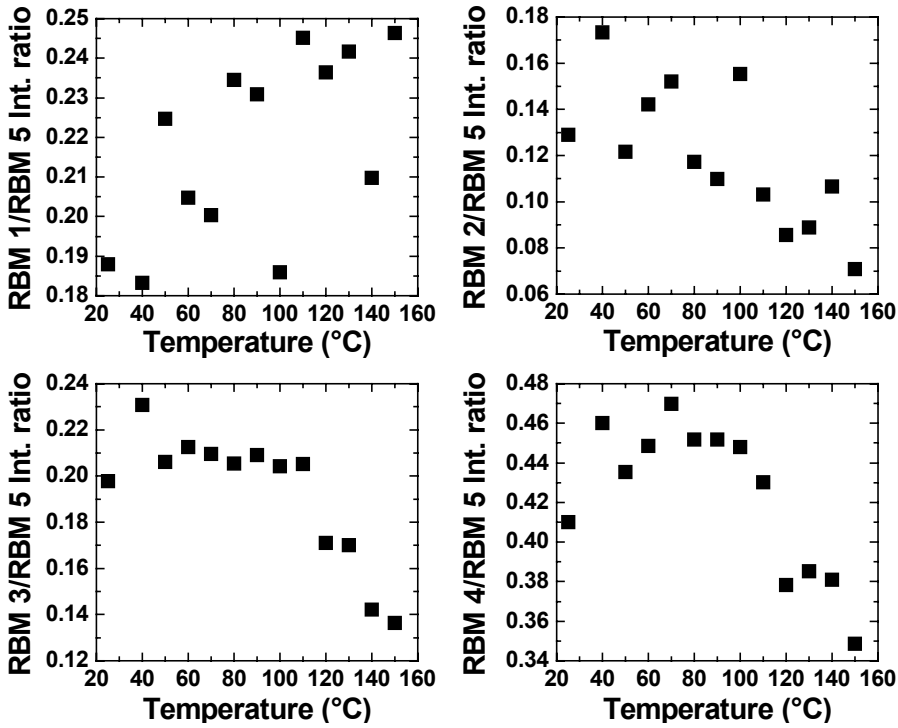


Figure II.48: Relative intensity of the 4 RBMs located at 207, 216, 226 and 234 cm^{-1} at room temperature (normalized to the intensity of the 267 cm^{-1} RBM) in epoxy/HiPco composites as a function of the temperature.

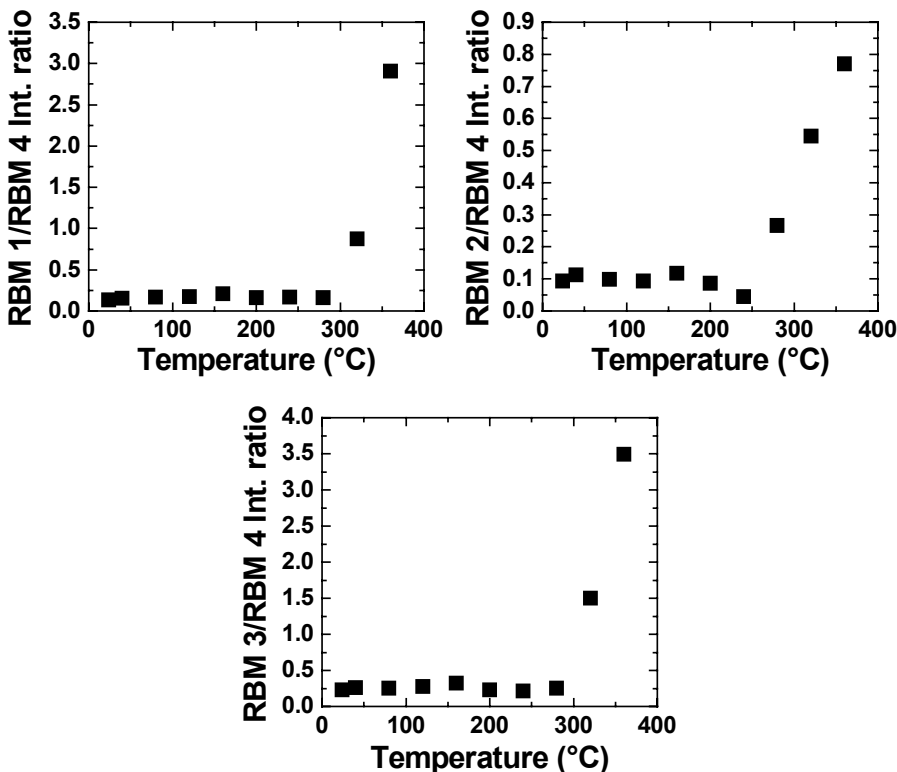


Figure II.49: Relative intensity of the 3 RBMs located at 208, 227 and 234 cm^{-1} at room temperature (normalized to the intensity of the 268 cm^{-1} RBM) in a PVA/HiPco film as a function of the temperature.

II.4 Discussion

These experiments show the significantly important effect of laser irradiation, focus conditions and heat on the Raman spectra. The effects of these three types of experiments were similar: all Raman bands shift to lower wave numbers and the RBM relative intensities vary with temperature. The local temperature increase cannot be estimated in the focus and laser irradiation experiments, since the method involving the anti-Stokes/Stokes intensity ratio is not valid in resonance conditions.

Overall, the temperature effect from the hot stage experiments was more intense on the nanotube powder than those from the focus conditions or laser irradiation. Nevertheless, the effects of focus conditions are important enough to explain the differences in the low-frequency Raman spectra of nanotubes in powder and in composites. Table II.2 are the extreme positions of the G, G' bands and the RBMs observed in HiPco and Elicarb nanotube powders and composites, as the distance lens-sample varies. The RBM upshift in composites is attributed to reduced heating effects under laser irradiation. High temperatures lead to the downshift of the RBM positions and nanotube heating in the composite is limited because of their low concentration in the polymer matrix.

However, heating effects are not the cause of the RBM intensity variations observed during the four-point bending tests on composite samples. The experiments on the focus conditions in epoxy composites indicate that the intensity variations depend on the local nanotube density in the material, as showed by the multiple intensity maxima, and therefore on the position of the laser spot on the sample. That was not the case during the four-point bending tests: the RBM intensities varied by different magnitudes but always following the same trend in different samples.

Moreover, the RBMs in epoxy composites and PVA films reached their maximum approximately at the same distance during the focus experiments, in contrast to the four-point bending results, which showed that the variation trend depends on the nanotube structure and not on the laser spot position. Also during the four-point bending tests, the RBM positions remained constant in

tension and compression within the resolution of the spectrometer in the whole series of spectra, which shows that the distance between the sample and the lens also was kept constant.

Table II.2: Extreme positions of the G, G' bands and the RBMs as the distance lens-sample varies.

Laser wavelength	Peak	Powder		Composite	
		Minimum	Maximum	Minimum	Maximum
HiPco SWNTs					
$\lambda = 830 \text{ nm}$	G band	1595	1596	1595	1596
	RBM 1	205	207	206	209
	RBM 2	214	215	217	218
	RBM 3	225	228	227	228
	RBM 4	234	235	237	238
	RBM 5	264	266	264	267
$\lambda = 780 \text{ nm}$	G' band	2574	2586	2587	2592
	RBM 1	202	206	208	211
	RBM 2	211	216	-	-
	RBM 3	223	230	228	233
	RBM 4	231	237	236	241
	RBM 5	256	267	265	270
$\lambda = 632 \text{ nm}$	G' band	2610	2616	2615	2619
	RBM 1	196	201	198	202
	RBM 2	220	226	220	227
	RBM 3	256	261	257	262
	RBM 4	282	288	284	292
	RBM 5	294	297	298	301
Elicarb SWNTs					
$\lambda = 830 \text{ nm}$	G band	1594	1598	1594	1597
	RBM 1	163	164	-	-
	RBM 2	182	183	-	-
	RBM 3	193	194	191	192
	RBM 4	204	205	207	209
	RBM 5	-	-	217	219
	RBM 6	224	226	228	230
	RBM 7	233	234	237	238
	RBM 8	262	265	-	-
$\lambda = 780 \text{ nm}$	G' band	2566	2578	2585	2591
	RBM 1	200	207	206	213
	RBM 2	207	215	216	221
	RBM 3	220	232	226	230
	RBM 4	226	242	234	243
	RBM 5	263	269	264	270
$\lambda = 632 \text{ nm}$	G' band	2616	2619	2636	2641
	RBM 1	191	194	199	206
	RBM 2	216	219	221	227
	RBM 3	251	254	254	260
	RBM 4	280	285	284	289

References

- [1] D.S. Bethune, C.H. Kiang, M.S. de Vries, G. Gorman, R. Savoy, J. Vazquez, and R. Beyers, "Cobalt-Catalysed Growth of Carbon Nanotubes with Single-Atomic-Layer Walls," *Nature* **363**, 605 (1993).
- [2] S. Iijima, T. Ichihashi, "Single-Shell Carbon Nanotubes of 1-nm Diameter," *Nature* **363**, 603 (1993).
- [3] M.S. Dresselhaus, G. Dresselhaus, and P. Avouris, *Carbon Nanotubes: Synthesis, Structure, Properties and Applications* Vol. 80 of Springer Series in Topics in Applied Physics (Springer-Verlag, Berlin, 2001).
- [4] T. Guo, P. Nikolaev, A. Thess, D.T. Colbert, and R.E. Smalley, "Catalytic Growth of Single-Walled Nanotubes by Laser Vaporization," *Chemical Physics Letters* **243**, 49 (1995).
- [5] A. Thess, R. Lee, P. Nikolaev, H. Dai, P. Petit, J. Robert, C. Xu, Y.H. Lee, S.G. Kim, A.G. Rinzler, D.T. Colbert, G.E. Scuseria, D. Tomanek, J.E. Fischer, and R.E. Smalley, "Crystalline Ropes of Metallic Carbon Nanotubes," *Science* **273**, 483 (1996).
- [6] M. Jose-Yacaman, M. Miki-Yoshida, L. Rendon, and J.G. Santiesteban, "Catalytic Growth of Carbon Microtubules with Fullerene Structure," *Applied Physics Letters* **62**, 202 (1993).
- [7] P. Nikolaev, M.J. Bronikowski, R.K. Bradley, F. Rohmund, D.T. Colbert, K.A. Smith, and R.E. Smalley, "Gas-phase Catalytic Growth of Single-walled Carbon Nanotubes from Carbon Monoxide," *Chemical Physics Letters* **313**, 91 (1999).
- [8] R. Saito, M. Fujita, G. Dresselhaus, and M.S. Dresselhaus, "Electronic Structure of Chiral Graphene Tubules," *Applied Physics Letters* **60**, 2204 (1992).
- [9] J.W.G. Wildoer, L.C. Venema, A.G. Rinzler, R.E. Smalley, and C. Dekker, "Electronic Structure of Atomically Resolved Carbon Nanotubes," *Nature* **391**, 59 (1998).
- [10] T.W. Odom, J.-L. Huang, P. Kim, and C.M. Lieber, "Atomic Structure and Electronic Properties of Single-walled Carbon Nanotubes," *Nature* **391**, 62 (1998).
- [11] R. Heyd, A. Charlier, and E. McRae, "Uniaxial-stress Effects on the Electronic Properties of Carbon Nanotubes," *Physical Review B* **55**, 6820 (1997).
- [12] L. Yang, M.P. Anantram, J. Han and J.P. Lu, "Band-gap Change of Carbon Nanotubes: Effect of Small Uniaxial and Torsional Strain," *Physical Review B* **60**, 13874 (1999).
- [13] L. Yang and J. Han, "Structure of Deformed Carbon Nanotubes," *Physical Review Letters* **85**, 154 (2000).
- [14] T. Ito, K. Nishidate, M. Baba, and M. Hasegawa, "First Principles Calculations for Electronic Band Structure of Single-walled Carbon Nanotube Under Uniaxial Strain," *Surface Science* **514**, 222 (2002).
- [15] J.-C. Charlier, P. Lambin, and T.W. Ebbesen, "Electronic Properties of Carbon Nanotubes with Polygonized Cross Sections," *Physical Review B* **54**, R8377 (1996).

- [16] A. Rochefort, D.R. Salahub, and P. Avouris, "The Effect of Structural Distortions on the Electronic Structure of Carbon Nanotubes," *Chemical Physics Letters* **297**, 45 (1998).
- [17] C.-J. Park, Y.-H. Kim, and K.J. Chang, "Band-gap Modification by Radial Deformation in Carbon Nanotubes," *Physical Review B* **60**, 10656 (1999).
- [18] A. Rochefort, P. Avouris, F. Lesage, and D.R. Salahub, "Electrical and Mechanical Properties of Distorted Carbon Nanotubes," *Physical Review B* **60**, 13824 (1999).
- [19] C. Kilic, S. Ciraci, O. Gulseren, and T. Yildirim, "Variable and Reversible Quantum Structures on a Single Carbon Nanotube," *Physical Review B* **62**, R16345 (2000).
- [20] O. Gulseren, T. Yildirim, S. Ciraci, and C. Kilic, "Reversible Band-gap Engineering in Carbon Nanotubes by Radial Deformation," *Physical Review B* **65**, 155410 (2002).
- [21] M.H.F. Sluitera, V. Kumara, and Y. Kawazoe, "Electronic Structure of Single Wall Carbon Nanotube Bundles Under Compression as Compared to Graphite and Hexagonal Graphene Stacking," *Physica B* **323**, 203 (2002).
- [22] R. Martel, T. Schmidt, H.R. Shea, T. Hertel, and P. Avouris, "Single- and Multi-Wall Carbon Nanotube Field-Effect Transistors," *Applied Physics Letters* **73**, 2447 (1998).
- [23] M.B. Nardelli and J. Bernholc, "Mechanical Deformations and Coherent Transport in Carbon Nanotubes," *Physical Review B* **60**, R16338 (1999).
- [24] A. Charlier, E. McRae, R. Heyd, and M.-F. Charlier, "Metal-Semiconductor Transitions Under Uniaxial Stress for Single- and Double-walled Carbon Nanotubes," *Journal of Physics and Chemistry of Solids* **62**, 439 (2001).
- [25] J.-Q. Lu, J. Wu, W. Duan, F. Liu, B.-F. Zhu, and B.-L. Gu, "Metal-to-Semiconductor Transition in Squashed Armchair Carbon Nanotubes," *Physical Review Letters* **90**, 156601 (2003).
- [26] A.A. Farajian, B.I. Yakobson, H. Mizuseki, and Y. Kawazoe, "Electronic Transport Through Bent Carbon Nanotubes: Nanoelectromechanical Sensors And Switches," *Physical Review B* **67**, 205423 (2003).
- [27] S. Paulson, M.R. Falvo, N. Snider, A. Helser, T. Hudson, A. Seeger, R.M. Taylor, R. Superfine, and S. Washburn, "In Situ Resistance Measurements of Strained Carbon Nanotubes," *Applied Physics Letters* **75**, 2936 (1999).
- [28] T.W. Tombler, C. Zhou, L. Alexseyev, J. Kong, H. Dai, L. Liu, C.S. Jayanthi, M. Tang, and S.-Y. Wu, "Reversible Electromechanical Characteristics of Carbon Nanotubes Under Local-probe Manipulation," *Nature* **405**, 769 (2000).
- [29] R. Gaal, J.-P. Salvetat, and L. Forro, "Pressure Dependence of the Resistivity of Single-walled Carbon Nanotube Ropes," *Physical Review B* **61**, 7320 (2000).
- [30] D.S. Tang, Z.X. Bao, L.J. Wang, L.C. Chen, L.F. Sun, Z.Q. Liu, W.Y. Zhou, and S.S. Xie, "The Electrical Behavior of Carbon Nanotubes Under High Pressure," *Journal of Physics and Chemistry of Solids* **61**, 1175 (2000).
- [31] J. Tang, L.-C. Qin, T. Sasaki, M. Yudasaka, A. Matsushita, and S. Iijima, "Revealing Properties of Single-walled Carbon Nanotubes under High Pressure," *Journal of Physics: Condensed Matter* **14**, 10575 (2002).
- [32] E.D. Minot, Y. Yaish, V. Sazonova, J.-Y. Park, M. Brink, and P.L.

- McEuen, "Tuning Carbon Nanotube Band Gaps with Strain," *Physical Review Letters* **90**, 156401 (2003).
- [33] J. Cao, Q. Wang, and H. Dai, "Properties of Metallic, Quasimetallic, and Semiconducting Carbon Nanotubes under Stretching," *Physical Review Letters* **90**, 157601 (2003).
- [34] T.A. Gloor and F. Mila, "Strain Induced Correlation Gaps in Carbon Nanotubes," *European Physical Journal B* **38**, 9 (2004).
- [35] A. Krishnan, E. Dujardin, T.W. Ebbesen, P.N. Yianilos, and M.M.J. Treacy, "Young's Modulus of Single-walled Nanotubes," *Physical Review B* **58**, 14013 (1998).
- [36] J. Chen, A.M. Rao, S. Lyuksyutov, M.E. Itkis, M.A. Hamon, H. Hu, R.W. Cohn, P.C. Eklund, D.T. Colbert, R.E. Smalley, and R.C. Haddon, "Dissolution of Full-Length Single-Walled Carbon Nanotubes," *Journal Physical Chemistry B* **105**, 2525 (2001).
- [37] W. Huang, S. Fernando, L.F. Allard, and Y.-P. Sun, "Solubilization of Single-Walled Carbon Nanotubes with Diamine-Terminated Oligomeric Poly(ethylene Glycol) in Different Functionalization Reactions," *Nano Letters* **3**, 565 (2003).
- [38] V. Derycke, R. Martel, J. Appenzeller, and P. Avouris, "Carbon Nanotube Inter- and Intramolecular Logic Gates," *Nano Letters* **1**, 453 (2001).
- [39] A. Allaoui, S. Bai, H.M. Cheng, and J.B. Bai, "Mechanical and Electrical Properties of a MWNT/epoxy Composite," *Composites Science and Technology* **62**, 1993 (2002).
- [40] J.C. Kearns, and R.L. Shambaugh, "Polypropylene Fibers Reinforced with Carbon Nanotubes Composite," *Journal of Applied Polymer Science* **86**, 2079 (2002).
- [41] C.A. Dyke and J.M. Tour, "Covalent Functionalization of Single-Walled Carbon Nanotubes for Materials Applications," *Journal of Physical Chemistry A* **108**, 11151 (2004).
- [42] R. Haggenmueller, H.H. Gommans, A.G. Rinzler, J.E. Fischer, and K.I. Winey, "Aligned Single-wall Carbon Nanotubes in Composites by Melt Processing Methods," *Chemical Physics Letters* **330**, 219 (2000).
- [43] B. Vigolo, P. Poulin, M. Lucas, P. Launois, and P. Bernier, "Improved Structure and Properties of Single-wall Carbon Nanotube Spun Fibers," *Applied Physics Letters* **81**, 1210 (2002).
- [44] N. de Jonge, M. Allioux, M. Doytcheva, M. Kaiser, K.B.K. Teo, R.G. Lacerda, and W.I. Milne, "Characterization of the Field Emission Properties of Individual Thin Carbon Nanotubes," *Applied Physics Letters* **85**, 1607 (2004).
- [45] J. Lawrence and G. Xu, "High Pressure Saturation of Hydrogen Stored by Single-Wall Carbon Nanotubes," *Applied Physics Letters* **84**, 918 (2004).
- [46] P.G. Collins, K. Bradley, M. Ishigami, A. Zettl, "Extreme Oxygen Sensitivity of Electronic Properties of Carbon Nanotubes," *Science* **287**, 1801 (2000).
- [47] A. Star, J.-C.P. Gabriel, K. Bradley, and G. Gruner, "Electronic Detection of Specific Protein Binding Using Nanotube FET Devices," *Nano Letters* **3**, 459 (2003).
- [48] R.J. Chen, H.C. Choi, S. Bangsaruntip, E. Yenilmez, X. Tang, Q. Wang, Y. Chang, and H. Dai, "An Investigation of the Mechanisms of Electronic

- Sensing of Protein Adsorption on Carbon Nanotube Devices," *Journal of the American Chemical Society* **126**, 1563 (2004).
- [49] A. Modi, N. Koratkar, E. Lass, B. Wei, and P.M. Ajayan, "Miniaturized Gas Ionization Sensors Using Carbon Nanotubes," *Nature* **424**, 171 (2003).
- [50] M.S. Dresselhaus, G. Dresselhaus, A. Jorio, A.G. Souza Filho, and R. Saito, "Raman Spectroscopy on Isolated Single Wall Carbon Nanotubes," *Carbon* **40**, 2043 (2002).
- [51] C.A. Cooper, R.J. Young, and M. Halsall, "Investigation into the deformation of carbon nanotubes and their composites through the use of Raman spectroscopy," *Composites: Part A* **32**, 401 (2001).
- [52] C. V. Raman and K.S. Krishnan, "A New Type of Secondary Radiation," *Nature* **121**, 501 (1928).
- [53] R.L. McCreery, *Raman spectroscopy for chemical analysis*, vol. 157 in Chemical Analysis, Wiley Interscience.
- [54] A.M. Rao, E. Richter, S. Bandow, B. Chase, P.C. Eklund, K.A. Williams, S. Fang, K.R. Subbaswamy, M. Menon, A. Thess, R.E. Smalley, G. Dresselhaus, and M.S. Dresselhaus, "Diameter-selective Raman Scattering from Vibrational Modes in Carbon Nanotubes," *Science* **275**, 187 (1997).
- [55] M.S. Dresselhaus, G. Dresselhaus, R. Saito, and A. Jorio, "Raman Spectroscopy of Carbon Nanotubes," *Physics Reports* **409**, 47 (2005).
- [56] H. Hiura, T.W. Ebbesen, K. Tanigaki, H. Takahashi, "Raman Studies of Carbon Nanotubes," *Chemical Physics Letters* **202**, 509 (1993).
- [57] A. Jorio, A.G. Souza Filho, G. Dresselhaus, M.S. Dresselhaus, A.K. Swan, M.S. Unlu, B.B. Goldberg, M.A. Pimenta, J.H. Hafner, C.M. Lieber, and R. Saito, "G-band Resonant Raman Study of 62 Isolated Single-wall Carbon Nanotubes," *Physical Review B* **65**, 155412 (2002).
- [58] M.E. Itkis, D.E. Perea, R. Jung, S. Niyogi, and R.C. Haddon, "Comparison of Analytical Techniques for Purity Evaluation of Single-Walled Carbon Nanotubes," *Journal of the American Chemical Society* **127**, 3439 (2005).
- [59] L. Zhang, V.U. Kiny, H. Peng, J. Zhu, R.F.M. Lobo, J.L. Murgrave, and V.N. Khabashesku, "Sidewall Functionalization of Single-Walled Carbon Nanotubes with Hydroxyl Group-Terminated Moieties," *Chemistry of Materials* **16**, 2055 (2004).
- [60] S.D.M. Brown, A. Jorio, M.S. Dresselhaus, and G. Dresselhaus, "Observations of the D-band Feature in the Raman Spectra of Carbon Nanotubes," *Physical Review B* **64**, 073403 (2001).
- [61] A. Jorio, M.A. Pimenta, C. Fantini, M. Souza, A.G. Souza Filho, G.G. Samsonidze, G. Dresselhaus, M.S. Dresselhaus, and R. Saito, "Advances in Single Nanotube Spectroscopy: Raman Spectra from Cross-Polarized Light and Chirality Dependence of Raman Frequencies," *Carbon* **42**, 1067 (2004).
- [62] A.G. Souza Filho, A. Jorio, G.G. Samsonidze, G. Dresselhaus, R. Saito, and M.S. Dresselhaus, "Raman Spectroscopy for Probing Chemically/Physically Induced Phenomena in Carbon Nanotubes," *Nanotechnology* **14**, 1130 (2003).
- [63] A.G. Souza Filho, A. Jorio, Ge.G. Samsonidze, G. Dresselhaus, M.S. Dresselhaus, A.K. Swan, M.S. Unlu, B.B. Goldberg, R. Saito, J.H. Hafner, C.M. Lieber, and M.A. Pimenta, "Probing the Electronic Trigonal Warping Effect in Individual Single-wall Carbon Nanotubes Using Phonon Spectra," *Chemical*

- Physics Letters* **354**, 62 (2002).
- [64] M.S. Dresselhaus, A. Jorio, A.G. Souza Filho, G. Dresselhaus, and R. Saito, "Raman Spectroscopy on One Isolated Carbon Nanotube," *Physica B* **323**, 15 (2002).
- [65] A. Kukovecz, C. Kramberger, V. Georgakilas, M. Prato, and H. Kuzmany, "A Detailed Raman Study on Thin Single-wall Carbon Nanotubes Prepared by the HiPCO Process," *European Physical Journal B* **28**, 223 (2002).
- [66] S.M. Bachilo, M.S. Strano, C. Kittrell, R.H. Hauge, R.E. Smalley, and R.B. Weisman, "Structure-Assigned Optical Spectra of Single-Walled Carbon Nanotubes," *Science* **298**, 2361 (2002).
- [67] L. Alvarez, A. Righi, T. Guillard, S. Rols, E. Anglaret, D. Laplaze, and J.-L. Sauvajol, "Resonant Raman Study of the Structure and Electronic Properties of Single-wall Carbon Nanotubes," *Chemical Physics Letters* **316**, 186 (1999).
- [68] Z. Yu and L.E. Brus, "(*n,m*) Structural Assignments and Chirality Dependence in Single-Wall Carbon Nanotube," *Journal of Physical Chemistry B* **105**, 6831 (2001).
- [69] J.-L. Sauvajol, E. Anglaret, S. Rols, and L. Alvarez, "Phonons in Single Wall Carbon Nanotube Bundles," *Carbon* **40**, 1697 (2002).
- [70] A. Jorio, R. Saito, J.H. Hafner, C.M. Lieber, M. Hunter, T. McClure, G. Dresselhaus, and M.S. Dresselhaus, "Structural (*n,m*) Determination of Isolated Single-Wall Carbon Nanotubes by Resonant Raman Scattering," *Physical Review Letters* **86**, 1118 (2001).
- [71] S.D.M. Brown, P. Corio, A. Marucci, M.A. Pimenta, M.S. Dresselhaus, and G. Dresselhaus, "Second-order Resonant Raman Spectra of Single-walled Carbon Nanotubes," *Physical Review B* **61**, 7734 (2000).
- [72] L. Alvarez, A. Righi, S. Rols, E. Anglaret, and J.L. Sauvajol, "Excitation Energy Dependence of the Raman Spectrum of Single-walled Carbon Nanotubes," *Chemical Physics Letters* **320**, 441 (2000).
- [73] V.W. Brar, Ge.G. Samsonidze, M.S. Dresselhaus, G. Dresselhaus, R. Saito, A.K. Swan, M.S. Unlu, B.B. Goldberg, A.G. Souza Filho, and A. Jorio, "Second-order Harmonic and Combination Modes in Graphite Single-wall Carbon Nanotube Bundles and Isolated Single-wall Carbon Nanotubes," *Physical Review B* **66**, 155418 (2002).
- [74] C. Thomsen, "Second-order Raman Spectra of Single and Multiwalled Carbon Nanotubes," *Physical Review B* **61**, 4542 (2000).
- [75] M. A. Pimenta, A. Marucci, S. D. M. Brown, M. J. Matthews, A. M. Rao, P. C. Eklund, R. E. Smalley, G. Dresselhaus, and M. S. Dresselhaus, "Resonant Raman Effect in Single-wall Carbon Nanotubes," *Journal of Materials Research* **13**, 2396 (1998).
- [76] A. Kasuya, M. Sugano, T. Maeda, Y. Saito, K. Tohji, H. Takahashi, Y. Sasaki, M. Fukushima, Y. Nishina, and C. Horie, "Resonant Raman Scattering and the Zone-folded Electronic Structure in Single-wall Nanotubes," *Physical Review B* **57**, 4999 (1998).
- [77] M. A. Pimenta, A. Marucci, S. A. Empedocles, M. G. Bawendi, E. B. Hanlon, A. M. Rao, P. C. Eklund, R. E. Smalley, G. Dresselhaus, and M. S. Dresselhaus, "Raman Modes of Metallic Carbon Nanotubes," *Physical Review B* **58**, R16016 (1998).
- [78] C. Fantini, M.A. Pimenta, M.S.S. Dantas, D. Ugarte, A.M. Rao, A. Jorio,

- G. Dresselhaus, and M.S. Dresselhaus, "Micro-Raman Investigation of Aligned Single-wall Carbon Nanotubes," *Physical Review B* **63**, R161405 (2001).
- [79] S.D.M. Brown, A. Jorio, P. Corio, M.S. Dresselhaus, G. Dresselhaus, R. Saito, and K. Kneipp, "Origin of the Breit-Wigner-Fano Lineshape of the Tangential G-band Feature of Metallic Carbon Nanotubes," *Physical Review B* **63**, 155414 (2001).
- [80] P.M. Rafailov, H. Jantoljak, and C. Thomsen, "Electronic Transitions in Single-walled Carbon Nanotubes: A Resonance Raman Study," *Physical Review B* **61**, 16179 (2000).
- [81] A. Jorio, A.G. Souza Filho, G. Dresselhaus, M.S. Dresselhaus, R. Saito, J.H. Hafner, C.M. Lieber, F.M. Matinaga, M.S.S. Dantas, and M.A. Pimenta, "Joint Density of Electronic States for One Isolated Single-wall Carbon Nanotube Studied by Resonant Raman Scattering," *Physical Review B* **63**, 245416 (2001).
- [82] A.G. Souza Filho, A. Jorio, A.K. Swan, M.S. Unlu, B.B. Goldberg, R. Saito, J.H. Hafner, C.M. Lieber, M.A. Pimenta, G. Dresselhaus, and M.S. Dresselhaus, "Anomalous Two-peak G'-band Raman Effect in One Isolated Single-wall Carbon Nanotube," *Physical Review B* **65**, 85417 (2002).
- [83] P.V. Huong, R. Cavagnat, P.M. Ajayan, and O. Stephan, "Temperature-dependent vibrational spectra of carbon nanotubes," *Physical Review B* **51**, 10048 (1995).
- [84] F. Huang, K.T. Yue, P. Tan, S.-L. Zhang, Z. Shi, X. Zhou, and Z. Gu, "Temperature Dependence of the Raman Spectra of Carbon Nanotubes," *Journal of Applied Physics* **84**, 4022 (1998).
- [85] H.D. Li, K.T. Yue, Z.L. Lian, Y. Zhan, L.X. Zhou, S.L. Zhang, Z.J. Shi, Z.N. Gu, B.B. Liu, R.S. Yang, H.B. Yang, G.T. Zou, Y. Zhang, and S. Iijima, "Temperature Dependence of the Raman Spectra of Single-wall Carbon Nanotubes," *Applied Physics Letters* **76**, 2053 (2000).
- [86] P. Tan, Y. Tang, C. Hu, F. Li, Y. Wei, and H. Cheng, "Identification of the Conducting Category of Individual Carbon Nanotubes from Stokes and Anti-Stokes Raman Scattering," *Physical Review B* **62**, 5186 (2000).
- [87] A.G. Souza Filho, A. Jorio, J.H. Hafner, C.M. Lieber, R. Saito, M.A. Pimenta, G. Dresselhaus, and M.S. Dresselhaus, "Electronic Transition Energy E_{ii} for an isolated (n,m) Single-wall Carbon Nanotube Obtained by Anti-Stokes/Stokes Resonant Raman Intensity Ratio," *Physical Review B* **63**, 241404 (2001).
- [88] S.D.M. Brown, P. Corio, A. Marucci, M.S. Dresselhaus, M.A. Pimenta, and K. Kneipp, "Anti-Stokes Raman Spectra of Single-walled Carbon Nanotubes," *Physical Review B* **61**, 5137 (2000).
- [89] P. Corio, P.S. Santos, M.A. Pimenta, and M.S. Dresselhaus, "Evolution of the Molecular Structure of Metallic and Semiconducting Carbon Nanotubes Under Laser Irradiation," *Chemical Physics Letters* **360**, 557 (2002).
- [90] U.D. Venkateswaran, M.-É. Gosselin, B. Postek, D.L. Masica, G. Chen, R. Gupta, and P.C. Eklund, "Radial and Tangential Vibrational Modes of HiPco-derived Carbon Nanotubes under Pressure," *Physica Status Solidi B* **235**, 364 (2003).
- [91] S.-L. Zhang, X. Hu, H. Li, Z. Shi, K.T. Yue, J. Zi, Z. Gu, X. Wu, Z. Lian, Y. Zhan, F. Huang, L. Zhou, Y. Zhang, and S. Iijima, "Abnormal Anti-Stokes

- Raman Scattering of Carbon Nanotubes," *Physical Review B* **66**, 35413 (2002).
- [92] H.H. Gommans, J.W. Alldredge, H. Tashiro, J. Park, J. Magnuson, and A.G. Rinzler, "Fibers of Aligned Single-walled Carbon Nanotubes: Polarized Raman spectroscopy," *Journal of Applied Physics* **88**, 2509 (2000).
- [93] A.M. Rao, A. Jorio, M.A. Pimenta, M.S.S. Dantas, R. Saito, G. Dresselhaus, and M.S. Dresselhaus, "Polarized Raman Study of Aligned Multiwalled Carbon Nanotubes," *Physical Review Letters* **84**, 1820 (2000).
- [94] A. Jorio, G. Dresselhaus, M.S. Dresselhaus, M. Souza, M.S.S. Dantas, M.A. Pimenta, A.M. Rao, R. Saito, C. Liu, and H.M. Cheng, "Polarized Raman Study of Single-Wall Semiconducting Carbon Nanotubes," *Physical Review Letters* **85**, 2617 (2000).
- [95] J. Hwang, H.H. Gommans, A. Ugawa, H. Tashiro, R. Haggenmueller, K.I. Winey, J.E. Fischer, D.B. Tanner, and A.G. Rinzler, "Polarized Spectroscopy of Aligned Single-wall Carbon Nanotubes," *Physical Review B* **62**, R13310 (2000).
- [96] G.S. Duesberg, I. Loa, M. Burghard, K. Syassen, and S. Roth, "Polarized Raman Spectroscopy on Isolated Single-Wall Carbon Nanotubes," *Physical Review Letters* **85**, 5436 (2000).
- [97] A. Jorio, A.G. Souza Filho, V.W. Brar, A.K. Swan, M.S. Unlu, B.B. Goldberg, A. Righi, J.H. Hafner, C.M. Lieber, R. Saito, G. Dresselhaus, and M.S. Dresselhaus, "Polarized Resonant Raman Study of Isolated Single-wall Carbon Nanotubes: Symmetry Selection Rules Dipolar and Multipolar Antenna Effects," *Physical Review B* **65**, R121402 (2002).
- [98] O. Lourie and H.D. Wagner, "Evaluation of Young's Modulus of Carbon Nanotubes by Micro-Raman Spectroscopy," *Journal of Materials Research* **13**, 2418 (1998).
- [99] L.S. Schadler, S.C. Giannaris, and P.M. Ajayan, "Load Transfer in Carbon Nanotube Epoxy Composites," *Applied Physics Letters* **73**, 3842 (1998).
- [100] P.M. Ajayan, L.S. Schadler, C. Giannaris, and A. Rubio, "Single-Walled Carbon Nanotube-Polymer Composites: Strength and Weakness," *Advanced Materials* **12**, 750 (2000).
- [101] M.D. Froley, Q. Zhao, and H.D. Wagner, "Polarized Resonance Raman Spectroscopy of Single-wall Carbon Nanotubes within a Polymer Under Strain," *Physical Review B* **65**, 113413 (2002).
- [102] V.G. Hadjiev, M.N. Iliev, S. Areppalli, P. Nikolaev, and B.S. Files, "Raman Scattering Test of Single-Wall Carbon Nanotube Composites," *Applied Physics Letters* **78**, 3193 (2001).
- [103] J.R. Wood, M.D. Froley, E.R. Meurs, A.D. Prins, T. Peijs, D.J. Dunstan, and H.D. Wagner, "Mechanical Response of Carbon Nanotubes under Molecular and Macroscopic Pressures," *Journal of Physical Chemistry B* **103**, 10388 (1999).
- [104] C. Thomsen, S. Reich, H. Jantoljak, I. Loa, K. Syassen, M. Burghard, G.S. Duesberg, and S. Roth, "Raman Spectroscopy on Single- and Multi-walled Nanotubes Under High Pressure," *Applied Physics A* **69**, 309 (1999).
- [105] U.D. Venkateswaran, A.M. Rao, E. Richter, M. Menon, A. Rinzler, R.E. Smalley, and P.C. Eklund, "Probing the Single-wall Carbon Nanotube Bundle: Raman Scattering Under High Pressure," *Physical Review B* **59**, 10928 (1999).
- [106] D. Kahn and J.P. Lu, "Vibrational Modes of Carbon Nanotubes and Nanoropes," *Physical Review B* **60**, 6535 (1999).

- [107] S. Reich, H. Jantoljak, and C. Thomsen, "Shear Strain in Carbon Nanotubes Under Hydrostatic Pressure," *Physical Review B* **61**, R13389 (2000).
- [108] U.D. Venkateswaran, E.A. Brandsen, U. Schlecht, A.M. Rao, E. Richter, I. Loa, K. Syassen, and P.C. Eklund, "High Pressure Studies of the Raman-Active Phonons in Carbon Nanotubes," *Physica Status Solidi B* **223**, 225 (2001).
- [109] J. Sandler, M.S.P. Shaffer, A.H. Windle, M.P. Halsall, M.A. Montes-Moran, C.A. Cooper, and R.J. Young, "Variations in the Raman Peak Shift as a Function of Hydrostatic Pressure for Various Carbon Nanostructures: A Simple Geometric Effect," *Physical Review B* **67**, 35417 (2003).
- [110] U.D. Venkateswaran, "Squeezing Carbon Nanotubes," *Physica Status Solidi B* **241**, 3345 (2004).
- [111] S. Kazaoui, N. Minami, H. Yamawaki, K. Aoki, H. Kataura, and Y. Achiba, "Pressure Dependence of the Optical Absorption Spectra of Single-Walled Carbon Nanotube Films," *Physical Review B* **62**, 1643 (2000).
- [112] J. Wu, W. Walukiewicz, W. Shan, E. Bourret-Courchesne, J.W. Ager III, K.M. Yu, E.E. Haller, K. Kissell, S.M. Bachilo, R.B. Weisman, and R.E. Smalley, "Structure-Dependent Hydrostatic Deformation Potentials of Individual Single-Walled Carbon Nanotubes," *Physical Review Letters* **93**, 17404 (2004).
- [113] R.B. Capaz, C.D. Spataru, P. Tangney, M.L. Cohen, and S.G. Louie, "Hydrostatic Pressure Effects on the Structural and Electronic Properties of Carbon Nanotubes," *Physica Status Solidi B* **241**, 3352 (2004).
- [114] A.C. Dillon, P.A. Parilla, J.L. Alleman, T. Gennett, K.M. Jones, and M.J. Heben, "Systematic Inclusion of Defects in Pure Carbon Single-Wall Nanotubes and Their Effect on the Raman D-band," *Chemical Physics Letters* **401**, 522 (2005).
- [115] J.G. Wiltshire, A.N. Khlobystov, L.J. Li, S.G. Lyapin, G.A.D. Briggs, and R.J. Nicholas, "Comparative Study on Acid and Thermal Based Selective Purification of HiPco Produced Single-Walled Carbon Nanotubes," *Chemical Physics Letters* **386**, 239 (2004).
- [116] K.J. Ziegler, Z. Gu, H. Peng, E.L. Flor, R.H. Hauge, and R.E. Smalley, "Controlled Oxidative Cutting of Single-Walled Carbon Nanotubes," *Journal of the American Chemical Society* **127**, 1541 (2005).
- [117] B.N. Khare, P. Wilhite, R.C. Quinn, B. Chen, R.H. Schingler, B. Tran, H. Imanaka, C.R. So, C.W. Bauschlicher Jr., and M. Meyyappan, "Functionalization of Carbon Nanotubes by Ammonia Glow-Discharge: Experiments and Modeling," *Journal of Physical Chemistry B* **108**, 8166 (2004).
- [118] A.M. Rao, P.C. Eklund, S. Bandow, A. Thess, and R.E. Smalley, "Evidence for Charge Transfer in Doped Carbon Nanotube Bundles from Raman Scattering," *Nature* **388**, 257 (1997).
- [119] K. McGuire, N. Gothard, P.L. Gai, M.S. Dresselhaus, G. Sumanasekera, and A.M. Rao, "Synthesis and Raman Characterization of Boron-Doped Single-Walled Carbon Nanotubes," *Carbon* **43**, 219 (2005).
- [120] S. Gupta, M. Hughes, A.H. Windle, and J. Robertson, "Charge Transfer in Carbon Nanotube Actuators Investigated Using In Situ Raman Spectroscopy," *Journal of Applied Physics* **95**, 2038 (2004).
- [121] M. Stoll, P.M. Rafailov, W. Frenzel, and C. Thomsen, "Electrochemical and Raman Measurements on Single-Walled Carbon Nanotubes," *Chemical*

- Physics Letters **375**, 625 (2003).
- [122] P. Corio, P.S. Santos, V.W. Brar, G.G. Samsonidze, S.G. Chou, and M.S. Dresselhaus, "Potential Dependent Surface Raman Spectroscopy of Single Wall Carbon Nanotube Films on Platinum Electrodes," *Chemical Physics Letters* **370**, 675 (2003).
- [123] L. Kavan, P. Rapta, L. Dunsch, M.J. Bronikowski, P. Willis, and R.E. Smalley, "Electrochemical Tuning of Electronic Structure of Single-Walled Carbon Nanotubes: In-situ Raman and Vis-NIR Study," *Journal of Physical Chemistry B* **105**, 10764 (2001).
- [124] P. Corio, A. Jorio, N. Demir, and M.S. Dresselhaus, "Spectro-Electrochemical Studies of Single Wall Carbon Nanotubes Films," *Chemical Physics Letters* **392**, 396 (2004).
- [125] P.M. Rafailov, M. Stoll, and C. Thomsen, "Strain Determination in Electrochemically Doped Single-Walled Carbon Nanotubes via Raman Spectroscopy," *Journal of Physical Chemistry B* **108**, 19241 (2004).
- [126] S. Lefrant, M. Baibarac, I. Baltog, J.Y. Mevellec, L. Mihut, and O. Chauvet, "SERS Spectroscopy Studies on the Electrochemical Oxidation of Single-Walled Carbon Nanotubes in Sulfuric Acid Solutions," *Synthetic Metals* **144**, 133 (2004).
- [127] M.N. Iliev, A.P. Litvinchuk, S. Areppalli, P. Nikolaev, and C.D. Scott, "Fine Structure of the Low-frequency Raman Phonon Bands of Single-wall Carbon Nanotubes," *Chemical Physics Letters* **316**, 217 (2000).
- [128] C.C. Kao and R.J. Young, "A Raman Spectroscopic Investigation of Heating Effects and the Deformation Behaviour of Epoxy/SWNT Composites," *Composites Science and Technology* **64**, 2291 (2004).
- [129] Y. Yosida, "High-Temperature Shrinkage of Single-Walled Carbon Nanotube Bundles up to 1600K," *Journal of Applied Physics* **87**, 3338 (2000).
- [130] Y. Maniwa, R. Fujiwara, H. Kira, H. Tou, H. Kataura, S. Suzuki, Y. Achiba, E. Nishibori, M. Takata, M. Takata, A. Fujiwara, and H. Suematsu, "Thermal Expansion of Single-Walled Carbon Nanotube (SWNT) Bundles: X-ray Diffraction Studies," *Physical Review B* **64**, 241402 (2001).
- [131] H. Jiang, B. Liu, Y. Huang, and K.C. Hwang, "Thermal Expansion of Single Wall Carbon Nanotubes," *Journal of Engineering Materials and Technology* **126**, 265 (2004).
- [132] Y. Kwon, S. Berber, and D. Tomanek, "Thermal Contraction of Carbon Fullerenes and Nanotubes," *Physical Review Letters* **92**, 15901 (2004).
- [133] A.C. Bailey and B. Yates, "Anisotropic Thermal Expansion of Pyrolytic Graphite at Low Temperatures," *Journal of Applied Physics* **41**, 5088 (1970).
- [134] N.R. Raravikar, P. Keblinski, A.M. Rao, M.S. Dresselhaus, L.S. Schadler, and P.M. Ajayan, "Temperature Dependence of Radial Breathing Mode Raman Frequency of Single-Walled Carbon Nanotubes," *Physical Review B* **66**, 235424 (2002).
- [135] S.V. Terekhov, E.D. Obraztsova, A.S. Lobach, and V.I. Konov, "Laser Heating Method for Estimation of Carbon Nanotube Purity," *Applied Physics A* **74**, 393 (2002).
- [136] Z. Yu and L.E. Brus, "Reversible Oxidation Effect in Raman Scattering from Metallic Single-Wall Carbon Nanotubes," *Journal of Physical Chemistry A* **104**, 10995 (2000).

- [137] S. Nagasawa, M. Yudasaka, K. Hirahara, T. Ichihashi, and S. Iijima, "Effect of Oxidation on Single-Wall Carbon Nanotubes," *Chemical Physics Letters* **328**, 374 (2000).
- [138] M. Yudasaka, H. Kataura, T. Ichihashi, L.-C. Qin, S. Kar, and S. Iijima, "Diameter Enlargement of HiPco Single-Wall Carbon Nanotubes by Heat Treatment," *Nano Letters* **1**, 487 (2001).
- [139] M. Zhang, M. Yudasaka, and S. Iijima, "Diameter Enlargement of Single-Wall Carbon Nanotubes by Oxidation," *Journal of Physical Chemistry B* **108**, 149 (2004).
- [140] C. Fantini, A. Jorio, M. Souza, M.S. Strano, M.S. Dresselhaus, and M.A. Pimenta, "Optical Transition Energies for Carbon Nanotubes from Resonant Raman Spectroscopy: Environment and Temperature Effects," *Physical Review Letters* **93**, 147406 (2004).
- [141] J. Lefebvre, P. Finnie, and Y. Homma, "Temperature-Dependent Photoluminescence from Single-Walled Carbon Nanotubes," *Physical Review B* **70**, 45419 (2004).
- [142] D. Bernaerts, A. Zettl, N.G. Chopra, A. Thess, and R.E. Smalley, "Electron Diffraction Study of Single-Wall Carbon Nanotubes," *Solid State Communications* **105**, 145 (1998).
- [143] H. Kataura, Y. Kumazawa, Y. Maniwa, Y. Ohtsuka, R. Sen, S. Suzuki, and Y. Achiba, "Diameter Control of Single-Walled Carbon Nanotubes," *Carbon* **38**, 1691 (2000).
- [144] C.L. Cheung, A. Kurtz, H. Park, and C.M. Lieber, "Diameter-Controlled Synthesis of Carbon Nanotubes," *Journal of Physical Chemistry B* **106**, 2429 (2002).
- [145] S. Han, T.Yu, J. Park, B. Koo, J. Joo, T. Hyeon, S. Hong, and J. Im, "Diameter-Controlled Synthesis of Discrete and Uniform-Sized Single-Walled Carbon Nanotubes Using Monodisperse Iron Oxide Nanoparticles Embedded in Zirconia Nanoparticle Arrays as Catalysts," *Journal of Physical Chemistry B* **108**, 8091 (2004).
- [146] M. Yudasaka, M. Zhang, and S. Iijima, "Diameter-selective Removal of Single-wall Carbon Nanotubes Through Light-assisted Oxidation," *Chemical Physics Letters* **374**, 132 (2003).
- [147] P.G. Collins, M.S. Arnold, and P. Avouris, "Engineering Carbon Nanotubes Using Electrical Breakdown," *Science* **292**, 706 (2001).
- [148] H. Butt, K. Graf, M. Kappl, *Physics and Chemistry of Interfaces*, Wiley-VCH (2003).
- [149] T.W. Odom, J. Huang, P. Kim, M. Ouyang, and C.M. Lieber, "Scanning Tunneling Microscopy and Spectroscopy Studies of Single Wall Carbon Nanotubes," *Journal of Materials Research* **13**, 2380 (1998).
- [150] W. Clauss, D.J. Bergeron, and A.T. Johnson, "Atomic Resolution STM Imaging of a Twisted Single-wall Carbon Nanotube," *Physical Review B* **58**, 4266 (1998).
- [151] T.W. Odom, J.-L. Huang, P. Kim, and C.M. Lieber, "Structure and Electronic Properties of Carbon Nanotubes," *Journal of Physical Chemistry B* **104**, 2794 (2000).
- [152] M. Ouyang, J. Huang, and C.M. Lieber, "Fundamental Electronic Properties and Applications of Single-Walled Carbon Nanotubes," *Accounts of*

- Chemical Research* **35**, 1018 (2002).
- [153] M. Ouyang, J.-L. Huang, C.L. Cheung, and C.M. Lieber, "Atomically Resolved Single-Walled Carbon Nanotube Intramolecular Junctions," *Science* **291**, 97 (2001).
- [154] J.M. Cowley, P. Nikolaev, A. Thess, and R.E. Smalley, "Electron Nano-Diffraction Study of Carbon Single-Walled Nanotube Ropes," *Chemical Physics Letters* **265**, 379 (1997).
- [155] L.-C. Qin, S. Iijima, H. Kataura, Y. Maniwa, S. Suzuki, and Y. Achiba, "Helicity and Packing of Single-Walled Carbon Nanotubes Studied by Electron Nanodiffraction," *Chemical Physics Letters* **268**, 101 (1997).
- [156] G.S. Duesberg, W.J. Blau, H.J. Byrne, J. Muster, M. Burghard, and S. Roth, "Experimental Observation of Individual Single-wall Nanotube Species by Raman Microscopy," *Chemical Physics Letters* **310**, 8 (1999).
- [157] M. Canonico, G.B. Adams, C. Poweleit, J. Menendez, J.B. Page, G. Harris, H.P. van der Meulen, J.M. Calleja, and J. Rubio, "Characterization of Carbon Nanotubes Using Raman Excitation Profiles," *Physical Review B* **65**, 201402 (2002).
- [158] M.S. Strano, S.K. Doorn, E.H. Haroz, C. Kittrell, R.H. Hauge, and R.E. Smalley, "Assignment of (n,m) Raman and Optical Features of Metallic Single-walled Carbon Nanotubes," *Nano Letters* **3**, 1091 (2003).
- [159] S.K. Doorn, D.A. Heller, P.W. Barone, M.L. Usrey, and M.S. Strano, "Resonant Raman Excitation Profiles of Individually Dispersed Single Walled Carbon Nanotubes in Solution," *Applied Physics A* **78**, 1147 (2004).
- [160] Y. Ohno, S. Kishimoto, T. Mizutani, T. Okazaki, and H. Shinohara, "Chirality Assignment of Individual Single-Walled Carbon Nanotubes in Carbon Nanotube Field-Effect Transistors by Micro-Photocurrent Spectroscopy," *Applied Physics Letters* **84**, 1368 (2004).
- [161] A. Hagen and T. Hertel, "Quantitative Analysis of Optical Spectra from Individual Single-Wall Carbon Nanotubes," *Nano Letters* **3**, 383 (2003).
- [162] M. J. O'Connell, S. M. Bachilo, C. B. Huffman, V. C. Moore, M. S. Strano, E. H. Haroz, K. L. Rialon, P. J. Boul, W. H. Noon, C. Kittrell, J. Ma, R. H. Hauge, R. B. Weisman, and R. E. Smalley, *Science* **297**, 593 (2002).
- [163] L. Li, R.J. Nicholas, R.S. Deacon, and P.A. Shields, "Chirality Assignment of Single-Walled Carbon Nanotubes with Strain," *Physical Review B* **70**, 156104 (2004).
- [164] R.B. Weisman, S.M. Bachilo, and D. Tsyboulski, "Fluorescence Spectroscopy of Single-Walled Carbon Nanotubes in Aqueous Suspension," *Applied Physics A* **78**, 1111 (2004).
- [165] L.C. Venema, V. Meunier, P. Lambin, and C. Dekker, "Atomic Structure of Carbon Nanotubes from Scanning Tunneling Microscopy," *Physical Review B* **61**, 2991 (2000).
- [166] A. Kleiner and S. Eggert, "Curvature, Hybridization, and STM Images of Carbon Nanotubes," *Physical Review B* **64**, 113402 (2001).
- [167] P. Lambin, V. Meunier, L. Henrard, and A.A. Lucas, "Measuring the Helicity of Carbon Nanotubes," *Carbon* **38**, 1713 (2000).
- [168] R. Saito, G. Dresselhaus, and M.S. Dresselhaus, "Trigonal Warping Effect of Carbon Nanotubes," *Physical Review B* **61**, 2981 (2000).
- [169] A. Kleiner and S. Eggert, "Band Gaps of Primary Metallic Carbon

- Nanotubes," *Physical Review B* **63**, 73408 (2001).
- [170] M. Ouyang, J.-L. Huang, C.L. Cheung, and C.M. Lieber, "Energy Gaps in "Metallic" Single-Walled Carbon Nanotubes," *Science* **292**, 702 (2001).
- [171] J. Kurti, V. Zolyomi, M. Kertesz, G. Sun, R.H. Baughman, and H. Kuzmany, "Individualities and Average Behavior in the Physical Properties of Small Diameter Single-Walled Carbon Nanotubes," *Carbon* **42**, 971 (2004).
- [172] A.G. Souza Filho, S.G. Chou, G.G. Samsonidze, G. Dresselhaus, M.S. Dresselhaus, L. An, J. Liu, A.K. Swan, M.S. Unlu, B.B. Goldberg, A. Jorio, A. Gruneis, and R. Saito, "Stokes and Anti-Stokes Raman Spectra of Small-Diameter Isolated Carbon Nanotubes," *Physical Review B* **69**, 115428 (2004).
- [173] J.W. Mintmire and C.T. White, "First-principles Band Structures of Armchair Nanotubes," *Applied Physics A* **67**, 65 (1998).
- [174] S. Reich, C. Thomsen, and P. Ordejon, "Electronic Band Structure of Isolated and Bundled Carbon Nanotubes," *Physical Review B* **65**, 155411 (2002).
- [175] V. Zolyomi and J. Kurti, "First-Principles Calculations for the Electronic Band Structures of Small Diameter Single-Wall Carbon Nanotubes," *Physical Review B* **70**, 85403 (2004).
- [176] V. Barone and G.E. Scuseria, "Theoretical Study of the Electronic Properties of Narrow Single-Walled Carbon Nanotubes: Beyond the Local Density Approximation," *Journal of Chemical Physics* **121**, 10376 (2004).
- [177] R. Saito, M. Fujita, G. Dresselhaus, and M.S. Dresselhaus, "Electronic Structure of Graphene Tubules Based on C_{60} ," *Physical Review B* **46**, 1804 (1992).
- [178] P. Kim, T.W. Odom, J. Huang, and C.M. Lieber, "STM Study of Single-Walled Carbon Nanotubes," *Carbon* **38**, 1741 (2000).
- [179] R.B. Weisman and S.M. Bachilo, "Dependence of Optical Transition Energies on Structure for Single-Walled Carbon Nanotubes in Aqueous Suspension: An Empirical Kataura Plot," *Nano Letters* **3**, 1235 (2003).
- [180] L. Henrard, E. Hernandez, P. Bernier, and A. Rubio, "Van der Waals Interaction in Nanotube Bundles: Consequences on Vibrational Modes," *Physical Review B* **60**, 8521 (1999).
- [181] L. Henrard, V.N. Popov, and A. Rubio, "Influence of Packing on the Vibrational Properties of Infinite and Finite Bundles of Carbon Nanotubes," *Physical Review B* **64**, 205403 (2001).
- [182] P. Delaney, H.J. Choi, J. Ihm, S.G. Louie, and M.L. Cohen, "Broken Symmetry and Pseudogaps in Ropes of Carbon Nanotubes," *Nature* **391**, 466 (1998).
- [183] Y.-K. Kwon, S. Saito, and D. Tomanek, "Effect of Intertube Coupling on the Electronic Structure of Carbon Nanotube Ropes," *Physical Review B* **58**, 13314 (1998).
- [184] A.M. Rao, J. Chen, E. Richter, U. Schlecht, P.C. Eklund, R.C. Haddon, U.D. Venkateswaran, Y.-K. Kwon, and D. Tománek, "Effect of Van der Waals Interactions on the Raman Modes in Single Walled Carbon Nanotubes," *Physical Review Letters* **86**, 3895 (2001).
- [185] M.J. O'Connell, S. Sivaram, and S.K. Doorn, "Near-Infrared Resonance Raman Excitation Profile Studies of Single-Walled Carbon Nanotube Intertube Interactions: A Direct Comparison of Bundled and Individually Dispersed HiPco

- Nanotubes," *Physical Review B* **69**, 235415 (2004).
- [186] S.K. Doorn, M.S. Strano, M.J. O'Connell, E.H. Haroz, K.L. Rialon, R.H. Hauge, and R.E. Smalley, "Capillary Electrophoresis Separations of Bundled and Individual Carbon Nanotubes," *Journal of Physical Chemistry B* **107**, 6063 (2003).
- [187] V.C. Moore, M.S. Strano, E.H. Haroz, R.H. Hauge, and R.E. Smalley, "Individually Suspended Single-walled Carbon Nanotubes in Various Surfactants," *Nano Letters* **3**, 1379 (2003).
- [188] S.G. Chou, H.B. Ribeiro, E.B. Barros, A.P. Santos, D. Nezich, G.G. Samsonidze, C. Fantini, M.A. Pimenta, A. Jorio, F. Plentz Filho, M.S. Dresselhaus, G. Dresselhaus, R. Saito, M. Zheng, G.B. Onoa, E.D. Semke, A.K. Swan, M.S. Unlu, and B.B. Goldberg, "Optical Characterization of DNA-Wrapped Carbon Nanotube Hybrids," *Chemical Physics Letters* **397**, 296 (2004).
- [189] D.A. Heller, P.W. Barone, J.P. Swanson, R.M. Mayrhofer, and M.S. Strano, "Using Raman Spectroscopy to Elucidate the Aggregation State of Single-Walled Carbon Nanotubes," *Journal of Physical Chemistry B* **108**, 6905 (2004).
- [190] A. Hartschuh, H.N. Pedrosa, L. Novotny, and T.D. Krauss, "Simultaneous Fluorescence and Raman Scattering from Single Carbon Nanotubes," *Science* **301**, 1354 (2003).
- [191] L. Li, R.J. Nicholas, C. Chen, R.C. Darton, and S.C. Baker, "Comparative Study of Photoluminescence of Single-Walled Carbon Nanotubes Wrapped with Sodium Dodecyl Sulfate, Surfactin and Polyvinylpyrrolidone," *Nanotechnology* **16**, S202 (2005).
- [192] S. Reich, J. Maultzsch, C. Thomsen, and P. Orderon, "Tight-Binding Description of Graphene," *Physical Review B* **66**, 35412 (2002).
- [193] P.R. Wallace, "The Band Theory of Graphite," *Physical Review* **71**, 622 (1947).
- [194] Ge.G. Samsonidze, R. Saito, A. Jorio, A.G. Souza Filho, A. Gruneis, M.A. Pimenta, G. Dresselhaus, and M.S. Dresselhaus, "Phonon Trigonal Warping Effect in Graphite and Carbon Nanotubes," *Physical Review Letters* **90**, 27403 (2003).
- [195] N. Bernstein and E. Kaxiras, "Nonorthogonal Tight-Binding Hamiltonians for Defects and Interfaces in Silicon," *Physical Review B* **56**, 10488 (1997).
- [196] M.S. Strano, "Probing Chiral Selective Reactions Using a Revised Kataura Plot for the Interpretation of Single-Walled Carbon Nanotube Spectroscopy," *Journal of the American Chemical Society* **125**, 16148 (2003).
- [197] I.W. Chiang, B.E. Brinson, R.E. Smalley, J.L. Margrave, and R.H. Hauge, "Purification and Characterization of Single-Wall Carbon Nanotubes," *Journal of Physical Chemistry B* **105**, 1157 (2001).
- [198] Y. Huang and R.J. Young, "Analysis of the Fragmentation Test for Carbon-Fibre/Epoxy Model Composites by Means of Raman Spectroscopy," *Composite Science and Technology* **52**, 505 (1994).
- [199] H. Kataura, Y. Kumazawa, Y. Maniwa, I. Umezawa, S. Suzuki, Y. Ohtsuka, and Y. Achiba, "Optical Properties of Single-Wall Carbon Nanotubes," *Synthetic Metals* **103**, 2555 (1999).
- [200] L. Valentini, J. Biagiotti, J.M. Kenny, and S. Santucci, "Effects of Single-

- Walled Carbon Nanotubes on the Crystallization Behavior of Polypropylene," *Journal of Applied Polymer Science* **87**, 708 (2002).
- [201] G. Chambers, C. Carroll, G.F. Farrell, A.B. Dalton, M. McNamara, M. in het Panhuis, and H.J. Byrne, "Characterization of the Interaction of Gamma Cyclodextrin with Single-Walled Carbon Nanotubes," *Nano Letters* **3**, 843 (2003).
- [202] M.A. Lopez-Manchado, J. Biagiotti, L. Valentini, and J.M. Kenny, "Dynamical Mechanical and Raman Spectroscopy Studies on Interaction Between Single-Walled Carbon Nanotubes and Natural Rubber," *Journal of Applied Polymer Science* **92**, 3394 (2004).
- [203] P.V. Teredesai, A.K. Sood, S.M. Sharma, S. Karmakar, S.K. Sikka, A. Govindaraj, and C.N.R. Rao, "Pressure Effects on Single Wall Carbon Nanotube Bundles," *Physica Status Solidi B* **223**, 479 (2001).
- [204] J.P. Lu, "Elastic Properties of Carbon Nanotubes and Nanoropes," *Physical Review Letters* **79**, 1297 (1997).
- [205] J. Liu, T. Wang, T. Uchida, and S. Kumar, "Carbon Nanotube Core-Polymer Shell Nanofibers," *Journal of Applied Polymer Science* **96**, 1992 (2004).
- [206] D. Hull, *An introduction to composite materials*, Cambridge Solid State Science Series (Cambridge University Press, Cambridge, 1981).
- [207] R.B. Yallee and R.J. Young, "Micromechanics of Fibre Fragmentation in Model Epoxy Composites Reinforced with α -alumina Fibres," *Composites: Part A* **29**, 1353 (1998).
- [208] J. Halary, P. Cookson, J.L. Stanford, P.A. Lovell, and R.J. Young, "Smart Nanostructured Polymeric Coatings for Use as Remote Optical Strain Sensors," *Advanced Engineering Materials* **6**, 729 (2004).
- [209] Q. Zhao, M.D. Frogley, and H.D. Wagner, "Direction-Sensitive Strain-Mapping with Carbon Nanotube Sensors," *Composites Science and Technology* **62**, 147 (2002).
- [210] J.-P. Salvetat, G.A.D. Briggs, J.-M. Bonard, R.R. Bacsa, A.J. Kulik, T. Stöckli, N.A. Burnham, and L. Forró, "Elastic and Shear Moduli of Single-Walled Carbon Nanotube Ropes," *Physical Review Letters* **82**, 944 (1999).
- [211] Y. Huang and R.J. Young, "Interfacial Behaviour in High Temperature Cured Carbon Fibre/Epoxy Resin Model Composite," *Composites* **26**, 541 (1995).
- [212] J. Lange, S. Toll, J.-A.E. Månsen, and A. Hult, "Residual Stress Build-Up in Thermoset Films Cured Above Their Ultimate Glass Transition Temperature," *Polymer* **36**, 3135 (1995).
- [213] H.-B. Wang, Y.-G. Yang, H.-H. Yu, and W.-M. Sun, "Assessment of Residual Stresses During Cure and Cooling of Epoxy Resins," *Polymer Engineering and Science* **35**, 1895 (1995).
- [214] R.I. Todd, A.R. Boccaccini, R. Sinclair, R.B. Yallee, and R.J. Young, "Thermal Residual Stresses and Their Toughening Effect in Al_2O_3 Platelet Reinforced Glass," *Acta Materialia* **47**, 3233 (1999).
- [215] M.I. Pope and M.D. Judd, *Differential Thermal Analysis, A Guide to the Technique and its Applications* (Heyden, London, 1977).
- [216] Y. Maniwa, R. Fujiwara, H. Kira, H. Tou, E. Nishibori, M. Takata, M. Sakata, A. Fujiwara, X. Zhao, S. Iijima, and Y. Ando, "Multiwalled Carbon

- Nanotubes Grown in Hydrogen Atmosphere: An X-ray Diffraction Study," *Physical Review B* **64**, 073105 (2001).
- [217] R.R. Bacsa, A. Peigney, C. Laurent, P. Puech, and W.S. Bacsa, "Chirality of Internal Metallic and Semiconducting Carbon Nanotubes," *Physical Review B* **65**, R161404 (2002).
- [218] S.B. Cronin, A.K. Swan, M.S. Unlu, B.B. Goldberg, M.S. Dresselhaus, and M. Tinkham, "Measuring the Uniaxial Strain of Individual Single-Wall Carbon Nanotubes: Resonance Raman Spectra of Atomic-Force-Microscope Modified Single-Wall Nanotubes," *Physical Review Letters* **93**, 167401 (2004).
- [219] J.M. Yang, W.Y. Su, T.L. Leu, and M.C. Yang, "Evaluation of Chitosan/PVA Blended Hydrogel Membranes," *Journal of Membrane Science* **236**, 39 (2004).
- [220] C. Shao, H. Kim, J. Gong, B. Ding, D. Lee, and S. Park, "Fiber Mats of Poly(vinyl alcohol)/Silica Composite via Electrospinning," *Materials Letters* **57**, 1579 (2003).